

# Production of Cold Antihydrogen during the Positron Cooling of Antiprotons

A thesis presented

by

Nathaniel Sean Bowden

to

The Department of Physics

in partial fulfillment of the requirements

for the degree of

Doctor of Philosophy

in the subject of

Physics

Harvard University

Cambridge, Massachusetts

October 2003

©2003 - Nathaniel Sean Bowden

All rights reserved.

Thesis advisor

Author

**Gerald Gabrielse**

**Nathaniel Sean Bowden**

## **Production of Cold Antihydrogen during the Positron Cooling of Antiprotons**

### **Abstract**

The production of cold antihydrogen is one of several significant advances made towards a precision comparison of hydrogen and antihydrogen. New and improved accumulation and manipulation techniques make large numbers of electrons, positrons, and antiprotons routinely available for interaction experiments. This has allowed an extensive study of the interaction of antiprotons with positrons in a nested Penning trap to be conducted. Measurements of rate at which positrons cool the axial motion of antiprotons allow the determination of a fundamental cutoff parameter central to a theoretical description of this process. The theory can then be used to determine parameters important to the recombination of positrons and antiprotons to form antihydrogen. Unexpected antiproton cooling and loss is observed in the nested Penning trap, even without positrons being present. This loss, which remains unexplained, has serious consequences for antihydrogen detection schemes based upon the detection of simultaneous positron and antiproton annihilations. Consequently, a completely unambiguous and background free antihydrogen detection method is employed to verify that antihydrogen is produced during the positron cooling of antiprotons.

# Contents

Title Page . . . . .	i
Abstract . . . . .	iii
Table of Contents . . . . .	iv
List of Figures . . . . .	vii
List of Tables . . . . .	xiv
Publications . . . . .	xv
Acknowledgments . . . . .	xvii
<b>1 Introduction</b>	<b>1</b>
1.1 Motivation: testing the <i>CPT</i> theorem . . . . .	2
1.2 Antihydrogen milestones . . . . .	7
1.3 Antihydrogen formation processes . . . . .	8
1.4 Thesis outline . . . . .	9
<b>2 Apparatus</b>	<b>11</b>
2.1 Penning traps . . . . .	11
2.1.1 Theory of the Penning trap . . . . .	11
2.1.2 The HBAR1 Penning trap . . . . .	16
2.2 Particle detection . . . . .	21
2.2.1 Radio frequency amplifiers . . . . .	21
2.2.2 Particle charge measurements . . . . .	24
2.2.3 The PPAC . . . . .	29
2.2.4 Antiproton annihilation detectors . . . . .	30
2.2.5 The positron annihilation detector . . . . .	33
2.2.6 The data acquisition system . . . . .	35
2.3 The Antiproton Decelerator . . . . .	36
2.4 The fast timing system . . . . .	37
<b>3 Positron Accumulation and Manipulation</b>	<b>39</b>
3.1 Obtaining positrons . . . . .	39
3.1.1 The positron source . . . . .	40

3.1.2	The positron shielding enclosure . . . . .	43
3.2	Positron accumulation . . . . .	57
3.2.1	Formation and ionization of strongly magnetized Rydberg positronium . . . . .	57
3.2.2	Comparison of different radioactive sources . . . . .	63
3.2.3	Limitations of Rydberg positronium accumulation method . . . . .	65
3.2.4	Magnetic field dependence of the accumulation rate . . . . .	71
3.2.5	Alternative positron accumulation schemes . . . . .	76
3.3	Positron transfer through the ball valve . . . . .	84
3.3.1	Positron transfer through the ball valve using voltage pulses . . . . .	85
3.3.2	Ball valve transfer limitations . . . . .	91
3.3.3	Pulse transfer of large particle clouds . . . . .	95
<b>4</b>	<b>Electrons and Antiprotons</b>	<b>100</b>
4.1	Electron accumulation . . . . .	100
4.1.1	Electron accumulation using a field emission point . . . . .	101
4.1.2	Large electron cloud accumulation using a field emission point . . . . .	103
4.1.3	Electron accumulation using a positron source . . . . .	106
4.2	Antiproton accumulation . . . . .	117
4.2.1	Energy tuning . . . . .	117
4.2.2	Antiproton capture . . . . .	119
4.2.3	Electron cooling . . . . .	126
4.2.4	Antiproton stacking . . . . .	133
<b>5</b>	<b>Positron Cooling of Antiprotons</b>	<b>137</b>
5.1	Accumulating particles for interaction experiments . . . . .	137
5.2	The nested Penning trap . . . . .	139
5.2.1	Optimization of the nested Penning trap structure . . . . .	142
5.2.2	Optimization of launching method . . . . .	145
5.3	Positron cooling of antiprotons . . . . .	147
5.4	Recycled evaporative cooling . . . . .	159
5.5	Particle loss from the nested Penning trap . . . . .	162
<b>6</b>	<b>Production and Detection of Cold Antihydrogen</b>	<b>168</b>
6.1	Antihydrogen detection . . . . .	168
6.1.1	Antihydrogen detection using annihilation detectors . . . . .	169
6.1.2	Antihydrogen detection via field ionization . . . . .	171
6.2	Antihydrogen production experiments . . . . .	172
6.2.1	Potential structure used for antihydrogen production . . . . .	172
6.2.2	Cold antihydrogen production . . . . .	175
6.2.3	Dependence of antihydrogen production rate on positron number . . . . .	177

---

6.2.4	Dependence of antihydrogen production rate on detection well distance . . . . .	178
6.3	Cooling rate analysis . . . . .	180
6.4	Extensions to the cooling rate analysis . . . . .	187
<b>7</b>	<b>Conclusion</b>	<b>196</b>
<b>A</b>	<b>Radiation Shielding Calculation</b>	<b>200</b>
<b>B</b>	<b>Positron Production Calculation</b>	<b>203</b>
	<b>Bibliography</b>	<b>206</b>

# List of Figures

1.1	<i>CPT</i> tests involving comparisons of particle and antiparticle properties.	5
1.2	Testing the <i>CPT</i> theorem to the level possible in the <i>K</i> -meson system using antihydrogen would require a measurement beyond the natural line width. Also indicated are the advances made by the TRAP collaboration, the predecessor to ATRAP, in the comparison of protons and antiprotons.	6
2.1	The three motions performed by a particle in a Penning trap.	13
2.2	The potential is on the Penning trap axis (solid) is different from that 4 mm off axis (dashed).	15
2.3	The complete HBAR1 Penning trap apparatus.	18
2.4	A detailed drawing of the HBAR1 Penning trap.	19
2.5	A simplified drawing of the HBAR1 Penning trap, showing the electrodes and the surrounding particle detectors.	20
2.6	Oscillating charges couple to the resonator in the amplifier.	22
2.7	The noise resonance of an amplifier (a) is modified when there are 5 million electrons present (b).	23
2.8	The potentials used to dump particles to the degrader for charge measurements.	24
2.9	Example charge spectra: (a) 17 million positrons, (b) 29 million electrons.	25
2.10	Summing many clouds.	27
2.11	Charge spectra before (a) and after (b) side band cooling is applied.	28
2.12	Position of the scintillating fiber detectors.	32
2.13	The BGO detector assembly.	34
2.14	The Antiproton Decelerator.	36
3.1	<sup>22</sup> Na level scheme.	41
3.2	The source rod and source capsule.	42
3.3	The source shielding enclosure, shown connected to the Penning trap apparatus.	47
3.4	The corner piece.	50

3.5	The source is guided around the corner by the carefully designed groove.	51
3.6	Tension and radiation readings as a function of motor encoder position.	55
3.7	(a) Electrodes used to study positron accumulation. (b) A typical potential configuration used to accumulate positrons. . . . .	58
3.8	Accumulation of positrons (and electrons) is optimized by varying the potential applied to TMOD. Taken from [6]. . . . .	60
3.9	By applying an appropriate potential to RMOD, a second positronium formation channel can be opened up. Taken from [6]. . . . .	62
3.10	Scans over the ionization well potentials. The potential applied to the electrode P2 acts to smooth the electric field at the entrance to the ionization well and thus allows the positronium to ionize more deeply in the well. The potential applied to P3 forms the well for trapped positrons and that applied to P4 provides the ionizing electric field. Taken from [48]. . . . .	64
3.11	The electric field applied to the surface of the transmission moderator is scanned to compare the accumulation characteristics of the system first used to study the accumulation mechanism [6] and that used here.	65
3.12	The accumulation characteristics change as the gas layer crucial to Rydberg positronium is gradually removed. Thermally cycling the Penning trap apparatus restores the original accumulation rate. Taken from [6]. . . . .	67
3.13	The accumulation rate decreases when the gas layer on the transmission moderator is exposed to the positron beam. . . . .	69
3.14	Positron currents measured at the chopper wheel, transmission moderator, and reflection moderator. Error bars, of equal magnitude to those displayed for TMOD, are omitted from the RMOD and chopper wheel measurements for clarity. . . . .	73
3.15	Measured dependence of positron accumulation rate on magnetic field strength. The accumulation rate has been scaled to take account of the lower positron currents reaching the transmission and reflection moderators at lower magnetic fields. Solid line is the best quadratic fit to the data. . . . .	74
3.16	TMOD scans taken at various magnetic fields. . . . .	75
3.17	A simple diagram demonstrating the behavior in the $x - y$ plane of a moderated positron-secondary electron pair originating at the same point with the same radial energy. The solid trajectory has an axial magnetic field three times stronger than the dashed. The separation of the particles averaged over one cyclotron period is proportional to $r_c$ , which is proportional to $B$ . The number of times that the two particles return to the point of origin, or “collide,” is proportional to $\nu_c$ , which is also proportional to $B$ . The quantity $\nu_c/r_c$ may then provide a measure of how well correlated a pair are, yielding a $B^2$ scaling. . . . .	77

3.18	Positrons are cooled into a well via collisions with a large electron cloud. The space charge of the electron cloud is many hundreds of volts, and the positron beam energy must be carefully tuned to match the space charge. . . . .	81
3.19	Potential configurations that allow particles to be: (a) rapidly launched when the electrode holding the cloud is pulsed, (b) rapidly launched when an electrode adjacent to the electrodes is pulsed, (c) rapidly caught when the electrode holding the cloud is pulsed, (d) rapidly caught when an electrode adjacent to the electrodes is pulsed. . . . .	87
3.20	Measured positron and electron transit times as a function of transit distance. Solid curve is a simple prediction obtained for a single particle. The prediction correctly predicts the dependence upon transit distance (the slope), but underestimates the time for particles to move off the launch potential structure and onto the catch potential structure (the offset). This is not surprising, as for a many particle cloud those particles on the outside screen those on the inside. It is only after those on the outside have been accelerated away by the potential ramp that those on the inside will feel the external electric field. . . . .	88
3.21	(a) Electrodes used for pulsing investigations. (b) The potential structure used. The DC potential (solid) is modified when a voltage pulse is applied to the electrode P3 (dashed). Positrons in the P3 well are launched when the pulse is applied, and can be recaptured if the pulse returns at the appropriate time (c). The positron bunch can bounce multiple times in the potential structure, with a period of 114.5 ns. After 100 oscillations, the bunch has spread out, and 100% recatch efficiency can no longer be achieved. . . . .	89
3.22	Typical potential structures for pulsing positrons through the ball valve (a) with no other particles present, or (b) over antiprotons. . . . .	90
3.23	Transfer efficiency through the ball valve as a function of initial cloud size. Taken from [28]. . . . .	91
3.24	The “dip” resulting from 8 million positrons accumulated by pulsing many small bunches through the ball valve. . . . .	94
3.25	Transfer efficiency for a cloud of 8 million electrons using a single pulse. The peak transfer efficiency is $\approx 85\%$ . . . . .	96
3.26	(a) Electrodes used to pulse transfer large clouds. (b) Initial potential structure used to pulse transfer large clouds. Electrons are stored on electrode T5 and B1. (c) Electrodes B1 and T8 are pulsed to transfer some fraction of the electrons on B1 to T8. Any ions remain trapped on B1. (d) The electrons transferred to T8 can be combined with those on T5. The transfer process can then be repeated. When most electrons have been transferred, the B1 well, containing any ions, can be dumped to the degrader. . . . .	97

3.27	Transfer efficiency for a cloud of 8 million electrons using many pulses. The peak transfer efficiency is $\approx 95\%$ . . . . .	98
3.28	Another pulse transfer scheme would use two electrodes, and should thus be able to catch longer clouds. Solid line is the potential ramp on which particles are caught. Dashed line is well formed when one electrode is pulsed, while the dotted line is that formed when two electrodes are pulsed. Horizontal lines represent the approximate cloud length that can be caught in each case. . . . .	99
4.1	Potential structure used to load electrons using the FEP. . . . .	102
4.2	Electron accumulation rate via the FEP as a function of the total amount of time the FEP has been fired. . . . .	104
4.3	The charge spectrum of a very large electron cloud. . . . .	105
4.4	Very large electron clouds rapidly lose particles. Solid curve is to guide the eye. . . . .	105
4.5	Initial potential structure used to accumulate electrons using the positron source. Dashed lines indicate wells added in sequence to investigate the accumulation mechanism. . . . .	107
4.6	Electron accumulation rate as a function of the numbers of wells present. . . . .	108
4.7	Number of electrons accumulated on the electrode ER as a function of time. A “seed” cloud of 1.6 million electrons, accumulated in 300 s onto TBE, was placed on ER at $t = 0$ s. . . . .	108
4.8	When a “seed” cloud of 1.9 million electrons is split, the accumulation rate into each well depends on the initial number of electrons present. . . . .	109
4.9	Electron accumulation rate as a function of the voltage applied to the degrader (a), the electrode TBE (b), the electrode UPHV (c), and the electrodes T4, T6, T8, ER, PR, and B1 (d). The maximum rates vary as other potentials are not necessarily at their peak values. . . . .	112
4.10	The optimized potential structure for electron accumulation. . . . .	113
4.11	(a) The optimized potential structure for electron accumulation in the top trap. (b) The potential structure used to pulse electrons to the lower trap. . . . .	115
4.12	Optimization of accumulation time for electrons in the top trap. . . . .	116
4.13	Range curves taken over several days. The most efficient gas ratio changes in time due to accretion of residual gas upon the entrance window of the Penning trap. Proper evacuation of the solenoid bore eliminates this behavior. . . . .	119
4.14	The antiproton capture process. (a) Electrodes used to capture antiprotons. (b) Antiprotons emerge from the degrader with a range of energies. (c) Those with an energy less than 3 keV are reflected by the potential applied to the UPHV electrode. (d) The degrader potential is rapidly switched to trap the antiproton bunch. . . . .	123

4.15	The number of trapped antiprotons depends upon when the trapping potential is applied. . . . .	124
4.16	Energy spectra for antiprotons trapped from a single pulse from the AD. . . . .	124
4.17	The number of antiprotons held in the long well decreases as a function of storage time. . . . .	125
4.18	The trapping efficiency varies exponentially with the depth of the high voltage well. . . . .	125
4.19	(a) Electrodes used to accumulate cold antiprotons. (b) A small well on electrode T6 is preloaded with electrons before any antiprotons are accumulated. (c) As before, the potential applied to the degrader is rapidly switched to trap antiprotons in flight. (d) More than one electron well can be used to cool antiprotons. . . . .	128
4.20	The energy of the antiprotons in the long well decreases as a function of electron cooling time. The number also decreases insofar as some antiprotons are cooled into the small well and others are lost from the trap. . . . .	129
4.21	AD antiprotons are injected into the long trap every 108 s. For the subsequent 85 s, with or without cooling electrons, the number lost is approximately the same, but electrons cool some into the small well (or wells). Uncooled antiprotons remaining in the long well are then ejected. . . . .	130
4.22	Number of antiprotons captured, uncooled, spilled, and cooled from a single pulse of AD antiprotons. . . . .	131
4.23	Potentials for electron ejection. . . . .	132
4.24	Electron cooled antiproton spectrum. . . . .	133
4.25	Stacking successive pulses of antiprotons. . . . .	135
4.26	The energy spectrum of 9 stacked antiproton shots. . . . .	136
5.1	A simple nested Penning trap formed with potentials applied to five electrodes. . . . .	140
5.2	The first demonstration of positron cooling of antiprotons. (a) Without positrons, antiprotons remain at the high axial energy at which they were injected into the nested Penning trap. (b) When positrons are placed in the central well, the axial energy of most antiprotons is reduced. . . . .	141
5.3	The period of antiprotons in the outer well of a typical nested Penning trap as a function of axial energy. Note that as the axial energy approaches that of the central well the period becomes much greater. . . . .	142
5.4	Nested Penning traps formed from (a) five and (b) seven endcap electrodes before (solid) and during (dashed) a LVR. Note that the side well depth changes dramatically when the end electrode is ramped in the five endcap electrode case . . . . .	144

5.5	Antiprotons are introduced into a nested Penning trap with many electron volts of axial energy by releasing them from an offset well at one end of the nested Penning trap. . . . .	145
5.6	Energy spectra of antiprotons introduced into a nested Penning trap using (a) slow high voltage op-amps and (b) a fast pulse. . . . .	146
5.7	The pulsed launch of antiprotons into a nested Penning trap; (a) cross-section of electrodes used, (b) the leading edge of the pulse, and (c) the trailing edge of the pulse. . . . .	148
5.8	The nested Penning trap used for cooling studies. (a) Antiprotons are launched through a 5 mm aperture to “skim” off those at larger radii. (b) One side of the nested Penning trap is pulsed open to allow the antiprotons to enter. (c) Antiprotons are trapped in the nested Penning trap when voltage pulse returns. . . . .	149
5.9	(a-f) Antiproton axial energy spectra after different hold times in the nested Penning trap (200,000 positrons present in the central well). . . . .	150
5.10	Rate of antiproton axial energy loss depends on the number of positrons placed in either a 15 V (a) or 10 V (b) well. Solid curves are exponential fits to the data. The primary source of error in the data points is a variation of about 10% in the number of positrons used. . . . .	151
5.11	Cooling time constant versus positron plasma areal density (areal density = cloud thickness $\times$ volume density). . . . .	152
5.12	The fraction of time that antiprotons spend in a plasma of 200,000 positrons. The solid curve is a 4 parameter fit to the data that is used to incorporate it into the cooling time calculation. . . . .	154
5.13	The antiproton cooling rate measured compared to that predicted by [62] (solid curves) for various values of $\rho_{max}$ . . . . .	156
5.14	(a),(d) Antiproton energy as a function of interaction time. (b),(e) As energy is transferred from the antiprotons to the positrons, the positron temperature increases. (c),(f) The cooling rate, adjusted for the fraction of time that the antiprotons spend in the positron plasma. . . . .	158
5.15	Antiproton axial energy spectra taken (a) with and (b) without positrons in the central well. . . . .	161
5.16	(a) Antiproton axial energy spectra resulting from the interaction of a bunch of antiprotons placed in a side well with a bunch of antiprotons launched into the nested Penning trap. (b) Superposition of two independent antiproton axial energy spectra, one from launching a bunch into an otherwise empty nested Penning trap, the other from a bunch placed in a side well. . . . .	162
5.17	Nested Penning trap used to localize the antiproton loss. . . . .	163
5.18	(a) Integrated antiproton loss. Antiproton loss per second (b) without and (c) with positrons. . . . .	164
5.19	BGO multiplicity spectra. . . . .	166

6.1	(a) Electrodes used in antihydrogen production experiments. (b) Potentials structure used to produce antihydrogen. Antiprotons are introduced into the nested well by pulsing open an offset well (dashed line). (c) Electric field magnitude on the axis of the Penning trap (solid) and 4 mm off axis (dashed). . . . .	174
6.2	657 antiproton (antihydrogen) counts seen in the ionization well with positrons (a) and zero seen without positrons (b). At the time this result was published [1], this was more than the total number of antihydrogen atoms that had been observed in all other experiments [16, 17, 9].	176
6.3	Dependence of antihydrogen production on positron number. . . . .	177
6.4	Detected antihydrogen number as a function of ionization well distance.	179
6.5	(a) Positron cloud density, (b) axial extent, and (c) overlap with a cloud of 150,000 antiprotons, as determined by P. K. Oxley, using the methods described in [59, 28]. . . . .	183
6.6	(a) The number of antiprotons and (b) ratio of number of antiprotons to positrons used in the antihydrogen production experiments. . . . .	184
6.7	(a) The predicted antiproton energy and (b) positron temperature for 1.7 million positrons. . . . .	185
6.8	(a) The predicted recombination probability distribution and (b) positron temperature as a function of antiproton energy for 1.7 million positrons.	186
6.9	(a) $t_{\max}$ that yields $P_{\text{TBR}}(t_{\max}) = 1$ as a function of positron number. (b) Predicted recombination yield, as determined from (cloud overlap)/ $t_{\max}$ compared with experimental results. Predicted yield is scaled to match observed yield at 0.15 million positrons. . . . .	188
6.10	The predicted antihydrogen angular distribution for radial antiproton temperatures of 4.2 K, 10 K, and 20 K. $0^\circ$ corresponds to the positive z-axis. There is no predicted emission at $90^\circ$ or $270^\circ$ , since antiprotons never reach zero axial energy. . . . .	190
6.11	The predicted dependence of the recombination rate on ionization well distance for 4.2 K and 420 K (dashed lines). The predictions have been scaled to match the experimental data at 4 cm (solid line is $1/r^2$ fit to experimental data). . . . .	191
6.12	The applied axial electric field required to ionize an atom with radial separation $\rho$ (a) or binding energy $E_b$ (b). The dotted vertical lines mark the electric field range of the ionization well. Taken from [69]. . . . .	192
6.13	The time evolution of $\rho$ for $T_{e^+} = 4.2$ K and 10 K, as described by Eqn. 6.8. Dashed horizontal lines give the approximate range between which atoms are stripped by the ionization well. . . . .	193

# List of Tables

2.1	Typical frequencies in a Penning trap. . . . .	13
3.1	Comparison of various positron accumulation schemes. . . . .	78

# Publications

1. "First positron cooling of antiprotons,"  
G. Gabrielse, J. Estrada, J. N. Tan, P. Yesley, N. S. Bowden, P. Oxley, T. Roach, C. H. Storry, M. Wessels, J. Tan, D. Grzonka, W. Oelert, G. Schepers, T. Sefsick, W. Breunlich, M. Carnielli, H. Fuhrmann, R. King, R. Ursin, H. Zmeskal, H. Kalinowsky, C. Wesdorp, J. Walz, K. S. E. Eikema, and T. W. Hänsch,  
Phys. Lett. B **507**, 1, 2001.
2. "Stacking of cold antiprotons,"  
G. Gabrielse, N. S. Bowden, P. Oxley, A. Speck, C. H. Storry, J. N. Tan, M. Wessels, D. Grzonka, W. Oelert, G. Schepers, T. Sefzick, J. Walz, H. Pittner, T. W. Hänsch, and E. A. Hessels,  
Phys. Lett. B **548**, 140, 2002.
3. "Background-Free Observation of Cold Antihydrogen with Field-Ionization Analysis of Its States,"  
G. Gabrielse, N. S. Bowden, P. Oxley, A. Speck, C. H. Storry, J. N. Tan, M. Wessels, D. Grzonka, W. Oelert, G. Schepers, T. Sefzick, J. Walz, H. Pittner, T. W. Hänsch, and E. A. Hessels,  
Phys. Rev. Lett. **89**, 213401, 2002.
4. "Driven Production of Cold Antihydrogen and the First Measured Distribution of Antihydrogen States,"  
G. Gabrielse, N. S. Bowden, P. Oxley, A. Speck, C. H. Storry, J. N. Tan, M. Wessels, D. Grzonka, W. Oelert, G. Schepers, T. Sefzick, J. Walz, H. Pittner, T. W. Hänsch, and E. A. Hessels,  
Phys. Rev. Lett. **89**, 233401, 2002.
5. "Positron Cooling of Antiprotons Requires a New Theoretical Cutoff,"  
N. S. Bowden, P. Oxley, A. Speck, C. H. Storry, J. N. Tan, M. Wessels, G. Gabrielse, D. Grzonka, W. Oelert, G. Schepers, T. Sefzick, J. Walz, H. Pittner, T. W. Hänsch, and E. A. Hessels,  
Anticipated, 2003.
6. "Magnetic Field Dependence of Positron Accumulation via the Ionization of Highly Magnetized Rydberg Positronium,"  
N. S. Bowden, P. Oxley, A. Speck, C. H. Storry, J. N. Tan, M. Wessels, and G. Gabrielse,  
Anticipated, 2003.

7. “Aperture Scraping Method for Characterizing Trapped Particle Distributions,”  
P. Oxley, N. S. Bowden, A. Speck, C. H. Storry, J. N. Tan, M. Wessels,  
G. Gabrielse, D. Grzonka, W. Oelert, G. Schepers, T. Sefzick, J. Walz, H. Pit-  
tner, T. W. Hänsch, and E. A. Hessels,  
Anticipated, 2003.

# Acknowledgments

I would like to begin by acknowledging the great energy and drive of my advisor, Jerry Gabrielse. It is due to his sustained effort and vision that this project exists at all, and I am grateful that I have been able to participate in it. As an advisor, Jerry was always willing and able to provide insightful solutions to both scientific and administrative problems, and he worked extremely hard behind the scenes to ensure that all the resources required to complete this work were available. As the spokesperson and driving force of the ATRAP collaboration, he has successfully guided my own efforts and those of the other members of the collaboration towards our common goal.

The single most rewarding aspect of my time as a graduate student in Jerry's group has been the fantastic *corp d'esprit*, both in the Harvard lab and amongst the members of the ATRAP collaboration. I have been truly fortunate to work with a group of such supportive and intelligent people, and I wish them all the greatest success in the future.

I owe an enormous debt to the two graduate students who preceded me on this project, John Estrada and Peter Yesley. While their many years of hard work building and installing the experiment at CERN were not immediately rewarded with the production of antihydrogen, they should take satisfaction from the results presented here – they are a direct result of their efforts.

During my time as a member of ATRAP, fellow graduate student Paul Oxley has been a constant presence. I would like to thank him for initially showing me the ropes, and for the assistance that he has provided at every stage of this endeavor.

I've had the pleasure of working closely with two Harvard postdocs. Cody Storry, whose infectious *joie de vivre* ensured that the lab was always a fun place to be, was

relentless in the pursuit of new results and his patience and skill in building apparatus has raised the bar by several notches. When he wasn't repairing the HBAR1 trap or providing theoretical insight, Joseph Tan could always be relied upon to come up with crazy ideas, many of which actually worked.

The detector expertise supplied by our collaborators from Forschungszentrum Jülich, Walter Oelert, Dieter Grzonka, and Georg Schepers, has proved invaluable. It is a testament to the quality of their work, and that of the Jülich workshop, that the ATRAP detector system has operated continuously for almost four years.

Now that antihydrogen has been produced, I am glad that our collaborators from the Max-Planck-Institut für Quantenoptik, Jochen Walz, Heiko Pittner, and Max Herrmann, will soon to be able to demonstrate their considerable prowess in all things relating to lasers. In the meantime they have always been ready to pitch in and help out where needed, for example in assuming responsibility for the PPAC system.

The addition of York University to ATRAP has only strengthened the collaboration. Eric Hessels could always be relied upon to provide a fresh perspective or insight into a problem, while Daniel Comeau was always eager to help in any way that he could.

Fellow Harvard graduate students Melissa Wessels and Andrew Speck took time from their own projects to complete the often tedious job of keeping the CERN lab stocked, and provided many essential electronic components. Their efforts were much appreciated, as was their willingness to drop everything and join us at CERN when help was urgently required.

Thanks also to the other members of Jerry's Harvard lab, Brian Odom, Brian

D'urso, David Hanneke, Tanya Zelevinsky, and Dan Farkas, who took the time to explain their own experiments to me. And a special thanks to Brian D'urso, Andrew Speck, and David Hanneke for providing a reliable and secure computing environment.

Also at Harvard, Jan Rugusa provided able and cheerful administrative support. I was especially grateful for her efforts while I was stationed at CERN, when she always made sure that we were paid on time, in the correct currency. On the technical side, Stan Cotreau taught me just about everything I know about the machining of metal, and was always happy to provide advice and assistance.

On a personal note, I would like to thank all my family for all their love and support during my time in graduate school. Being half a world removed from home has been made easier by the knowledge that they were only a phone call away.

And last, but by no means least, I would like to thank JuNelle Harris for her unwavering love and encouragement during both the good times and the bad.

# Chapter 1

## Introduction

The major advance presented in this thesis is the production of cold antihydrogen [1]. This has been made possible by many experimental advances made by our ATRAP collaboration, and its predecessor, the TRAP collaboration, and is a significant milestone on the path to the ultimate goal of ATRAP: Testing the *CPT* theorem using antihydrogen [2]. The crucial experimental techniques are:

- The trapping, cooling, and stacking of antiprotons [3, 4],
- The efficient trapping of positrons in a near perfect vacuum [5, 6],
- The use of the nested Penning trap [7] to allow the interaction of trapped positrons and antiprotons [8].

So central are the antiproton accumulation and interaction techniques to this field of research, that they are utilized without modification by the only other group seeking to study antihydrogen [9]. In this work we study and further refine all of these techniques and apply them to antihydrogen production.

Much of the work presented here is the result of the efforts of many people, as the preceding publication list indicates. As one of two graduate students responsible for the day to day operation of the Penning trap and the more than 100 devices associated with it, I was heavily involved in the design and implementation of experiments, as well as the collection and analysis of almost all the data presented here. I had a leading role in the implementation of a more general form of the fast timing system (Sec. 2.4), the design, construction, and installation of the positron source shielding enclosure (Sec. 3.1.2), investigating the performance of a new, more intense positron source (Sec. 3.2.2), measurement of the magnetic field dependence of the positron accumulation rate (Sec. 3.2.4), and the comparison of experimental positron cooling results to theory (Sec. 5.3).

In the remainder of this chapter our motivation for performing these experiments will be described in more detail, as will significant milestones along the path. This will be followed by a brief review of the antihydrogen recombination processes likely to occur in our experiments and finally, the remainder of the thesis will be outlined.

## 1.1 Motivation: testing the $CPT$ theorem

The  $CPT$  theorem [10] states that all Lorentz-invariant, local field theories describing point particles are invariant under the combined transformation  $CPT$ , where  $C$  is the transformation that replaces particles with antiparticles (charge conjugation),  $P$  is that which reverses the coordinate axes (parity), and  $T$  is that which reverses time (time reversal). Examples of Lorentz-invariant, local field theories include the standard model and quantum electrodynamics, so it appears that the transformation

*CPT* is truly a fundamental symmetry of nature.

Of course, there have been occasions in the past where such statements have been proven by experiment to be false. In particular, it was a widely held belief that *P* alone was a fundamental symmetry. But it was pointed out by Lee and Yang [11] in 1956 that this had never been tested for the weak interaction. Shortly thereafter, in 1957, Wu *et al* found *P*-violation in the  $\beta$ -decay of polarized nuclei [12]. Experiments of this type were invariant under the combined transformation *CP*, and this was rapidly adopted as a fundamental symmetry. However, in 1964, Cronin and Fitch found a *CP* violating decay in the *K*-meson sector [13]. This history highlights the need to conduct experimental tests of basic physical theories, particularly those as fundamental as the *CPT* theorem. Furthermore, gravity has still resisted description by a quantum field theory. Possible candidates for a more fundamental theory, for example string theory, may include spontaneous breaking of the *CPT* symmetry [14].

Among the predications of the *CPT* theorem is that the charges, magnetic moments, masses, and lifetimes of particles and antiparticles should be identical. For bound matter/antimatter systems, the *CPT* theorem predicts identical spectroscopic structure. It is these relations that can be tested experimentally (Fig. 1.1). The *CPT* theorem should be tested in as many physical systems as is possible, hence our desire to study antihydrogen. The 1s-2s transition in hydrogen/antihydrogen is an especially attractive candidate for a precision comparison, due to the very high accuracy with which it can be measured. Presently, members of the ATRAP collaboration are able to measure this transition in hydrogen to an accuracy  $1.8 \times 10^{-14}$  [15]. If a measurement approaching this level of accuracy could be made of this transition in

---

antihydrogen, the *CPT* theorem could be tested to a level surpassing that possible in many other sectors. However, reaching the extraordinary level of accuracy possible in the *K*-meson sector, which would require a hydrogen/antihydrogen measurement better than the natural line width, would be extremely difficult (Fig. 1.2).

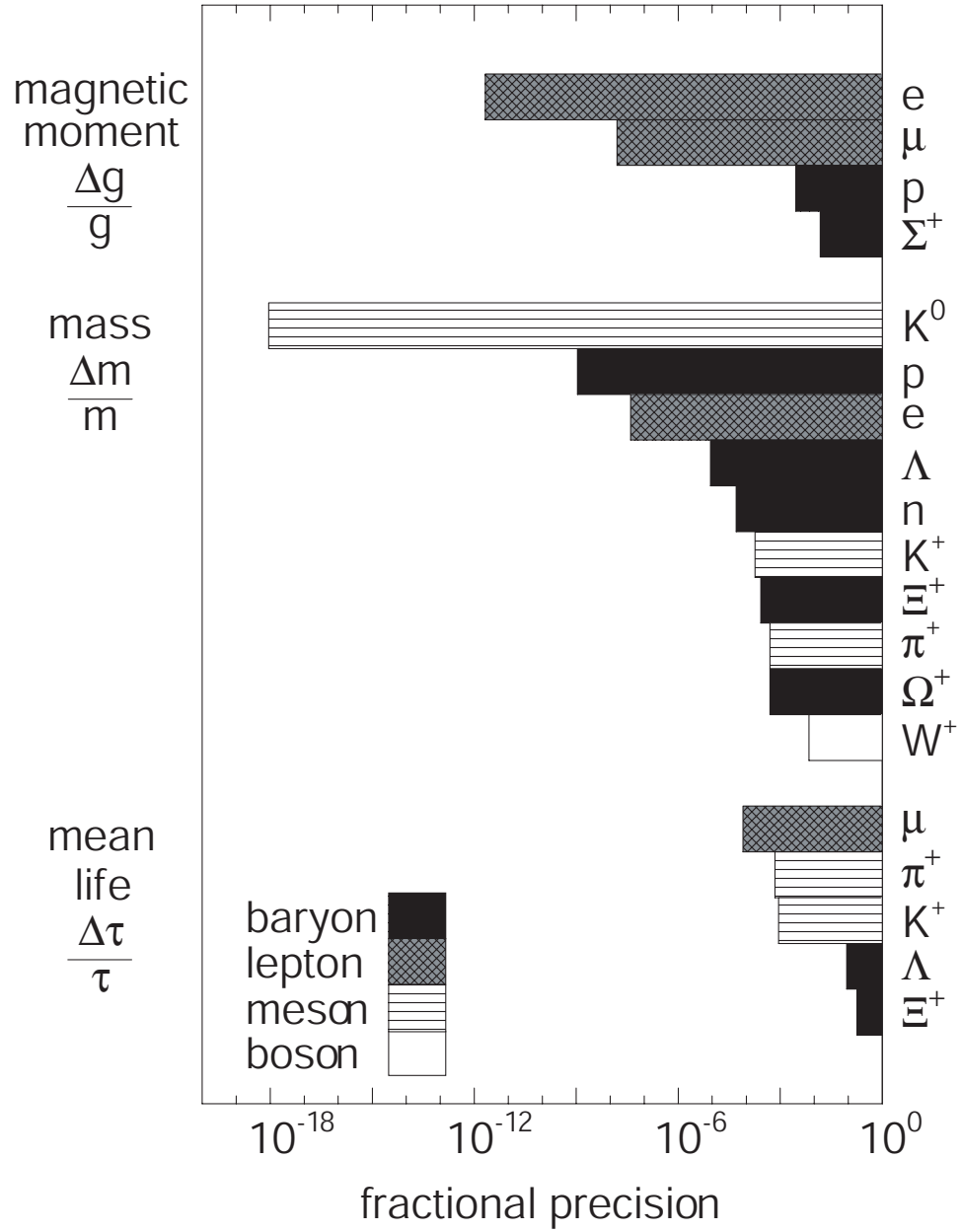


Figure 1.1: *CPT* tests involving comparisons of particle and antiparticle properties.

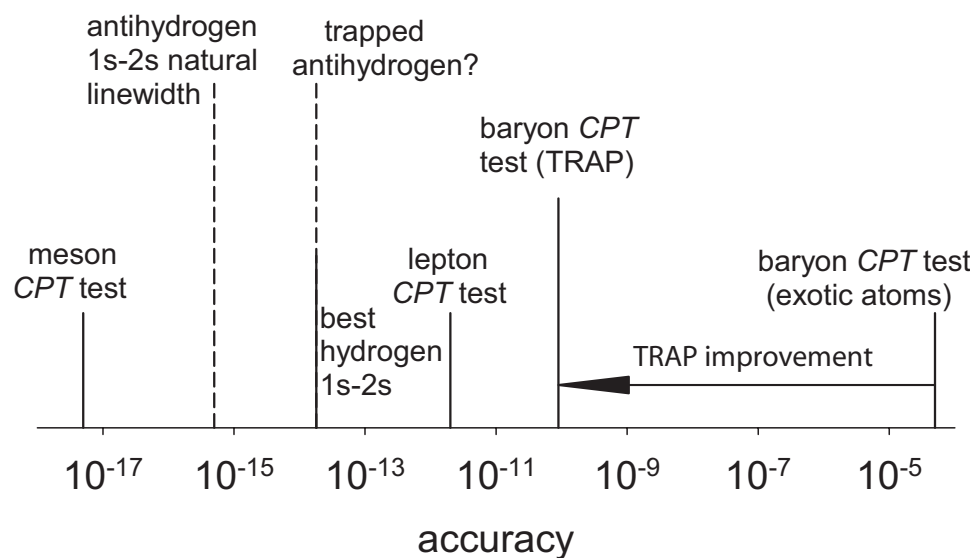


Figure 1.2: Testing the  $CPT$  theorem to the level possible in the  $K$ -meson system using antihydrogen would require a measurement beyond the natural line width. Also indicated are the advances made by the TRAP collaboration, the predecessor to ATRAP, in the comparison of protons and antiprotons.

## 1.2 Antihydrogen milestones

It should be noted that high velocity antihydrogen has been produced before [16, 17]. However, this antihydrogen was unsuitable for precision measurements, since it was produced directly from a relativistic beam of antiprotons and thus, was travelling at relativistic velocities. The goal of ATRAP is to produce antihydrogen that is cold enough to trap and then measure. There are many steps which must be taken:

- production of slow antihydrogen,
- de-excitation and trapping of antihydrogen,
- cooling and spectroscopy of trapped antihydrogen.

In this work, we describe the completion of the first of these tasks, but many challenges remain. Trapping of ground state antihydrogen is the next significant milestone for ATRAP – this will require de-excitation of the antihydrogen produced here. Recent work by members of ATRAP [18] suggests that a combined trap for antihydrogen and its ingredients may be stable for low charged particle densities, but this has yet to be tested experimentally. Following the trapping of antihydrogen, it will be laser-cooled using a continuous Lyman- $\alpha$  source developed by members of the collaboration [19]. Finally, spectroscopic measurements could be made on cooled, trapped antihydrogen. The great challenge at this stage, of course, is that many fewer antihydrogen atoms will be available than are presently used in precision hydrogen measurements.

### 1.3 Antihydrogen formation processes

Several methods have been proposed to recombine antiprotons and positrons into antihydrogen [7, 20, 21, 22, 23], but here we will only concentrate on those that seem most possible to implement in a nested Penning trap [7]: three-body recombination (TBR) and radiative recombination (RR).

As the name suggests, TBR involves the collision of three particles – an antiproton and two positrons. One positron becomes bound to the antiproton, while the other carries away the excess momentum and energy. The rate for this process is expected to be very high. To use the example given in [7], for  $10^4$  antiprotons, a positron density of  $10^7 \text{ cm}^{-3}$ , and a positron temperature of 4.2 K, a production rate of  $6 \times 10^6/\text{s}$  is predicted. The addition of a strong magnetic field reduces the rate by a factor of  $\approx 10$  [24]. Unfortunately, the unbound positron carries away an energy of only  $\approx kT_{e^+}$ , meaning that the states produced are weakly bound. Hence, de-excitation processes [24, 25] are required to produce the deeply bound atoms that are desired.

By contrast, RR [26] preferentially produces atoms in or near the ground state, but at a low rate. The third body in this case is a photon, emitted by the recombined atom. The rate is low since the average antiproton-positron collision duration is short compared to the radiative lifetime of hydrogen states. Deeply bound states are preferentially produced as these have the shortest lifetime. Using the parameters above, the predicted production rate is only 3/s [7] during the time that antiprotons and positrons can be made to interact.

Due to the much higher rate, we expect TBR to be the dominant recombination mechanism and we designed our experiments accordingly.

## 1.4 Thesis outline

Following this introduction, the apparatus used to make measurements are described in Chapter 2. At the center is the Penning trap, which is used to collect and manipulate the ingredients of antihydrogen. Also, several particle annihilation detectors are required to investigate events occurring within the Penning trap.

A large number of positrons are required to produce antihydrogen. The techniques used to greatly increase our positron number and to manipulate these will be described in Chapter 3, along with possible improvements.

Antiproton and electron accumulation will be discussed in Chapter 4. Obviously, antiprotons are required to form antihydrogen, but electrons also play an important role. The technique of antiproton stacking [27] is investigated and refined [4] – presently this is the only technique available to accumulate the large numbers of antiprotons required for interaction experiments.

Such interaction experiments are the theme of Chapter 5. Of course, to produce antihydrogen, antiprotons and positrons must be brought into contact. This is done in a device known as a nested Penning trap. Extensive investigations into the interaction of the particles in the nested Penning trap will be presented, as will investigation of the behavior of particles in the nested Penning trap itself. Our results are used to determine a theoretical parameter, allowing the theory to be used to gain further insight into the interaction of the interaction of antiprotons with positrons.

Chapter 6 describes how all of these techniques are used in concert to produce cold antihydrogen. Interaction experiments will be performed in a nested Penning trap optimized for antihydrogen production and detection, while the theory developed

in Chapter 5 will be applied to attempt to explain the results obtained.

Finally, in Chapter 7, we will summarize the important results from the previous chapters, and make suggestions for future investigations.

The Ph.D. thesis of P .K. Oxley [28] is a companion to this work. Important measurements of cloud parameters are made and an improved technique for producing cold antihydrogen in a nested Penning trap is thoroughly investigated.

# Chapter 2

## Apparatus

In this chapter the various pieces of equipment used in this work will be described. First, a brief review of the theory of a Penning trap will be given, followed by a description of the trap used in these experiments. Also important are the particle annihilation detectors installed nearby.

Within the ATRAP collaboration, the group from Harvard University is responsible for the construction, maintenance, and operation of the Penning trap, while that from Jülich is responsible for the particle annihilation detectors. Collaborators from Garching constructed and installed the most recent PPAC beam steering detector.

### 2.1 Penning traps

#### 2.1.1 Theory of the Penning trap

To confine charged particles we use Penning traps. Only a brief summary of the most relevant properties of these traps will be given here. A complete treatment of

the many aspects of particle behavior in a Penning trap can be found in [29].

A Penning trap comprises static magnetic and electric fields. A uniform magnetic field  $\mathbf{B}$  is applied along the  $z$ -axis; a particle of charge  $e$  and mass  $m$  will perform cyclotron motion about a magnetic field line with an (angular) frequency  $\omega_c$ ,

$$\omega_c = \frac{eB}{m} \quad (2.1)$$

where  $c$  is the speed of light. Thus, the particle is confined in the  $x$ - $y$  plane, but is completely unconfined along the  $z$  axis. To provide axial confinement an electrostatic quadrupole potential of the form

$$V(\rho, z) = V_0 \frac{z^2 - \rho^2/2}{2d^2} \quad (2.2)$$

is superimposed upon the magnetic field, where  $V_0$  is the applied trapping potential and  $d$  is a characteristic trap length. The axial potential has a harmonic variation along the  $z$ -axis near  $\rho = 0$  and the particle thus performs a simple harmonic motion along the  $z$ -axis with (angular) frequency  $\omega_z$ ,

$$\omega_z = \sqrt{\frac{eV_0}{md^2}}. \quad (2.3)$$

Note that the application of the quadrupole potential also introduces a radial electric field, as is required to satisfy Laplace's equation. The radial electric field modifies the radial motion of the particle, adding a slow  $\mathbf{E} \times \mathbf{B}$  drift (magnetron) motion with frequency  $\omega_m$ , and modifying the cyclotron frequency:

$$\omega'_c = \omega_c - \omega_m \quad \text{and} \quad \omega_m = \frac{\omega_z^2}{2\omega'_c}. \quad (2.4)$$

The three particle motions are illustrated in Fig. 2.1, and typical frequencies are given in Table 2.1. All motions are well separated in frequency, and that both the

	electron/positron	proton/antiproton
magnetic field	5.3 Tesla	5.3 Tesla
trapping potential ( $ V_0 $ )	15 V	15 V
cyclotron frequency ( $\omega'_c$ )	$2\pi \times 148$ GHz	$2\pi \times 84$ MHz
axial frequency ( $\omega_z$ )	$2\pi \times 37$ MHz	$2\pi \times 0.9$ MHz
magnetron frequency ( $\omega_m$ )	$2\pi \times 5$ kHz	$2\pi \times 5$ kHz

Table 2.1: Typical frequencies in a Penning trap.

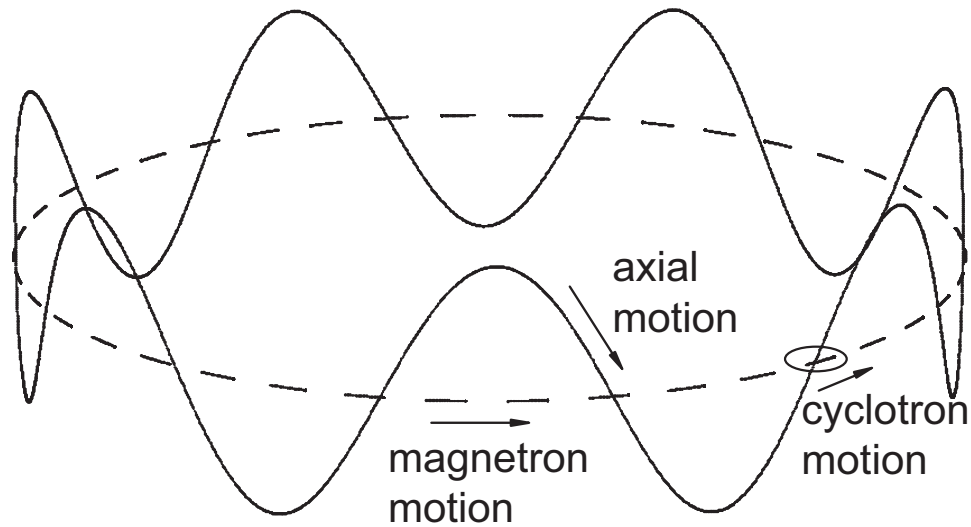


Figure 2.1: The three motions performed by a particle in a Penning trap.

cyclotron and axial frequencies are quite different for electrons and protons (due to the large mass difference).

The high frequency of the cyclotron motion is of particular practical importance. The cyclotron motion of a particle in a Penning trap can come into thermal equilibrium with its surroundings via the emission of synchrotron radiation. However, the efficiency with which this occurs varies strongly with the cyclotron frequency, and

thus mass, of the particle. The cyclotron energy decays as [29]

$$E(t) = E_0 e^{-\gamma_c t} \quad (2.5)$$

with

$$\gamma_c \propto \frac{B^2}{m^3}. \quad (2.6)$$

For an electron (positron)  $\gamma_c^{-1} \approx 0.1$  s, and the damping of the cyclotron motion is very rapid. In a cloud of many electrons, collisions transfer energy from the axial motion to the cyclotron motion, and thus the axial motion of electrons in a many electron cloud will also come into thermal equilibrium with the surroundings [30]. By contrast, protons (antiprotons) have  $\gamma_c^{-1} \approx 10^9$  s, so that radiation damping is completely negligible. It is only via collisions with other particles or via a coupling to a tuned circuit [29] that the axial and cyclotron motions of protons and antiprotons can be cooled.

Detailed descriptions of the electrodes used to apply the electric quadrupole potential can be found in [31]. Instead of using hyperbolic surfaces of revolution to apply the potential, open cylinders are used. These allow access along the  $z$ -axis of the Penning trap, which is required to accumulate both positrons and antiprotons. The aspect ratio of some of the cylinders is carefully chosen and tightly machined to produce a high quality quadrupole potential near the trap axis in desired locations.

As demonstrated in Fig. 2.2, there is, of course, a difference in the potential on the axis of the trap and that off it. This must be considered when designing potential structures for experiments. For example, when dumping a well the applied potential must be changed sufficiently to ensure that no well remains at any radius. Fig. 2.2 also demonstrates that the potential applied to one electrode can “leak” into adjacent

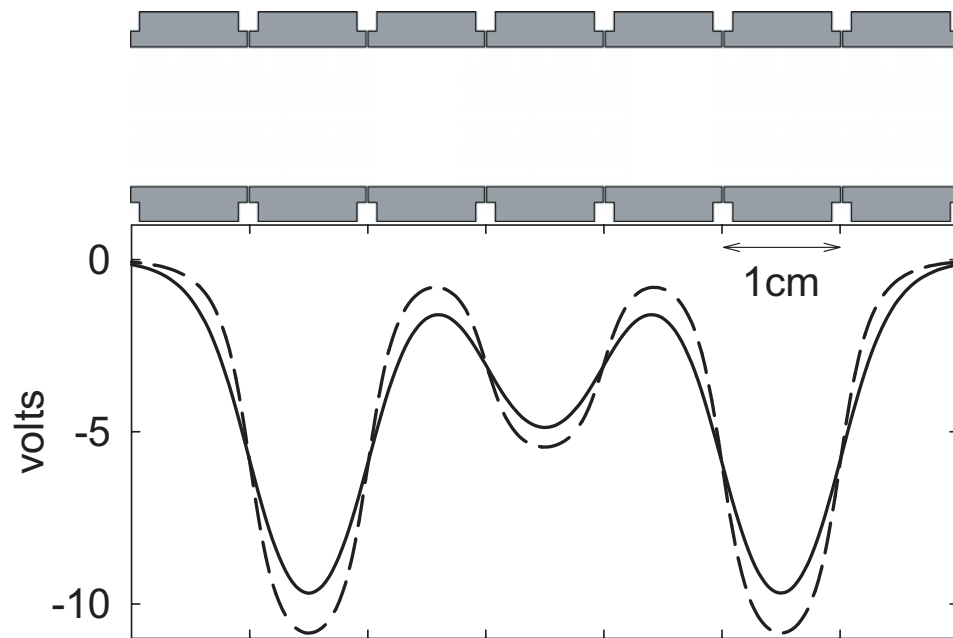


Figure 2.2: The potential is on the Penning trap axis (solid) is different from that 4 mm off axis (dashed).

electrodes. This can have practical consequences when trying to measure particle axial energy spectra, as will be discussed in Sec. 5.2.1. Forming a well from two or more electrodes (applying the same potential to two or more electrodes) better shields the potential from adjacent electrodes, but can result in radially unstable particles. Wells formed from electrodes with large aspect ratios (length/diameter) have a flat potential at their center, and thus little applied electric field. Particles confined in such a well will thus “feel” the effect of any imperfection in the trap electrodes or alignment of the electrodes with the magnetic field more strongly. Experimentally, the result of confining particles in such a well is often rapid radial particle loss.

### 2.1.2 The HBAR1 Penning trap

The Penning trap used to conduct the experiments presented in this thesis is designated HBAR1. Since a detailed description can be found elsewhere [32], only a summary of the most relevant features will be presented here. An essentially identical copy, HBAR2, was also used to gather some of the data presented in Ch. 6.

The HBAR1 trap (Figs. 2.3,2.4,2.5) is perhaps the most intricate such device ever assembled. It fulfills the many requirements necessary for accumulating and manipulating antimatter particles in a very limited space. These include separated positron and antiproton accumulation regions and an extremely high vacuum to minimize antiparticle annihilations on background gas atoms. Space is particularly limited in the antiproton accumulation region, since this is surrounded by particle annihilation detectors.

The trap consists of a stack of 32 cylindrical electrodes that are aligned with a magnetic field from a superconducting solenoid. An essential feature of this apparatus is the ball valve electrode that rotates (at 4.2 K and in high magnetic fields) to separate the positron and antiproton accumulation regions. This is required to protect a crucial gas layer from antiprotons, as will be discussed in Sec. 3.2.3. The ball valve also houses a reflection moderator and field emission point (FEP) that can be rotated off the trap axis when not in use.

The electrodes are contained in a copper vacuum enclosure that is evacuated, then sealed. The structure supporting the electrodes and vacuum enclosure are held at 4.2 K via thermal contact with a LHe dewar. Cryopumping reduces the pressure in the vacuum enclosure to less than  $5 \times 10^{-17}$  Torr [33], which in no way limits the

lifetime of trapped antiprotons on the time scale of typical experiments. Positrons and antiprotons enter the trap through 10  $\mu\text{m}$  Ti windows at the top and bottom of the vacuum enclosure, respectively.

Potentials can be applied to each electrode independently, allowing Penning traps to be formed at almost any position in the electrode stack. Computer controlled voltages supplies are used for this purpose. The electrical connections between the voltage supplies and the electrodes are heavily filtered to prevent RF noise reaching the trapped particles. Such noise can drive the particle motions, resulting in heating. A complete circuit diagram for the HBAR1 Penning trap is in [32].

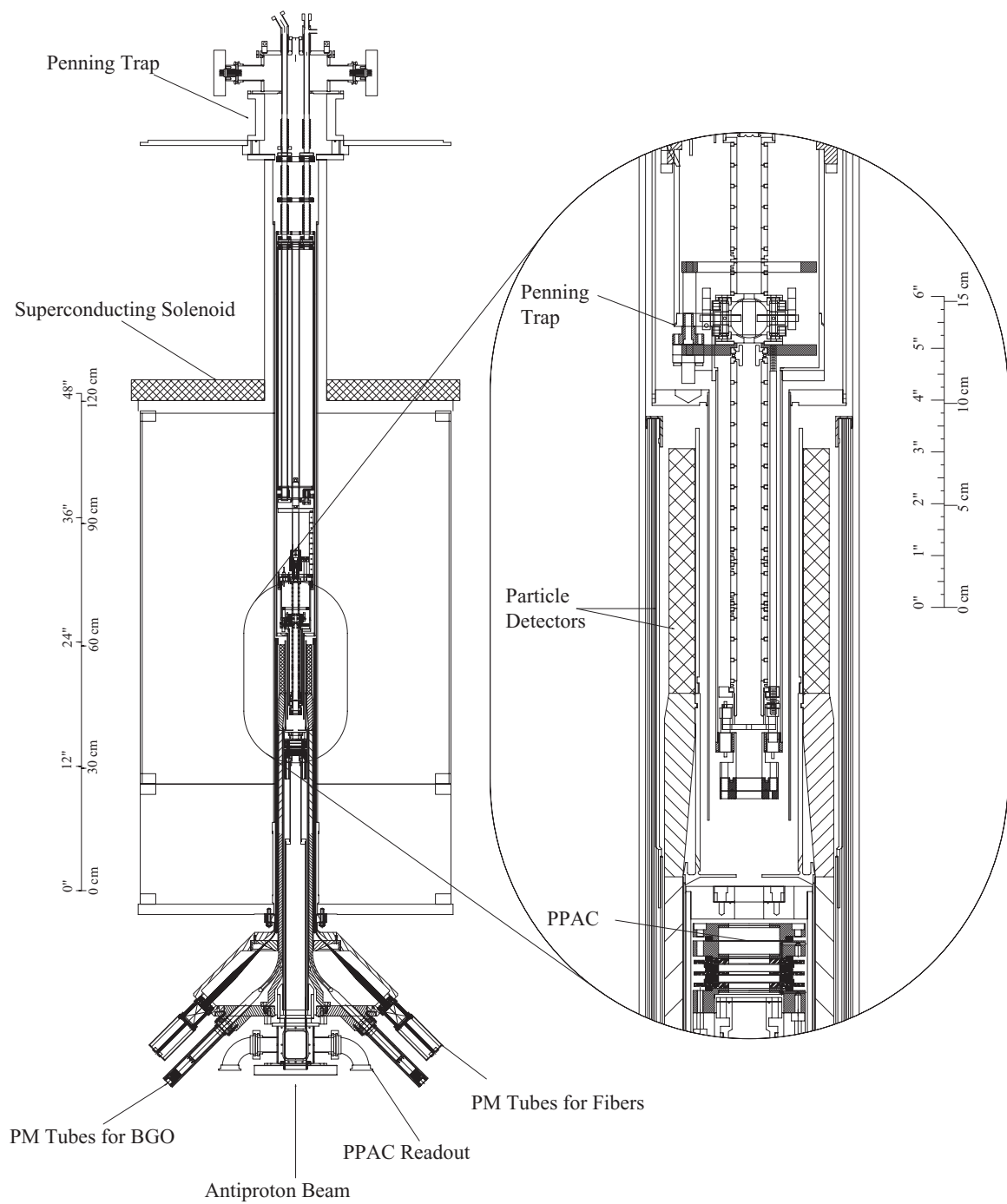


Figure 2.3: The complete HBAR1 Penning trap apparatus.

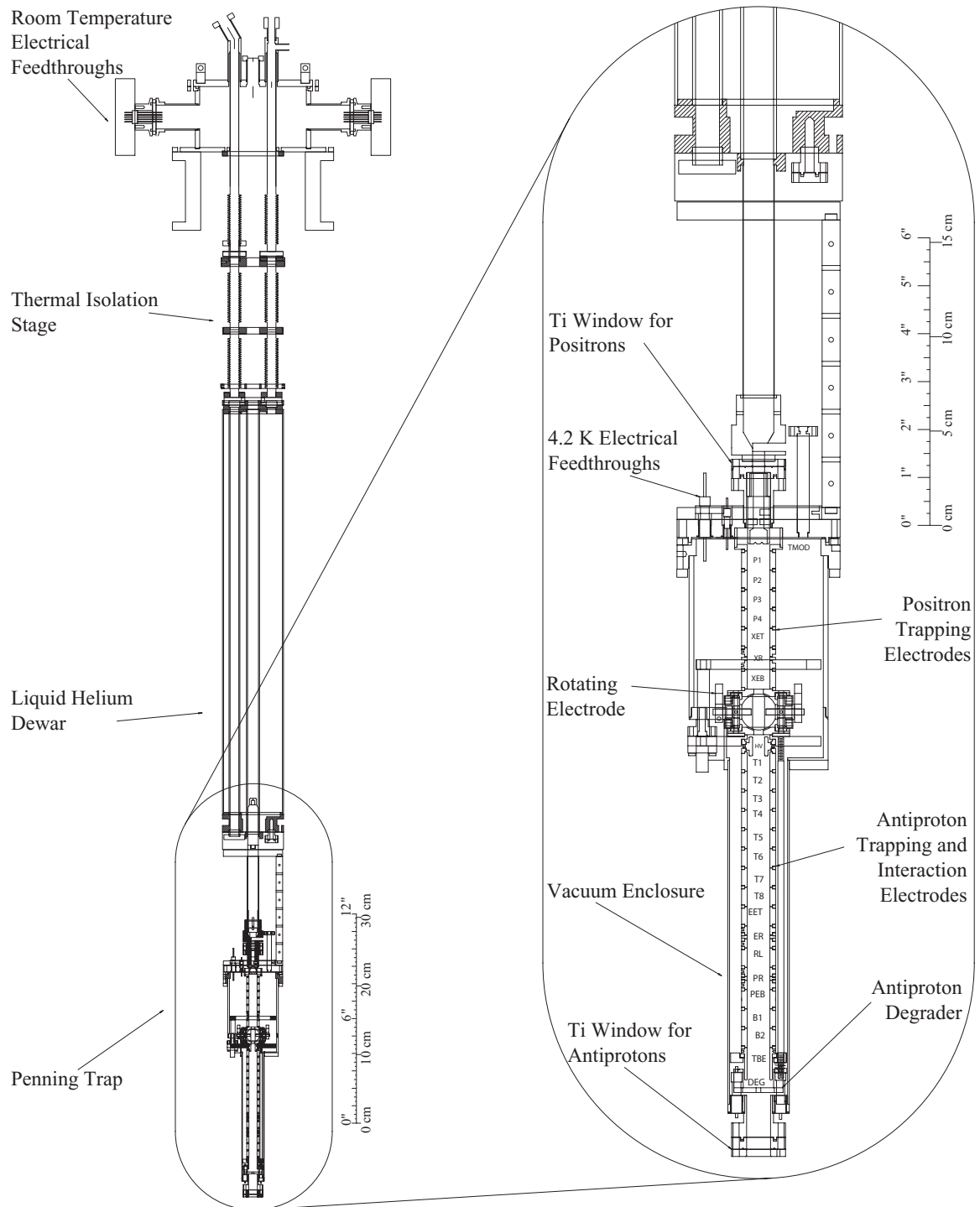


Figure 2.4: A detailed drawing of the HBAR1 Penning trap.

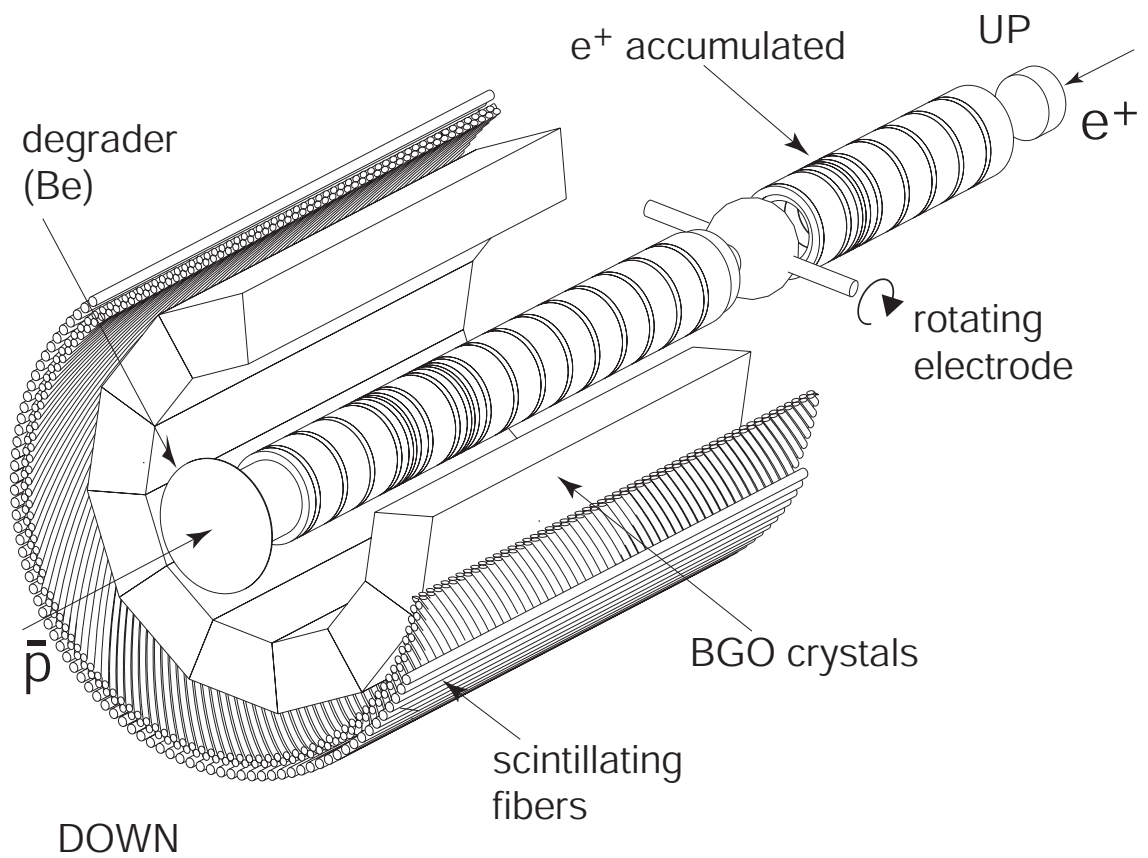


Figure 2.5: A simplified drawing of the HBAR1 Penning trap, showing the electrodes and the surrounding particle detectors.

## 2.2 Particle detection

### 2.2.1 Radio frequency amplifiers

Particles in a Penning trap can be detected and counted non-destructively via the oscillating image charges that the particle motions induce in the confining electrodes. In particular, the axial motion of electrons and positrons is at a convenient frequency for detection. An LCR resonator is formed by attaching a carefully chosen inductor to an electrode (Fig. 2.6). The capacitance amongst the trap electrodes and the parasitic resistance of the inductor completes the circuit. Voltage fluctuations across the circuit are amplified by a FET and analyzed using a spectrum analyzer. Much detailed information about the construction and operation of such amplifiers can be found in [34].

When there are no particles confined in the Penning trap, Johnson noise in the resistor drives the LCR circuit, as shown in Fig. 2.7(a). When particles are present, there is a system of two coupled oscillators, with the induced image charges supplying the coupling. The frequency spectrum splits into two peaks<sup>1</sup> (Fig. 2.7(b)), representing the two normal modes of the coupled oscillator system. The square of the frequency separation of the two peaks is proportional to the number of particles confined in the Penning trap [35]. Most measurements presented of positron or electron number, and hence of accumulation rates, were made in this fashion.

It appears that this measurement technique is only reliable for particle numbers less than 10 million. For clouds known to be larger by other means this non-destructive measurement tends to underestimate the number of particles present

---

<sup>1</sup>This type of frequency spectrum is referred to as a “dip.”

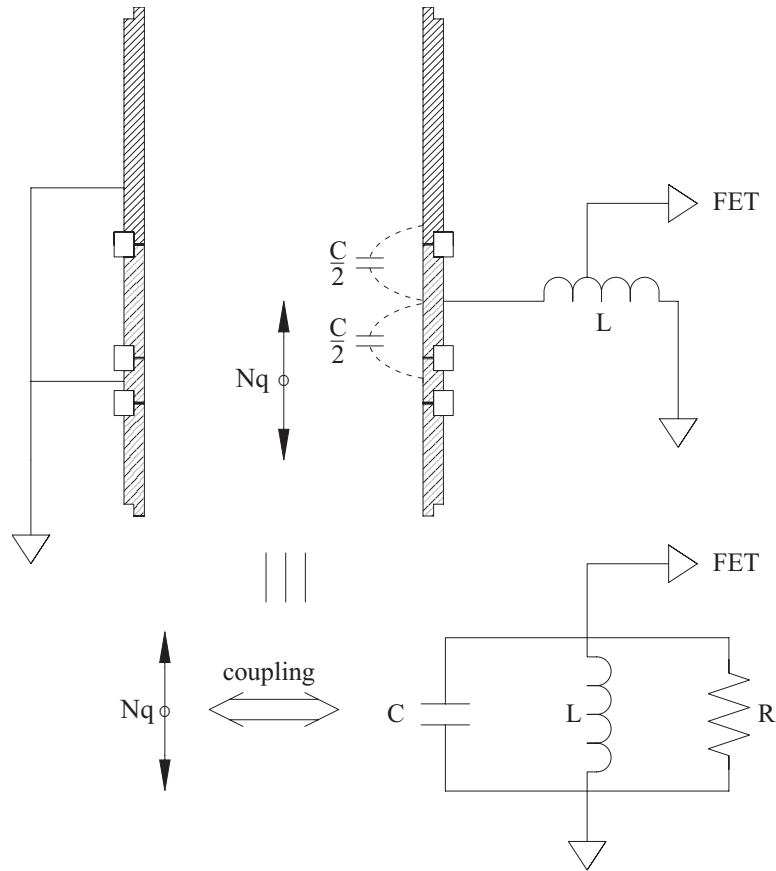


Figure 2.6: Oscillating charges couple to the resonator in the amplifier.

(Sec. 2.2.2). This is not surprising, since this is a resonant detection technique. As clouds become larger, there are many particles trapped at large radii where the potential is less harmonic and the axial oscillation frequency is different. This is also seen when large electron clouds are accumulated using a field emission point (FEP) (Sec. 4.1.1). Initially, no “dip” in the frequency spectrum is seen. Only after sideband cooling [35] to reduce the cloud radius (and probably drive many particles from the trap – see next section) can a “dip” be obtained.

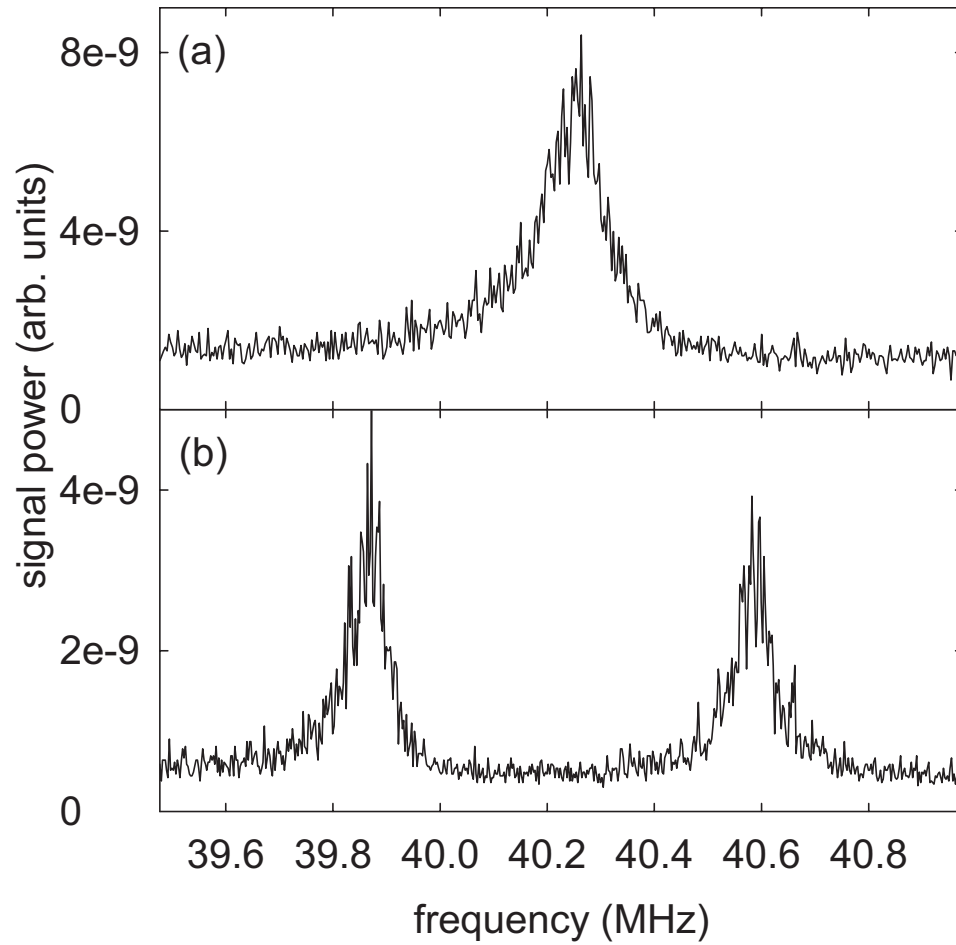


Figure 2.7: The noise resonance of an amplifier (a) is modified when there are 5 million electrons present (b).

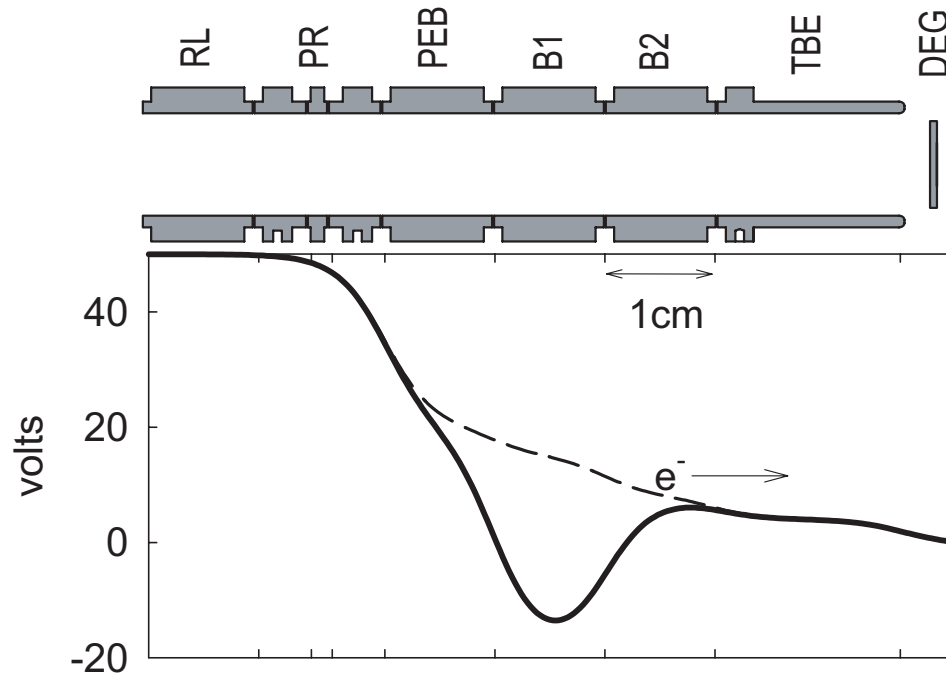


Figure 2.8: The potentials used to dump particles to the degrader for charge measurements.

### 2.2.2 Particle charge measurements

There are also destructive methods of measuring particle number. Particles can be dumped onto a Faraday cup and the charge integrated using a charge sensitive amplifier. The degrader is ideal for use as a Faraday cup as it lies on the  $z$ -axis of the trap. Dumping particles to the degrader is straightforward: One simply opens the electrostatic well on the side closest to the degrader, and as particles leave the well, they will travel along magnetic field lines to the degrader. It is necessary to have a potential ramp in place so that there is an electric field guiding the particles in the correct direction (Fig. 2.8). Dumping particles in this fashion, either for charge or annihilation measurements is our main experimental tool, and will be discussed further in Sec. 2.4.

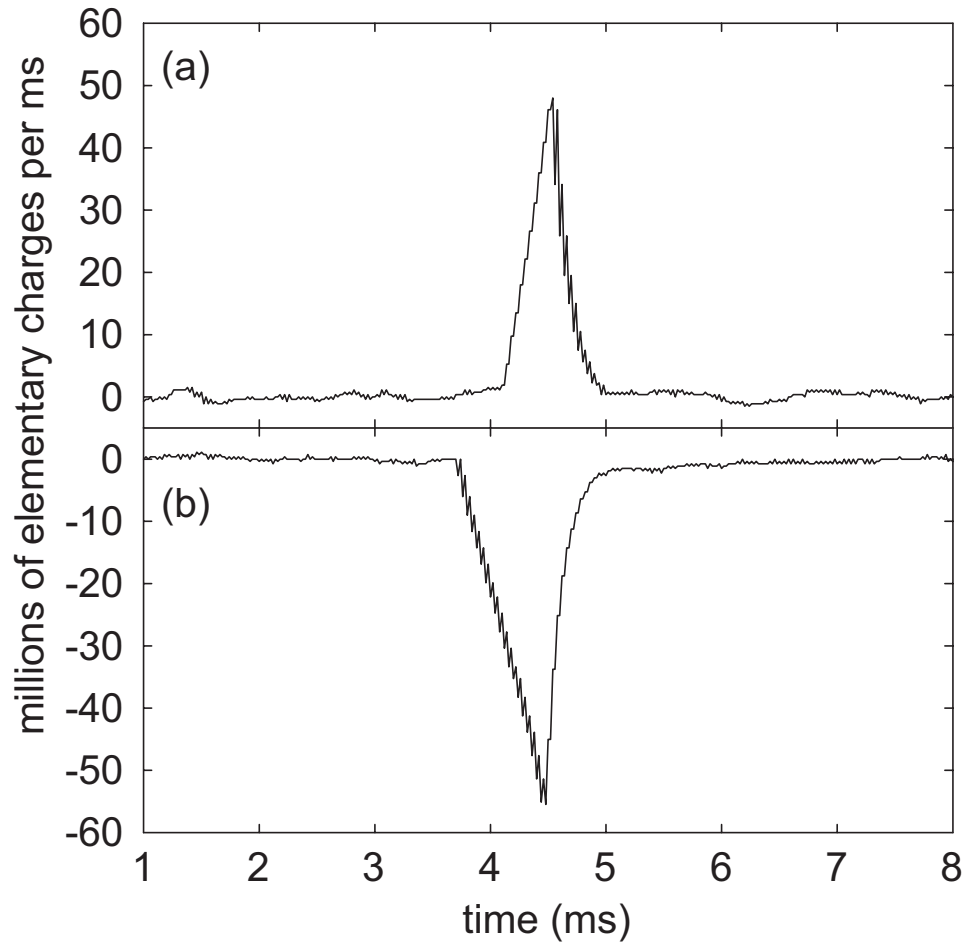


Figure 2.9: Example charge spectra: (a) 17 million positrons, (b) 29 million electrons.

Particles are dumped during a 10 ms window and the output of the charge sensitive amplifier is captured on a digital oscilloscope. Integration of the voltage trace and knowledge of the amplifier sensitivity yields the total charge and thus, particle number. Example charge spectra are shown in Fig. 2.9. The manufacturer's quoted sensitivity is used to determine the particle number.

As noted earlier, only clouds with less than 10 million particles can be counted using RF amplifier techniques. In the future it may be necessary to use much larger clouds, both for positron trapping (Sec. 3.2.5) and for antihydrogen de-excitation

(Sec. 6.4). Charge measurements were used to investigate the accumulation and stability of large electron clouds (Sec. 4.1.2).

The results of counting using RF amplifiers and charge measurements have also been compared. For example, it has often been noted that if two clouds are combined, the resulting cloud is not measured to be as large as would be expected. This is demonstrated in Fig. 2.10. For each data point, electrons were accumulated into several wells. The number of electrons in each well was counted using an RF amplifier. The wells were then combined and the number again counted on the amplifier. Finally, the electrons were dumped to the degrader and the number of particles determined via a charge measurement. As the total number of particles increases beyond about 7 million, the RF amplifier begins to underestimate the total particle number. Eventually, even the current measurement does not agree with total expected number, suggesting that particles are lost when combining clouds that together total more than 15 million particles.

If the particle number is below 7 million, the RF and current measurements disagree. Indeed, it has been found that the cloud size obtained via charge measurements is  $\approx 20\%$  higher than that from amplifier measurements. Since neither the charge nor the RF amplifiers are absolutely calibrated, it is difficult to draw a strong conclusion from this. However, given that RF techniques can clearly miscount the total size of large clouds, the charge measurements are certainly more reliable for clouds larger than 7 million particles.

Another interesting feature has been noted in charge measurements. As was mentioned in the previous section, it is often necessary to sideband cool an electron cloud

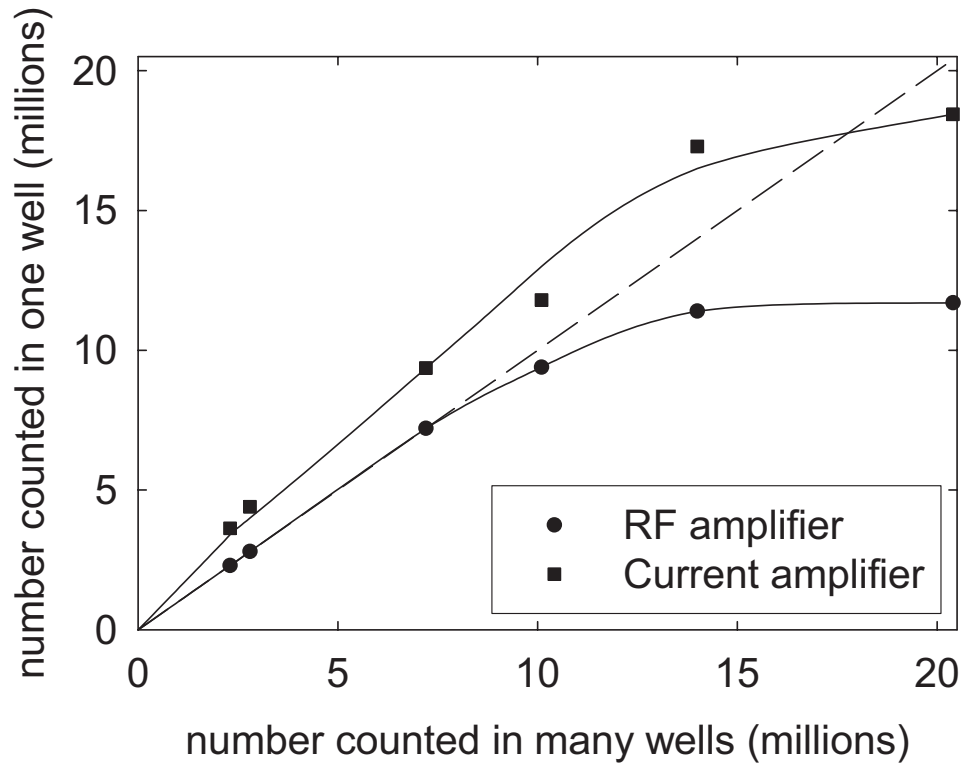


Figure 2.10: Summing many clouds.

that has been accumulated using the FEP before a “dip” can be observed using the RF amplifier. Charge spectra from two clouds accumulated using similar FEP settings, one sideband cooled and one not, are shown in Fig. 2.11. The cloud that has been cooled emerges over a narrower voltage range and has only a single prominent feature. That which has not been cooled has multiple features, is spread over a larger voltage range, and has a higher total particle number. This suggests that sideband cooling of clouds of this size is effective due partially to reducing the radii of particles, but also to ejecting some particles at large radii.

In summary, charge measurements of this type provide an interesting counterpoint to those made with RF amplifiers. Since it is a destructive measurement it can

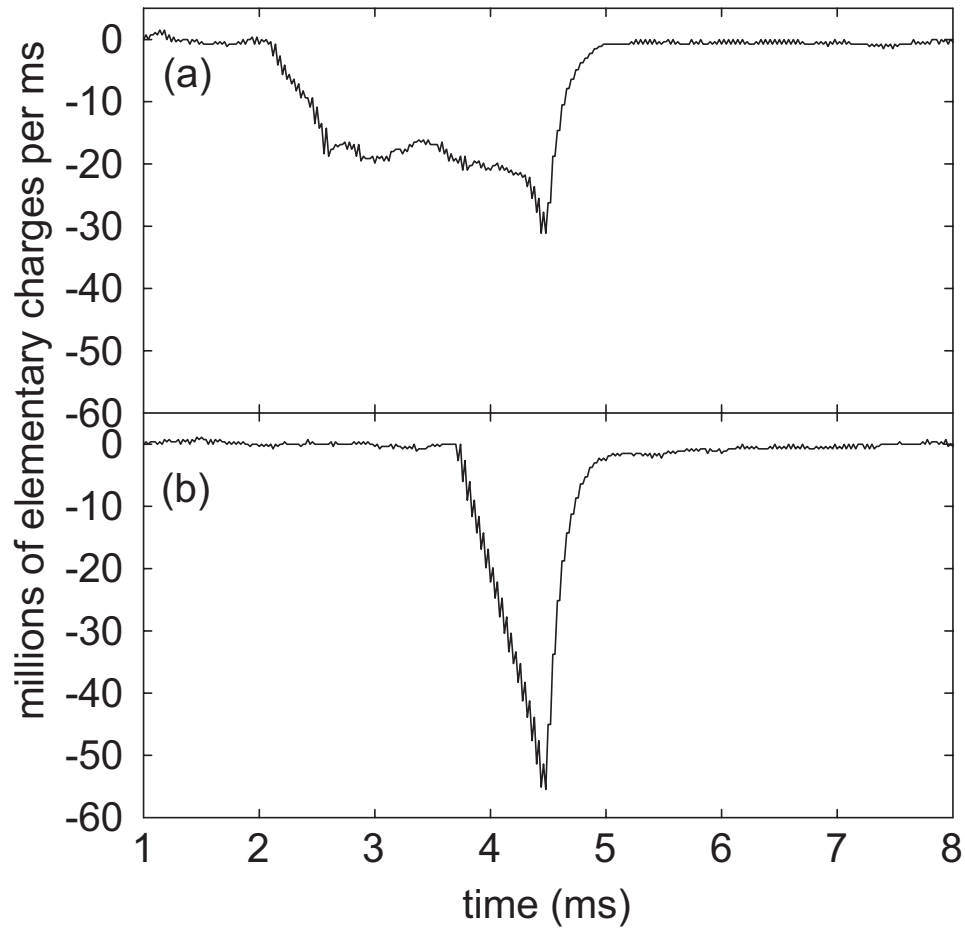


Figure 2.11: Charge spectra before (a) and after (b) side band cooling is applied.

not be used to determine the number of particles before an experiment, but it does allow general crosschecking of the RF amplifier results. With further refinement, it is possible to imagine using this technique to detect hundreds of protons in a well. Then experiments of the type to be described in Ch. 6 could be conducted with protons and electrons when no antiproton beam is available.

### 2.2.3 The PPAC

To be able to steer the antiproton beam into the Penning trap, a position sensitive detector is required close to the Penning trap. Since space is very limited, this detector can not be retracted and thus it must be non-destructive. This reinforces the need to have the detector close to the trap, as it will cause both positional and energy straggling. To keep such straggling to a minimum we require that the detector have a low areal density. The type of detector used is a Parallel Plate Avalanche Counter (PPAC) [36]. This comprises a gas cell and several electrodes. Antiprotons passing through the cell ionize the gas (typically an argon-methane mixture). An applied potential accelerates the resulting charged particles to 2 mm wide collecting strips, and the resulting charge is integrated using a digital oscilloscope. The gas cell has two regions with collecting strips aligned orthogonally to one another, giving  $x$ - $y$  position information about the beam. By applying a large enough accelerated potential, the transit of even a single antiproton can be detected [37], although it is not necessary for us to operate in this regime. The antiproton beam is steered using dipole magnets and electrostatic beam steers installed in the beam line. These elements are adjusted until the beam is centered on the middle strip of the PPAC in each direction.

Mounted directly above the PPAC is another gas cell. This contains a mixture of He and SF<sub>6</sub> gas at atmospheric pressure. Changing the ratios of these two gases allows the energy of the beam to be tuned, as will be discussed further in Sec. 4.2.1.

### 2.2.4 Antiproton annihilation detectors

While we could use RF detection techniques to measure the number of antiprotons, it is often easier to simply eject the antimatter particles from the trap, since this can be done from any location with the electrode structure. There are two distinct detectors used for detecting antiproton annihilations, which can be utilized separately or in coincidence. They are both scintillating detectors, i.e. the passage of charged antiproton annihilation products through the detector material causes it to scintillate. The scintillation light is converted into an electrical signal by a photomultiplier tube.

The first of the detectors is installed outside the solenoid cryostat and comprises two layers of plastic scintillator sheets. The two layers are operated in coincidence to suppress noise and background events. Charged pions from antiproton annihilations can easily traverse the solenoid and register a clear signal. The efficiency of these detectors was carefully calibrated by the TRAP collaboration [38]; 50% of antiproton annihilations produce a signal. Background counts occur at a rate of  $\approx 60/s$ , due primarily to cosmic ray muons.

The second detector is installed in the magnet bore, and comprises 328 scintillating fibers. Scintillation light is carried out of the magnet bore by each fiber to a photomultiplier. The fibers are arranged in three layers. The two inner layers are wound in a helix and are layered to maximize the coverage of the detector. A third straight layer lies outside these. The combination of straight and twisted fibers provides limited position resolution, although not on an event-by-event basis.

We generally require a coincidence between two of the three layers for a count to be registered. The background count rate in a single layer is  $\approx 45/s$ , while with

the double coincidence it is  $\approx 10/s$ . Because the fibers are not symmetric about the radial plane of the interaction region (Fig. 2.12), the detection efficiency is different for particles annihilating on the ball valve and the degrader.

It is often convenient to operate both the external scintillators and the fibers in coincidence. Such an event is denoted a “trigger” (Sec. 2.2.6). Although the antiproton detection efficiency is reduced to 38% for particles annihilating on the degrader, the background count rate is reduced to only 1/s. This makes “triggers” particularly useful for recording rare events. In what follows, any report of an observed antiproton number will have been derived from an observed number of hits in these detectors. The observed number of hits is scaled by the appropriate (experimentally determined) efficiency to yield antiproton number.

Signals from the external scintillators and fibers are available in real time, although all that can be determined is that at least two external panels or two fibers were hit in coincidence. This amount of information is sufficient for many purposes. More complete information can be logged by the data acquisition system (Sec. 2.2.6).

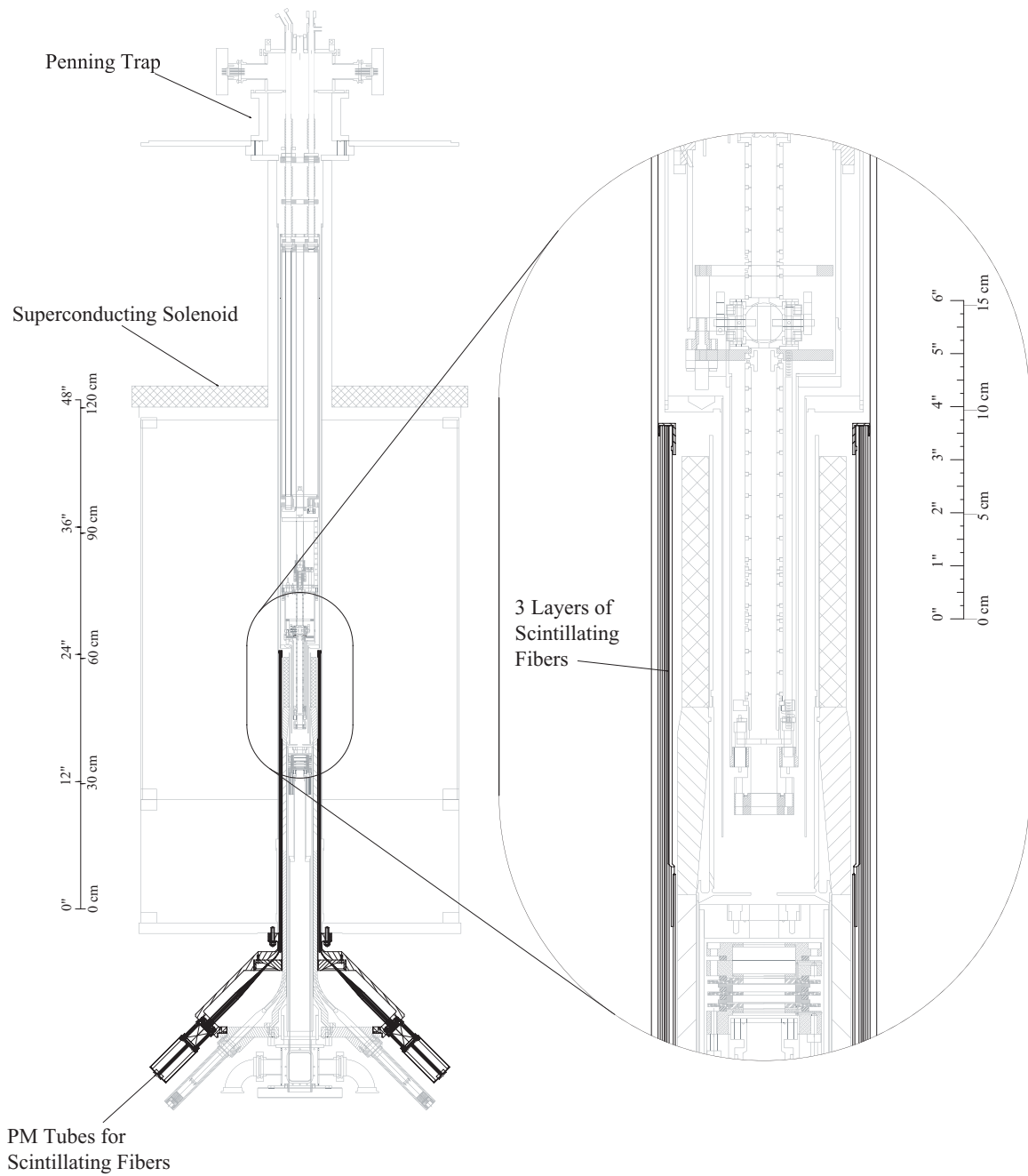


Figure 2.12: Position of the scintillating fiber detectors.

### 2.2.5 The positron annihilation detector

A segmented scintillation crystal detector is used to detect 511 keV  $\gamma$ -rays produced by positron annihilations. Segmentation is important for several reasons. Most obviously, a positron annihilation produces two back-to-back 511 keV  $\gamma$ -rays. Thus, the detection of such back-to-back events is a strong indication of a positron annihilation. Segmenting a detector allows for such an identification, with more segments producing finer angular resolution. Also, when attempting to identify an antihydrogen annihilation there will be many other particles produced by the annihilation of the antiproton that can deposit energy in the scintillator crystals. Segmenting the crystals reduces the probability that a 511 keV  $\gamma$ -ray and an antiproton decay product will interact with the same crystal.

In this system the crystals can only be segmented vertically, since their scintillation light is carried to photomultipliers outside of the magnet bore by vertical light guides (Fig. 2.13). There is insufficient space in the present system for more layers of light guides. In total there are 12 radial segments.

BGO crystals are used, since they have a high photo peak efficiency, have a scintillation light that is well matched to photomultipliers, and are not hygroscopic. The efficiency for detecting a single 511 keV  $\gamma$ -ray is 58% [39], and hence the efficiency for detecting simultaneous back-to-back 511 keV  $\gamma$ -rays is 34%.

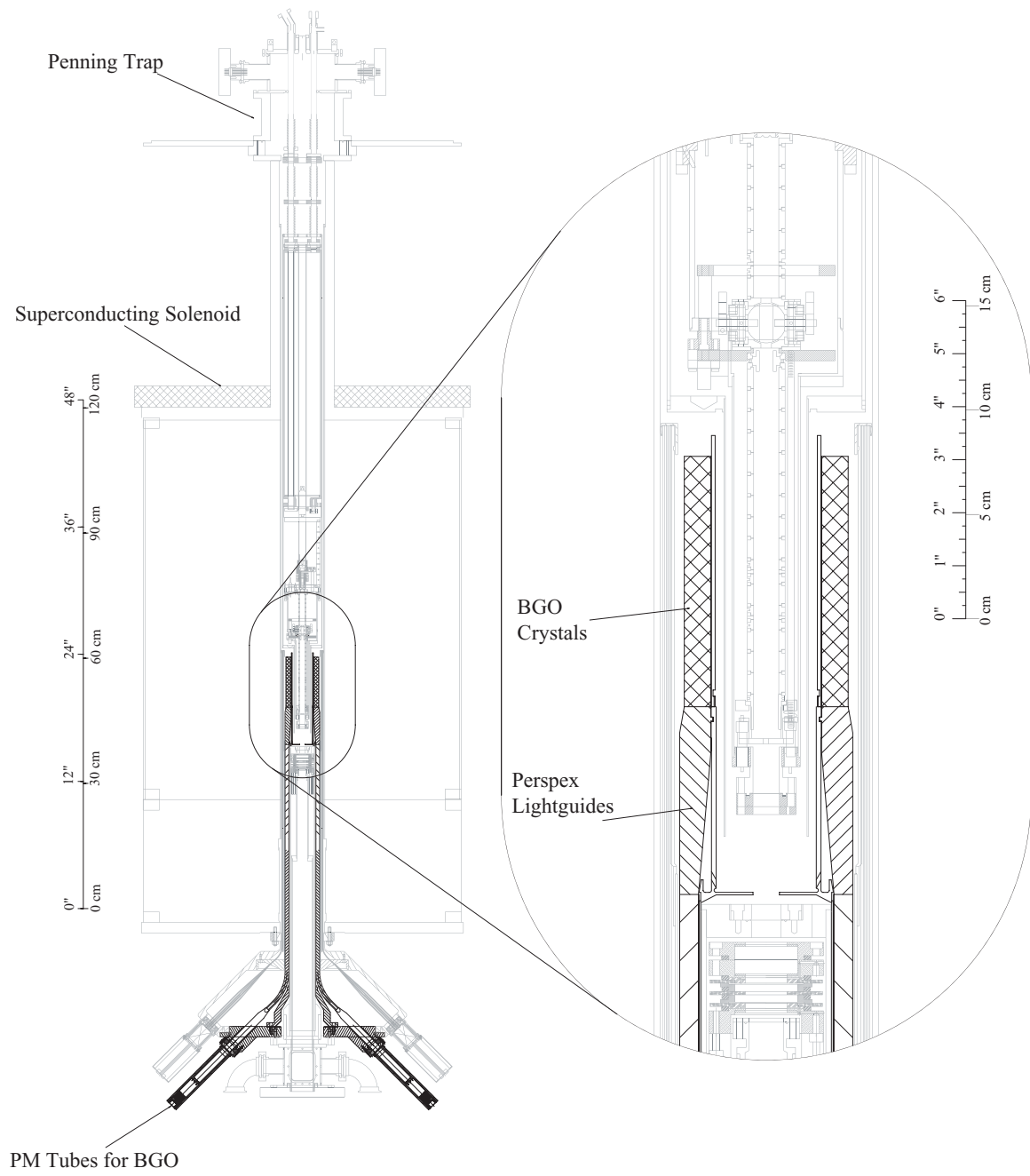


Figure 2.13: The BGO detector assembly.

## 2.2.6 The data acquisition system

While limited detector data can be obtained in real time, much more information can be obtained about any given event. For example, one could record which of the  $\approx 300$  fibers was hit to form a fiber event. The data acquisition system (DAQ) records essentially all the information that can be gathered about an event:

- each fiber that is hit, and the energy deposited;
- each BGO crystal hit, and the energy deposited;
- each external panel hit, and the energy deposited.

This detailed data allows sophisticated post-analysis to be performed. For example, cosmic ray events can be eliminated with high efficiency, since they typically deposit a large amount of energy in only one or two fibers [40]. However, reading all this information from the various detectors and storing it takes of order of 1 ms, so one must be careful not to exceed count rates of 1 kHz. The DAQ is triggered when the external scintillators and fibers are hit simultaneously, and thus, this type of event is denoted a “trigger.”

A scaler that is advanced by an externally provided clock pulse is also recorded, allowing events recorded by the DAQ to be precisely correlated in time with actions taken by the experimenter.

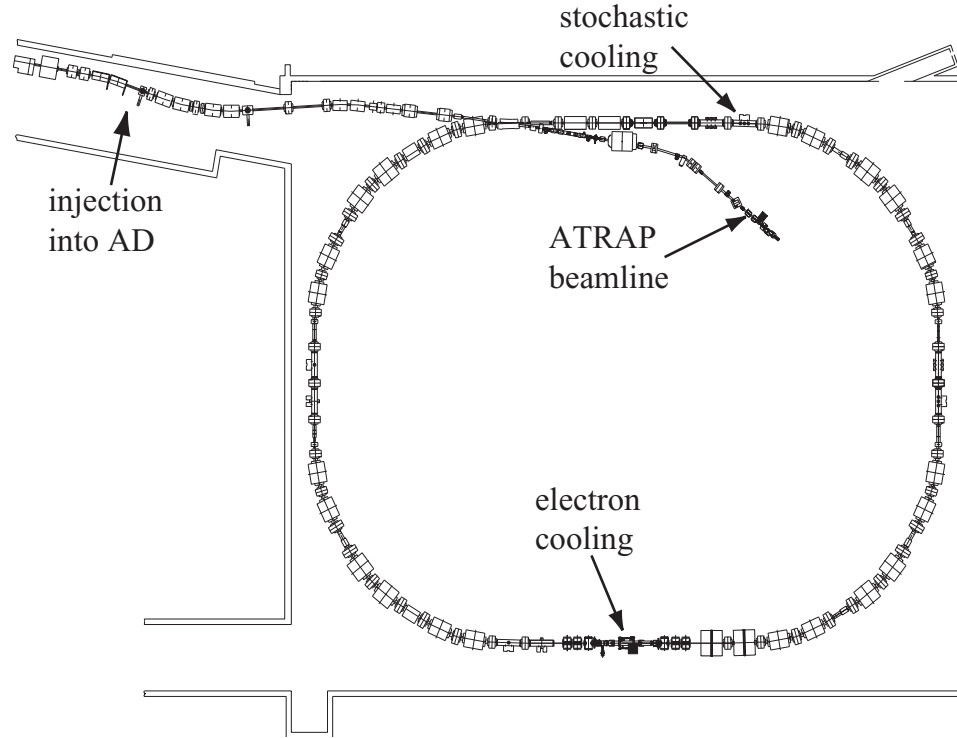


Figure 2.14: The Antiproton Decelerator.

## 2.3 The Antiproton Decelerator

Antiprotons are obtained from a dedicated facility at the CERN laboratory near Geneva, Switzerland. The Antiproton Decelerator (AD) (Fig. 2.14) can deliver 80 ns pulses of  $3 \times 10^7$  100 MeV/c antiprotons every 108 s. Antiprotons are produced when a pulse of  $10^{13}$  26 GeV/c protons strikes an iridium target. Antiprotons enter the AD ring with a momentum of 3.57 GeV/c. Stochastic cooling [41] is applied to reduce the emittance of the beam at this stage, and also after the first deceleration to a momentum of 2 GeV/c. The beam is then decelerated to 300 MeV/c, at which point electron cooling [42] is applied. Finally, the beam is decelerated to 100 MeV/c and electron cooling is applied before ejection to the experimental beamlines.

## 2.4 The fast timing system

Most aspects of the operation of the Penning trap are controlled using LabView. However, only very coarse timing can be obtained in this fashion. Since there are many operations that require timing as precise as 1 ns, it is necessary to have a hardware timing system. This hardware system is ultimately controlled by LabView, insofar as parameters are loaded into the timing devices via a computer interface, but the relative timing of actions is completely determined by hardware.

The hardware timing system is built around several SRS DG535 Pulse and Delay generators. These supply trigger pulses to voltage pulsers, ramp generators, oscilloscopes, and clocks. The hardware is arranged so that the trigger pulse to each device can be delayed relative to that for any other device, allowing great flexibility. The entire system can be triggered by either an external trigger pulse (e.g. from the CERN AD, indicating the imminent arrival of an antiproton pulse) or LabView.

Amongst the most common uses of the timing system is coordinating a low voltage ramp (LVR). This is the main experimental tool used to investigate antiprotons in the Penning trap. A ramp generator is used to open a well containing antiprotons, which are then guided by magnetic field lines to either end of the Penning trap, where they annihilate. Antiproton annihilations are recorded by the surrounding detectors, and the electrical signals thus generated are stored in multi-channel scalers which are advanced by pulses from an external clock. An oscilloscope captures the voltage ramp that releases the antiprotons.

In this case the ramp generator, oscilloscope, and external clock are all triggered by timing system. The multi-channel scalers record annihilation counts versus time and

the oscilloscope records voltage versus time. Since all devices were triggered at well known times, the two measurements can be easily combined to obtain a measurement of voltage versus annihilation counts, i.e. the energy spectrum of the antiprotons.

Other uses of the hardware timing system include:

- triggering the high-voltage pulser used to trap antiprotons, and as part of same sequence, ramping the potential to zero while recording antiproton annihilations (Sec. 4.2.2) – the trigger pulse for the timing system in this instance is provided by CERN;
- recording annihilations as antiprotons are pulsed into a nested Penning trap (Sec. 5.2.2);
- triggering voltage pulsers used to “pulse” transfer particles in the Penning trap (Sec. 3.3).

# Chapter 3

## Positron Accumulation and Manipulation

As positrons are one ingredient of antihydrogen, the ability to rapidly and reliably accumulate them is obviously important. In this chapter, the accumulation technique used will be described, as will its limitations. The variation of the accumulation rate as the magnetic field strength is varied is measured, since this is an important consideration for future experiments. Also, various options for improving the positron accumulation rate will be considered. Finally, a novel particle transfer scheme, devised with positrons in mind, will be discussed.

### 3.1 Obtaining positrons

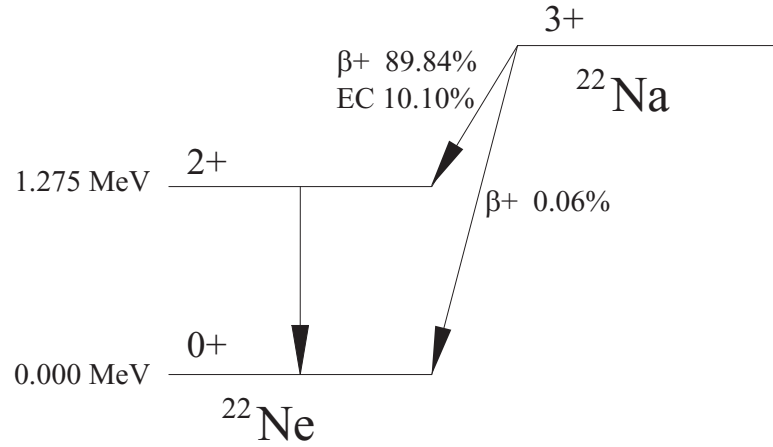
Positrons are readily obtained from the  $\beta$  decay of certain radioactive isotopes. However, care must be taken to shield both personnel and equipment from the  $\gamma$ -rays

that such sources inevitably produce in large numbers. In addition, positrons are emitted with a wide range of energies, almost all of which are unsuitable for positron accumulation. Moderator crystals [43] are required to produce positrons with low energies (around 1 eV). Even then, an additional process is required to efficiently damp moderated positrons into a Penning trap well.

### 3.1.1 The positron source

The radioactive isotope that we use as a positron source is  $^{22}\text{Na}$ . This is a convenient choice, since strong sources are available commercially, the half life of 2.6 years is relatively long, and 90% of decays produce positrons (Fig. 3.1), with an endpoint energy of 546 keV. The radioactive material is a sodium salt that is sealed in a titanium capsule (Fig. 3.2). Positrons exit the capsule via a thin Ti window. A thick tungsten backing plate increases the fraction of positrons that exit from the source through the window. Due to self absorption in the source material and attenuation in the backing plate and window, only about 20% of positrons generated in the source emerge [44, 45, 35]. Great care must be taken when handling such capsules, as if the window were punctured radioactive material could contaminate other apparatus, rendering them both useless and dangerous to personnel.

Results from two different sources will be compared in Sec. 3.2.1. The first was a relatively weak source with an activity of 2.5 mCi at the time measurements were made. This source had an active area with a diameter of 2 mm. The second was much stronger – 150 mCi at the time of purchase – the strongest source that was commercially available at the time. This source had a larger active diameter of 3 mm

Figure 3.1:  $^{22}\text{Na}$  level scheme.

in order to minimize self absorption of positrons in the source material. The stronger source had an activity of 79 mCi at the time measurements described here were made.

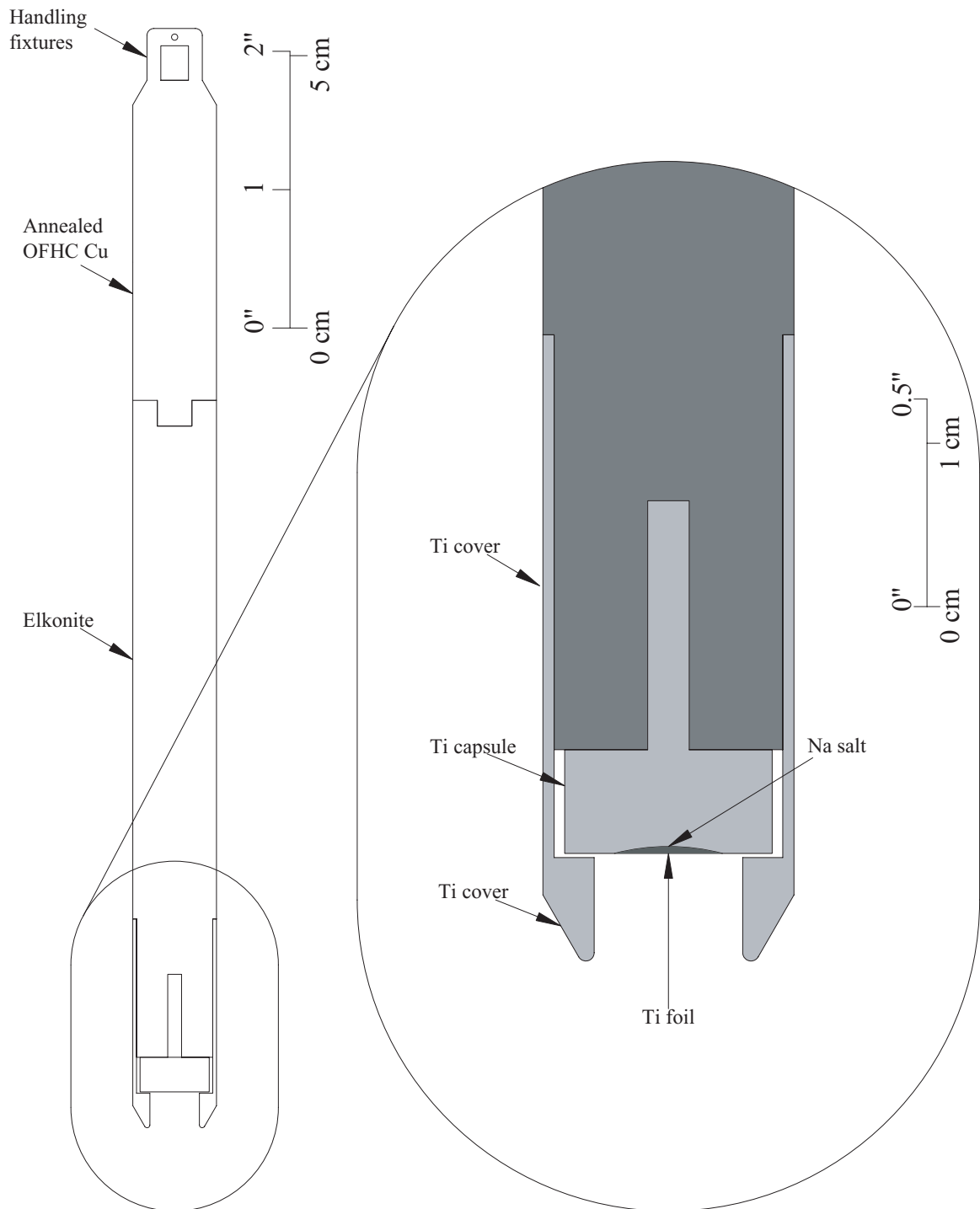


Figure 3.2: The source rod and source capsule.

### 3.1.2 The positron shielding enclosure

As mentioned, the source capsules must be handled with great care in order to maintain their structural integrity. In addition, great care must be taken to shield nearby personnel and equipment from the large  $\gamma$  ray flux that these sources produce. Examination of the level scheme for  $^{22}\text{Na}$  (Fig. 3.1) reveals that almost all decays produce a 1.275 MeV  $\gamma$ -ray and 90% produce two 0.511 keV  $\gamma$ -rays from the annihilation of positrons. A 150 mCi (5.5 GBq) source thus emits  $1.6 \times 10^{10}$   $\gamma$ -rays per second. Effective shielding must absorb the vast majority of these.

There are two distinct shielding objectives that must be met: shielding personnel and shielding the particle detectors surrounding the Penning trap. In each case, shielding is achieved by surrounding the source by dense material. In the first instance, the goal is to keep the dose rate at a distance of 1 m at or below that due to the natural background. This requires that at least 7" of lead be placed around the source.<sup>1</sup> In the second instance, the goal is to keep the count rate due to the source in the BGO  $\gamma$  ray detector at less than 1 Hz, requiring a thickness of 7.5" of lead.

With the source in place at the top of the Penning trap apparatus, there is insufficient space to place enough shielding material between the source capsule and the various particle detectors. To shield personnel with the source in this position would require many inches of lead to be placed around the entire solenoid. Since this is impractical, the following shielding strategy is adopted. When positrons are not being accumulated, the source rod is retracted into a shielding enclosure placed above the Penning trap apparatus. This enclosure is designed to provide sufficient shielding for

---

<sup>1</sup>For an example shielding calculation see Appendix A.

both personnel working next to the enclosure and the detectors. When the source rod is lowered for positron accumulation, the detectors are turned off and shielding for personnel is provided by a combination of the solenoid and concrete walls surrounding the experimental area. Measurements with a smaller source in combination with shielding calculations [46] determined that concrete walls 60 cm thick were required.<sup>2</sup>

Of course, personnel are not allowed to enter the experimental zone when the source is in the accumulation position. This is ensured by an interlocked door; the control software for the source rod will only allow it to be lowered if the experimental zone is empty of personnel and the door is locked, and once the source has been lowered the door can not be opened. This same interlock system prevents the antiproton beam from entering the zone if there are personnel present.

The first shielding element is the rod on which the source is mounted (Fig. 3.2), which has several safety features incorporated into its design. First, most of the rod is formed from Elkonite,<sup>3</sup> so that it provides complete shielding in the backwards direction. Of course, any handling of the rod is done from this direction, so this is an important safety feature. Once the capsule is in place on the rod, a titanium cap is attached to ensure that the source capsule does not touch any surfaces as the source rod is raised and lowered into the Penning trap.

The top portion of the source rod is made of annealed OFHC copper. In the unlikely event that the source rod is dropped into the Penning trap, eddy currents induced in the copper would slow the rod before impact with the top of the Penning

---

<sup>2</sup>Concrete shielding blocks at CERN have a higher density than normal concrete ( $2.7 \text{ g/cm}^{-3}$  vs  $2.3 \text{ g/cm}^{-3}$ ), allowing these walls to be thinner than they might be otherwise.

<sup>3</sup>Elkonite is a high density composite formed from tungsten and copper. The material used here is 90% W and 10% Cu. It has a density of  $17.2 \text{ g/cm}^3$ , and an exponential attenuation coefficient of only  $\approx 1/(1 \text{ cm})$ . In comparison, the corresponding values for lead are  $11.4 \text{ g/cm}^3$  and  $\approx 1/(1.5 \text{ cm})$ .

trap vacuum enclosure. Experiments were carried out dropping masses attached to copper rods into a 5.4 T solenoid. At room temperature the copper rods used would simply fall through the region of high magnetic field gradient. While they would have slowed when passing through the large magnetic field gradient, it was not possible to measure this with the simple setup used. When cooled to 77 K, the rods would “levitate” for a short time, since the induced eddy currents are larger and persist for longer due to the higher electrical conductivity at this temperature. Annealed OFHC copper cooled to 77 K came to a halt soonest and for the longest time and hence, was used in the source rod. Finally, the top of the source rod has a slot that can, with the aid of a brass clip, be used to extract it from the Penning trap apparatus in the event of such an accident.

The source capsule was received bare from the manufacturer, inside a perspex shipping container. Of course, this small perspex container was shipped in a lead container to provide shielding during transportation.<sup>4</sup> A cautious procedure was developed to transfer the source capsule from the shipping container to the source rod and into the shielding enclosure. The primary aim of the procedure was to completely shield personnel at all times, while ensuring the integrity of the source capsule. The procedure was practiced continuously for two days using a dummy source capsule before the actual transfer was attempted. During the procedure, video cameras were used to monitor events occurring behind the large shielding walls required. In particular, a remotely controlled camera, provided by the CERN radiation protection division, that could pan and zoom over a wide range was essential. Special radiation

---

<sup>4</sup>However, the container was only 7.5 cm thick so the shielding provided was far from complete. At a distance of 1 m a dose of  $\approx 1.5$  mrem/hr would be received. To receive a dose equivalent to natural background personnel should remain  $\approx 10$  m away from this container.

monitors were worn during the transfer; these provided an audible signal if an above normal dose was being received. Once the source capsule was installed, the source rod was placed in another portable lead container, known as the “ATRAP pig.” Because the “pig” provides similar shielding to the shipping container, personnel remained some distance from it as much as possible. The “pig” was installed in the concrete wall between the two ATRAP experimental zones. Once in this position, complete shielding was provided. From here, the shielding enclosure could be positioned above the “pig” and the source rod raised into it.

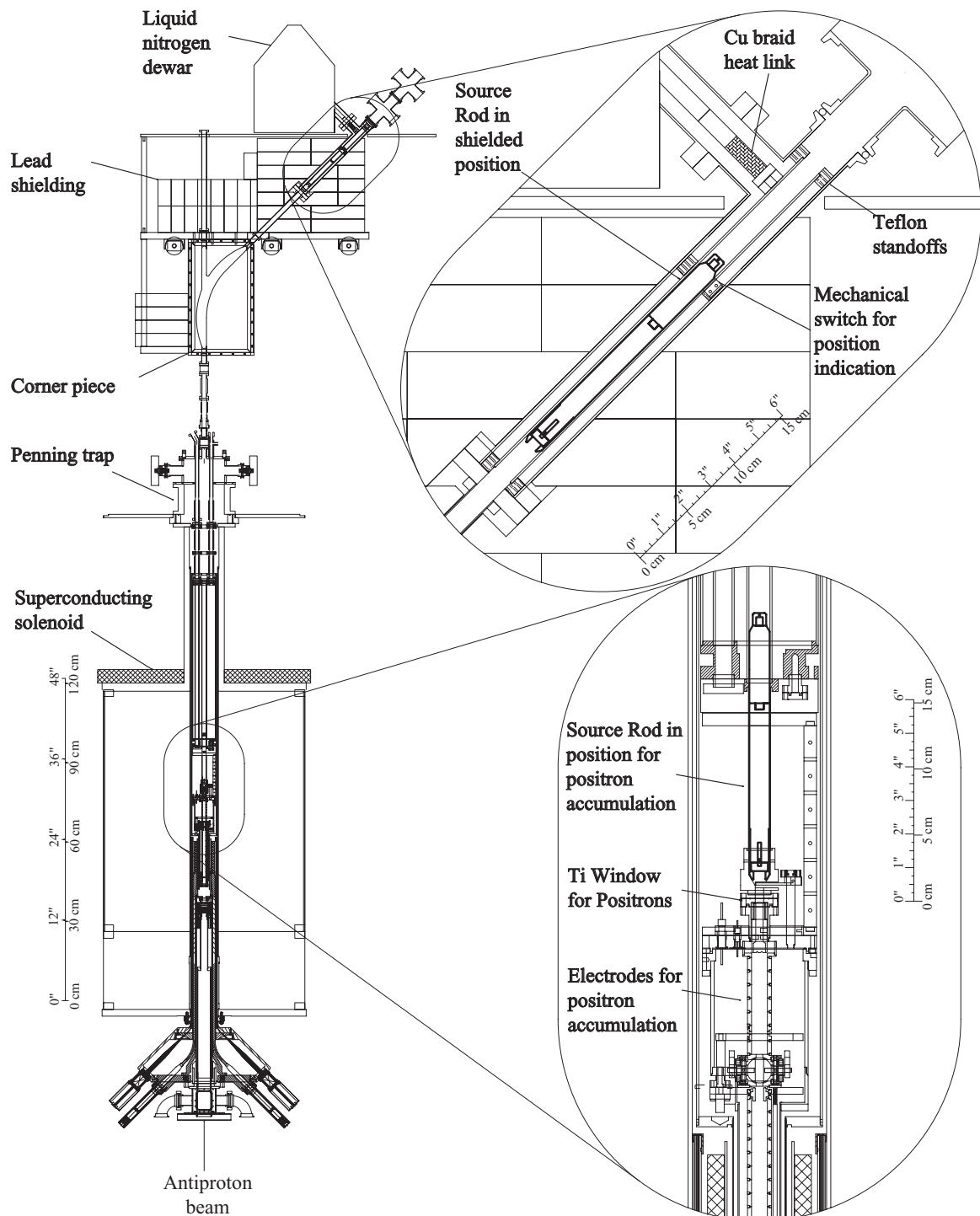


Figure 3.3: The source shielding enclosure, shown connected to the Penning trap apparatus.

Aside from providing shielding, the shielding enclosure serves several other important functions. It must include a vacuum system that can connect to that surrounding the separate vacuum enclosure for the Penning trap and, ideally, a pre-cooling system to reduce the thermal load upon the Penning trap when the source rod is lowered. Inside the vacuum system, there is a mechanical system for lowering and raising the source rod and for monitoring its position. Finally, placing a large lead enclosure directly above the Penning trap apparatus severely limits access to the central axis of the trap. To allow access to the central axis, the source rod is retracted around a 45° corner. In addition to allowing easy access to the central axis, this feature also allows shielding material to be placed between the source and the various particle detectors without the need to move heavy shields. Lead shielding material completely surrounds the vacuum system and a 3.5" thick Elkonite cylinder replaces an equivalent thickness of lead between the source and the inner detectors - this ensures that particle detectors are sufficiently shielded from the source. Finally, there are several lead blocks placed on the opposite side of the corner from the source to attenuate radiation that travels along the path that the source follows.

The support structure for the shielding material is built around a 1" thick aluminium plate. Attached to this plate are axles and wheels that allow the shielding enclosure to move. The corner piece is the center of the enclosure vacuum system. It is machined from a single piece of 1.25" brass plate. On one side, the path for the corner and an o-ring groove are milled out of the brass. A plexiglass cover is sealed, using this groove, and allows visual monitoring of the progress of the source as it rounds the corner. Three conflat flanges are brazed into the corner piece: one at a

45° angle and the other two in line vertically, providing a straight-shot.

The design of the corner shape is characterized by one length and two radii, as marked in Fig. 3.4. The length,  $L$ , determines the overall height of the corner piece. This determines the height of the entire shielding enclosure above the Penning trap. This in turn determines how high the concrete shielding blocks around the experimental zone must be. Due to the large mass of these blocks, this height was minimized. However, if  $L$  is too short compared to the length of the source rod a large tension will have to be applied to the string supporting the source rod to get it around the corner. After experimentation with a mock-up of the corner, the present length was chosen as a compromise. The two radii were chosen so that the front and back ends of the source are always in contact with part of the corner when the transition is being made between the vertical and 45° orientations. This helps to guide the source around the corner during its decent and control its ascent (Fig. 3.5). The titanium cap installed over the source capsule is an essential feature, since it prevents the source capsule from coming into contact with the walls of the corner piece.

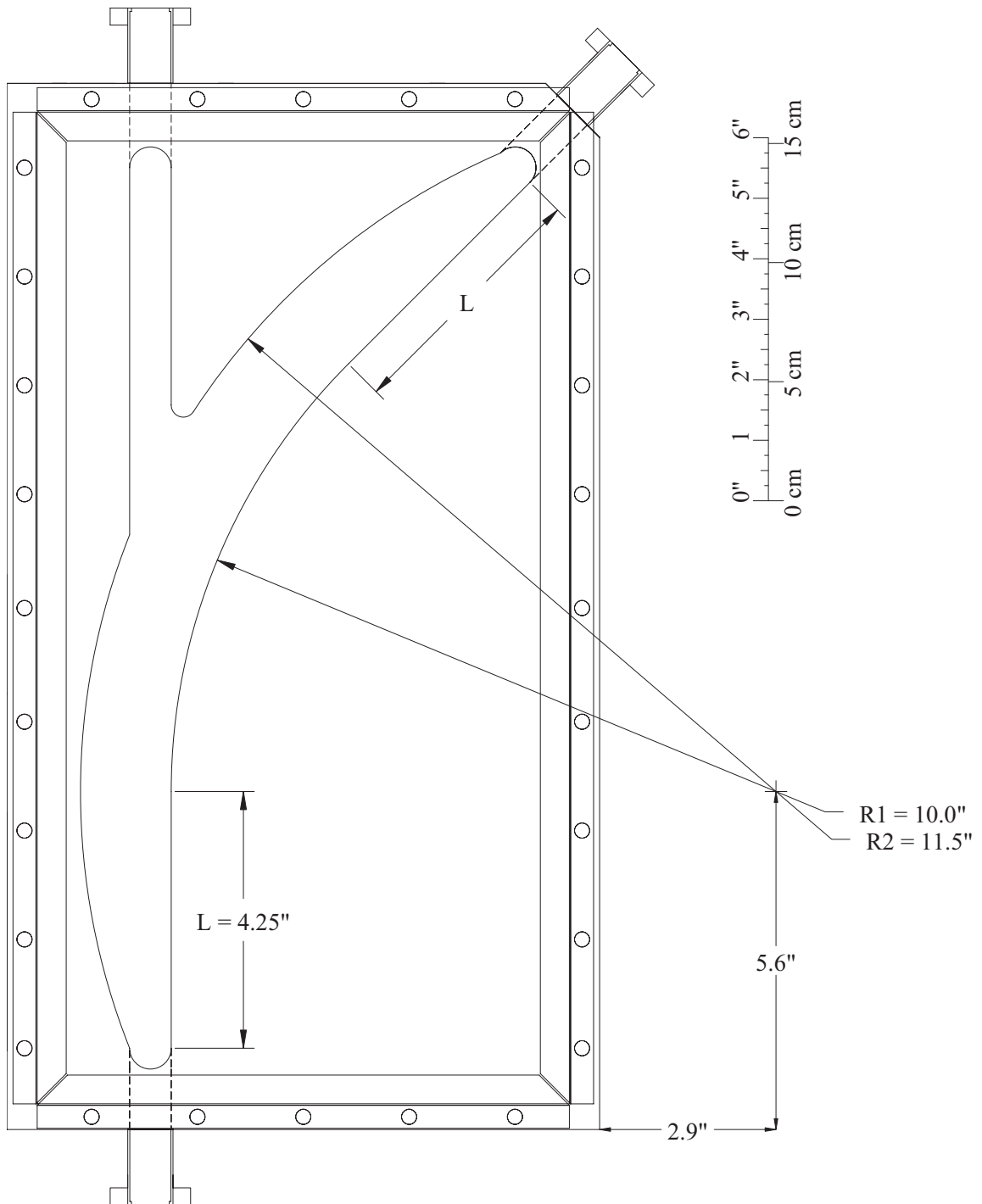


Figure 3.4: The corner piece.

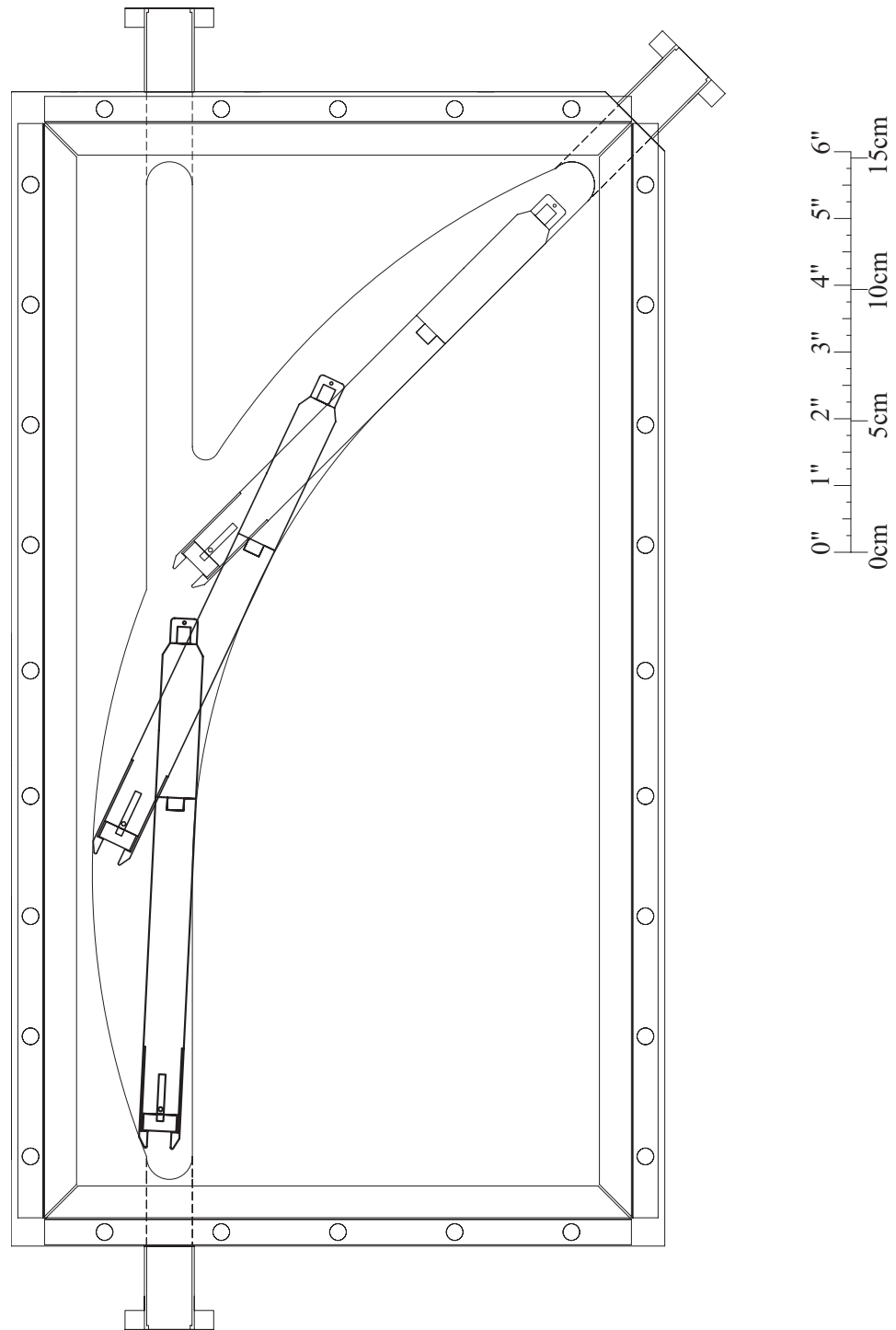


Figure 3.5: The source is guided around the corner by the carefully designed groove.

Attached to the corner piece is the remainder of the shielding enclosure vacuum system. Conflat nipple sections extend from the top vertical and 45° flanges. That extending vertically is simply a continuation of the straight shot. That extending at 45° leads to the normal housing position of the source rod. There is then a transition to a larger diameter nipple; this extra space is required to house the source rod pre-cooling system and a mechanical switch. The mechanical switch is activated by the source rod and indicates that it is in the position that provides maximum shielding. This switch is connected to the door interlock system. If the source rod is off the switch, the door can not be opened from the outside.<sup>5</sup>

The pre-cooling system is comprised of a liquid nitrogen dewar, a copper braid heat link, a copper tube, and Teflon standoffs. The copper tube houses the source rod and is centered within the conflat nipple by the Teflon standoffs. The copper tube is thermally connected to the liquid nitrogen by the copper braid heat link. The mechanical switch is mounted on the copper tube, as is a platinum resistor temperature sensor. In retrospect, Teflon was a poor choice of material for the standoffs as it contracts a great deal when cold. A material such as G-10 or Vespal would have been a better choice. Fortunately, this only caused difficulty with regard to the piece that held the mechanical switch and this problem was solved by careful fine tuning.

Because of its high density, the source rod has a substantial thermal mass. To cool the source rod from 300 K to 4.2 K would require the vaporization of  $\approx 9$  liters of liquid helium, while cooling from 77 K requires only  $\approx 0.5$  liters. Given that the capacity of liquid helium dewar attached to the Penning trap is only  $\approx 3$  liters, it is clear that pre-cooling is essential. In practise, the source is not cooled to 4.2 K every

---

<sup>5</sup>An emergency release that can be activated from the inside has never been used.

time it is lowered into the cryogenic environment. Instead, the source rod is held about 1 cm above the bottom. It is then in poor thermal contact with the cold apparatus, and the temperature and boil off of liquid helium rise only slightly. However, if this is attempted when the source rod has not been pre-cooled, the temperature rises by several Kelvin and the liquid helium dewar is rapidly emptied.

Beyond the pre-cooling system, there are many Kwik-flange components which house the string handling system. The string itself is a Dacron fishing line, rated 50 lbs test. This string was extensively tested for strength, both at room temperature and at 77 K. The string is attached to the source using a “bowline” knot. As a precaution the knot is covered with an epoxy glue, ensuring that it can not come undone. From the source rod, the string passes through a centering string guide that is mounted in a Kwik-flange o-ring. This string guide also prevents the source from being pulled out of the shielded region. The string then passes through a tension meter and another centering string guide and finally onto a motor-driven spool. The combination of the design of the spool and the centering string guide ensures that the string winds onto the spool, and not onto the axle that connects the spool to the motor.

The spool subsystem is built off a kwik-flange to conflat converter. A bearing mount is held off the vacuum side of the kwik-flange. The axle on which the spool is mounted rotates in these bearings. The axle is driven by a rotational motion feedthrough that is sealed to the conflat side of the kwik-flange to conflat converter. A computer controlled stepper motor drives the air side of the motion feedthrough.

Motion is transmitted between the various shafts and axles by flexible shaft couplings – these remedy any small misalignments between the various rotating shafts

and are essential to ensure a long lifetime for the bearings in the system. In addition, the bearing mount is machined to high precision to ensure that the bearings on each side of the spool are parallel and co-axial, and that the fit of the bearings in the mount is correct [47].

Obviously, the string handling system is critically important from the point of view of safety. Extensive testing was carried out using a dummy source rod to ensure the robustness of the system. The major difficulty encountered during testing was the robustness of the bearings – these were found to be very sensitive to the precision with which the bearing mount was constructed and held relative to the motion feedthrough shaft. The final system was tested for about 5000 source rod retraction cycles before being installed at CERN. Since then it has operated without incident.

The tension meter provides important information about the state of the source rod as it is in motion (Fig. 3.6). Most importantly, if the source rod were to become held up somewhere as it was being lowered the string tension would drop. If this occurs, it is essential that no more string be paid out to avoid the string coming off the spool and fouling upon the spool shaft. Hence, the software that controls the stepper motor is very carefully designed. If the string tension drops below a preset limit, the software will not allow the source rod to be lowered further. In addition, there is a small possibility that the source rod could become struck when it is being raised. Hence, if the string tension rises above a preset limit, the software will not allow the source rod to be raised further.

As a further precaution, the control software only sends small packets of motion to the motor controller. If, for example, the user requests that the source be lowered

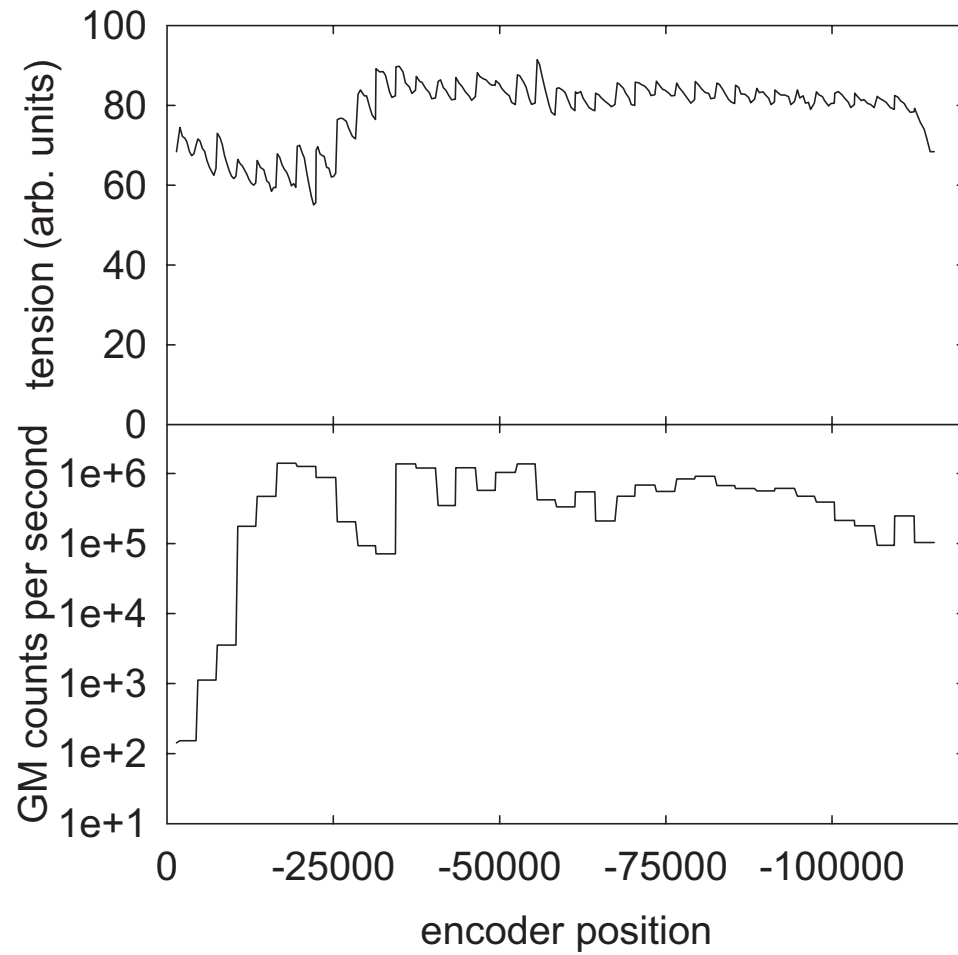


Figure 3.6: Tension and radiation readings as a function of motor encoder position.

from the shielding enclosure to the top of the Penning trap, the source could become snagged if the enclosure was misaligned relative to the Penning trap. This would be a dangerous situation if the software commanded the motor controller to move to that position in one step and the source rod became snagged half way down. Then string would continue to be paid out, even though the source was stuck. Instead, the software commands the motor controller to move a small amount ( $\approx 2$  cm) and then checks the string tension. If the tension is within the preset limits, the source rod is again moved a small amount, the string tension checked, etc.

There are several means of determining the position of the source rod as it is moved. The most obvious of these is the value of the motor encoder. The encoder is set to zero when the source rod is resting on the mechanical switch in the shielding enclosure. By experiment, it was found that the encoder value when the source rod just touches the Penning trap is about  $-118,000$ . In practice, we do not lower the source rod until it touches the Penning trap, as this imposes an unnecessary heat load upon it. Instead, we lower the source until it is about 1 cm from touching the Penning trap.

Plots of radiation intensity and string tension versus encoder position (Fig. 3.6) provide verification that motion is proceeding as normal. Variations in tension are seen as the source rod descends at  $45^\circ$ , rotates to a vertical position, and descends into the Penning trap. Similar variations are seen as the source rod is raised. As the source rod is lowered, the radiation count rate rises rapidly. Variations are seen as the source passes behind the corner shielding material and into the solenoid, particularly once the source is within the solenoid coils.

Finally, the source can be observed visually using a video camera, as it rounds the corner. Careful inspections are made of the source rod and supporting string in this position. A camera is also positioned to observe the string as it winds onto the spool. Even when the source rod itself is not in view, the string itself can be observed using marks on it that are at 12" intervals.

## 3.2 Positron accumulation

To accumulate positrons into a Penning trap well, a mechanism is required that can remove axial energy very rapidly (during one transit along the length of the Penning trap), otherwise a moderated positron will simply annihilate on the ends of the Penning trap. Finding an efficient mechanism is indeed a challenge, as there are many other requirements that must be met. There are several techniques in use, each with advantages and disadvantages. These will be described and compared in Sec. 3.2.5. The accumulation method used in this work, chosen because of its simplicity and compatibility with the extremely high vacuum required for antiproton trapping, will first be discussed in detail.

### 3.2.1 Formation and ionization of strongly magnetized Rydberg positronium

The electrodes and potentials used for positron accumulation in the HBAR1 Penning trap are shown in Fig. 3.7. A mechanical chopper wheel is located between the  $^{22}\text{Na}$  source and the transmission moderator (to the left in Fig. 3.7). This is used

to allow or prevent positrons from entering the trap enclosure, and also to measure the positron current from the  $^{22}\text{Na}$  source. This is followed by the  $10\ \mu\text{m}$  Ti window that separates the cryogenic vacuum of the Penning trap enclosure from the vacuum of the magnet bore. A small fraction of the high energy positrons thermalize in a  $2\ \mu\text{m}$  tungsten single crystal transmission moderator (TMOD) that comes next. Those positrons that are not attenuated or moderated in TMOD carry on through the Penning trap until they strike a 2 mm thick tungsten single crystal reflection moderator (RMOD). Each of the moderator crystals is specially heat treated in the manner described in [6] to remove impurities that reduce the moderation efficiency.

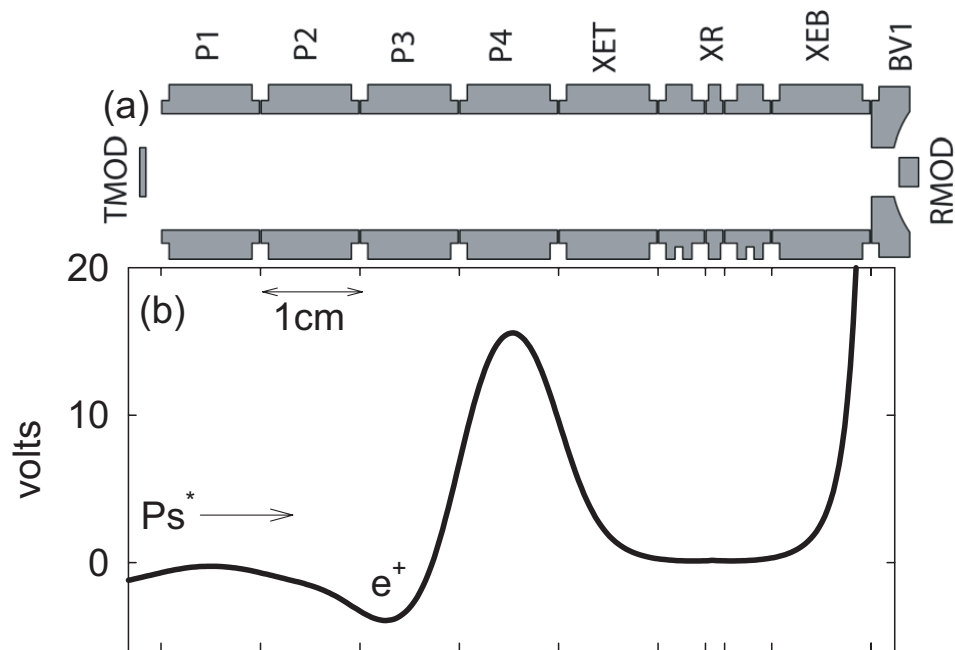


Figure 3.7: (a) Electrodes used to study positron accumulation. (b) A typical potential configuration used to accumulate positrons.

Positrons are accumulated by first forming strongly magnetized Rydberg positronium from a moderated positron and secondary electron at the surface of a moderator and then ionizing it after it travels several centimeters to a Penning trap well. By

carefully arranging the potentials forming the well, the positron from positronium can be trapped. This method was first studied in [5, 35] and detailed investigations were later described in [6, 48]. The remainder of this section is a brief summary of this previous work.

The positron accumulation process begins when a moderated positron leaves the transmission moderator followed by a secondary electron. The strong magnetic field keeps the positron and electron on nearby field lines. By biasing the transmission moderator with respect to the surrounding electrodes, energy can be added to one species and removed from the other. Thus, by optimizing this bias (Fig. 3.8) the axial spacing between the positron and electron can be minimized and their axial velocity matching improved. If the electric field within the trapping well is strong enough, the positronium will be ionized and the positron captured if its axial kinetic energy is sufficiently low. The electron carries away the excess energy. Note that no interactions are required with other species, e.g. background gas atoms or trapped electrons, for this to occur.

The most definite signature of this process is that when the well potentials are reversed, electrons and positrons are accumulated at the same rate (Fig. 3.8). Other potentials involved in the formation of Rydberg positronium, in particular that applied to TMOD, are left unchanged during this demonstration. The positronium hypothesis was tested further by the imposition of a gentle potential barrier between TMOD and the accumulation well. The slope of the barrier was gentle enough that its electric field was not strong enough to ionize the positronium, yet was high enough to prevent the passage of moderated positrons. Positron (and electron) accumulation

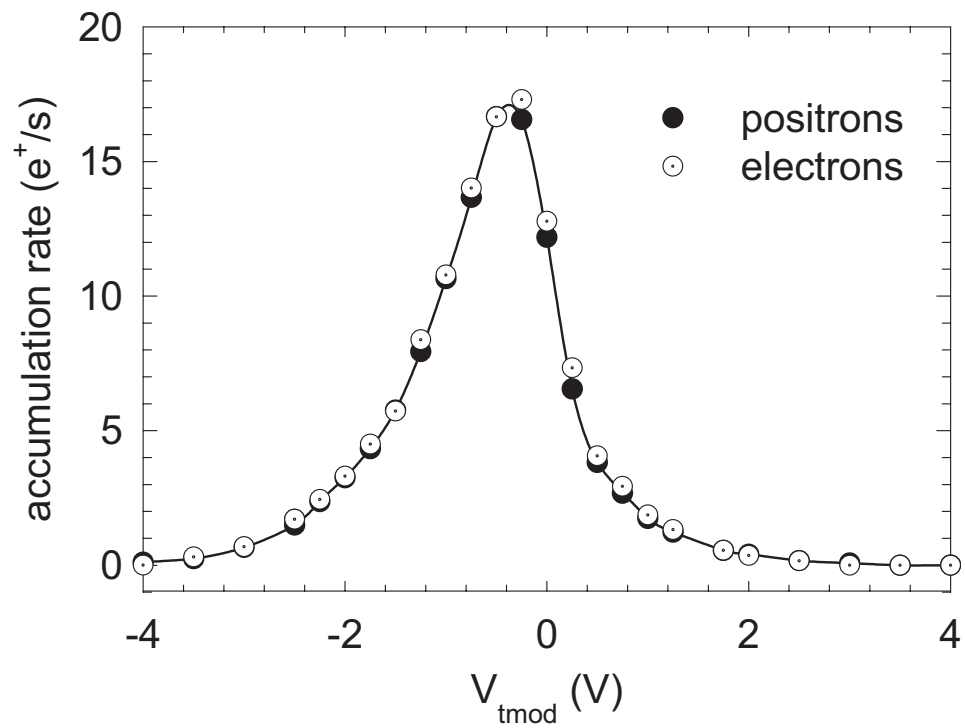


Figure 3.8: Accumulation of positrons (and electrons) is optimized by varying the potential applied to TMOD. Taken from [6].

was unaffected by this barrier, indicating that positrons (and electrons) were reaching the accumulation well as neutral particles (positronium).

There are two distinct channels for the formation of Rydberg positronium. The first is simply that described above: A high-energy positron from the radioactive source is moderated in TMOD and, as it emerges, it forms Rydberg positronium. This travels along the direction of the magnetic field to the accumulation well, where it is ionized and the positron captured. However, a large fraction of the incident positrons simply pass through TMOD without slowing much and strike RMOD. Some small fraction of these are moderated and emerge from the surface of RMOD with low energy. By applying a positive potential to RMOD, these moderated positrons can be accelerated back towards TMOD. There they can be remoderated and form Rydberg positronium, just as described above. The effect of varying the potential applied to RMOD is shown in Fig. 3.9. When a negative potential is applied, moderated positrons from RMOD cannot reach TMOD and the second channel is closed. When a positive potential is applied, the second channel is opened. Applying a greater positive potential presumably implants the positrons from RMOD to a greater depth in TMOD. From Fig. 3.9 we see there is an optimum depth for highest remoderation efficiency. When fully optimized, the second channel increases the accumulation rate by a factor of 2.6.

The potential structure displayed in Fig. 3.7 has been carefully optimized to maximize the accumulation rate. The potential applied to each electrode serves a different purpose. For example, the potential applied to TMOD acts to velocity match a moderated positron and a secondary electron, while that applied to the electrode P2

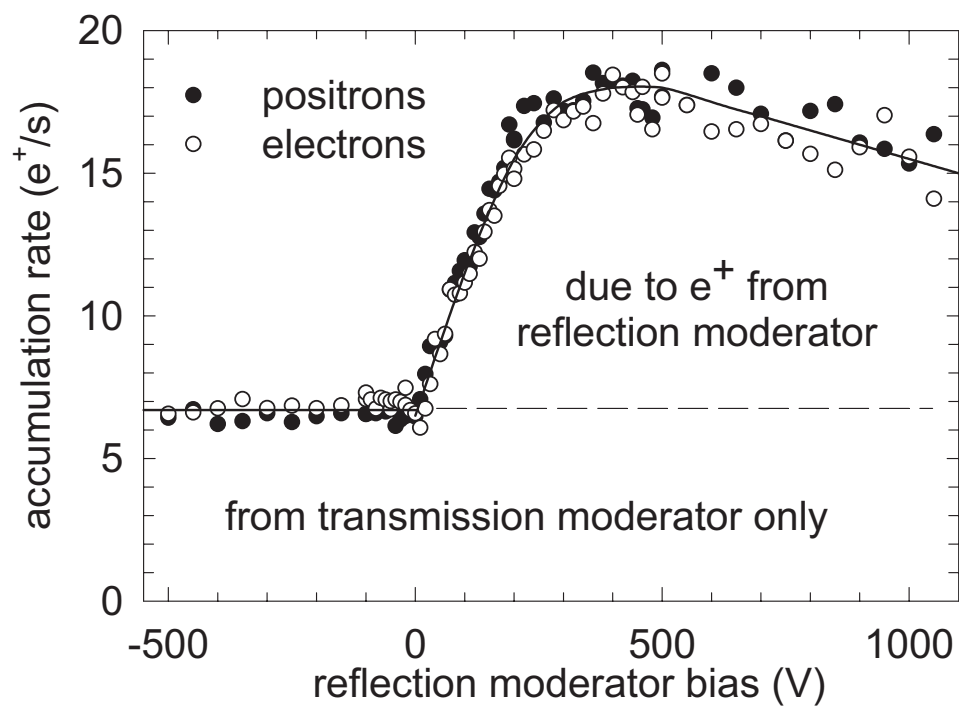


Figure 3.9: By applying an appropriate potential to RMOD, a second positronium formation channel can be opened up. Taken from [6].

moves the point of ionization deeper into the accumulation well on electrode P3. The optimal potential value for any one electrode is largely independent of that for other electrodes. Scans over the three potentials that form the ionization well are shown in Fig. 3.10.

Note how simple this accumulation method is. One simply has to apply appropriate potentials and then wait for positrons to accumulate. No active control is required and the accumulation proceeds despite the extremely high vacuum.

### 3.2.2 Comparison of different radioactive sources

The initial studies of positron accumulation from highly magnetized Rydberg positronium [6] were carried out with a 2.5 mCi  $^{22}\text{Na}$  source that was 2 mm in diameter. Based on the success of these studies, a much stronger  $^{22}\text{Na}$  source (150 mCi initially but 79 mCi at the time these experiments were performed) was obtained. To avoid self absorption in this more intense source, the active diameter was increased to 3 mm. Fig. 3.11 contrasts the observed dependence of the normalized positron accumulation rate upon the electric field applied to TMOD for the weaker and the stronger sources. In addition to the different source diameters, the geometry of the surrounding electrodes that form the electric field is different. Hence, the profile of the electric field across the moderator is different in each case. This, in combination with the difference in the source diameters, may be responsible for the additional shoulder seen on the peak for the more intense source. The accumulation rate, integrated over all electric field values, is equal in each case. As the maximum relative rates for the two sources are similar, the absolute accumulation rate is much greater

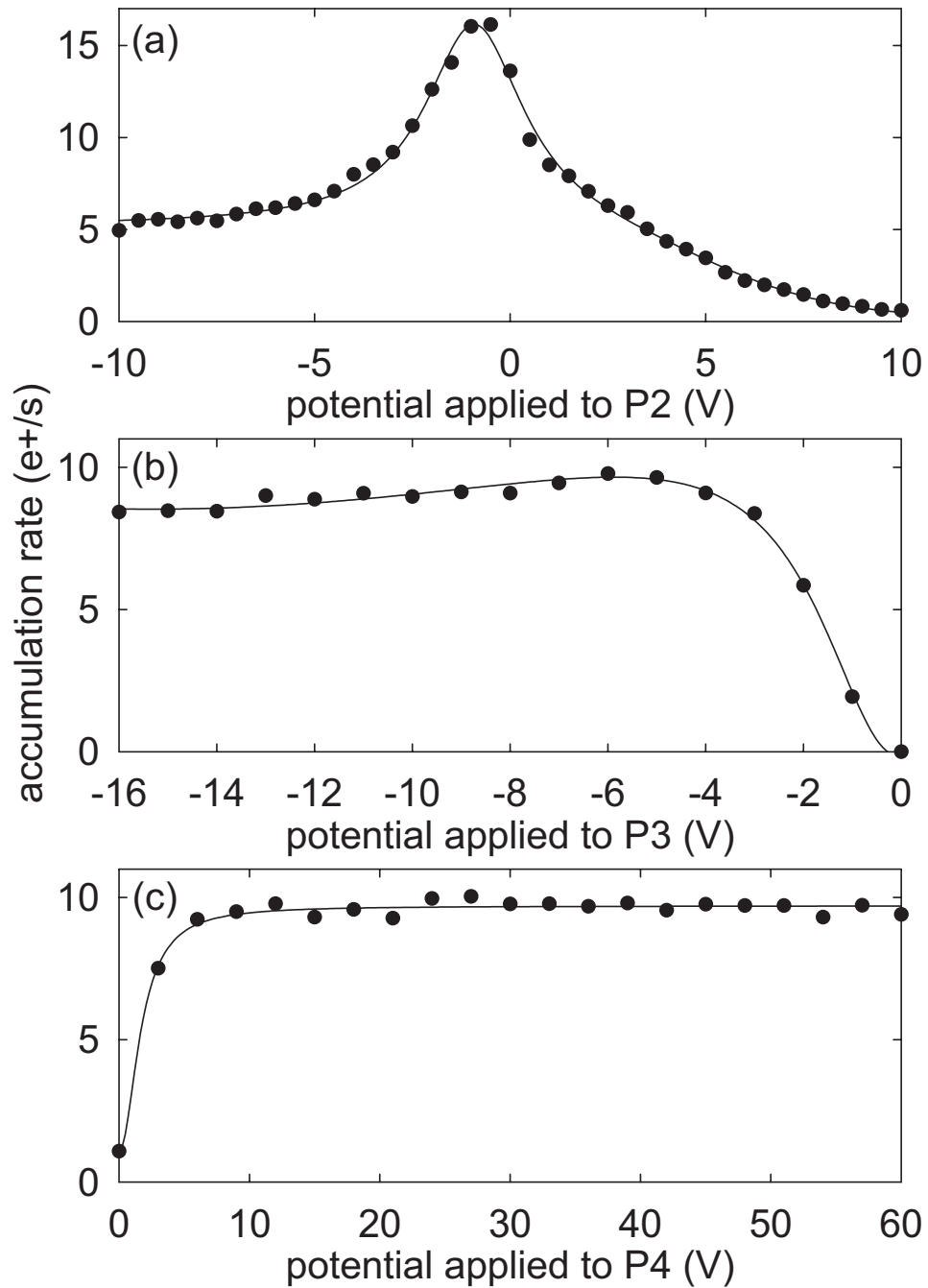


Figure 3.10: Scans over the ionization well potentials. The potential applied to the electrode P2 acts to smooth the electric field at the entrance to the ionization well and thus allows the positronium to ionize more deeply in the well. The potential applied to P3 forms the well for trapped positrons and that applied to P4 provides the ionizing electric field. Taken from [48].

with the more intense source, as desired.

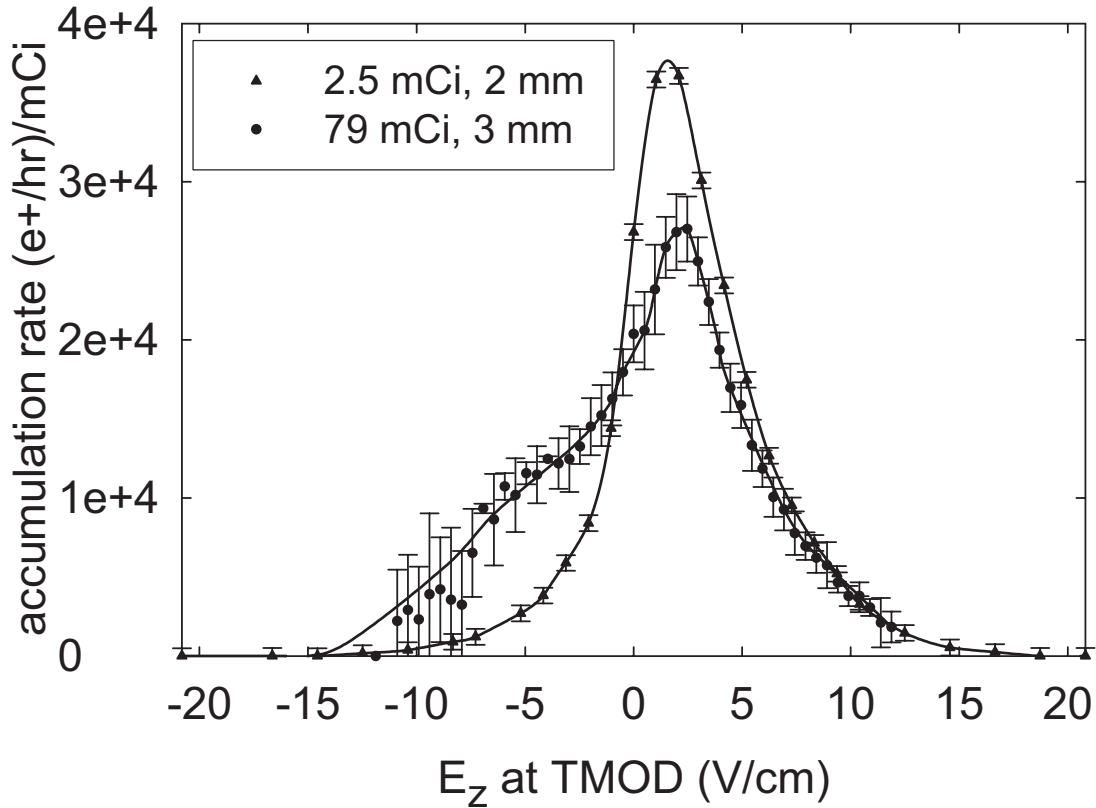


Figure 3.11: The electric field applied to the surface of the transmission moderator is scanned to compare the accumulation characteristics of the system first used to study the accumulation mechanism [6] and that used here.

### 3.2.3 Limitations of Rydberg positronium accumulation method

While this accumulation mechanism is very simple and compatible with the extremely high vacuum required to store antiprotons almost indefinitely, it is not without its limitations. First, as will be discussed further in the Sec. 3.2.5, the efficiency with which positrons from the source are trapped is lower than other methods. A second limitation is the strong dependance of the accumulation rate upon a surface

layer deposited on the transmission moderator. This layer is simply the gas adsorbed upon the moderator as it is exposed to the residual gas in the Penning trap vacuum enclosure – its composition and exact role is unknown and is not optimized for the purpose of Rydberg positronium formation.

This accumulation method was first used with antiprotons at the end of the LEAR run [5]. In the Penning trap used, antiprotons would enter from the bottom and positrons from the top. Those antiprotons that were not trapped would strike the transmission moderator. It was found that after many antiproton shots were taken, the positron accumulation rate would be much reduced. Warming the Penning trap to room temperature and then returning it to 4.2 K would restore the accumulation rate. While it is possible that extended exposure to a beam could affect the crystal structure of the moderator and thus its moderation efficiency, simply warming the crystal to about 300 K would be insufficient to repair such damage. Hence, it was theorized [35] that a layer of adsorbed gas was being removed by the antiproton beam, and this gas was important to the Rydberg positronium formation process.

To test this hypothesis, scans were taken over the potential applied to TMOD as the gas layer was gradually removed by radiation from a laser [6] (Fig. 3.12). Heating the moderator in this way should remove adsorbed gas from the crystal surface, but should not affect the structure of the crystal. As can be seen the accumulation rate decreased as the moderator was exposed to the laser for greater amounts of time, i.e. as the adsorbed gas layer was removed. In addition the peak of the TMOD scan shifted as the gas layer was removed. Thermally cycling the Penning trap apparatus to room temperature restored the original accumulation characteristics.

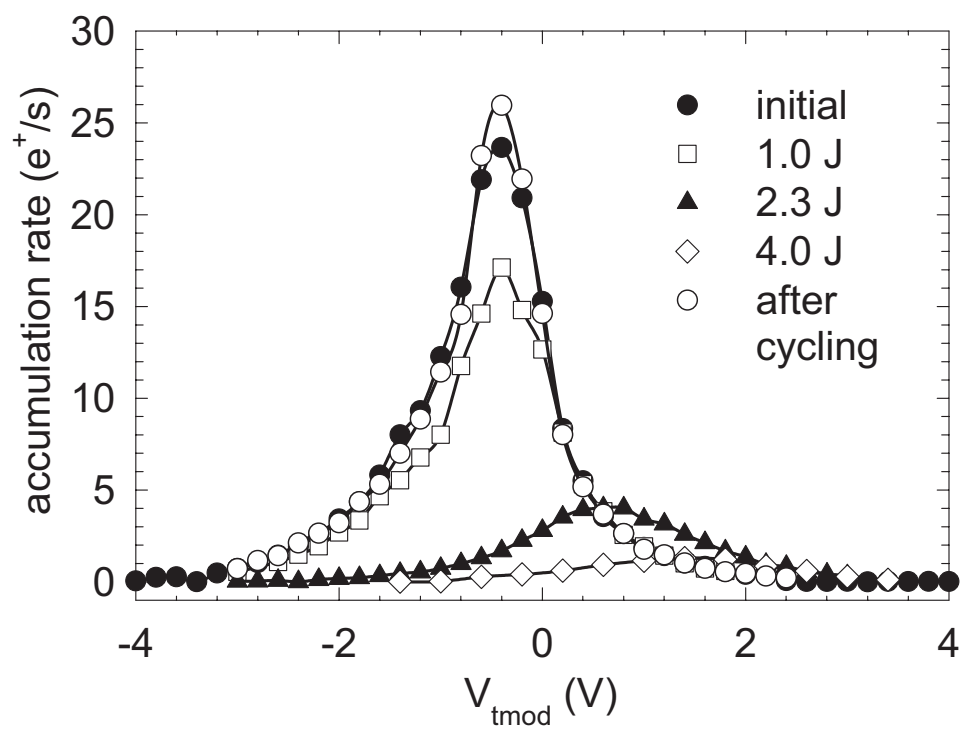


Figure 3.12: The accumulation characteristics change as the gas layer crucial to Rydberg positronium is gradually removed. Thermally cycling the Penning trap apparatus restores the original accumulation rate. Taken from [6].

It is for this reason that the ball valve is an essential feature of the HBAR1 Penning trap. Without it, antiprotons would rapidly clean the transmission moderator and positron accumulation would cease, as it did at LEAR. As mentioned in Sec. 2.1.2, the ball valve also holds the reflection moderator, which boosts the accumulation rate by over 100%.

Antiprotons and laser light are not the only means by which to remove the crucial gas layer. High energy positrons from the intense source can have the same effect though the cleaning time is much longer. During the early investigations of positron accumulation from Rydberg positronium, it was found that the accumulation rate was stable over months [6, 5]. The initial studies were conducted with the 2.5 mCi  $^{22}\text{Na}$  source. With the more intense  $^{22}\text{Na}$  source, the positron accumulation rate also seemed stable over many months [8]. However, during these months positrons were sent into the apparatus as needed for other experiments, but only for a small fraction of the time. In addition, the apparatus was warmed up to room temperature on a weekly to monthly basis in order that the apparatus could be adjusted, repaired, etc.

With positrons from the more intense source sent into a cold apparatus for longer times (without warming the apparatus), a slow reduction of the positron accumulation rate is observed. Fig. 3.13 shows an example of the loading rate decreasing as a function of the time that positrons are actually being sent into the trap apparatus. Presumably, positrons from the intense source travel through the moderator in sufficient numbers to be able to slowly clean the crucial adsorbed gas layer from the transmission moderator just as antiprotons and a laser were able to do much more rapidly. Beam-induced sputtering of frozen gas layers has been widely studied [49].

It is likely that beam-induced evaporation is the dominant cause of layer loss for the high intensity sources (antiprotons, laser) and knock-on sputtering for the low intensity positron beam. The decrease is slow enough that it was not observed with the weaker source used for the initial studies.

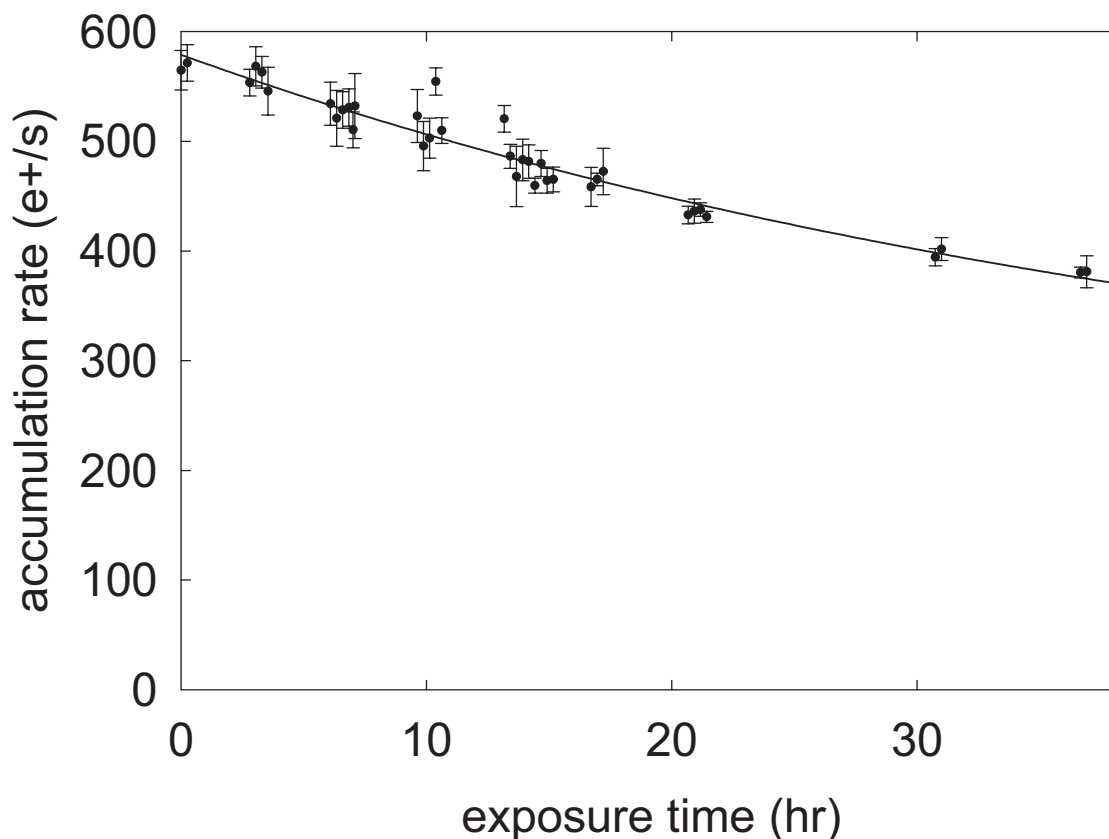


Figure 3.13: The accumulation rate decreases when the gas layer on the transmission moderator is exposed to the positron beam.

In all cases that the accumulation rate has decreased, it is restored by warming the apparatus to room temperature. However, warming the apparatus to 77 K does not restore the accumulation rate. This suggests that the crucial component of the surface layer is not, for example, He, N<sub>2</sub>, Ar, or O<sub>2</sub>, all of which have a substantial vapor pressure at this temperature, but rather could be H<sub>2</sub>O or some other substance that

would remain adsorbed. A more detailed investigation, measuring the restorative effects of warming to different temperatures, might be able to isolate the crucial component.

The effects of various surface layers on the secondary electron emission properties of tungsten have been studied in [50] (NaCl, KCl, LiF, and CaF<sub>2</sub> layers) and [51] (O and Cl adsorbate layers). In both studies, secondary electrons emission was enhanced, and the energy distribution of secondaries and the work function was modified by the presence of a surface layer. In [50] erosion of the surface layer by an incident electron beam gradually returned the secondary electron emission characteristics to that of bare tungsten. These reports suggest an explanation for why the gas layer is crucial to our positron accumulation mechanism. The gas layer substantially increases the emission of secondary electrons with energies matching those of the moderated positrons. As the gas layer is gradually removed by the high energy positron beam, secondary electron emission and thus positronium formation, is reduced. This raises the exciting possibility that the positron accumulation rate could be substantially increased by the use of a carefully chosen surface layer that maximizes the secondary electron emission in the appropriate energy range, a possibility being actively pursued by our research group.

To maintain a relatively high positron accumulation rate, it is necessary to thermally cycle the Penning trap apparatus every one to two weeks. The Penning trap apparatus can be taken from 4.2 K to about 280 K and back to 4.2 K in 24 hours without removing it from the magnet bore. Blowing room temperature nitrogen gas into the liquid helium dewar warms the trap in about 15 hours; the apparatus is

pre-cooled with liquid nitrogen for about 8 hours and then cooled to 4.2 K in about 1 hour using liquid helium. This procedure restores the peak accumulation rate. Resistive heaters have been installed to substantially reduce the time required to heat, and thus thermally cycle, the Penning trap.

### 3.2.4 Magnetic field dependence of the accumulation rate

The applied magnetic field is thought to play a crucial role in the formation of the highly magnetized Rydberg positronium because the strong magnetic field pins the moderated positron and secondary electron to nearby field lines. To verify this and to further investigate the formation process, the magnetic field dependence of the accumulation rate was measured. This dependence is also a critical design parameter for future antihydrogen experiments. One simplifying feature of the Rydberg ionization method is that positrons can be accumulated directly into the same trap structure used to accumulate antiprotons. In this situation, the magnetic field strength at the site of antihydrogen production will be the same as that at the site of Rydberg positronium formation (the surface of the tungsten moderator). As a smaller magnetic field than that used to date [6, 8] is likely to be used to simultaneously trap both antihydrogen and its ingredients,<sup>6</sup> a knowledge of the dependence of the positron accumulation rate on the magnetic field strength is essential for future antihydrogen experiments.

The positron accumulation rate and the positron currents reaching several impor-

---

<sup>6</sup>A realistic neutral trap (of the Ioffe-Pritchard type) will have a radial strength of order 1 T. To find the depth of the neutral trap we add the neutral trap strength in quadrature with the axial magnetic field of the Penning trap. For example, for a Penning trap field of 5.3 T and a neutral trap field of 1 T the effective neutral trap depth is 0.1 T (0.07 K). With a Penning trap field of 1 T the effective neutral trap depth would be 0.4 T (0.28 K).

tant locations in the Penning trap were measured as a function of the magnetic field strength. Fig. 3.14 displays the primary positron current measured in the Penning trap as a function of the magnetic field strength. During this measurement, care was taken to measure and eliminate secondary electron currents generated by the high energy positron beam. As the magnetic field becomes weaker, the positrons are more weakly guided along the central axis of the Penning trap. The solid lines in Fig. 3.14 are the results of a simple Monte-Carlo simulation that predicts the fraction of high energy positrons from the  $^{22}\text{Na}$  source that should travel through the Penning trap given the size of various apertures through which the beam must pass. In this simulation, a positron energy is selected from the energy distribution for  $^{22}\text{Na}$ , an emission position is uniformly selected from the 3 mm diameter active source area, and an emission angle is selected from the isotropic emission distribution. The energy and emission angle determine the cyclotron radius of the positron, which in combination with the initial position determines the maximum excursion in the  $x-y$  plane. Those positrons that travel too far strike the apertures and are removed from the beam.

The Penning trap apparatus was thermally cycled twice at each magnetic field value and the accumulation rate measured immediately after the thermal cycle, to ensure that the peak rate was being measured. Also, scans were performed over all potentials (TMOD, RMOD, and ionization well) at each magnetic field value to ensure that the optimum potential structure was used. Examples of scans over the voltage applied to TMOD are given in Fig. 3.16. These scans were taken immediately after a thermal cycle with all other potentials set to their optimum value, and are used to determine the peak accumulation rate.

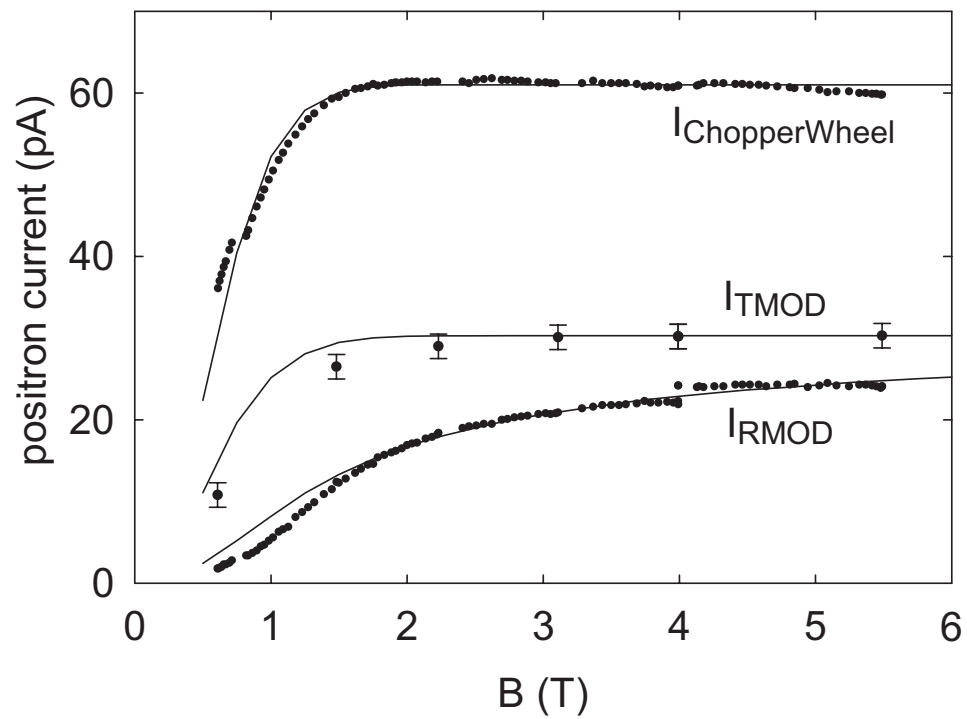


Figure 3.14: Positron currents measured at the chopper wheel, transmission moderator, and reflection moderator. Error bars, of equal magnitude to those displayed for TMOD, are omitted from the RMOD and chopper wheel measurements for clarity.

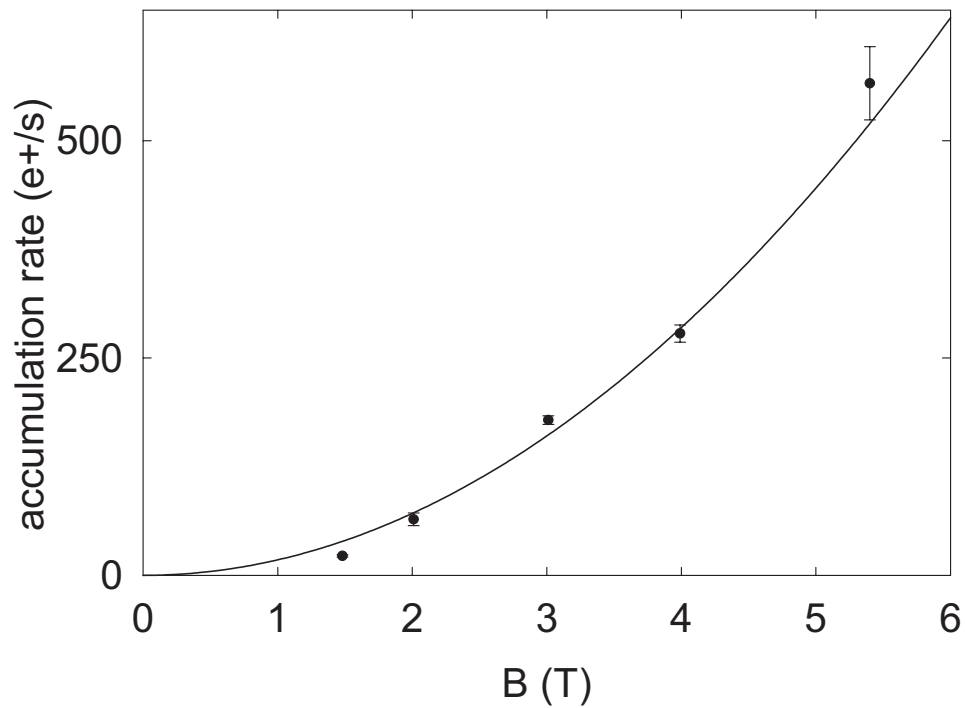


Figure 3.15: Measured dependence of positron accumulation rate on magnetic field strength. The accumulation rate has been scaled to take account of the lower positron currents reaching the transmission and reflection moderators at lower magnetic fields. Solid line is the best quadratic fit to the data.

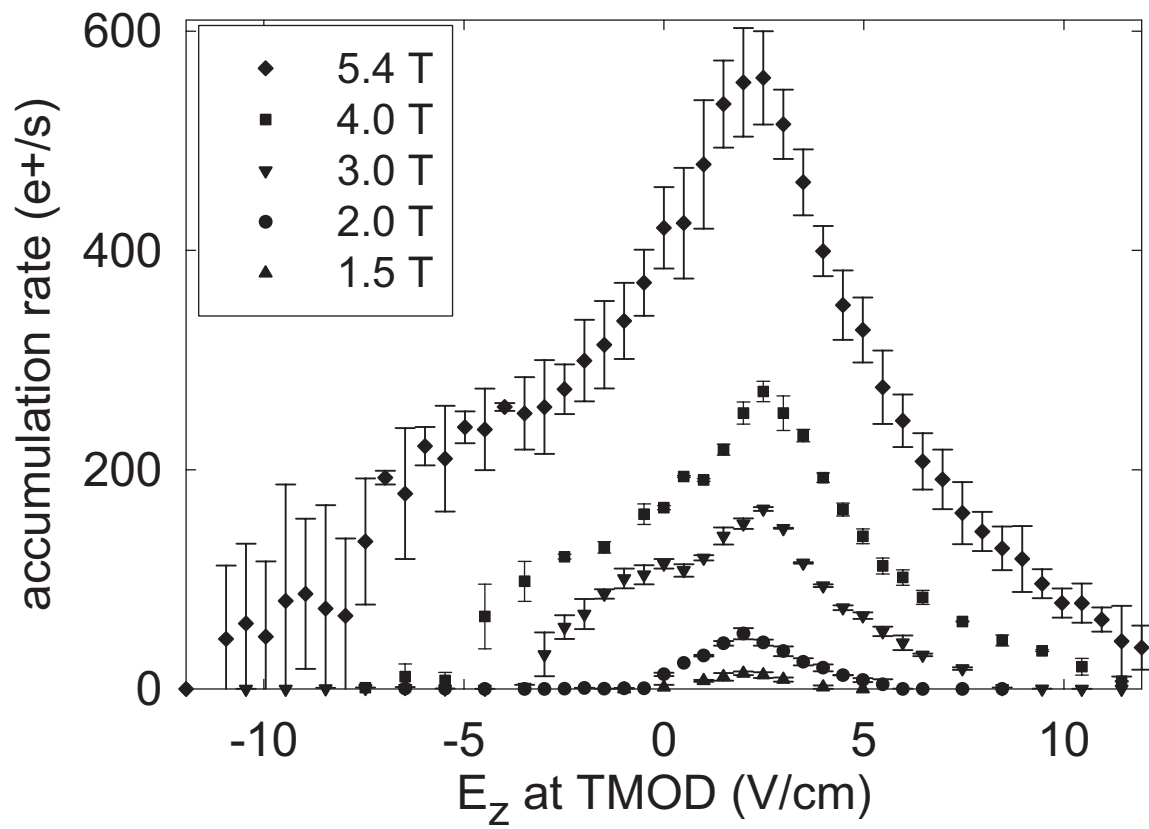


Figure 3.16: TMOD scans taken at various magnetic fields.

The variation of the peak positron accumulation rate (Fig. 3.15) is consistent with a quadratic dependence upon the magnetic field strength. The accumulation rate at lower fields in Fig. 3.15 has been scaled to take account of the lower positron currents reaching the transmission and reflection moderators so the magnetic field dependence exhibited is that of the Rydberg positronium formation process.

As the strength of the magnetic field is reduced, positrons (and electrons) are less strongly guided, as Fig. 3.14 demonstrates. This strong guiding at high fields seems to enhance the Rydberg positronium formation process. An example of a potentially relevant quantity that scales as  $B^2$  is  $\nu_c/r_c$ , the ratio of cyclotron frequency to the cyclotron radius (Fig. 3.17). This quantity could be relevant to the positronium formation process since it is proportional to the ratio of the number of times a positron and electron would collide per second to their average separation.

Careful attention will have to be paid in the design of future apparatus to the field dependence of both the positron currents and accumulation rate. Larger apertures and moderator crystals should ensure that most positrons have the chance to be moderated. However, as the Rydberg positronium formation rate appears to drop severely at low fields an additional solenoid centered on the transmission moderator may be needed. Such a solenoid could also act as a pinch coil for a Ioffe-Pritchard neutral trap.

### 3.2.5 Alternative positron accumulation schemes

As will become apparent in Ch. 6, larger positron clouds than those used in this work will be needed for future antihydrogen experiments. In the next section,

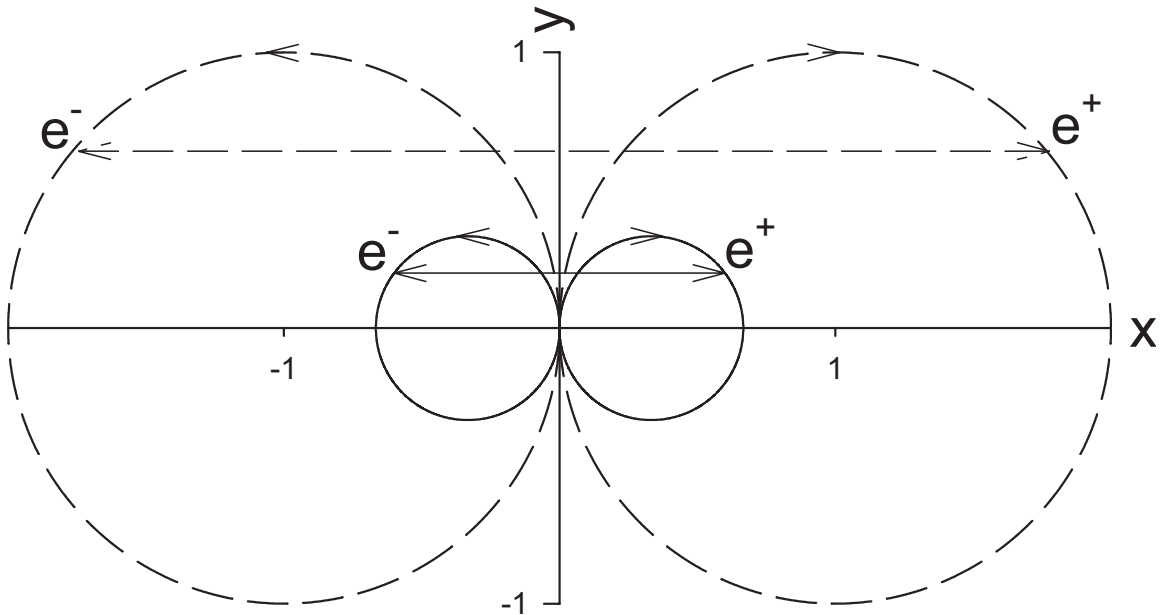


Figure 3.17: A simple diagram demonstrating the behavior in the  $x - y$  plane of a moderated positron-secondary electron pair originating at the same point with the same radial energy. The solid trajectory has an axial magnetic field three times stronger than the dashed. The separation of the particles averaged over one cyclotron period is proportional to  $r_c$ , which is proportional to  $B$ . The number of times that the two particles return to the point of origin, or “collide,” is proportional to  $\nu_c$ , which is also proportional to  $B$ . The quantity  $\nu_c/r_c$  may then provide a measure of how well correlated a pair are, yielding a  $B^2$  scaling.

Group	Method	Loading Rate (e+/s)	Source Strength (mCi)	Loading Rate (e+/s/mCi)	Maximum Number Accumulated
ATHENA	Buffer Gas	500,000	50	10,000	300,000,000
ASACUSA -proposal -experiment	Electron Cooling	1,000,000	44	20,000	
		7,000	20	350	400,000
ATRAP	Rydberg Positronium	500	75	7	17,000,000

Table 3.1: Comparison of various positron accumulation schemes.

techniques for efficiently reusing positrons will be suggested. In this section, we will review other more efficient accumulation mechanisms, and assess their compatibility with the long term objectives of the ATRAP experiment.

There are three known techniques for rapidly accumulating large numbers of positrons in a Penning trap:

- Ionization of Rydberg positronium. Rydberg positronium is formed at the surface of a moderator and ionized in a trapping well. Used by ATRAP [6].
- Buffer gas loading. Collisions with a background gas are used to trap moderated positrons. Used by ATHENA [52].
- Electron cooling. A very large electron cloud is used to collisionally cool moderated positrons. Being developed by ASACUSA [53].

The efficiencies of these three methods are compared in Table 3.1.

The mechanism involving the ionization of Rydberg positronium has been described in detail in the preceding sections. The best features of this method are its

great simplicity and its compatibility with the extremely high vacuum required to store antiprotons (and hence antihydrogen) without loss. However, it has the lowest accumulation rate of any of the methods.

The buffer gas loading mechanism has a very high accumulation rate. However, positrons are loaded via collisions with a buffer gas, thus the vacuum in the accumulation region is inherently poor. This poor vacuum also severely limits the lifetime of the positrons themselves, and it is thus necessary to have a long (1 m) differential pumping stage to rapidly bring the pressure down sufficiently.

In this case, it is not possible to separate regions of different vacuum quality using a window that is able to support a differential pressure of one atmosphere, since the positron energy (a few volts) is too low to traverse such a window. To keep the vacuum in the antiproton region sufficiently low, a valve separates the positron and antiproton accumulation regions. It is opened only briefly when positrons are transferred into the antiproton accumulation region. This valve is at room temperature, as are most of the transfer elements, and hence the gas load upon the cryogenic system maintaining the vacuum in the antiproton region is substantial. The lifetime of antiprotons in this system is hence limited to about 1 hour.

On the plus side, very large numbers of positrons can be accumulated very rapidly. In a typical experiment cycle, ATHENA report [9] obtaining 150 million positrons for interaction experiments from a 5 minute accumulation. In that same time, they are able to accumulate around 10,000 antiprotons. Interaction experiments can thus be carried out about once every 15 minutes, and the 1 hour antiproton lifetime is not a limitation. However, whether this is long enough to make high precision measure-

ments of trapped antihydrogen is not clear.

To be able to incorporate such an accumulation system into the ATRAP experiment would be extremely difficult. First, the experimental area available is rather small, and the only way to fit all the required equipment would be to have a  $90^\circ$  bend in the transfer stage. Of course, the most difficult problem to overcome would be the poor vacuum that results from using such a system. To improve upon that used by ATHENA, there are several possible approaches. Having a cold valve would reduce the gas load from warm areas of the system, but would be very difficult to build and maintain. Another difficult feature of such a valve is the fact that it would have to be contained inside the solenoid, placing even more stringent constraints upon its design and operation. Another option would be to separate the vacuum regions by an extremely thin window that could not support a differential pressure of one atmosphere. However, this approach requires that the antiproton and positron accumulation regions be pumped down simultaneously, which may well result in room temperature elements being part of the antiproton vacuum space. Also, such windows are extremely fragile, and could be destroyed easily by accident.

An accumulation scheme that shows great promise is currently being developed by members of the ASACUSA collaboration [53]. This scheme is compatible with the extremely high vacuum required to hold antiprotons indefinitely and is, in principle, very simple. Collisions with electrons are used to cool moderated positrons into a well (Fig. 3.18). However, this scheme is not without complications and large numbers of positrons have not yet been accumulated. The electron cooling must occur within one pass through the Penning trap, otherwise a moderated positron would simply strike

the moderator again. As moderated positrons have a typical energy spread of about 1 eV, of order 1 eV must be lost in a single pass.

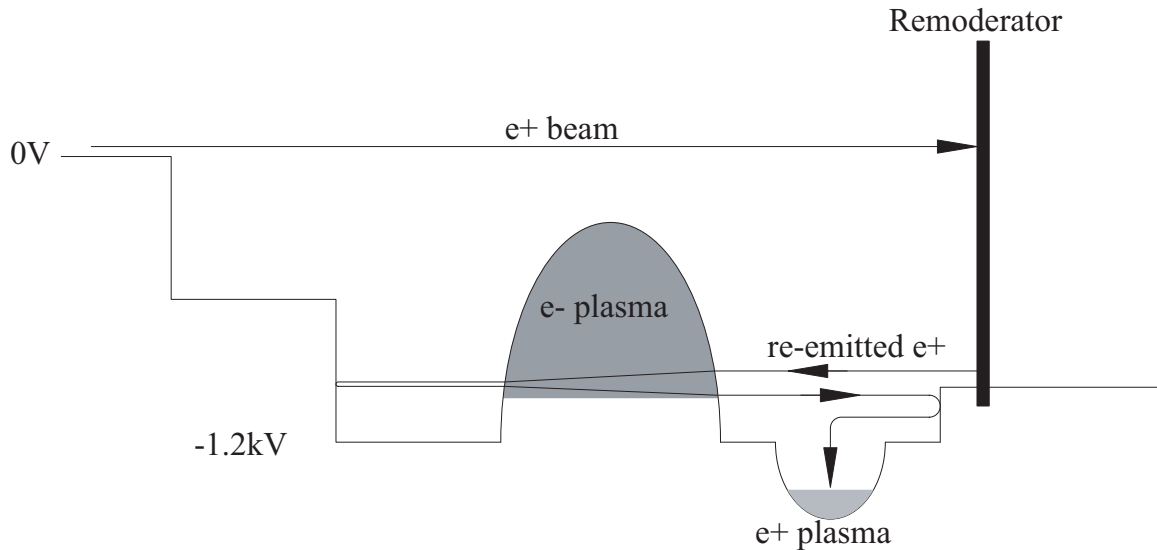


Figure 3.18: Positrons are cooled into a well via collisions with a large electron cloud. The space charge of the electron cloud is many hundreds of volts, and the positron beam energy must be carefully tuned to match the space charge.

Oshima *et al.* estimate that an electron cloud 25 cm long with a density of  $10^{11} \text{ cm}^{-3}$  is required to cool all positrons emerging from the moderator. A cloud with this density and length would contain a very large number of electrons ( $\approx 10^{10}$ ). A 1000 V well would be required to confine it. Then, the radial variation of the potential would be considerable, due both to the applied trapping potential and the space charge of the electrons. The energy loss of a positron passing through the cloud depends strongly upon the energy of the positron [53], and hence the energy loss for positrons on and off axis will be substantially different. To minimize this effect Oshima, *et al.*, magnetically focus positrons from a beam diameter of 2.5 mm to 0.1 mm. With this small radial extent, the maximum on-off axis voltage difference

is only 4.5 V.

With this setup, Oshima *et al.* expected to be able to cool all positrons that are moderated. Reference to Table 3.1 will reveal that to date they have not been able to achieve this design goal [54]. There are several reasons for this, but the primary problem is control of the large electron cloud. As the cooling rate depends strongly on the energy of the incoming (moderated) positron beam, it must be carefully matched to the space charge of the electron cloud. The space charge depends on the shape and density of the cloud. Particles in such a large electron cloud are strongly correlated and instabilities occur rapidly. These cause the shape, and hence density, to change rapidly with time,; in particular, the radial extent of the cloud grows on a time scale of about 10 s [54]. Hence, it is necessary to vary the energy of the positron beam in time to maximize the energy loss.

Implementing this scheme in the ATRAP experiment would be difficult, but should be possible. A very long trap would be required to hold the electron cloud. To successfully hold such a cloud, electrodes with a smaller aspect ratio than typically used would be needed so that a long harmonic potential could be formed. A particular problem is the diameter of the positron beam. In the present apparatus the positron source is lowered into the high field region, so very little focusing occurs and the positron beam has a diameter of  $\approx 3$  mm. This beam is much wider than the electron cloud used in [53]. Even if it were possible to trap a cloud with the same density and length as that in [53] but a radius of 3 mm, the potential difference between the axis and a radius of 1.5 mm would be 1000 V. Because of the energy dependence of the energy loss rate, most moderated positrons would not be cooled appreciably in one

pass.

To see what could be achieved using this method with a simple Penning trap similar to those that we already use, the following calculation was performed. The Penning trap considered was a stack of 10 “X3” electrodes (electrodes three times larger than those in the HBAR1 Penning trap). Electrodes of this size were considered as these are likely to be used in the next generation of antihydrogen Penning traps (Sec. 4.2.2). From destructive measurements made of large electron clouds in normal electrodes (Sec. 4.1.2), it seems reasonable to assume that a cloud of 100 million electrons would be stable if held in a X3 endcap. Eight such clouds could be held in the hypothetical Penning trap being considered. Assuming a cloud radius of 6 mm, the cloud density would be  $\approx 3 \times 10^8$ . From this, we can estimate the energy loss of moderated positron beam and the accumulation rate. For this conservative situation, we would expect to accumulate  $\approx 200$  positrons/s, comparable to that using the Rydberg positronium.

Note that the electron clouds used were chosen conservatively and hence, with experimentation, it should be possible to do better. Also, the magnetic field dependence of this accumulation mechanism should be much less strong than that for the Rydberg positronium scheme. A weaker field will make it more difficult to contain large electron clouds, but with experimentation this can likely be overcome. Hence, it seems likely that, even with this conservative estimate, electron cooling will outperform Rydberg positronium at low magnetic fields.

Given the relative simplicity and greater compatibility of the electron cooling scheme compared to the buffer gas loading scheme, it has been decided to pursue

the former in the next generation of antihydrogen experiments. In addition, the apparatus will be designed so that the Rydberg positronium technique can also be used. This may yet prove to be the best technique if an improved surface coating can be found. Reuse of the same positron cloud for several interaction experiments would also increase the effective accumulation rate. Techniques developed to make this possible will be discussed in Sec.3.3.3.

We will finish this section by mentioning a tantalizing prospect for the future. Recently, femto-second pulses with a peak power of 1.2 TW, but average power of only 2.4 W, have been used to create high energy electron beams [55]. These electrons can be directed onto a lead target to produce positrons via pair-production from bremsstrahlung. This system is, in effect, a table top pulsed positron source. Positrons are produced with a range of kinetic energies extending from zero to more than 5 MeV. If these positrons could be directed into a moderator, then a pulsed low energy beam would result. These low energy positrons could be trapped by rapidly switching a potential, with switching being triggered by the production laser pulse. Such a scheme does away with the need for a radioactive source altogether, and solves the problem of removing energy from the moderated positrons because their time of arrival would be well known. They could then be trapped by rapidly changing a potential by just a few volts.

### **3.3 Positron transfer through the ball valve**

For reasons described above, the HBAR1 Penning trap is split into two sections separated by a rotating electrode, the ball valve. Positrons are accumulated above

the ball valve, while antiprotons are accumulated below it. Hence, in order to carry out an interaction experiment, it is necessary to transfer one species or the other through the ball valve. In practice it is the positrons that are transferred, since the particle annihilation detectors are centered on the lower region and there are more electrodes, allowing greater experimental flexibility.

Transferring particles through the ball valve is difficult, since it has a smaller diameter than the other electrodes and it has a large aspect ratio (length/diameter). The small diameter can cause particles at large radii to be “skimmed” off. Because of the large aspect ratio, the electric field from neighboring electrodes does not penetrate far into the ball valve and the axial potential inside is relatively flat. As discussed in Sec. 2.1.1, low energy particles in a well formed from such an electrode are radially unstable. Thus, particles must be moved quickly, i.e. in as few axial oscillation periods as possible, through the ball valve.

### **3.3.1 Positron transfer through the ball valve using voltage pulses**

Initially, positrons were transferred through the ball valve by changing potentials in sequence every 10 ms using ELVIS [32]. The transfer efficiency of this method was initially found to be 80% for clouds as large as 1 million positrons. However, the relative calibrations of the RF amplifiers in the upper and lower sections were not checked by returning positrons to the upper section from the lower section. Later, using amplifiers whose relative calibration was known to be good, a maximum transfer efficiency of 50% was achieved.

It was decided to develop a different transfer technique that moved particles more quickly through the ball valve region. It was hoped that this would be more efficient, and would lead to less radial loss of particles due to the region of flat potential. By changing the potential on an electrode in just a few ns (“pulsing” the electrode) it is possible to place a cloud of particles on a potential ramp in a time less than the axial period of the cloud. Two possible ways of doing this are shown in Figs. 3.19(a)&(b), one where the electrode holding the particles is pulsed, the other where an adjacent electrode is pulsed. The particles are accelerated by the potential ramp and travel along the  $z$ -axis of the Penning trap, guided by magnetic field lines. By placing another potential ramp further down the Penning trap, and pulsing it to a well when the particle cloud arrives (Figs. 3.19 (c) and (d)), particle clouds that have been launched in this manner can be recaptured.

The pulse transfer scheme is implemented using the fast timing system (FTS) described in Sec. 2.4. The desired pulse parameters are sent to the pulsing hardware via a computer interface, and a trigger pulse is sent to all hardware devices simultaneously. As these pulsing devices are integrated into the FTS, pulses applied to particle wells can be precisely correlated in time with annihilation counter spectra and ramps applied to particle wells. This ability is used, for example, to study the properties of the Nested Penning trap when particles are launched using pulses (Sec. 5.2.2).

In order to transfer particles in this fashion, it is necessary to know at what time the particle cloud will arrive at the catching potential structure. This time can be determined experimentally simply by varying the time and measuring the recatch efficiency. The results of such an experiment are shown in Fig. 3.21. For clouds

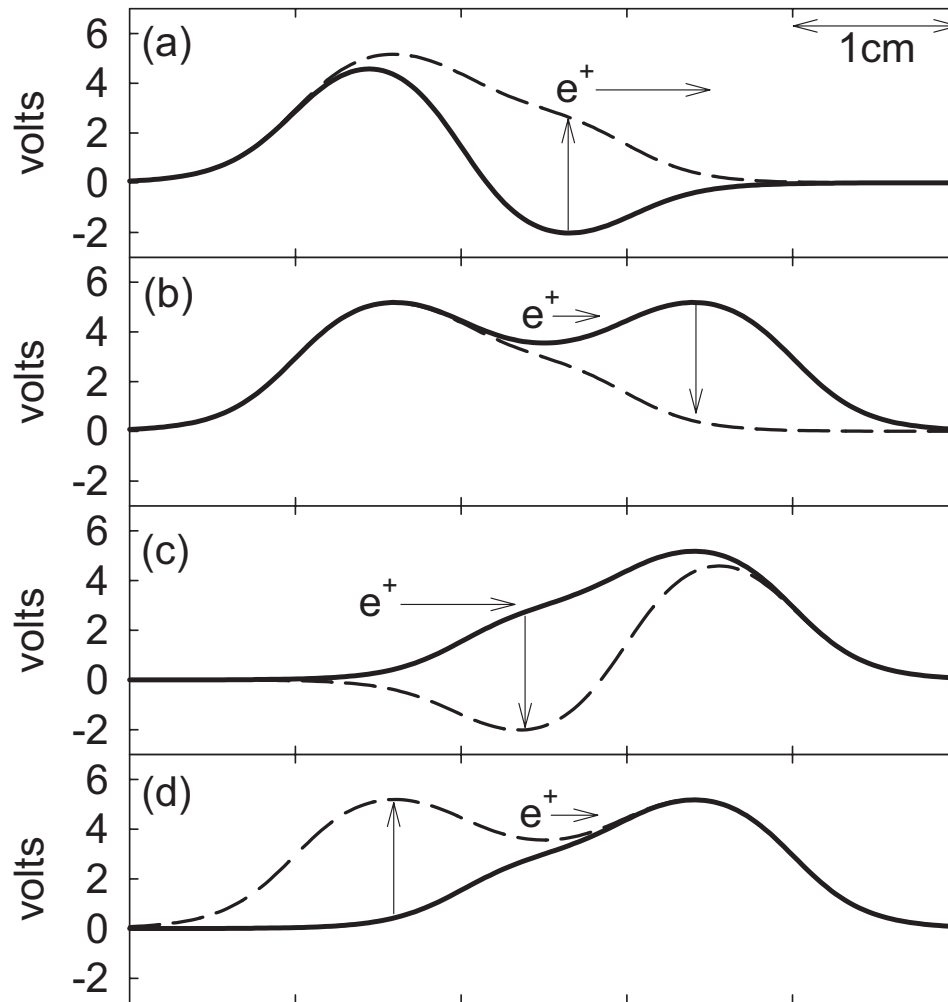


Figure 3.19: Potential configurations that allow particles to be: (a) rapidly launched when the electrode holding the cloud is pulsed, (b) rapidly launched when an electrode adjacent to the electrodes is pulsed, (c) rapidly caught when the electrode holding the cloud is pulsed, (d) rapidly caught when an electrode adjacent to the electrodes is pulsed.

of this size, 100% transfer efficiency is readily achieved. Indeed, as can be seen from Fig. 3.21, a cloud can make many bounces before being recaptured. In addition, the transit time can be simply predicted for one particle by numerically integrating Newton's equations, and the prediction agrees well with experiment (Fig. 3.20).

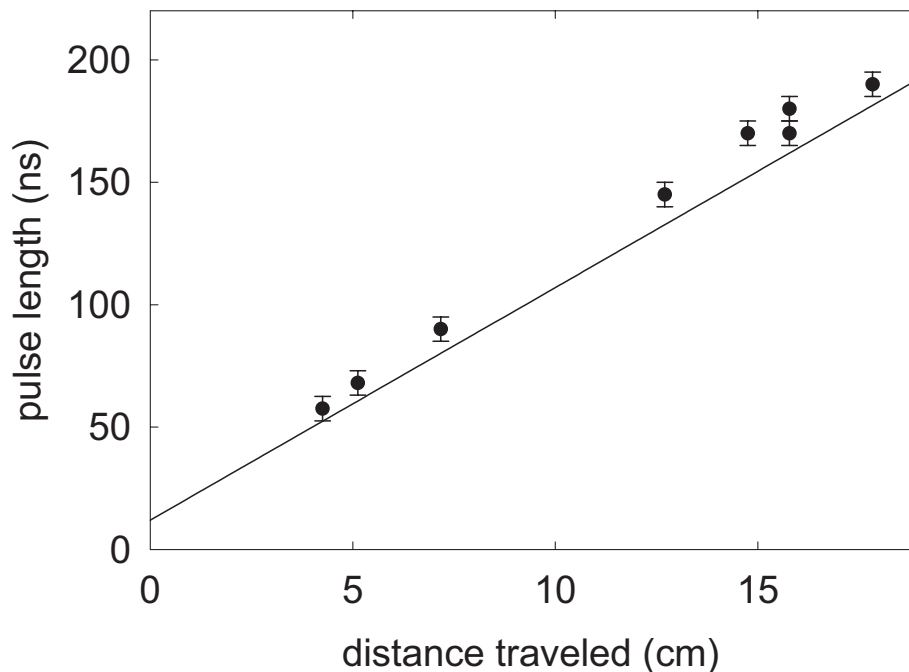


Figure 3.20: Measured positron and electron transit times as a function of transit distance. Solid curve is a simple prediction obtained for a single particle. The prediction correctly predicts the dependence upon transit distance (the slope), but underestimates the time for particles to move off the launch potential structure and onto the catch potential structure (the offset). This is not surprising, as for a many particle cloud those particles on the outside screen those on the inside. It is only after those on the outside have been accelerated away by the potential ramp that those on the inside will feel the external electric field.

Transferring particles in this way has several advantages and disadvantages when compared to the traditional slow method [35]. Obviously, the transfer is very rapid, avoiding radial instability problems in an electrode like the ball valve. Pulsing can be used to transfer particles through particles of another species, something that can not

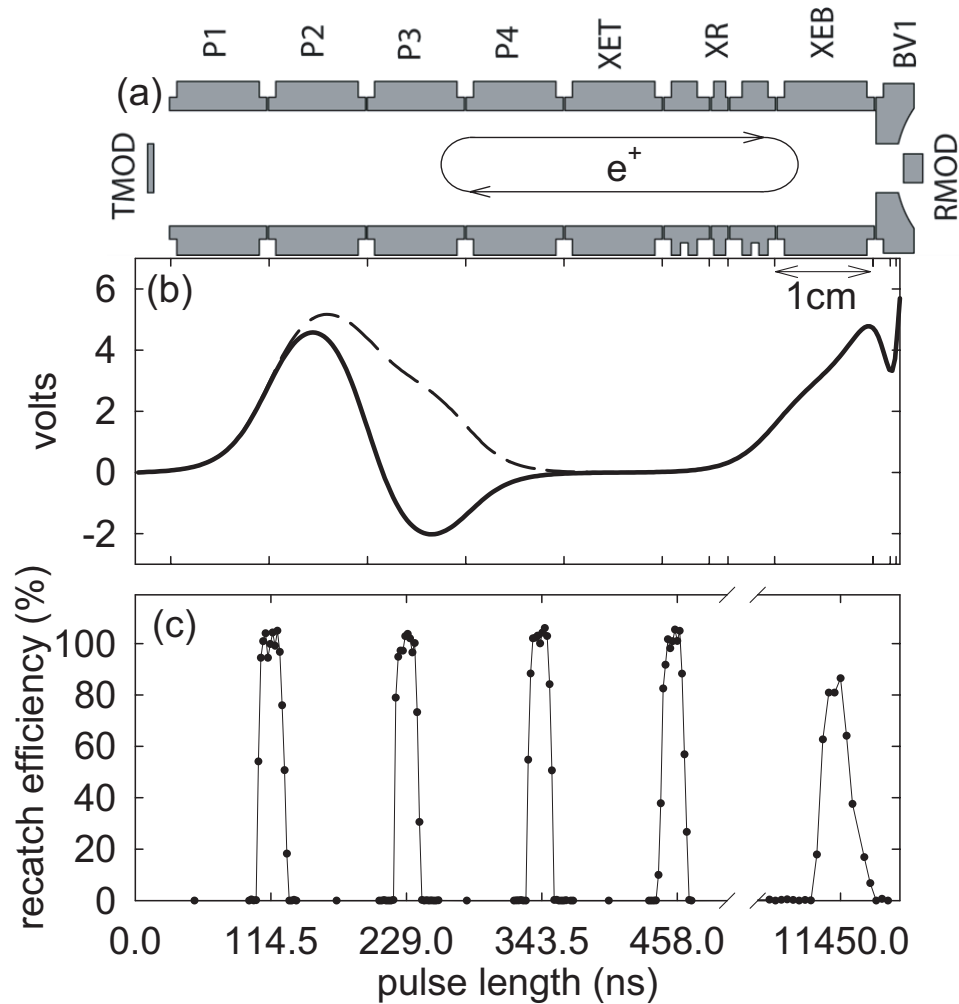


Figure 3.21: (a) Electrodes used for pulsing investigations. (b) The potential structure used. The DC potential (solid) is modified when a voltage pulse is applied to the electrode P3 (dashed). Positrons in the P3 well are launched when the pulse is applied, and can be recaptured if the pulse returns at the appropriate time (c). The positron bunch can bounce multiple times in the potential structure, with a period of 114.5 ns. After 100 oscillations, the bunch has spread out, and 100% recatch efficiency can no longer be achieved.

be done using the slow method. This is useful, since it is often necessary to change the order in which different particles are stored in the Penning trap. An example of such a situation is shown in Fig. 3.22(b). In this situation, two antiprotons bunches have been accumulated in the lower trap. If we wish to have positrons confined between these two bunches, it is necessary to transfer the positrons through the antiproton bunch closest to the upper trap. The addition of the antiproton well along the path of positrons alters the transit time, which can be determined simply by experiment.

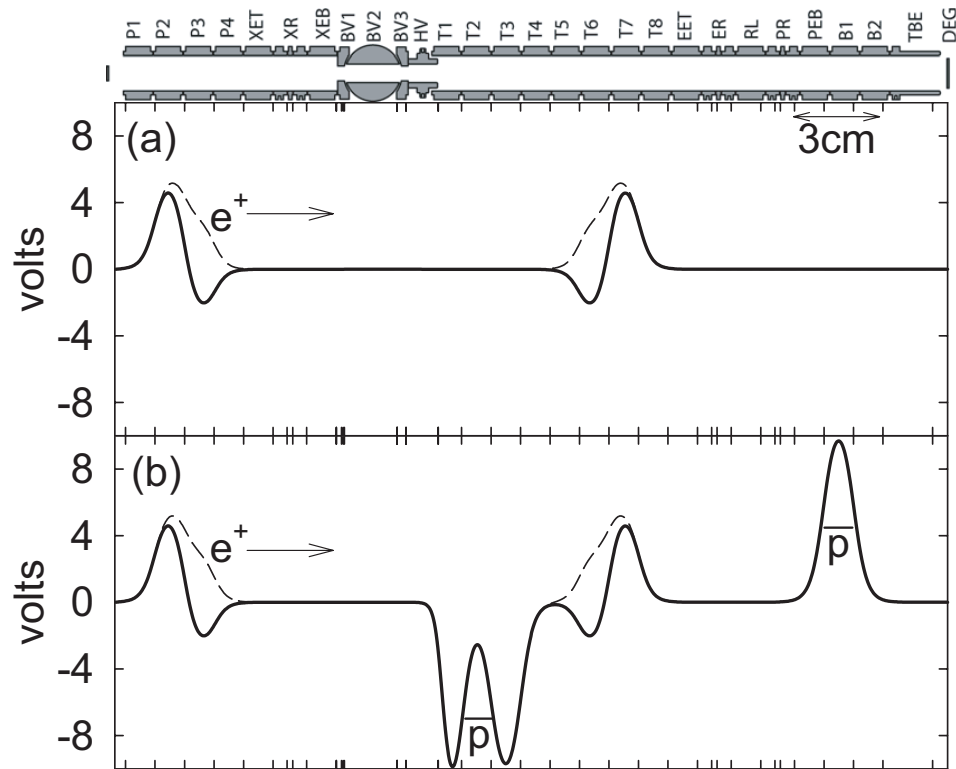


Figure 3.22: Typical potential structures for pulsing positrons through the ball valve (a) with no other particles present, or (b) over antiprotons.

Pulsing particles from place to place is riskier than moving them slowly. When pulsing, the particles are not axially confined during transit. If the particles are not recaptured at the proper time they will be lost. By contrast, when using the slow

method, the particles are always confined and can not be easily lost. For this reason, the pulse transfer is used only when necessary, for example, to transfer particles through the ball valve, or to change the order of particles in the Penning trap.

### 3.3.2 Ball valve transfer limitations

While pulsing particles through the ball valve avoids them spending a long time on a flat potential, it does not avoid the other problem described above. The ball valve has a small 5 mm aperture, compared to the 12 mm aperture of the trap electrodes, so that particles at too great a radius will strike it and be removed from the cloud. Fig. 3.23 displays the efficiency with which positrons can be transferred through the ball valve, as a function of cloud size [28].

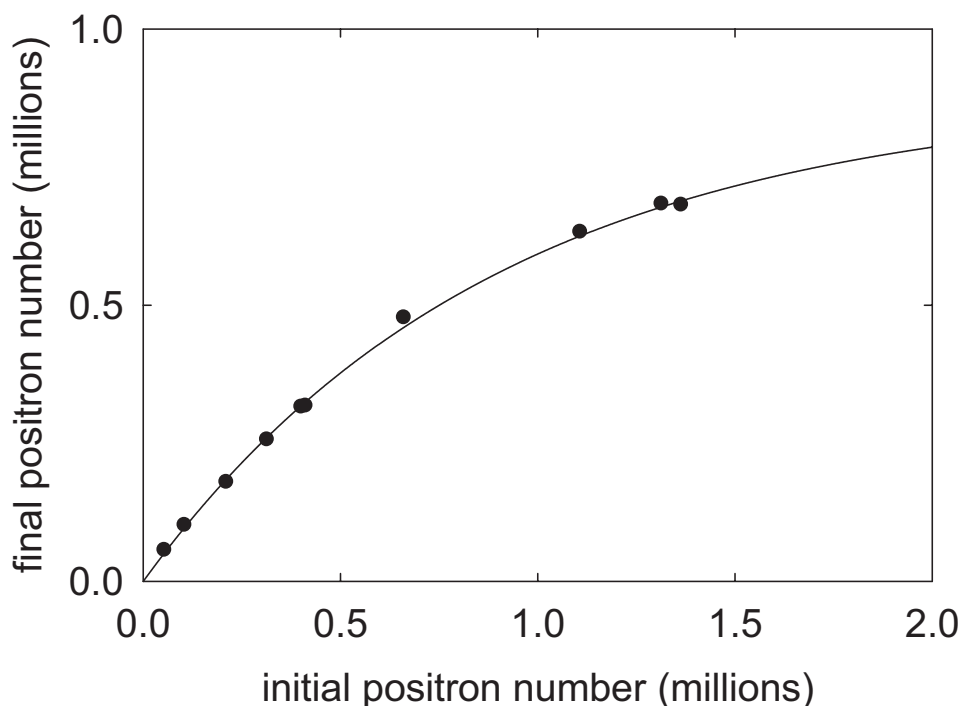


Figure 3.23: Transfer efficiency through the ball valve as a function of initial cloud size. Taken from [28].

Fig. 3.23 indicates that it is more efficient to pulse smaller clouds. Thus, to optimize the transfer of a large cloud, it should be transferred as a sequence of as many small clouds as possible. Note that taking a large cloud and dividing it into smaller portions does not work – while a particle cloud may grow in diameter as particles are added to it, the reverse does not appear to hold. Also, the technique available for dividing clouds is not reliable and can result in radially heated particles. Thus, the number of smaller bunches that can be used is limited by the number of available electrodes for accumulating, holding, and transferring particles. In the upper section of the HBAR1 Penning trap, this limits the number of bunches to two. Reference to Fig. 3.23 reveals that pulsing a single cloud of 1 million positrons would be 59% efficient, while pulsing two clouds of 0.5 million positrons would be 75% efficient.

Fig. 3.23 also demonstrates that attempting to reuse positrons by transferring them back to the upper trap after use in interaction experiments gains little. Say, for example, that we begin with two clouds of 0.5 million positrons in the upper trap. These can be transferred to the interaction region with an efficiency of 75%, yielding 0.75 million positrons for interaction experiments. However, these would have to be transferred back to the upper trap as one bunch, yielding 0.5 million for storage in the upper trap. Let us suppose that 1.0 million positrons are accumulated before the next interaction experiment. We would thus have two bunches of 0.75 million antiprotons to transfer, yielding 1.0 million positrons in the interaction region. After this 33% increase from the first recycling step, there is little to be gained, since larger clouds are being transferred.

Thus, for experiments using more than about 1.0 million positrons, a different approach is needed. There are several possibilities. The first is to accumulate positrons in the upper trap for longer than one antiproton accumulation cycle, either before or after the allocated antiproton beam time, or during it. Much of the data to be presented in Ch. 6 was taken with positron clouds that were accumulated during two antiproton accumulation cycles. Only at the end of the second cycle were the positrons transferred to the interaction region. The antiprotons from the first cycle were used for a control experiment conducted without positrons. In this way, no antiproton beam time was wasted. Referring again to Fig. 3.23, it can be seen that there is little to be gained by accumulating beyond the time at which there will be more than 2 million positrons in each of the wells in the upper trap. Transferring clouds larger than this does not result in a larger number of positrons being available in the lower trap and hence, the largest number of positrons that can be obtained in the interaction region by this method is  $\approx 2$  million.

However, it will be necessary to conduct recombination experiments with more than 2 million positrons. The only alternative to the methods described above is to transfer many small bunches of positrons to the lower trap – here around 0.75 million positrons are accumulated in two bunches and then transferred to the interaction region. This process is repeated as often as necessary to yield the desired number of positrons in the interaction region. Large clouds have been successfully accumulated in this way (Fig. 3.24). This must either be done after the antiproton beam time has finished, with the last antiprotons accumulated stored in the lower trap, or before any antiprotons are accumulated. The first approach allows only one experiment

per day to be carried out with a large positron cloud – an unacceptably low data rate. In addition, large antiproton clouds can become radially unstable after a few hours, limiting the time in which positrons can be usefully accumulated. The second approach is more promising, since there will typically be at least 12 hours available for positron accumulation between antiproton accumulation periods. However, as positrons can not be efficiently returned to the upper trap, the resulting large cloud will have to be stored in the lower trap during antiproton accumulation.

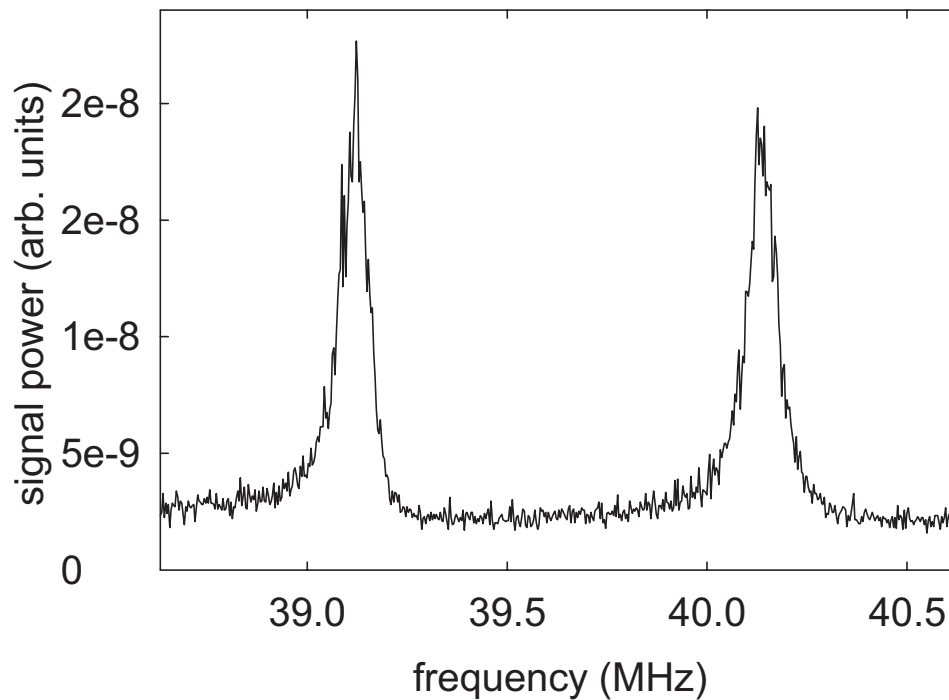


Figure 3.24: The “dip” resulting from 8 million positrons accumulated by pulsing many small bunches through the ball valve.

If positrons are stored in the lower trap during antiproton accumulation, there are several things to be considered. Collisions with antiprotons will heat the positrons, so a comparable number of electrons should also be stored in the lower trap (Sec. 4.2.3) to reduce this effect. Most importantly, positive ions liberated from the degrader will be

cooled into the well with the positrons. These contaminant ions will make it difficult or impossible to measure the number of positrons using RF amplifier techniques, and could annihilate antiprotons during interaction experiments. Thus, a technique for cleaning ions from positron clouds is required. Pulse transfer of clouds does just this. Due to the very large mass difference between positrons and the positive ions, when a cloud is pulse launched, the positrons will leave well before the ions. In this way, the two species can be separated, and the ions disposed of.

### 3.3.3 Pulse transfer of large particle clouds

Having accumulated large clouds, we must also be able to manipulate them. In particular, we wish to be able to pulse transfer large clouds to remove positive ions that could be trapped during antiproton accumulation. The high efficiency particle transfers shown in Fig. 3.21 were obtained with rather small clouds. For large clouds (greater than 1 million particles), the peak transfer efficiency, even when not through the ball valve, is less than 100%. For example, transfer efficiency as a function of pulse time for 8 million electrons is shown in Fig. 3.25. Clearly, not all of the particles are located in the correct position to be recaptured when the catching well is pulsed into place. This is due to the axial extent of the cloud being large, which will be due in part to a screening effect. When the launching potential ramp is pulsed into place, only those particles on the edge of the cloud will immediately be accelerated by it. Those in the center of the cloud will be shielded by those on the outside. As those on the outside are accelerated away, those on the inside feel the external electric field also. Thus, for larger clouds, it will take longer for all the particles to move off the

launch potential ramp, effectively increasing the axial extent of the cloud.

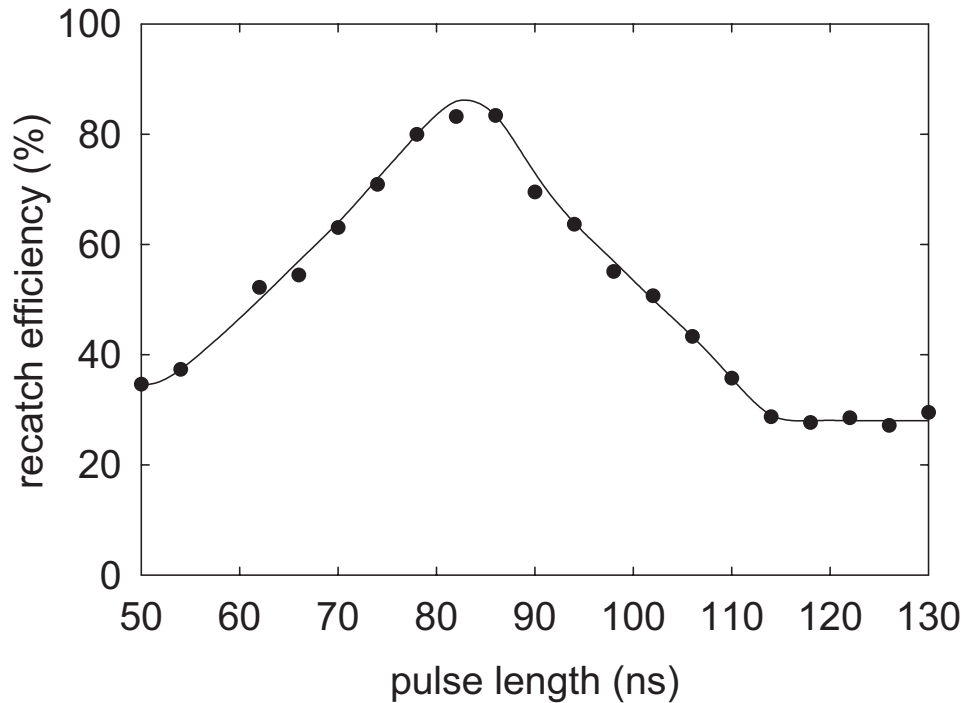


Figure 3.25: Transfer efficiency for a cloud of 8 million electrons using a single pulse. The peak transfer efficiency is  $\approx 85\%$ .

Of course, we wish to transfer large clouds as efficiently as possible. Working on the assumption that large clouds are simply too long to be completely recaptured, a pulsing scheme was developed that used several short pulses. It was thought that each short pulse would release a fraction of the large cloud, which could be recaptured with high efficiency. Once caught, the small bunch can be stored in a separate well, and the process repeated (Fig. 3.26). The results from such a transfer are shown in Fig. 3.27, where a 95% transfer efficiency is achieved.

Fig. 3.28 demonstrates another way in which pulses could be used to transfer a large (long) cloud. The catching potential structure could be formed from three electrodes, two of which would be pulsed. As indicated in the figure, this should catch

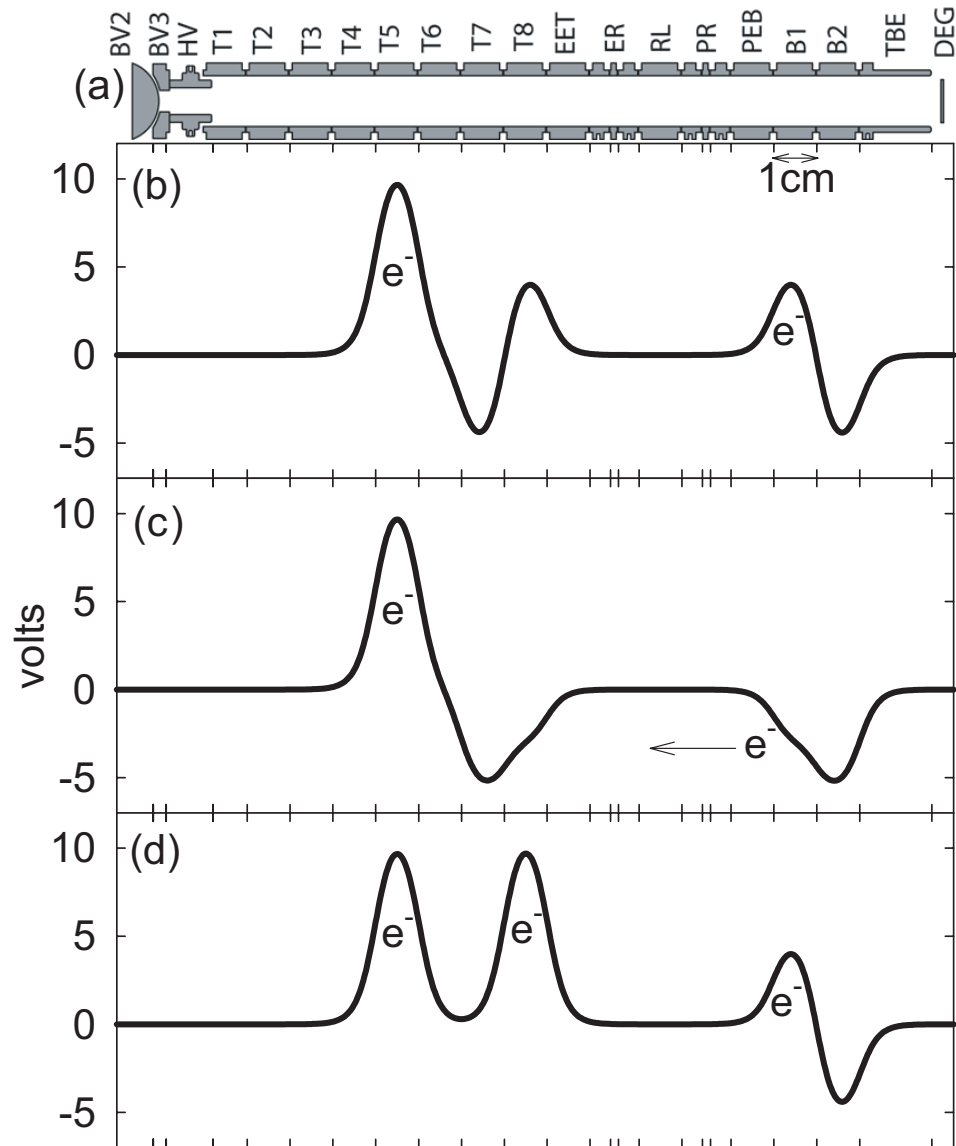


Figure 3.26: (a) Electrodes used to pulse transfer large clouds. (b) Initial potential structure used to pulse transfer large clouds. Electrons are stored on electrode T5 and B1. (c) Electrodes B1 and T8 are pulsed to transfer some fraction of the electrons on B1 to T8. Any ions remain trapped on B1. (d) The electrons transferred to T8 can be combined with those on T5. The transfer process can then be repeated. When most electrons have been transferred, the B1 well, containing any ions, can be dumped to the degrader.

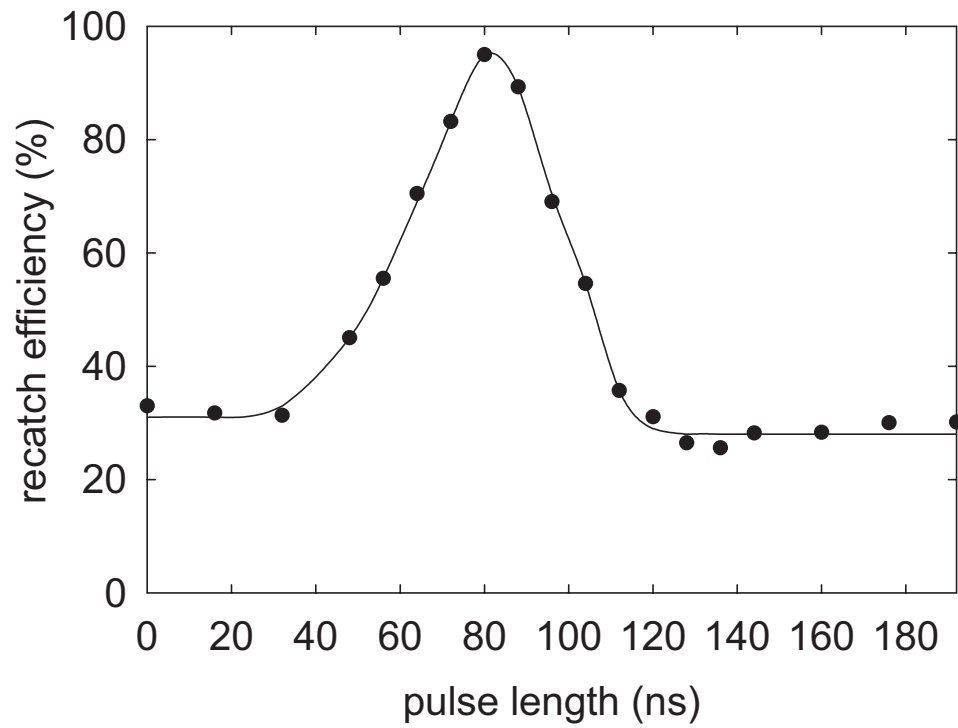


Figure 3.27: Transfer efficiency for a cloud of 8 million electrons using many pulses. The peak transfer efficiency is  $\approx 95\%$ .

longer clouds. This method has yet to be attempted, but provides another option should the multi-pulse method prove unreliable when used to clean ions from large clouds.

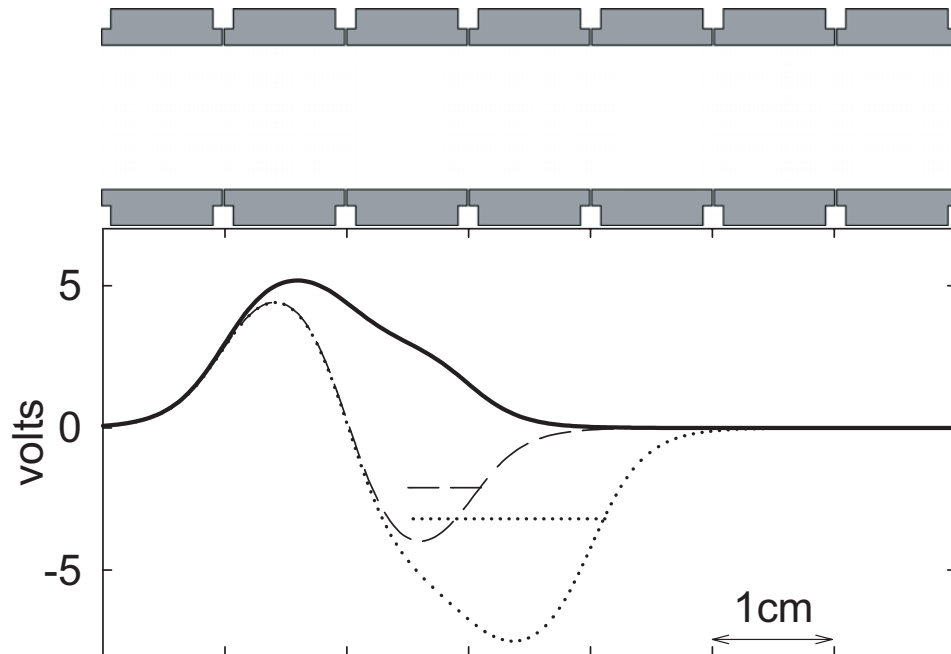


Figure 3.28: Another pulse transfer scheme would use two electrodes, and should thus be able to catch longer clouds. Solid line is the potential ramp on which particles are caught. Dashed line is well formed when one electrode is pulsed, while the dotted line is that formed when two electrodes are pulsed. Horizontal lines represent the approximate cloud length that can be caught in each case.

# Chapter 4

## Electrons and Antiprotons

The most difficult ingredients of antihydrogen to obtain are antiprotons. The various techniques used to accumulate these will be described. Of particular importance is the technique of antiproton stacking, in which successive AD shots are trapped. Presently, this is the only way to obtain the large number of cold antiprotons needed for antihydrogen experiments.

Not to be forgotten are electrons. Electron plasmas are not only an important diagnostic tool, but they also play a crucial role in the antiproton accumulation process. The various methods used to accumulation electrons will be described.

### 4.1 Electron accumulation

As they are much easier to accumulate than positrons or antiprotons, clouds of electrons are our standard trap diagnostic tool. Also, as electron and positron clouds generally behave in a similar fashion, manipulation techniques can often be developed

much more quickly using electrons than positrons. Finally, electrons are essential for antiproton accumulation, as will be discussed in Sec. 4.2.3. Clearly, it is essential that we be able to accumulate electrons quickly and reliably and hence, several accumulation techniques have been developed. However, in the future it may be necessary to load much larger numbers of electrons (Sec. 3.2.5) and this will require a more efficient method than any that we presently have. The rate at which we can accumulate electrons is limited by quality of our vacuum - it is too good. One way to overcome this would be to use a pulsed source of electrons and a rapidly changing voltage to initially capture the particles.

#### 4.1.1 Electron accumulation using a field emission point

The most simple electron accumulation technique is the use of a field emission point (FEP, a very sharp point chemically etched from a tungsten rod) that is mounted on the bottom of the ball valve. A typical trap potential configuration for accumulating electrons in this way is shown in Fig. 4.1. When an appropriate potential is applied to the FEP (typically about  $-800$  V relative to the surrounding electrodes) a beam of electrons is extracted from it by the very high electric field that is generated. The FEP electron beam current depends upon the applied potential, but 20 nA is a typical value. The electrons in the beam travel along the magnetic field lines and strike the degrader, dislodging cryo-pumped gas atoms and generating low energy secondary electrons and ions. These secondary electrons are trapped in the applied potential well via collisions with residual gas atoms.

Most of the residual gas atoms that aid the accumulation process come from the

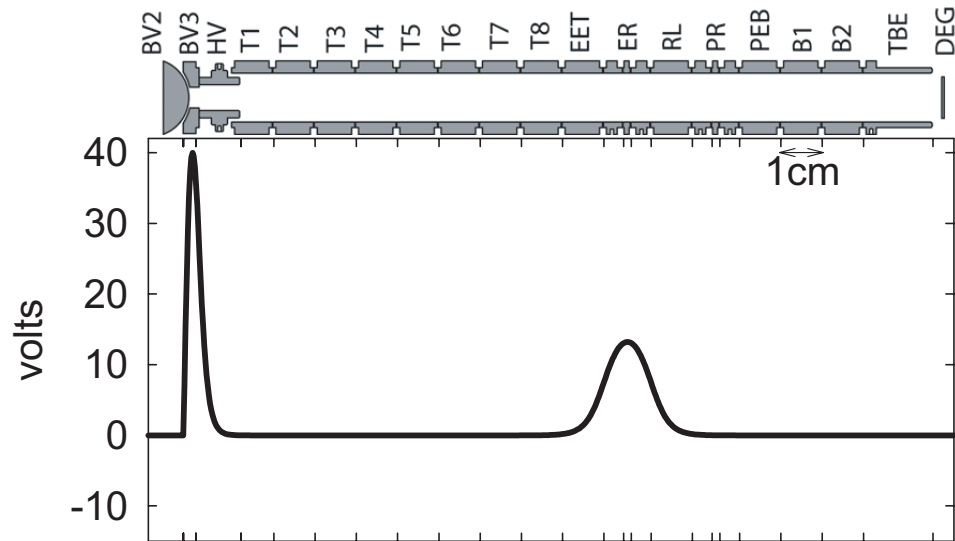


Figure 4.1: Potential structure used to load electrons using the FEP.

degrader. As was mentioned earlier (Sec. 2.1.2), the vacuum in the Penning trap enclosure is extremely good, so in addition to producing low energy electrons the FEP beam creates a locally “bad” vacuum. After the FEP has been fired many times, the accumulation efficiency diminishes, suggesting that the electron beam has cleaned the degrader surface of cryo-pumped gas. Turning the ball valve a small amount restores the accumulation rate for a short time.<sup>1</sup> Secondary electrons are clearly central to the accumulation mechanism, as when the degrader is biased so as to prevent their escape, electron accumulation ceases [35].

<sup>1</sup>The ball valve is bistable, either open or closed, so turning it a little only results in the FEP striking a dirty portion of the degrader in the short time that the ball valve takes to return to the closed position.

### 4.1.2 Large electron cloud accumulation using a field emission point

As was discussed in Sec. 3.2.5, large electron clouds may be used in future to accumulate positrons. Hence, the ability to accumulate and store such clouds was investigated. Of course, these clouds were too large to be counted using RF amplifiers, so charge measurement techniques were used (Sec. 2.2.2). The first step was to determine how large a cloud could be accumulated in a simple well formed from a single electrode. Fig. 4.2 displays the number of electrons accumulated into a 350 V well as a function of the time that the FEP was fired. Clearly, there is a dramatic increase in the accumulation rate once there are  $\approx 500$  million electrons in the well. This could be due to a transition from a weakly correlated plasma (gas like) to one that is strongly correlated (liquid or solid like). Cooling collisions in a strongly correlated plasma could be much more efficient, since the effective mass involved is greater in the liquid or solid like case. It appears that once the more efficient cooling begins, the well rapidly fills with as many electrons as it can hold ( $\approx 2$  billion). When such a large cloud is dumped to the degrader, the charge spectrum covers about 10 ms, or several hundred volts, confirming that the 350 V confining well is very full.

The very large electron plasmas accumulated above seem ideal for cooling positrons, particularly if the rapid increase in the electron accumulation rate is due to a transition to a strongly correlated plasma. Unfortunately, the very large plasmas of about 2 billion electrons rapidly lose particles (Fig. 4.4). For these large clouds to be useful for positron accumulation, this loss would have to be very well characterized so that the energy of the incoming positron beam could be adjusted to match the space

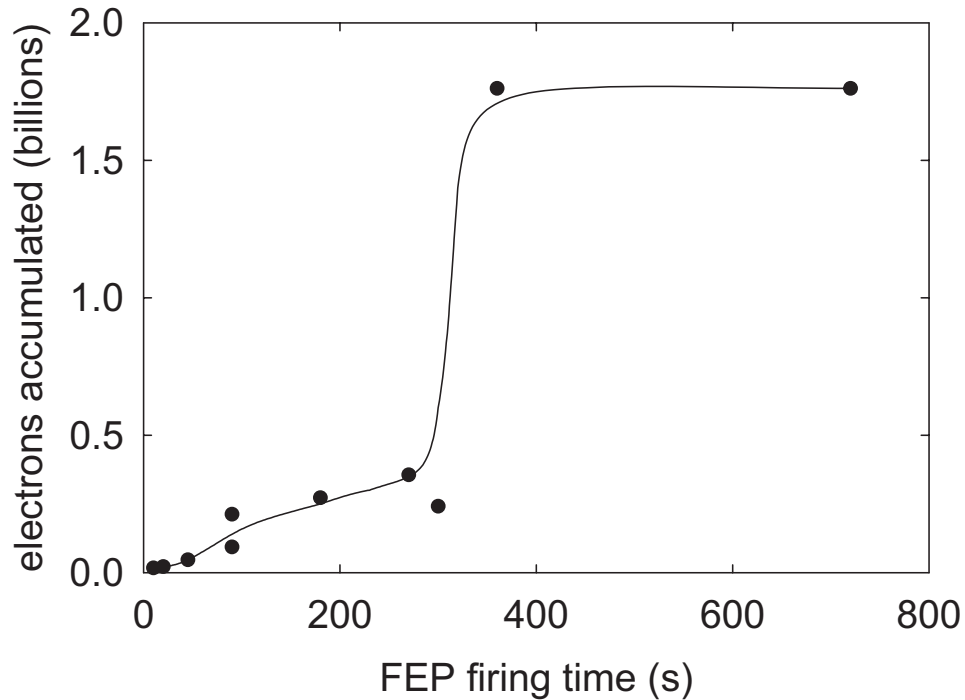


Figure 4.2: Electron accumulation rate via the FEP as a function of the total amount of time the FEP has been fired.

charge of the electron cloud (Sec. 3.2.5). However, clouds of about 100 million electrons appear to be stable in this configuration, so it was this number that was used in Sec. 3.2.5 to make a conservative estimate of the positron accumulation rate that might be achieved using electron cooling.

As can be seen in Fig. 4.2, the FEP must be fired for several minutes to accumulate the very large clouds. Over time that the FEP must be fired to accumulate such clouds increases, until it becomes impossible to do so. This is presumably because the FEP beam “cleans” the section of the degrader on which it impinges, meaning that there is no longer a “bad” vacuum near the degrader to load secondary electrons into the wells. As was mentioned above, rotating the ball valve a little temporarily solves this problem.

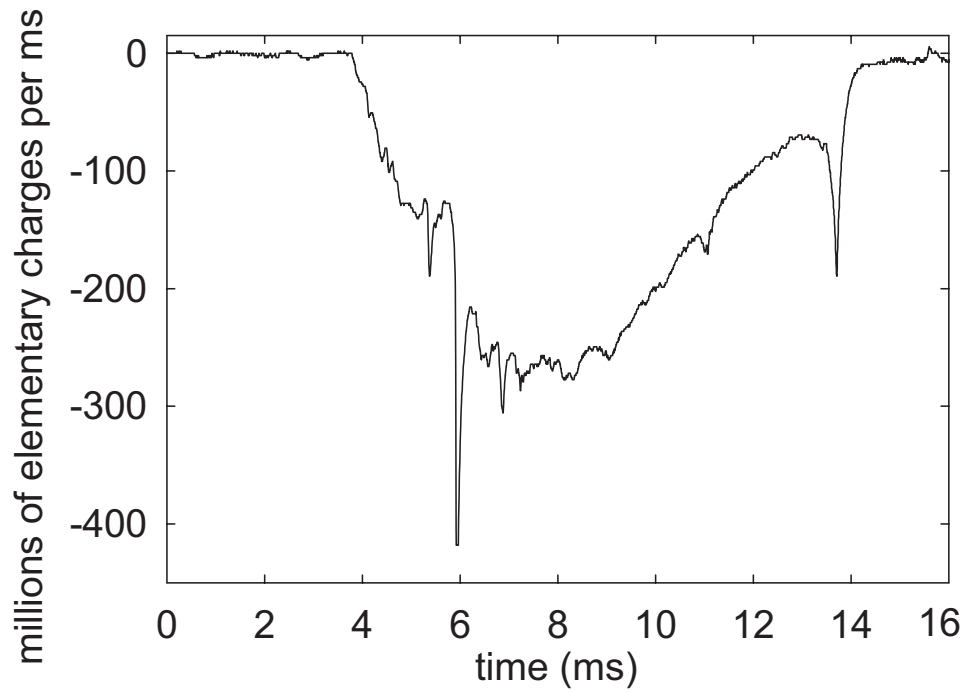


Figure 4.3: The charge spectrum of a very large electron cloud.

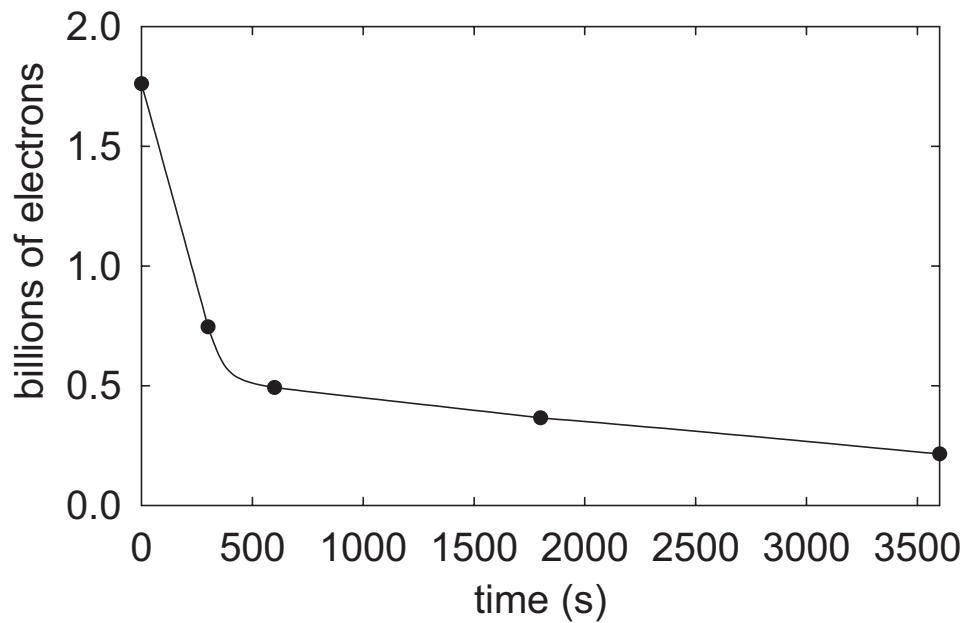


Figure 4.4: Very large electron clouds rapidly lose particles. Solid curve is to guide the eye.

### 4.1.3 Electron accumulation using a positron source

On occasion, it was not possible to use the FEP for electron accumulation. In these instances we were forced to (rapidly) devise other accumulation techniques. One obvious technique is to adapt our positron accumulation mechanism, arranging to trap the electron from ionized Rydberg positronium rather than the positron, simply by changing the sign of the accumulation potentials (Sec. 3.2.1). However, the accumulation rate using this method is equal to that for positrons, which is too slow given the number of electrons that are required for antiproton accumulation.

A different approach was needed. The high energy positron beam from the radioactive source can also generate secondary electrons. Indeed, there are many more secondary electrons generated than moderated positrons and thus, Rydberg positronium atoms. It seems reasonable to suppose that the action of the high energy positron beam on the degrader would be similar to that of the FEP electron beam: secondary electrons would be generated and cryo-pumped gas atoms dislodged. Collisions between secondary electrons and dislodged gas atoms could result in electron accumulation into a well placed near the degrader. Of course, the ball valve must be open for the positron beam to be able to impinge upon the degrader.

This was attempted using the potential structure shown in Fig. 4.5. As the number of wells was increased, as indicated in the figure, the accumulation rate increased (Fig. 4.6) but, electrons were found *exclusively* on the TBE electrode. However, if a “seed” cloud was accumulated on TBE and then moved, say, to the electrode ER, electrons would then be found exclusively on ER. By placing a “seed” cloud on ER in this fashion, we could then monitor the accumulation rate in real time using RF

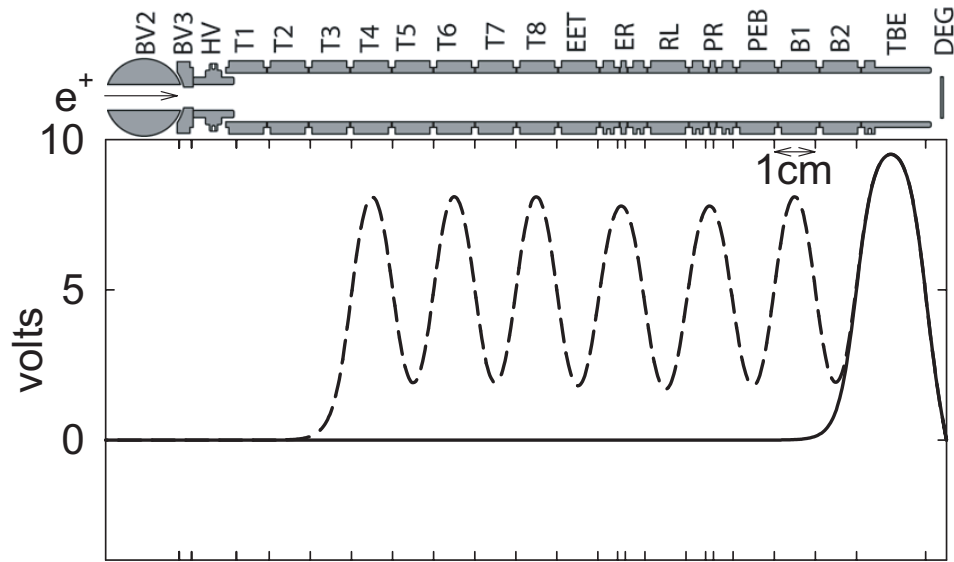


Figure 4.5: Initial potential structure used to accumulate electrons using the positron source. Dashed lines indicate wells added in sequence to investigate the accumulation mechanism.

counting techniques (Sec. 2.1.1). The results of such an experiment are presented in Fig. 4.7. As can be seen, the loading rate is independent of the number of electrons present in the accumulation well (the well in which there are electrons). Finally, when the “seed” cloud is split amongst several electrodes, electrons are loaded into these additional wells in a proportion similar to the initial number present (Fig. 4.8). This behavior gives us important clues as to the details of the loading mechanism.

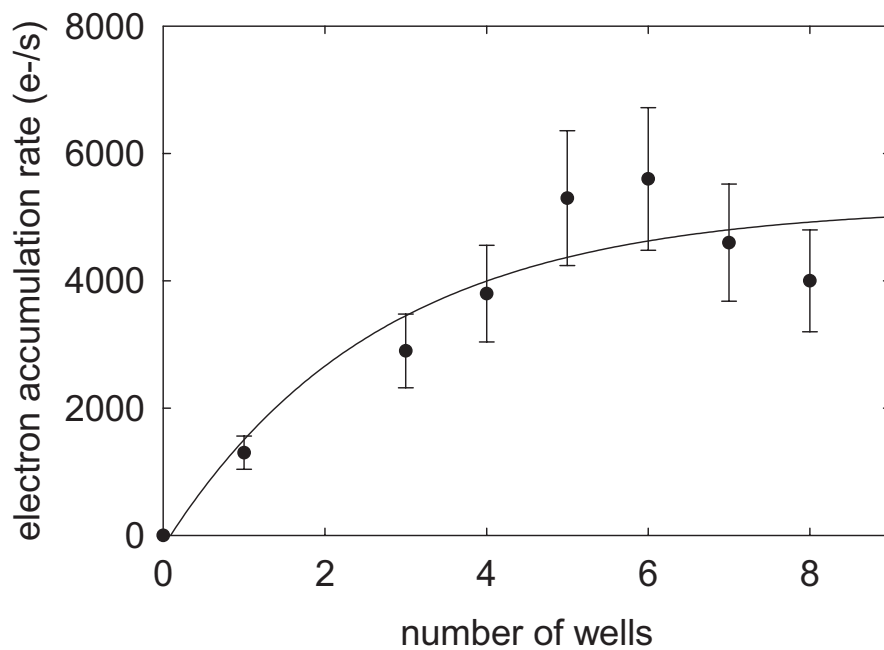


Figure 4.6: Electron accumulation rate as a function of the numbers of wells present.

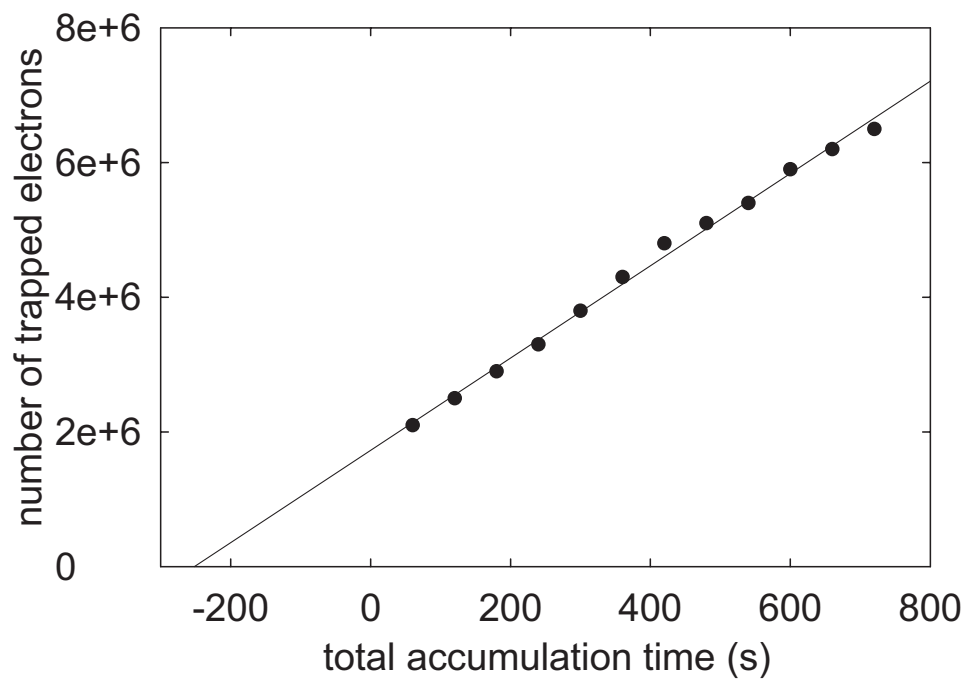


Figure 4.7: Number of electrons accumulated on the electrode ER as a function of time. A “seed” cloud of 1.6 million electrons, accumulated in 300 s onto TBE, was placed on ER at  $t = 0$  s.

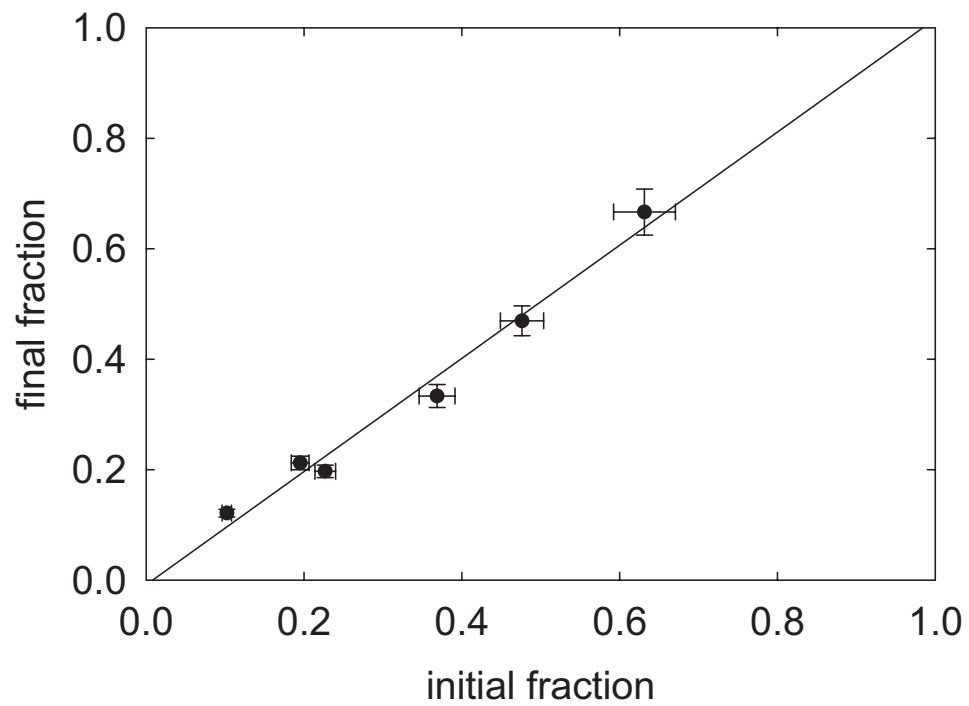


Figure 4.8: When a “seed” cloud of 1.9 million electrons is split, the accumulation rate into each well depends on the initial number of electrons present.

The features noted above are consistent with a two stage accumulation process. First, secondary electrons are collisionally loaded into the long well formed by the superposition of the many individual wells. Second, electrons in the long well are cooled into the individual wells via collisions with electrons already in the individual wells. Evidence for the first stage comes from the fact that as the length of the long well is increased, the accumulation rate increases – as the length of the long well increases, a secondary electron has a great chance of having a collision and being trapped. We would not expect the rate to increase linearly with length, since the degrader itself is expected to be the source of the residual gas atoms and these should be emitted isotropically. Another piece of evidence for this first stage is the fact that the loading rate is independent of the number of electrons present (Fig. 4.7). If the loading mechanism were entirely due to electron-electron collisions, we would expect the rate to increase with increasing electron number. Evidence for the second stage comes from the fact that electrons accumulate only into wells in which there are already electrons and *nowhere* else. Initially, there are no electrons present – how can we accumulate electrons? The first electrons will have to be accumulated via multiple collisions with residual gas atoms and these are most likely to occur near the degrader. Hence, electrons accumulate first on the electrode TBE and then all other electrons loaded into the long well cool into TBE via collisions with these first electrons, as observed if no “seed” is planted.

Scans over all accumulation potentials, like those used to optimize positron accumulation (Sec. 3.2.1), were carried out (Fig. 4.9). The accumulation rate is quite sensitive to the potential applied to the degrader and the electrode TBE (Fig. 4.9a&b).

These potentials control the energy secondary electrons have relative to the long well, so the optimum values for the degrader and TBE presumably minimize this energy, making any collision more likely to load an electron into the long well. The optimum value for the electrode UPHV (Fig. 4.9c) tracks that for the degrader: as this forms the other end of the long well, it is most important that this potential be lower than that applied to the degrader. Finally, the dependence of the accumulation rate upon the potential applied to the other electrodes inside the long well (Fig. 4.9d) is not understood. The optimum potential structure determined from these maps is displayed in Fig. 4.10.

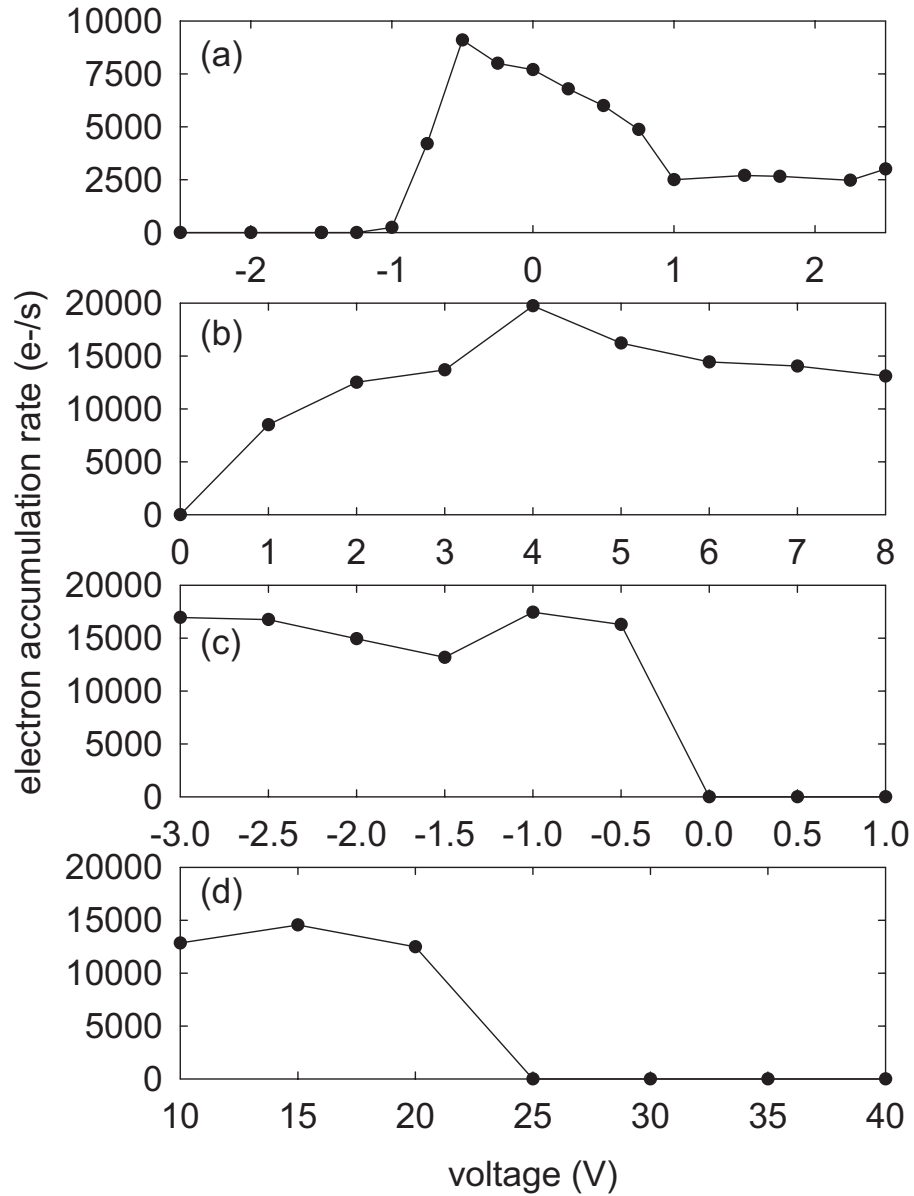


Figure 4.9: Electron accumulation rate as a function of the voltage applied to the degrader (a), the electrode TBE (b), the electrode UPHV (c), and the electrodes T4, T6, T8, ER, PR, and B1 (d). The maximum rates vary as other potentials are not necessarily at their peak values.

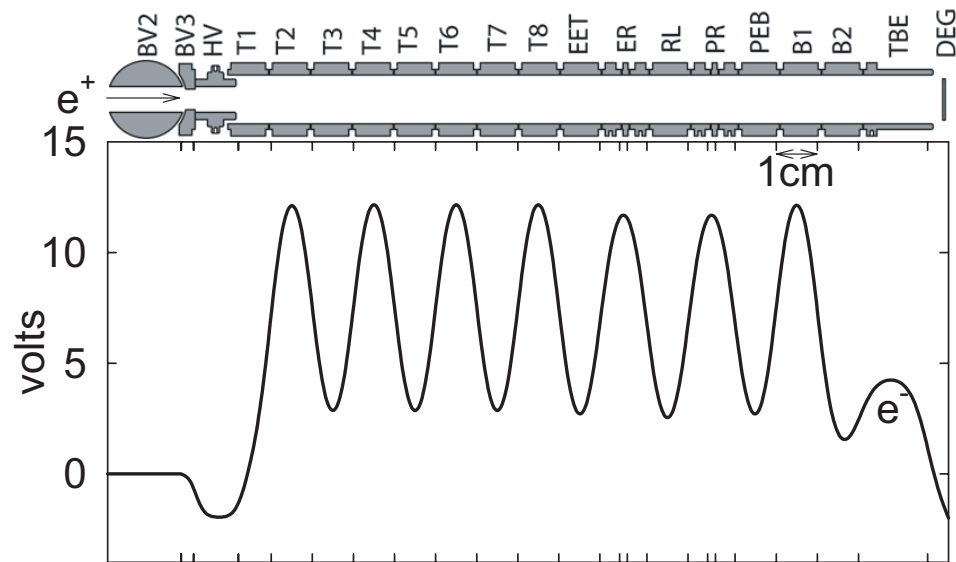


Figure 4.10: The optimized potential structure for electron accumulation.

In some circumstances, it has been necessary to accumulate electrons in the section of the Penning trap above the ball valve. This requires a different set of potentials and the accumulated electrons must be pulsed to the interaction section of the trap in the same manner that positrons are. The optimized potential configuration for this style of accumulation is shown in Fig. 4.11. An offset well on the electrode XR stores positrons. As a result, there are only a few electrodes available for electron accumulation and the optimum potential configuration is substantially different from that for the lower trap (Fig. 4.10). Electrons are accumulated onto electrode P3 and then pulsed through the positron cloud to the electrode T6. As was discussed in Sec. 3.3, the transfer efficiency through the ball valve decreases with increasing particle number. Hence, it is more efficient to accumulate many small bunches, pulsing each one to the lower trap in turn for storage. To obtain the maximum possible accumulation rate into the lower trap, we optimize the electron accumulation time (Fig. 4.12).

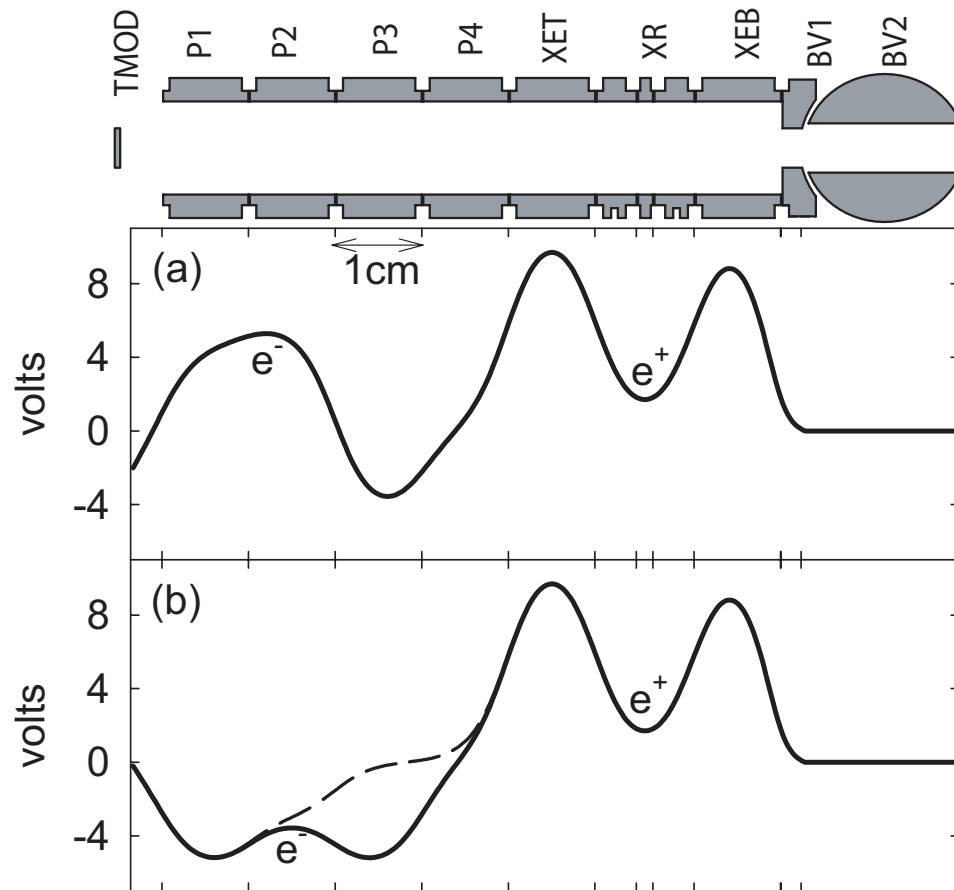


Figure 4.11: (a) The optimized potential structure for electron accumulation in the top trap. (b) The potential structure used to pulse electrons to the lower trap.

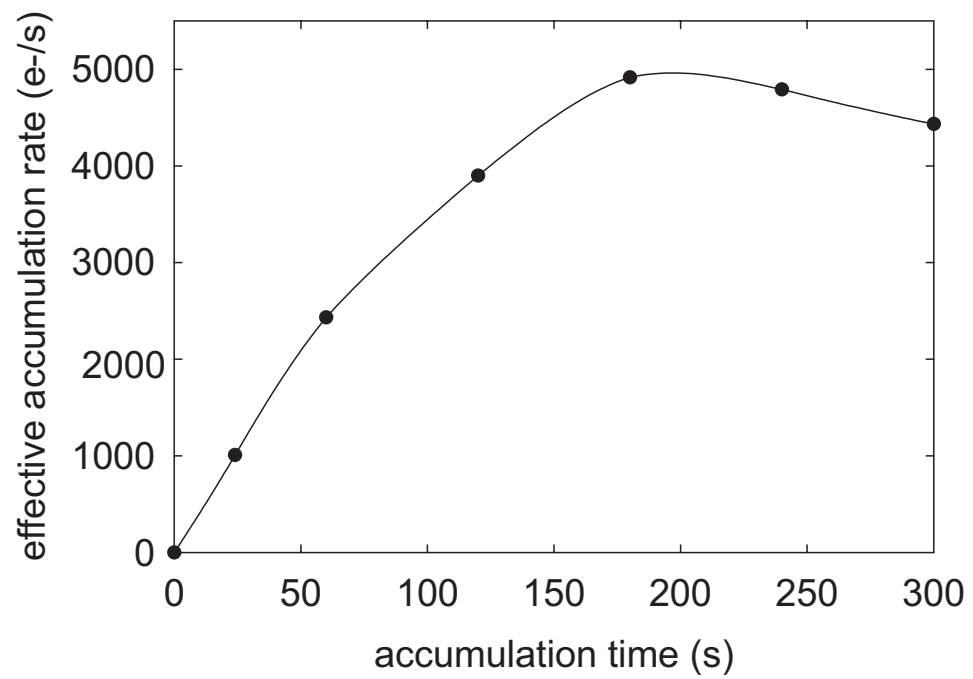


Figure 4.12: Optimization of accumulation time for electrons in the top trap.

## 4.2 Antiproton accumulation

To form antihydrogen we need large numbers of cold antiprotons. Cold here means 4.2 K or an energy of 0.3 meV, 10 orders of magnitude less than the energy of the antiprotons delivered by the AD. The techniques used to accumulate antiprotons were developed over many years by the TRAP collaboration, the predecessor to ATRAP. These include investigations of antiproton slowing in matter [37], capturing antiprotons in a Penning trap [56], cooling trapped antiprotons to 4.2 K [27], and the stacking of many antiproton shots [27, 57]. Some of these techniques have been refined here for our purposes, particularly antiproton stacking [4].

### 4.2.1 Energy tuning

Antiprotons arrive from the AD with an energy of 5.3 MeV. We must reduce this energy by more than 3 orders of magnitude to be able to trap them. This is done by using a carefully chosen Be degrader foil. Degraders are typically used to reduce the energy of a particle beam by a small fraction and this can be done with high efficiency. However, we wish to essentially stop the beam. The lower the energy of beam, the greater the energy (and position) straggling that results during passage through matter. Hence, we are in a situation where the energy straggling will be large and as a result only a small fraction of the incident antiprotons emerge with energies low enough to trap [38].

Of course, we wish to maximize this fraction of trapped antiprotons. This is done by tuning the energy of the antiprotons beam before it reaches the degrader. The beam energy of the AD is fixed, so we tune by passing the antiproton

beam through a short gas cell containing a mixture of He and SF<sub>6</sub> gas at atmospheric pressure. By changing the ratio of the two gases, we can change the density of the gas in the cell and thus, the  $dE/dx$ , allowing us to tune the beam energy. The use of gases with very different molar masses provides a large tuning range.

The thickness of the degrader is determined considering this tuning range, as well as the energy loss of the various other elements of the beam line system. Great care must be taken when choosing the degrader, as if it is too thick or too thin, we will be unable to trap antiprotons.

One can predict the gas ratio that will give the highest antiprotons trapping efficiency. This can only be done approximately, since the  $dE/dx$  has not been well measured at low energies. In practice, the antiproton trapping efficiency is maximized by varying the ratio of the two gasses in the cell and measuring the number of antiprotons captured (Fig. 4.13). The optimal gas ratio has been found to vary between thermal cycles, perhaps because thin ice layers grow on the various windows through which the antiproton beam must pass. A rather dramatic example of this effect was observed when the BGO detector was first installed. This detector completely filled the space surrounding the Penning trap, severely reducing the pumping conductance between the bottom and the top of the magnet bore. With a pump installed only on the top of the magnet bore and the BGO detector in place, the energy tuning calibration curve was seen to drift over the course of several days (Fig. 4.13). Once the HBAR1 Penning trap was cooled down to 4.2 K, it began to cryopump the considerable amount of residual gas remaining in the lower portion of the magnet bore, some of which condensed on the layers through which the antiproton beam must

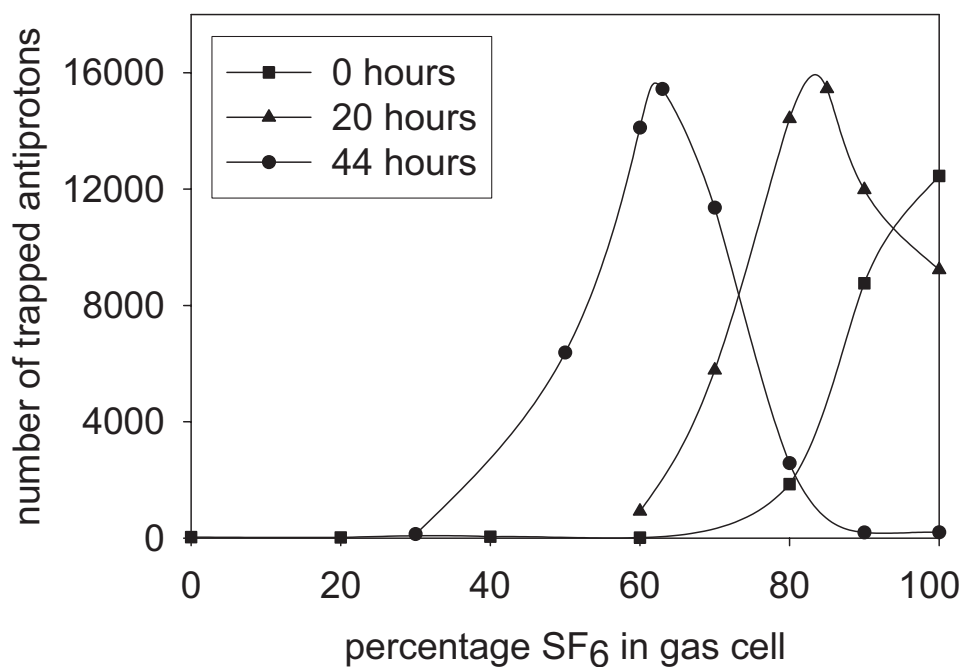


Figure 4.13: Range curves taken over several days. The most efficient gas ratio changes in time due to accretion of residual gas upon the entrance window of the Penning trap. Proper evacuation of the solenoid bore eliminates this behavior.

pass. As these ice layers become thicker over time, the beam loses more energy passing through them and a less dense gas cell (i.e. less SF<sub>6</sub> in the gas cell) is required to achieve the maximum trapping efficiency. This was an unacceptable situation, since eventually the trapping peak drifted below our energy tuning range. Installation of a pump on the bottom of the magnet bore remedied this problem immediately.

### 4.2.2 Antiproton capture

Once some antiprotons have emerged from the degrader with a relatively low energy, it still remains to trap them. One approach would be to cool the antiprotons into a well via collisions with a trapped plasma, but insufficient energy can be removed from the axial motion of antiprotons in this fashion in just one pass. Instead, we form

a well around the antiprotons before they can leave the Penning trap, by very rapidly switching a potential. This process is illustrated in Fig. 4.14. Before the antiproton pulse enters, a large negative potential (typically  $-3$  keV) is applied to the UPHV electrode. This forms one end of the Penning trap for the antiprotons. Antiprotons enter through the degrader and any that emerge with a low enough axial energy will be reflected off the UPHV potential. While these antiprotons are still in flight, the potential applied to the degrader is rapidly switched to be the same as that applied to UPHV. The antiprotons are then trapped in the long well formed by the potential applied to UPHV and the degrader.

Of course, the number of antiprotons trapped in this fashion will depend on the time at which the degrader voltage is applied, relative to the time at which the antiproton pulse from the AD arrives. If the potential is switched too early, antiprotons will be accelerated by it off the degrader and will have too much axial energy to be reflected by the potential applied to the UPHV electrode.<sup>2</sup> If the potential is applied too late, antiprotons will have enough time to make one round trip through the trap and will return to strike the degrader. These two effects can be seen in Fig.4.15. As the switching of the degrader potential is delayed relative to the arrival of the antiproton pulse, the antiproton capture efficiency increases at a rate consistent with the temporal length of antiproton pulse. As the switching is delayed further the capture efficiency slowly decreases. This is can be explained by recalling that the antiprotons captured have a range of energies and thus, a range of transit times in the trap. Those

---

<sup>2</sup>Even if that potential were large enough to reflect them, they would have enough axial energy to return and strike the degrader.

lower energies, say 100 eV, return after 2  $\mu$ s.

Once antiprotons have been captured in the long well formed by UPHV and the degrader, we can measure their total number and energy distribution by ramping the potential applied to the degrader to 0 V. This is done using the Fast Timing System, so that a measurement of applied potential vs time can be correlated with the measured time spectrum of antiproton annihilations. Displayed in Fig. 4.16 is the energy spectrum of antiprotons held in the long well for 30 s. As can be seen, the energy distribution appears to be exponential. This is not the initial axial energy distribution, but rather that which evolves over time due to collisions between antiprotons. In Fig. 4.17, we see that antiprotons are lost, most likely over the top of the 3 keV well, resulting in a form of evaporative cooling. As many as 28000 antiprotons have been captured from a single AD pulse, but this number depends upon the beam quality.

We expect the axial energy distribution of the antiprotons emerging from the degrader to be uniform, since we are considering a small energy range (keV) compared to the scale over which the energies are varying (MeV). By changing the potential applied to the electrode UPHV and measuring the trapping efficiency we can probe the initial axial energy distribution of the trapped antiprotons (Fig. 4.18). The trapping efficiency rapidly saturates, presumably because antiprotons emerging from the degrader with a large axial energy will also have a large radial energy, resulting in a large cyclotron radius. If the cyclotron radius is too large, the particles will strike the electrodes during their first pass through the Penning trap. This could be confirmed by either using larger electrodes, or by varying the magnetic field and thus, the cyclotron radius. In future experiments, where a lower magnetic field is likely to

be used, it may be necessary to use electrodes with a larger diameter to counter this effect.

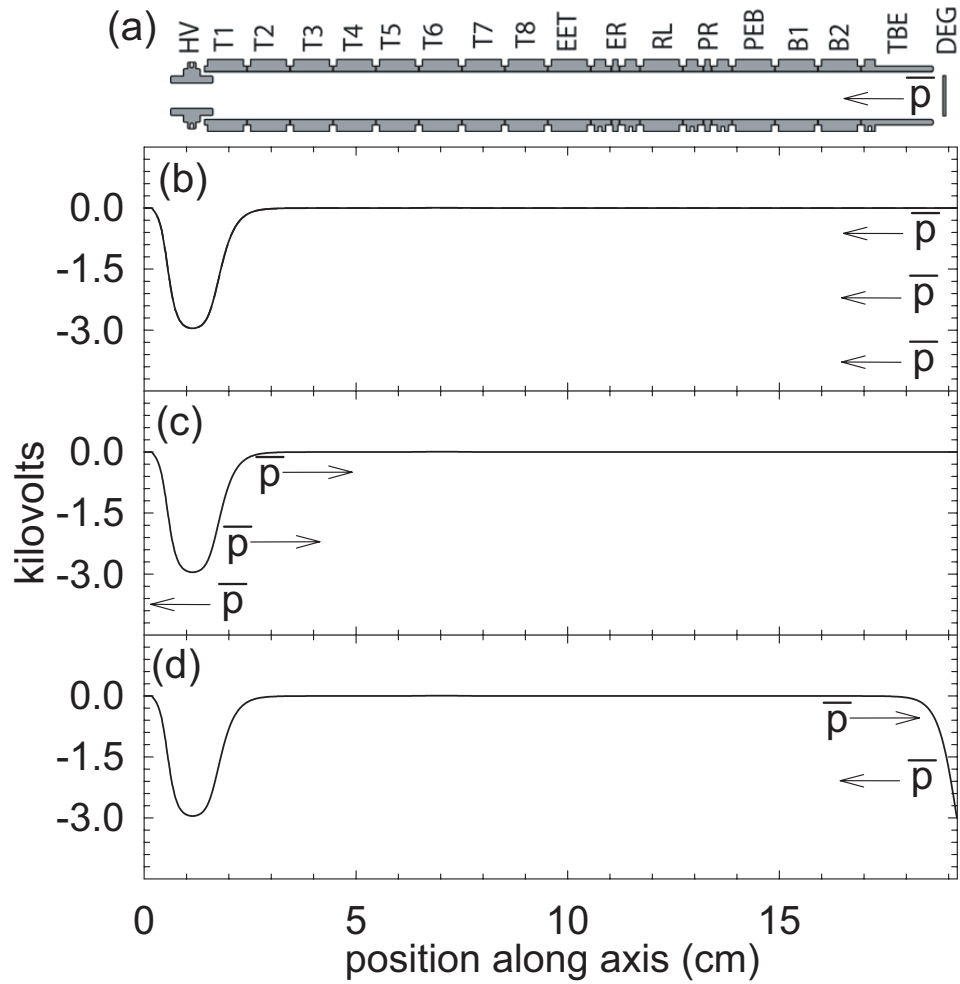


Figure 4.14: The antiproton capture process. (a) Electrodes used to capture antiprotons. (b) Antiprotons emerge from the degrader with a range of energies. (c) Those with an energy less than 3 keV are reflected by the potential applied to the UPHV electrode. (d) The degrader potential is rapidly switched to trap the antiproton bunch.

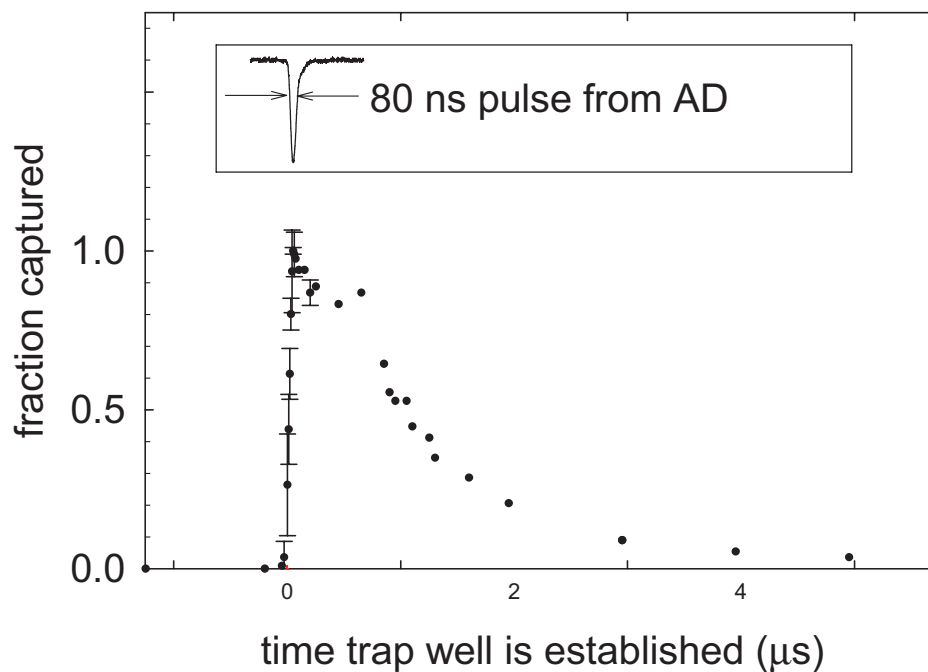


Figure 4.15: The number of trapped antiprotons depends upon when the trapping potential is applied.

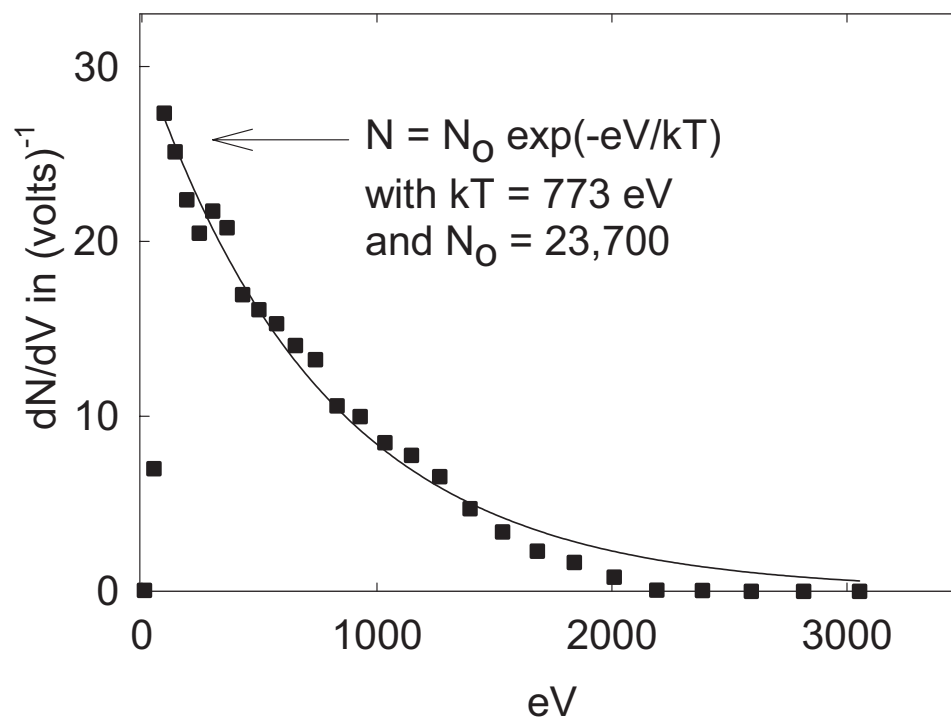


Figure 4.16: Energy spectra for antiprotons trapped from a single pulse from the AD.

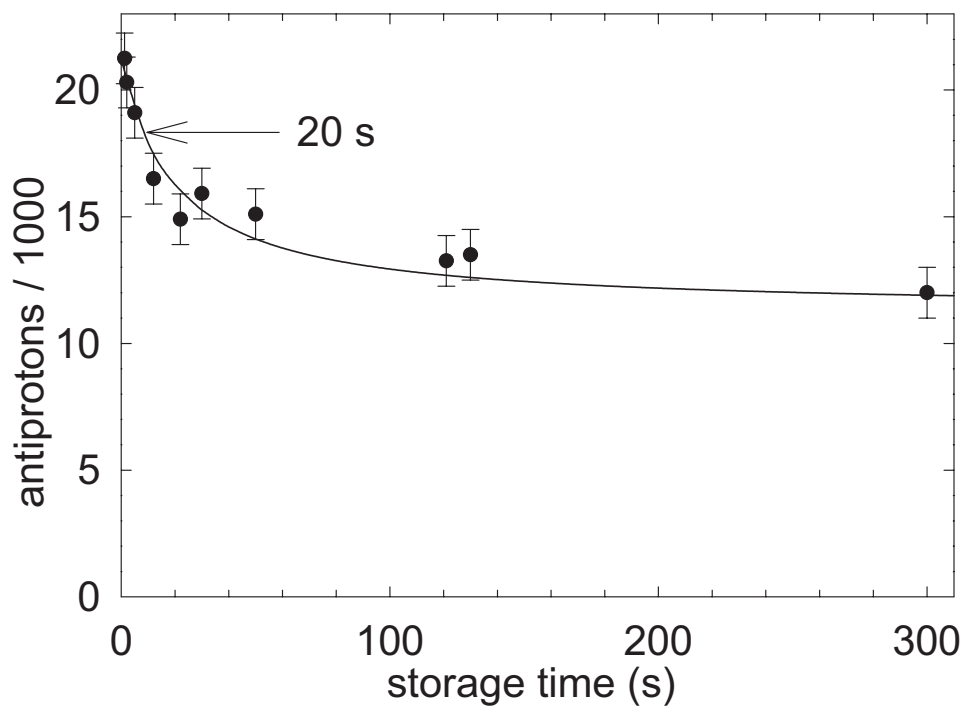


Figure 4.17: The number of antiprotons held in the long well decreases as a function of storage time.

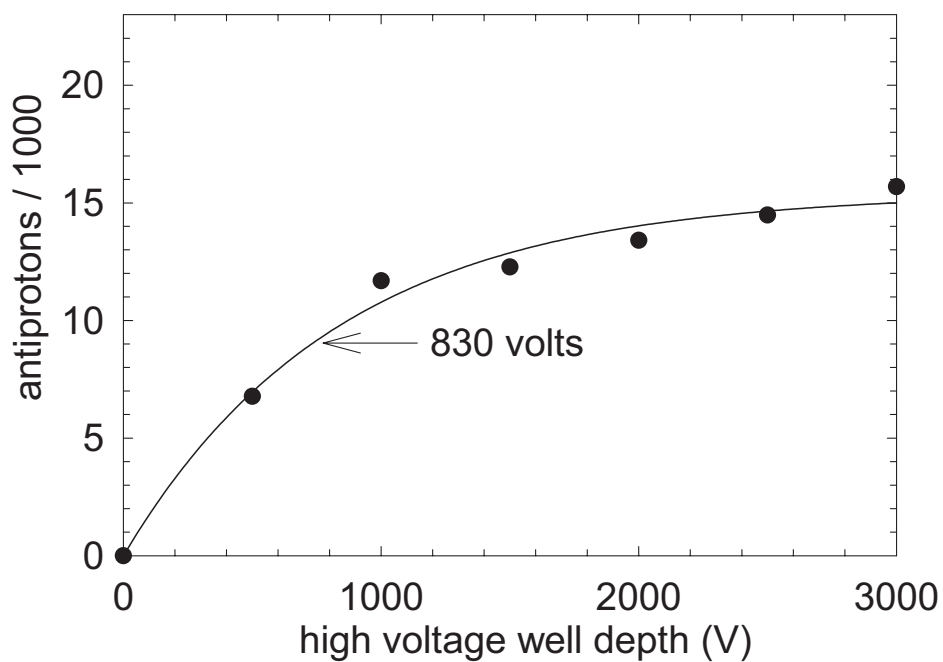


Figure 4.18: The trapping efficiency varies exponentially with the depth of the high voltage well.

### 4.2.3 Electron cooling

While the ability to trap relatively energetic antiprotons was demonstrated above, to undertake interaction experiments we wish to have antiprotons that are as cold as possible. To cool antiprotons, we also confine electrons in the long well, as shown in Fig. 4.19. As the antiprotons oscillate in the long well, they collide with electrons, exchanging axial energy. Collisions amongst electrons can transfer axial energy to the cyclotron motion, which can then cool via the emission of cyclotron radiation as described in Sec. 2.1.1. Thus, the antiprotons cool into thermal equilibrium with the electrons at 4.2 K and finally reside in the same single electrode well containing the electrons. We use electrons for this purpose since they have the same sign of charge as antiprotons, they can be accumulated fairly rapidly, and they efficiently cool themselves via the emission of cyclotron radiation.

The progression of the electron cooling can be seen in Fig. 4.20 and is consistent with the expected rate [58]. For these studies, about 4 million electrons accumulated using the positron source were used. Note that only those antiprotons not cooled by the electrons are visible in the figure. Even after allowing 85 s for cooling, a small fraction of the antiprotons remain uncooled. Presumably, these are at too large a radius to interact with the electrons. Also, as the cooling progresses, a small fraction of the antiprotons that are initially confined leave the trap. This spilling also occurs without electrons, as can be seen in Fig. 4.21. These antiprotons are presumably weakly confined (have large axial energy or are at a large radius) and leave via collisions with other antiprotons or a radial instability. Displayed in Fig. 4.22 are the number of antiprotons that are cooled, uncooled, and spilled as the cooling

progress. As can be seen, the total number of antiprotons captured in the long well is accounted for. It is likely that the only way in which the cooling efficiency could be improved is by reducing the fraction that are spilled. As those that are uncooled are likely to be at large radii, they would be of little use for interaction experiments. However, it is also possible that those spilled leave the trap because they are at large radii and thus, are close to any imperfections on the electrode surfaces. In this case, it would not be possible to improve the cooling efficiency.

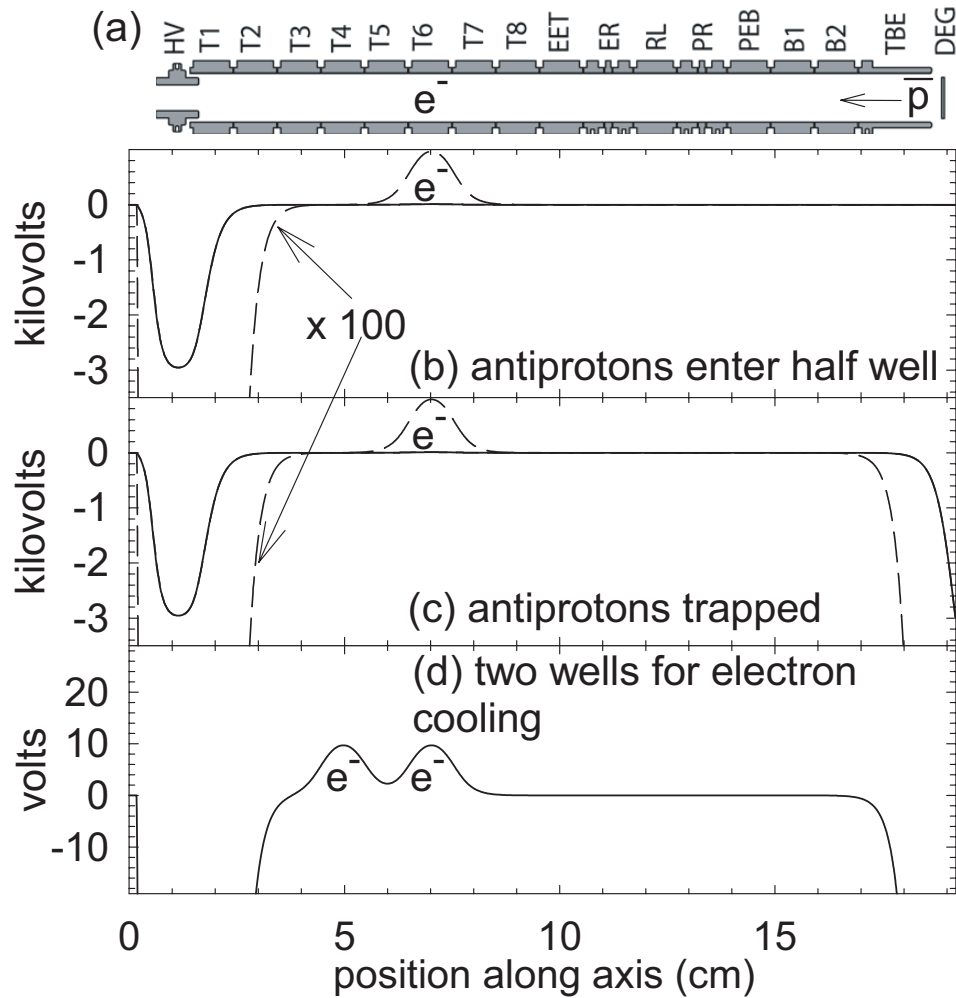


Figure 4.19: (a) Electrodes used to accumulate cold antiprotons. (b) A small well on electrode T6 is preloaded with electrons before any antiprotons are accumulated. (c) As before, the potential applied to the degrader is rapidly switched to trap antiprotons in flight. (d) More than one electron well can be used to cool antiprotons.

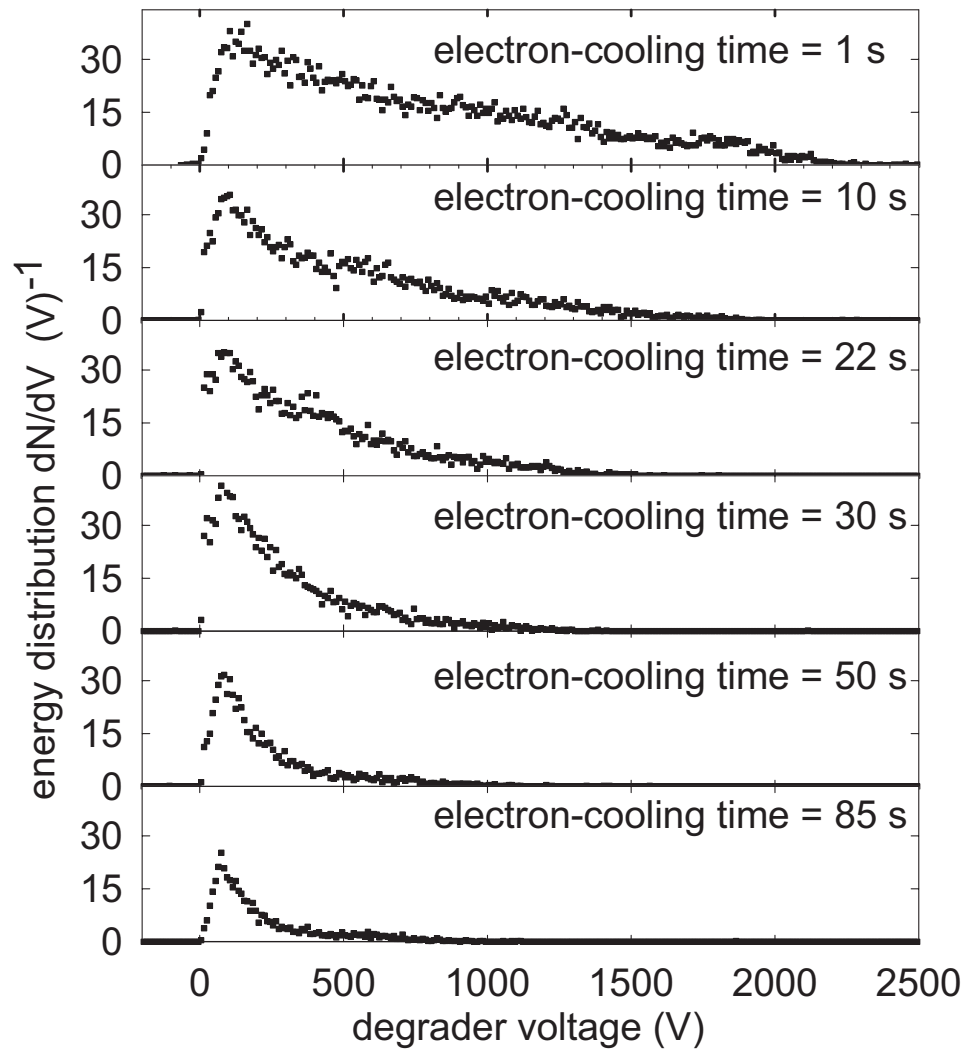


Figure 4.20: The energy of the antiprotons in the long well decreases as a function of electron cooling time. The number also decreases insofar as some antiprotons are cooled into the small well and others are lost from the trap.

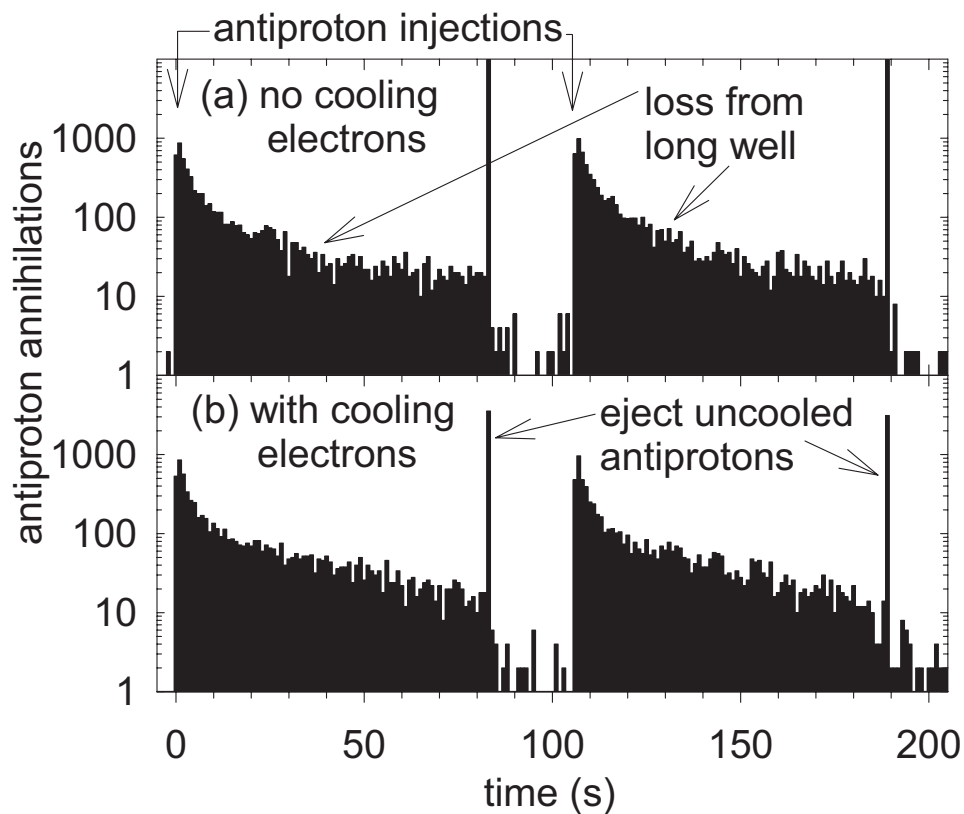


Figure 4.21: AD antiprotons are injected into the long trap every 108 s. For the subsequent 85 s, with or without cooling electrons, the number lost is approximately the same, but electrons cool some into the small well (or wells). Uncooled antiprotons remaining in the long well are then ejected.

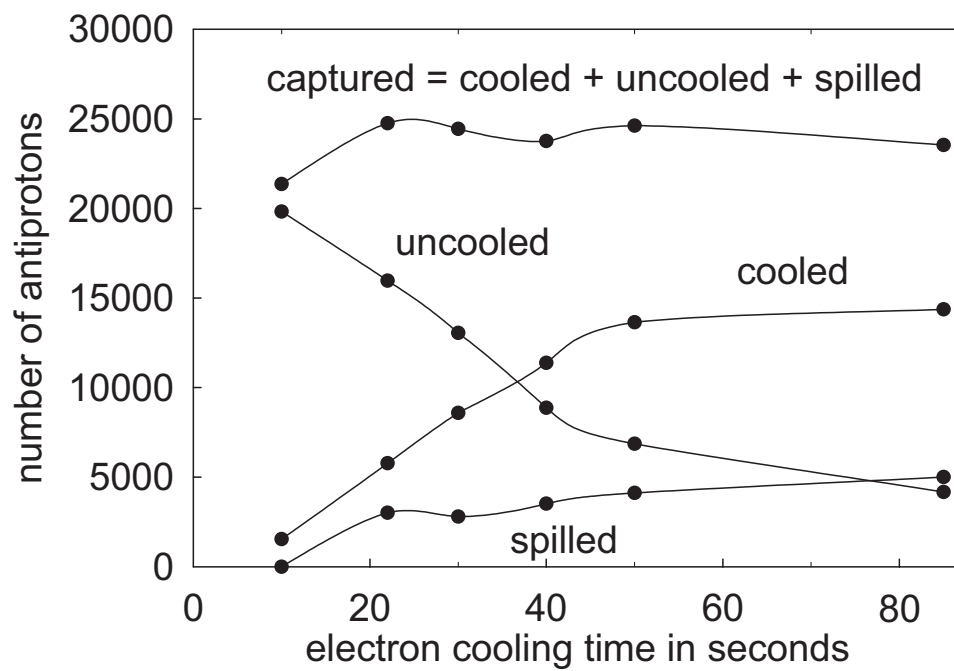


Figure 4.22: Number of antiprotons captured, uncooled, spilled, and cooled from a single pulse of AD antiprotons.

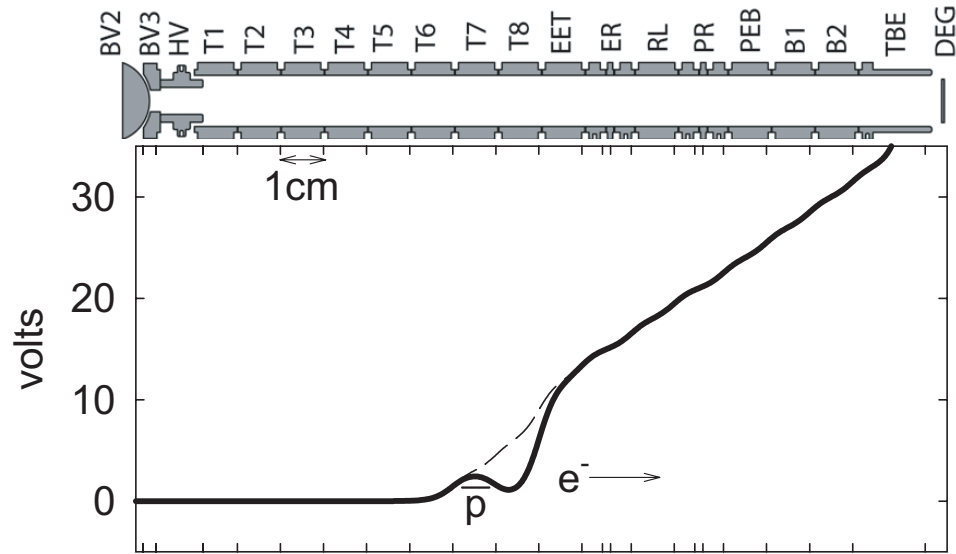


Figure 4.23: Potentials for electron ejection.

Electrons can be readily removed by pulsing open the well containing the antiproton/electron mixture. The potentials used for this purpose are shown in Fig. 4.23. The principal is identical to that applied to clean positive ions from positron clouds. Due to the large mass difference between electrons and antiprotons, electrons will feel a much greater acceleration from a given force. Thus, when a well is opened, they will leave long before the antiprotons move significantly. Application of several 100 ns pulses is found to be sufficient.

The dramatic effect of the electron cooling is demonstrated by comparing Fig. 4.24, a cooled antiproton energy spectrum, with Fig. 4.16. The width of the spectrum has been reduced approximately 5 orders of magnitude. Compared to the antiprotons that enter the Penning trap at an energy of 5.3 MeV, the energy has been reduced by 10 orders of magnitude. The width of the spectrum is primarily due to the space charge repulsion of the particles and radial variations in the confining potential: if

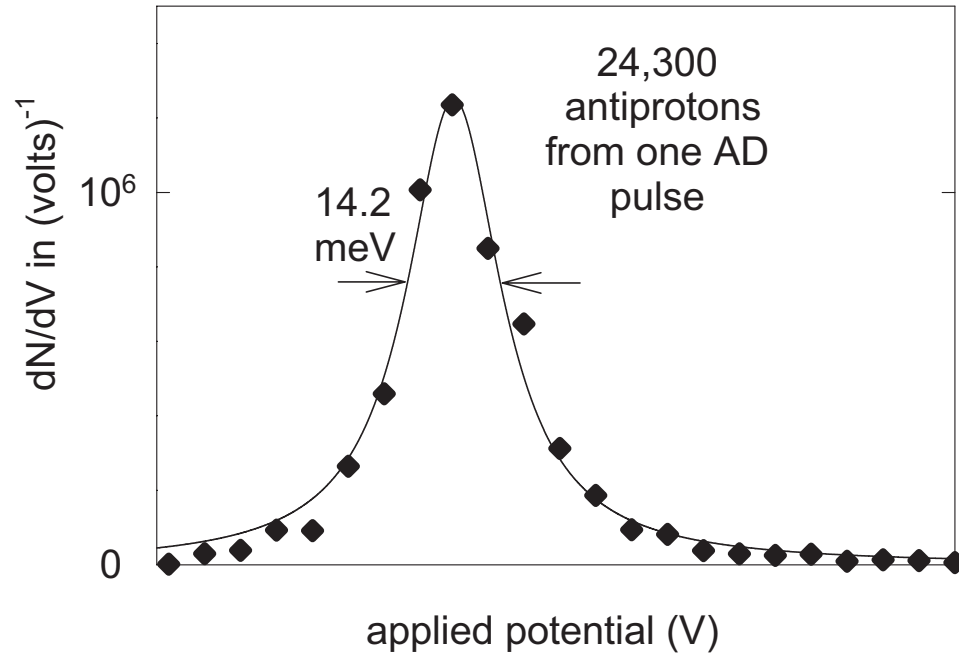


Figure 4.24: Electron cooled antiproton spectrum.

this could somehow be eliminated we would expect the width to be 0.34 meV, i.e. 4.2 K [27]. Note that the cooled spectrum is obtained after electrons have been ejected, otherwise the space charge of the electrons would yield a much larger width.

#### 4.2.4 Antiproton stacking

We wish to have the largest number of antiprotons possible for interaction experiments. To get more than about 20,000, it is necessary to stack the antiprotons trapped from successive AD pulses. The electron cooling technique makes this easy to implement. Once antiprotons from one shot have been cooled into single electrode well(s) with the electrons, the degrader potential can be lowered in preparation to receive another pulse from the AD. Note that the 85 s electron cooling time used

above is compatible with the 108 s period of the AD.

The progression of the stacking process is displayed in Fig. 4.25. For this demonstration, there was a single electron well containing about 4 million electrons. As can be seen, the number of antiprotons captured is a linear function of the number of AD pulses stacked. The efficiency with which antiprotons are electron cooled when stacking is similar to that when just a single AD pulse is captured. Of course, this is less than the short term capture efficiency (also shown in Fig. 4.25a) as not all antiprotons are electron cooled. Comparing Fig. 4.25b and Fig. 4.22 at a cooling time of 85 s we see that proportions of antiprotons cooled, uncooled, and spilled remain similar whether one is stacking or simply captured a single AD pulse.

An example of a stacked antiproton energy spectrum is shown in Fig. 4.26. In this instance, 118,000 antiprotons were stacked from 9 AD pulses. The width of the spectrum is again dominated by the antiproton space charge.

If many more AD pulses than the number shown in Fig. 4.25 are stacked, the spilling loss is observed to increase sharply. This is most likely because a radial instability develops in the antiprotons cloud. It is known that large antiproton cloud have a very large radius [59], i.e. many antiprotons reside close to the electrodes where the potential is rather flat and any imperfections on the electrode surface will have a large affect. If too many antiprotons are added to a cloud, its radial extent may grow to the point that those at large radii simply leave the trap. This can be avoided somewhat by using more than one electron well however, large losses can occur when two large clouds are combined. To successfully accumulate clouds much larger than about 400,000 antiprotons, it will be necessary to develop a radial cooling technique.

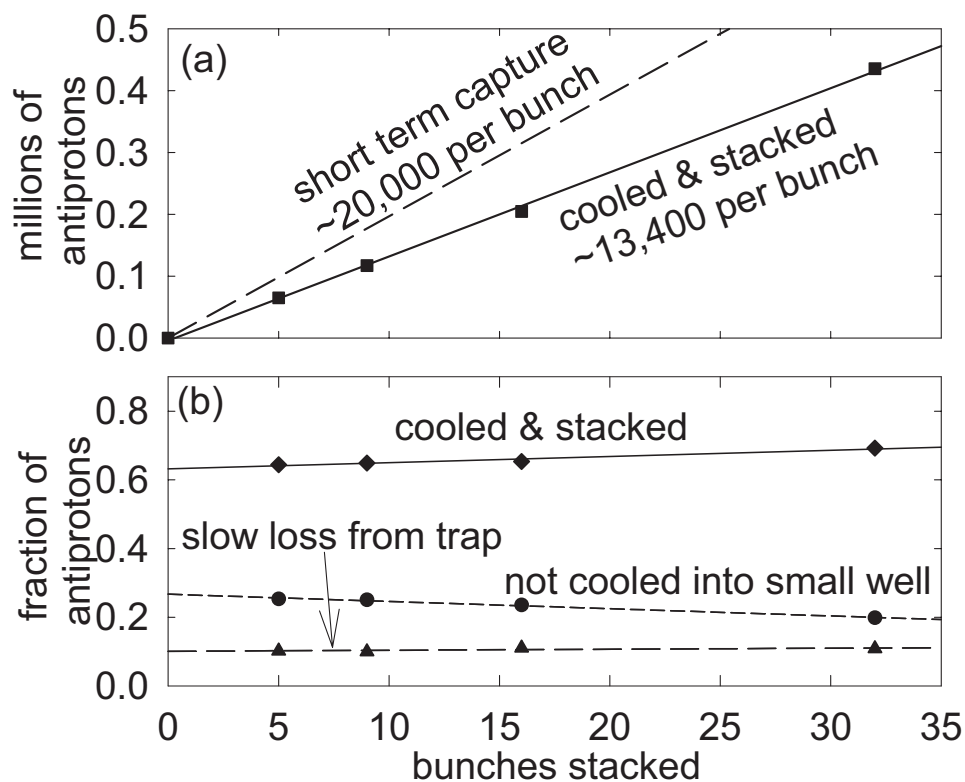


Figure 4.25: Stacking successive pulses of antiprotons.

Sideband cooling has been attempted on large clouds, but has meet with little success, presumably because the radius of the clouds is so very large. Fortunately, we do not need clouds larger than this at present.

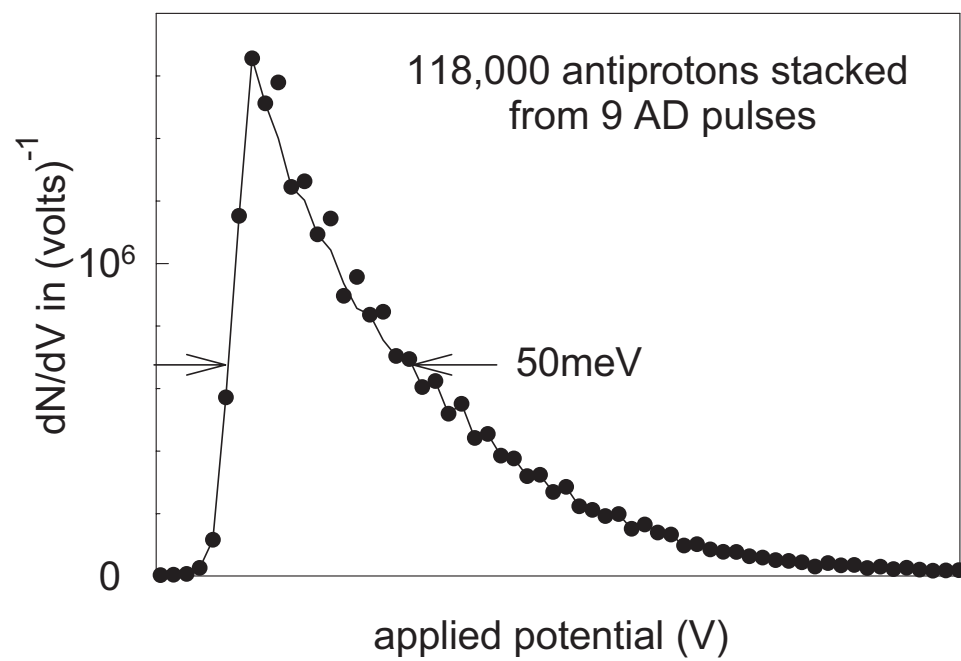


Figure 4.26: The energy spectrum of 9 stacked antiproton shots.

# Chapter 5

## Positron Cooling of Antiprotons

Having accumulated the ingredients of antihydrogen, we must now arrange for them to interact. To do this we use a nested Penning trap, which allows the two oppositely charged species to be trapped simultaneously. Studies used to optimize both the nested well structure and the techniques used to introduce the particles into the nested Penning trap will be presented, followed by investigations of the interaction of the two species in the nested Penning trap .

### 5.1 Accumulating particles for interaction experiments

Interaction experiments require us to accumulate all three species that have been discussed in the previous chapters: electrons, positrons, and antiprotons. In order to make the best use of the antiproton beam, control sequences were devised to efficiently accumulate, manipulate, and transfer the species in an appropriate way.

Of particular importance is the ability, provided by the ball valve, to accumulate positrons and antiprotons simultaneously.

The first step in any loading cycle is to lower the positron source from its lead enclosure down into the solenoid. During the 3 minutes required no other activities are undertaken, as the control software for the positron source is very computationally intensive.

This is followed by the accumulation of electrons, using either the FEP or positron source (Sec. 4.1), typically taking 5 to 10 minutes. Once electron accumulation and preparation are complete and the ball valve is closed, antiproton and positron accumulation can begin (Sec. 4.2 and 3.2). Fortunately, the positron accumulation technique is very simple, requiring little active control once the appropriate voltages are set. This is not the case for antiproton accumulation, as there are many devices to set up and read out, and many potentials to manipulate.

Once about half the number of desired antiproton pulses have been stacked, the positrons loaded up to that point are moved from the accumulation electrode to a storage trap. Then, antiproton accumulation continues as before. Once antiproton accumulation is complete, there are thus two equally sized bunches of positrons to pulse down to the interaction region, as required for the highest possible transfer efficiency (Sec. 3.3).

Once the desired number of antiproton pulses have been accumulated, electrons are ejected, except in rare circumstances where an antiproton-electron mixture is required. At this point the ball valve is opened, and the positrons transferred to the section of the Penning trap appropriate for the intended experiment.

The total length of this preparation will vary depending upon the desired numbers of antiprotons and positrons. Typical numbers were 100,000 antiprotons and 250,000 positrons, yielding a total accumulation time of about 30 minutes.

## 5.2 The nested Penning trap

Due to the long confinement time that can be achieved and the ease with which particles can be manipulated, Penning traps are an ideal device for collecting and studying charged antimatter particles. However, since a trap that is confining for one species will be anti-confining for a species with the opposite sign of charge, it may not seem to be an ideal device for attempting recombination experiments. The nested Penning trap was proposed [7] to overcome this problem, and all observations of cold antihydrogen to date [9, 1, 60] have used the nested Penning trap to bring positron and antiproton plasmas into contact.

The simplest nested Penning trap is formed using five electrodes; one species resides in an inverted central well, while the other resides in the outer well (Fig. 5.1). It is advantageous to place the positrons in the central well and to allow the antiprotons to oscillate high in the outer well. If we were to place the positrons in the outer well they would quickly cool via synchrotron radiation into the two side wells. They would then spend very little time interacting with antiprotons in the central well. In addition, as discussed in Sec. 1.3, the most important recombination rate scales as  $n_{e^+}^2$ . Placing the positrons in the central well results in a much higher density than if they were placed in the outer well and thus, makes recombination more likely.

As the antiprotons oscillate high in the outer well they will collide with the

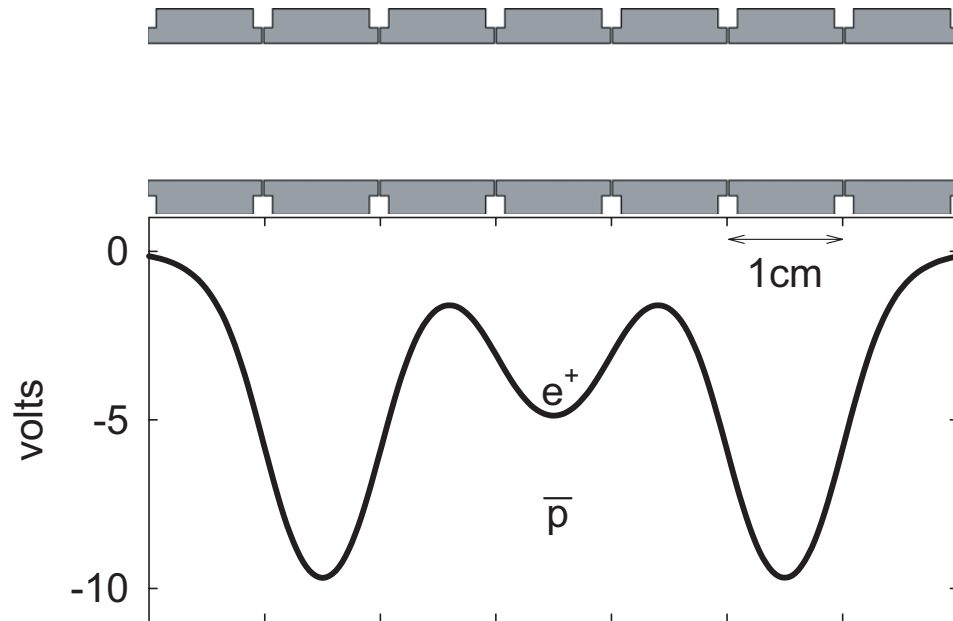


Figure 5.1: A simple nested Penning trap formed with potentials applied to five electrodes.

positrons, and as the positrons can re-cool via the emission of synchrotron radiation, the net effect is for the antiprotons to lose axial energy. This is very similar to the electron cooling of antiprotons described in Sec. 4.2.3, except the two species have the opposite sign of charge. Such cooling was first demonstrated with electrons and protons [61] and then more recently with positrons and antiprotons (Fig. 5.2 from [8]). When there are no positrons present in the central well the antiprotons remain higher in the outer well. When positrons are present, the axial energy of the antiprotons is reduced with a time scale of several seconds. As the axial energy of the particles in the outer well approaches that of the central well, they spend an increasing amount of time interacting with the other particle species (Fig. 5.3). This is a situation favorable for recombination.

The axial energy reduction is crucial for antihydrogen formation, as this will

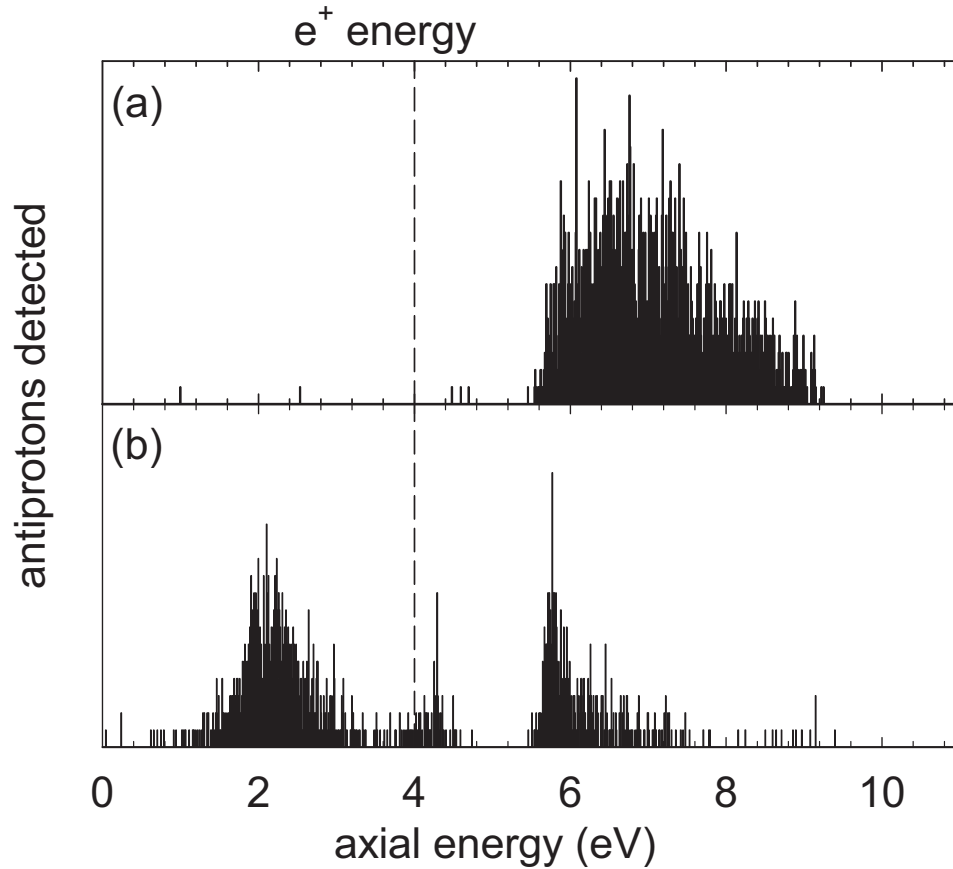


Figure 5.2: The first demonstration of positron cooling of antiprotons. (a) Without positrons, antiprotons remain at the high axial energy at which they were injected into the nested Penning trap. (b) When positrons are placed in the central well, the axial energy of most antiprotons is reduced.

largely determine the interaction time of the two species. A new form of cooling is represented in Fig. 5.2, insofar as antiprotons cool below the level of the positrons, beyond where they interact efficiently with the positrons. Experiments characterizing the initial cooling will be described in Sec. 5.3, while the cooling below the positrons will be discussed in Sec. 5.4. The stability of antiprotons in the nested Penning trap during these processes is an important consideration. If the confinement time of antiprotons in the nested Penning trap is short, the interaction time of the

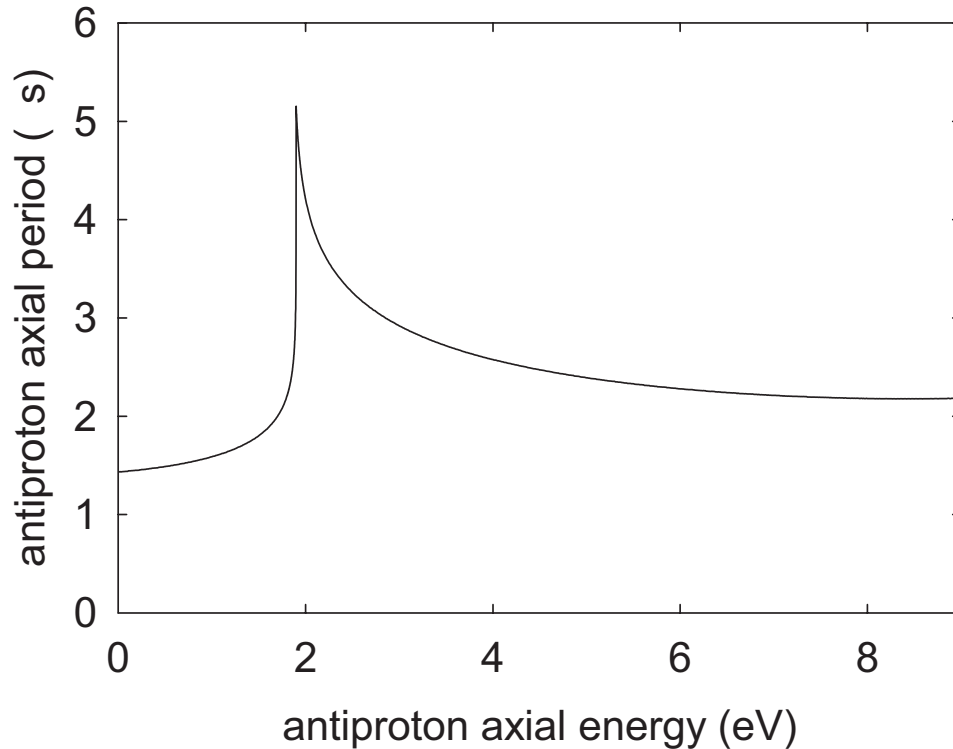


Figure 5.3: The period of antiprotons in the outer well of a typical nested Penning trap as a function of axial energy. Note that as the axial energy approaches that of the central well the period becomes much greater.

positrons and antiprotons will be reduced and there will be a large background of antiproton annihilations. Since some of these annihilations inevitably produce positrons (Sec. 6.1.1), there is a chance that they could be confused with antihydrogen annihilation events, at least with the most straight forward detection scheme. Experiments probing this aspect of the nested Penning trap are described in Sec. 5.5.

### 5.2.1 Optimization of the nested Penning trap structure

Our studies of the nested Penning trap have two main aims:

- to understand the positron cooling of antiprotons;

- to investigate the stability of antiprotons in the nested Penning trap.

As will become apparent, the optimal well structure for each of these investigations is different.

As mentioned above, the simplest nested well is formed by five electrodes but, depending on the application, this may not be the best number to use. To study the characteristics of positron cooling of antiprotons, our main experimental tool is the low voltage ramp (LVR) (Sec. 2.4). By repeating the same experiment many times but analyzing the antiproton energy spectrum at different times, we can determine how rapidly the antiprotons are cooled and identify any other interesting features. So, for this aspect of our study we require that the axial energy spectrum obtained from a LVR not be adversely affected by the ramp itself.

Fig. 5.4 shows how the LVR is implemented in five and seven electrode nested Penning traps. In the case of seven electrodes, each side well is formed from two electrodes. The reason for choosing this configuration can be seen by examining the effect that ramping the end wall has on the depth of the side well. In the seven electrode configuration, the side well changes very little, while with five electrodes the effect is substantial. This can be easily understood by referring to Sec. 2.1.1. A side well formed from two electrodes screens out the change in potential from the ramp more effectively than could one electrode. Hence, seven electrode nested Penning traps were used to investigate the cooling characteristics.

However, side wells formed from two electrodes have one important disadvantage. As was mentioned in Sec. 2.1.1, particles with little axial energy are radially unstable in a longer, two electrode well. Thus, we would expect that antiprotons in the side

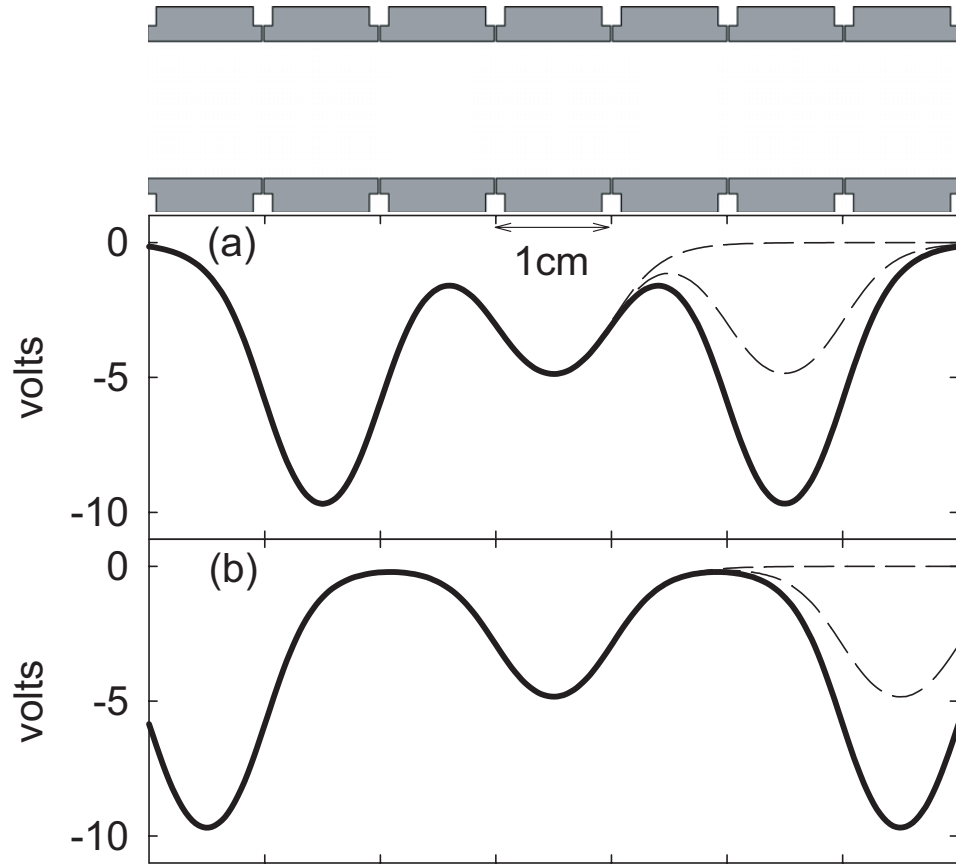


Figure 5.4: Nested Penning traps formed from (a) five and (b) seven endcap electrodes before (solid) and during (dashed) a LVR. Note that the side well depth changes dramatically when the end electrode is ramped in the five endcap electrode case

wells with little axial energy would eventually be lost radially from the trap. This is unacceptable when we are trying to investigate the stability of antiprotons in the nested Penning trap. Hence, when this was to be studied five electrode nested Penning traps were used.

Energy spectra from five electrode nested Penning traps that will be presented in the following sections have been approximately corrected to account for the distortion that results. A smaller correction due to adiabatic cooling [61, 35] has been neglected in all cases.

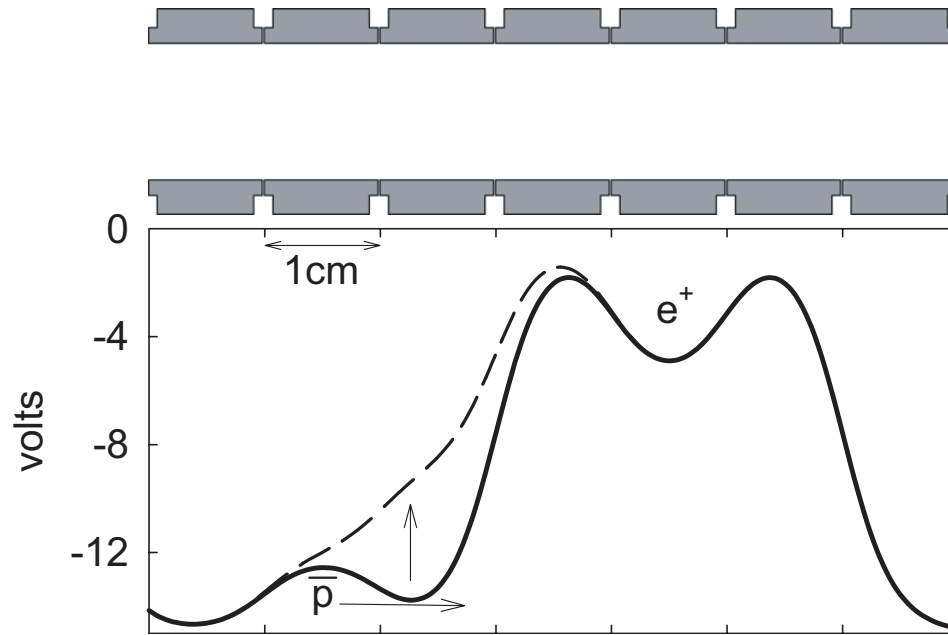


Figure 5.5: Antiprotons are introduced into a nested Penning trap with many electron volts of axial energy by releasing them from an offset well at one end of the nested Penning trap.

### 5.2.2 Optimization of launching method

To be able to study positron cooling of antiprotons, the antiprotons must be introduced into the nested Penning trap with enough axial energy to pass through the positron cloud. One approach is to start with antiprotons in thermal equilibrium in the side wells of the nested Penning trap, and then add axial energy by applying resonant RF drives [60, 28]. The approach used here is illustrated in Fig. 5.5. Antiprotons are held in a well that is offset from the base of the nested Penning trap. By opening this offset well, the antiprotons are allowed to enter the nested Penning trap and they do so with several electron volts of axial energy relative to the central well.

There are two ways in which the well can be opened:

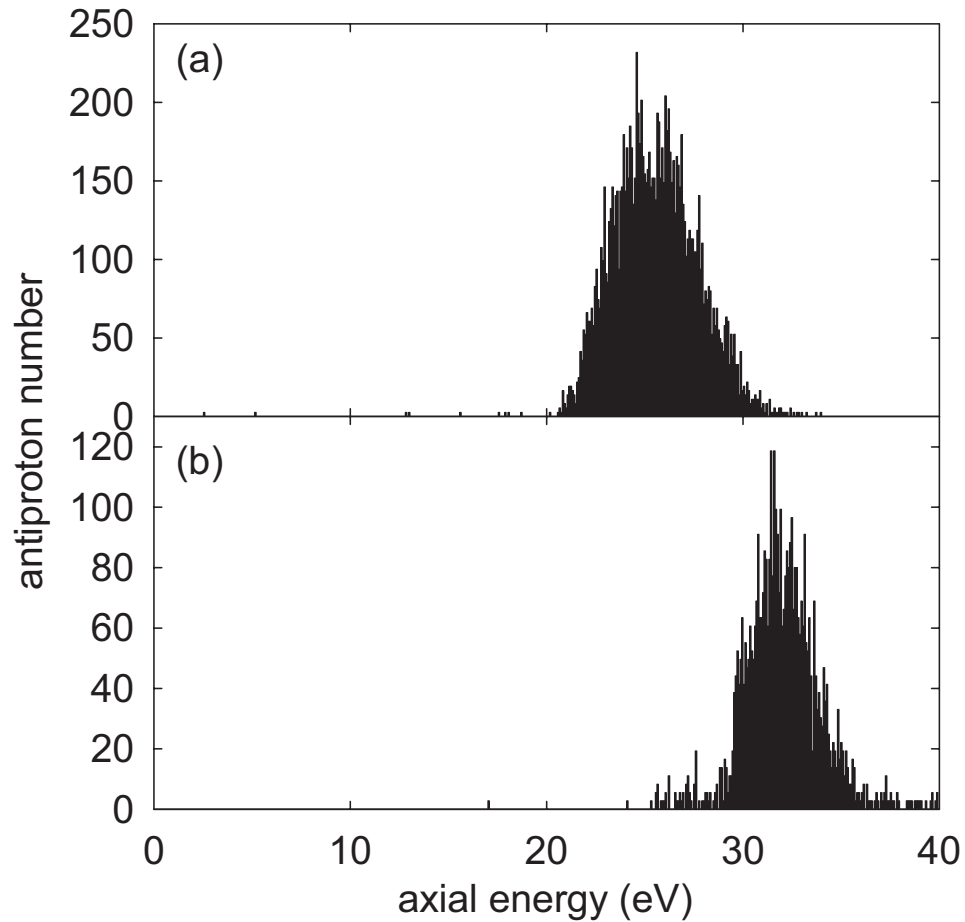


Figure 5.6: Energy spectra of antiprotons introduced into a nested Penning trap using (a) slow high voltage op-amps and (b) a fast pulse.

- by using high voltage op-amps to slowly change the voltage applied to the electrode that forms the offset well;
- by applying a fast voltage pulse to the electrode that forms the offset well.

The result of each method can be seen in Fig. 5.6. Clearly, slowly opening the offset well results in an antiproton energy spectrum that is broader and lower in the well than that resulting from using a fast pulse.

This difference is easy to understand. The op-amp voltage supplies typically have

output filters with a time constant of tens of milliseconds. Thus, as the voltage settles to its final value an antiproton in the nested Penning trap will make many axial oscillations. Each time an antiproton passes near the changing voltage its axial energy will be slightly reduced. Antiprotons released at different times will have their energy altered differently, resulting in a larger energy spread.

Neither of these effects occurs when the antiprotons are introduced into the nested Penning trap by pulsing open the offset well. The rise time of the pulses used is typically around 5 ns. About 20 ns after the leading edge of a pulse all ringing has died away. On these time scales antiprotons are essentially immobile and thus, when the offset well is pulsed open, the particles find themselves on a potential ramp. There is no reduction or broadening of energy due to the voltage pulse once the antiprotons have entered the nested Penning trap. The return of the pulse is timed to coincide with the antiproton bunch reaching the far side of the nested Penning trap so as to ensure that it does not alter the antiproton energy spectrum. This is demonstrated in Fig. 5.7.

From these results it is clear that a fast pulsed launch is superior to that using slow voltage changes in all respects. Hence, this style of launching was used exclusively in what follows.

### 5.3 Positron cooling of antiprotons

To study the characteristics of the positron cooling, we inject antiprotons into a nested Penning trap by first pulsing them through a 5 mm diameter aperture and then catching those remaining ( $\approx 5000$ ) in the nested Penning trap (Fig. 5.8). Sending

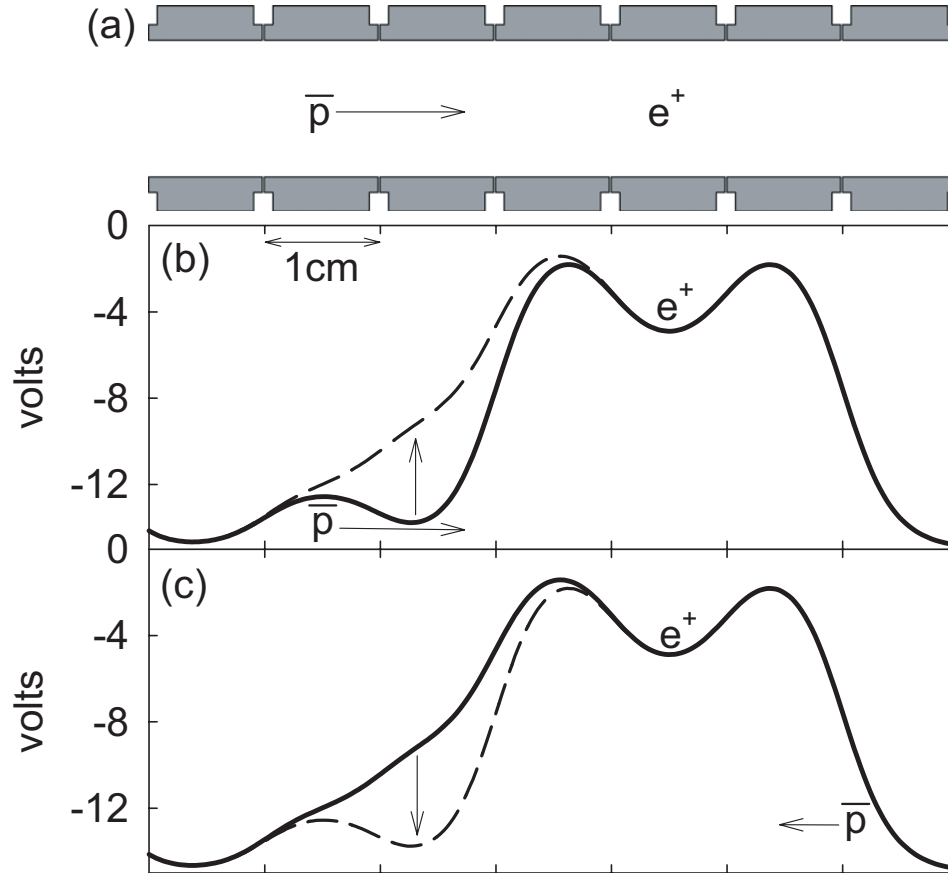


Figure 5.7: The pulsed launch of antiprotons into a nested Penning trap; (a) cross-section of electrodes used, (b) the leading edge of the pulse, and (c) the trailing edge of the pulse.

the antiprotons through the aperture “skims” off antiprotons trapped far off axis and thus, ensures a good overlap with the 6 mm diameter positron cloud, eliminating the uncooled section of the spectrum seen in Fig. 5.2. After a given interaction time, one side of the nested Penning trap is opened over 30 ms, allowing the antiprotons to escape. By recording the voltage and antiproton annihilations as a function of time we determine the axial energy spectrum of the antiprotons in the nested Penning trap (Fig. 5.9).

The decay of average antiproton axial energy for different positron clouds is shown

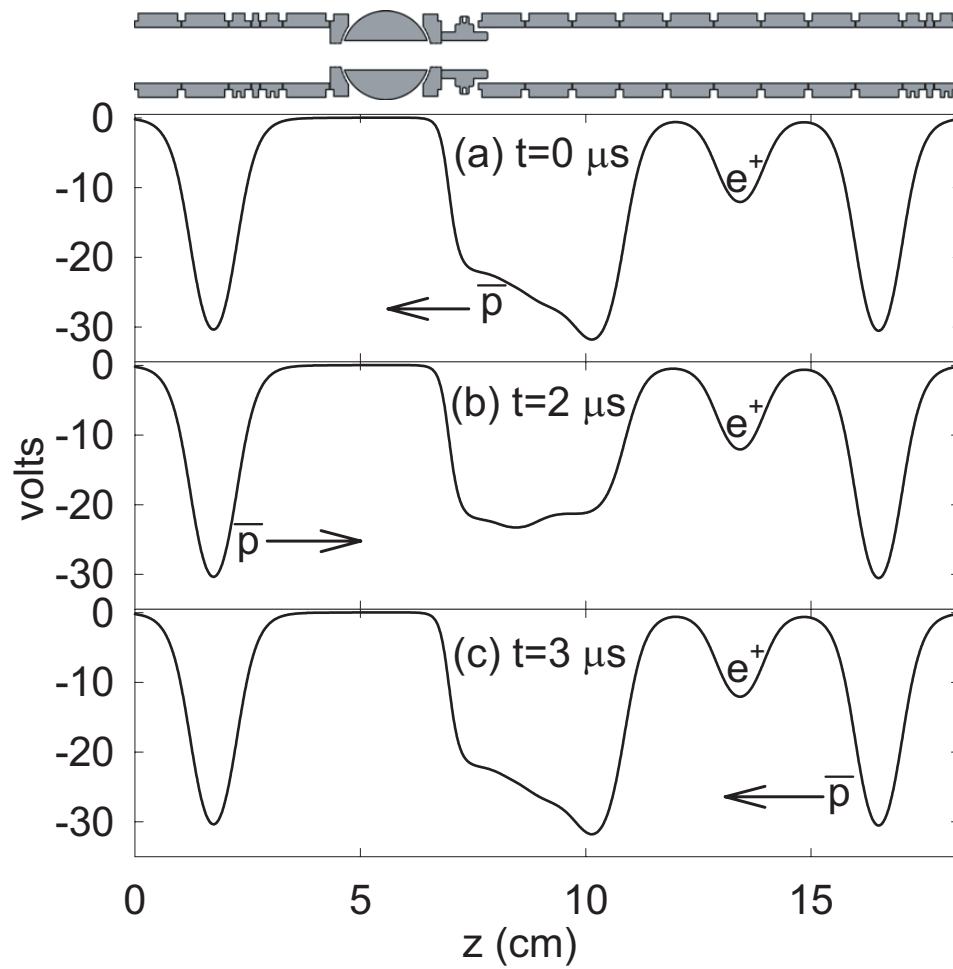


Figure 5.8: The nested Penning trap used for cooling studies. (a) Antiprotons are launched through a 5 mm aperture to “skim” off those at larger radii. (b) One side of the nested Penning trap is pulsed open to allow the antiprotons to enter. (c) Antiprotons are trapped in the nested Penning trap when voltage pulse returns.

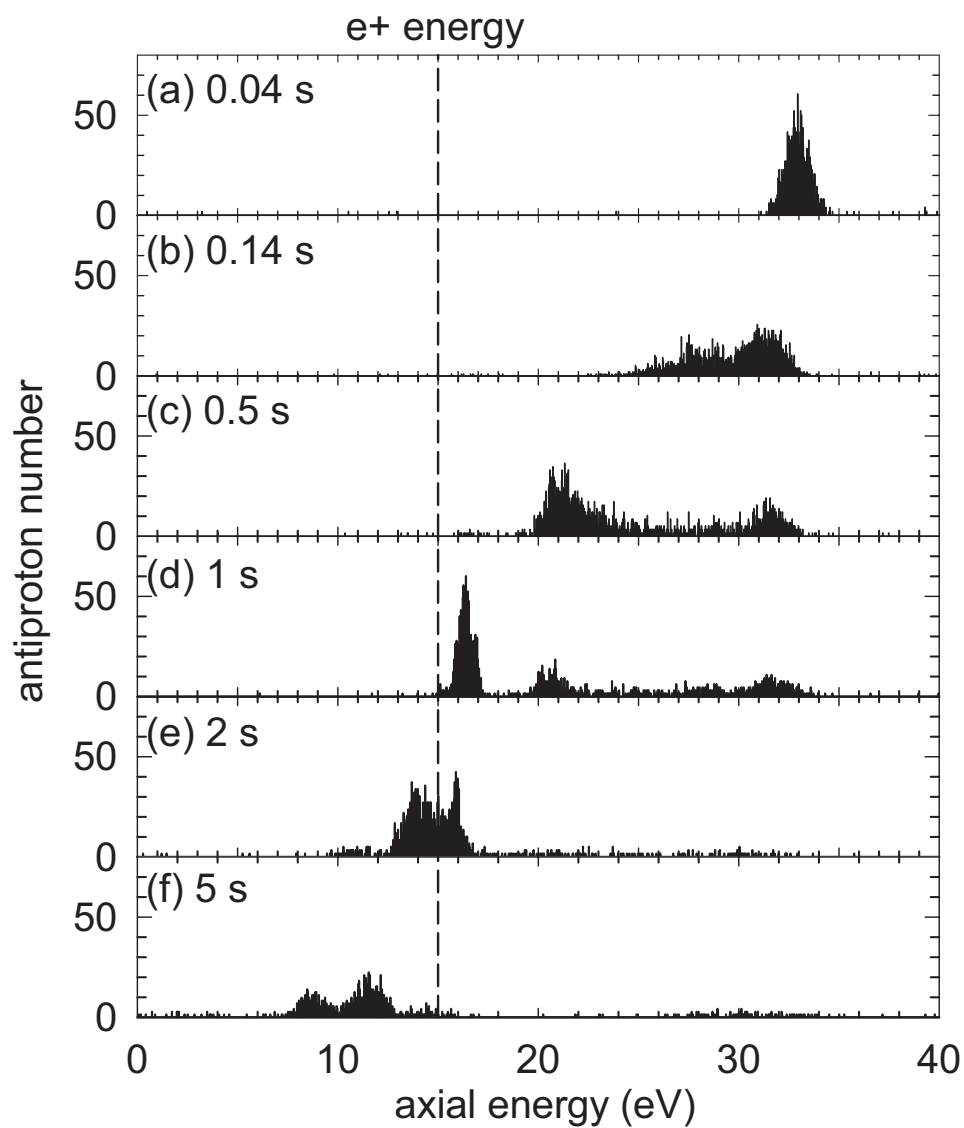


Figure 5.9: (a-f) Antiproton axial energy spectra after different hold times in the nested Penning trap (200,000 positrons present in the central well).

in Fig. 5.10. There are two sets of data: one in which the positrons are held in a 15 V well, the other in which they are held in a 10 V well. This change alters the initial antiproton energy relative to the positrons, and alters the positron cloud shape and density for a given number of particles. The cloud shapes and densities used have been determined [59], and the observed cooling time (determined from the simple exponential fit) appears to scale linearly with the areal density of the positron cloud (Fig. 5.11) over the range of values used. The clouds used vary in axial extent from 0.18 mm to 0.68 mm, diameter from 5.4 mm to 6.2 mm, and density from  $1.48 \times 10^7 \text{ cm}^{-3}$  to  $2.38 \times 10^7 \text{ cm}^{-3}$ .

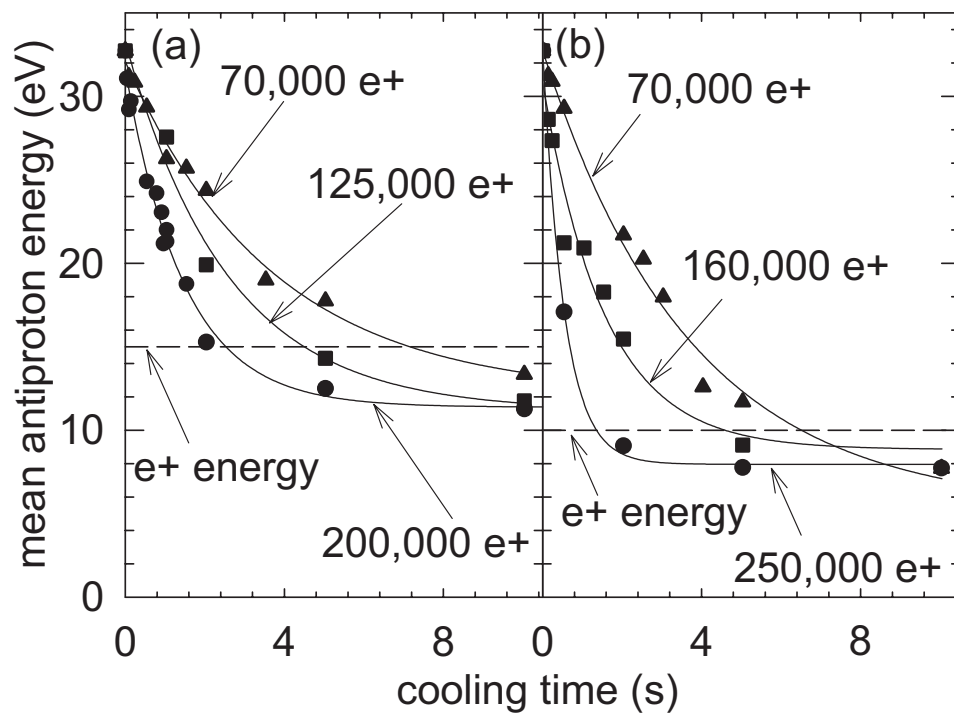


Figure 5.10: Rate of antiproton axial energy loss depends on the number of positrons placed in either a 15 V (a) or 10 V (b) well. Solid curves are exponential fits to the data. The primary source of error in the data points is a variation of about 10% in the number of positrons used.

A theoretical expression for the rate at which mono-energetic antiprotons lose axial

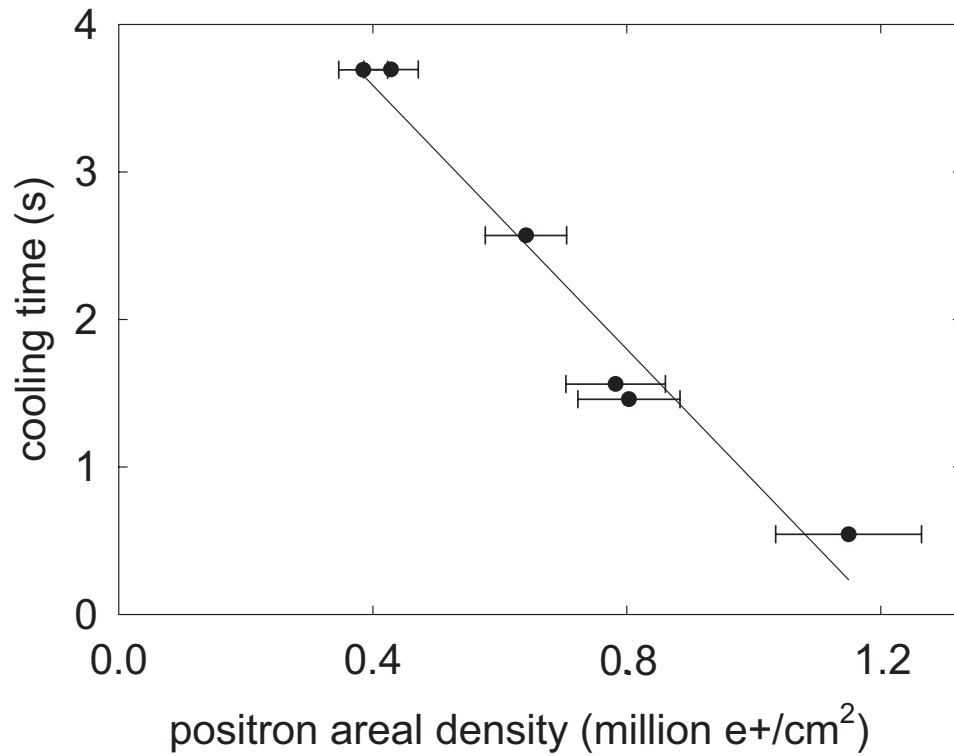


Figure 5.11: Cooling time constant versus positron plasma areal density (areal density = cloud thickness  $\times$  volume density).

energy when completely immersed in a positron cloud in thermal equilibrium,  $dE_{\bar{p}}/dt$ , was derived in [62]. The antiprotons that we inject into the nested Penning trap are nearly mono-energetic insofar as they begin with a narrow energy spread about the injection energy of  $\approx 15$  V. While it is clear that the energy spread can become large as the cooling proceeds (Fig. 5.9), this theoretical description will provide a useful comparison to the observed cooling of the mean antiproton energy.

When evaluating the cooling rate we use a recent expression for the coulomb logarithm [63],

$$\lambda = \frac{(1 + \Lambda_a)^2 \ln[(1 + \Lambda_a^2)]}{2(2 + \Lambda_a)^2} - \frac{\Lambda_a}{2(2 + \Lambda_a)}, \quad (5.1)$$

with

$$\Lambda_a = \frac{2\rho_{max}E_c}{q_{e^+}q_{\bar{p}}/4\pi\epsilon_0}, \quad (5.2)$$

where  $\rho_{max}$  is the maximum impact parameter for a collision that can transfer axial energy from an antiproton to a plasma positron,  $E_c$  is the average center of mass energy of a colliding positron and antiproton, and  $q_{e^+}$  and  $q_{\bar{p}}$  are the positron and antiproton charges, respectively. This expression is accurate for a large range of values for  $\lambda$  and takes account of the different sign of charge of the interacting species. The resulting expression for the cooling rate is a complicated function of both the antiproton energy and positron temperature that must be evaluated numerically.

Coupled rate equations are solved to determine the time dependence of the antiproton energy and positron temperature,

$$\begin{aligned} \frac{dE'_{\bar{p}}}{dt} &= f(E_{\bar{p}}) \frac{dE_{\bar{p}}}{dt}(E_{\bar{p}}, T_{e^+}) \\ \frac{dT_{e^+}}{dt} &= -\frac{f(E_{\bar{p}})}{k} \frac{N_{\bar{p}}}{N_{e^+}} \frac{dE_{\bar{p}}}{dt}(E_{\bar{p}}, T_{e^+}) - \frac{1}{\tau_c} (T_{e^+} - 4.2), \end{aligned} \quad (5.3)$$

where  $f(E_{\bar{p}})$  is the fraction of time that an antiproton of axial energy  $E_{\bar{p}}$  spends in the positron cloud,  $N_{\bar{p}}$  is the number of antiprotons that overlap with a positron cloud containing  $N_{e^+}$  positrons,  $k$  is Boltzmann's constant, and  $\tau_c$  is the cyclotron cooling time constant of the positrons ( $\approx 0.1$  s). The factor  $N_{\bar{p}}/N_{e^+}$  accounts for the fact that we use many antiprotons, rather than just one, and for the finite heat capacity of the positron cloud [58]. The fraction of time that antiprotons spend in the positron cloud is determined by numerically integrating the equations of motion in the axial direction as a function of axial energy (Fig. 5.12). For this calculation, the modification of the potential due to the presence of the positron cloud is neglected, since this only becomes important at low axial energies.

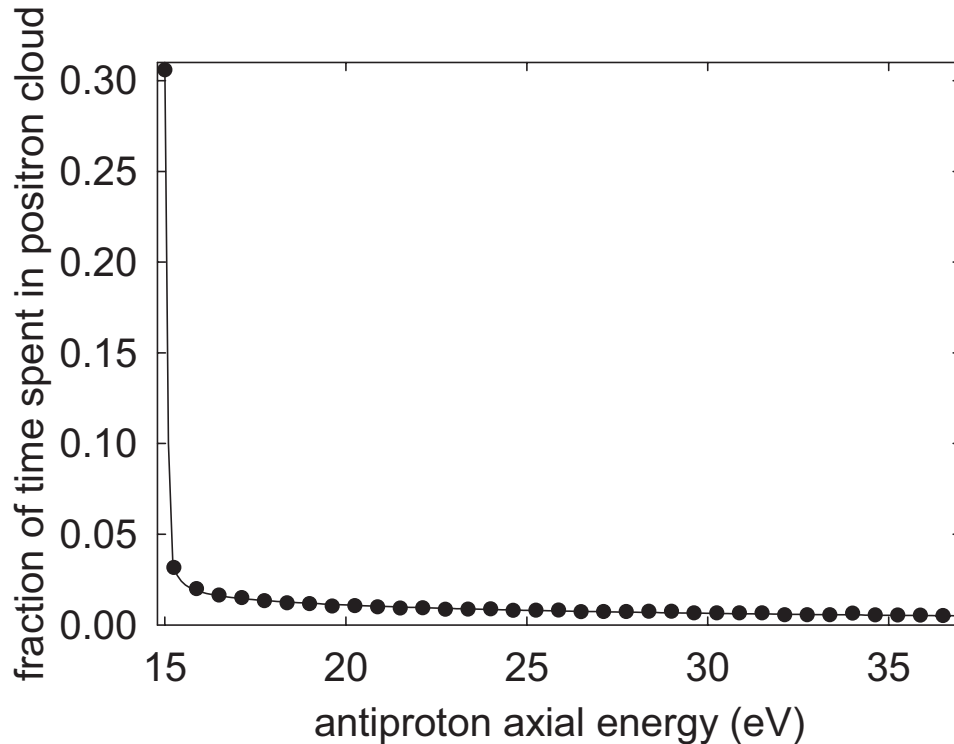


Figure 5.12: The fraction of time that antiprotons spend in a plasma of 200,000 positrons. The solid curve is a 4 parameter fit to the data that is used to incorporate it into the cooling time calculation.

In evaluating the cooling rate, one must select a value for  $\rho_{max}$ , the maximum impact parameter for a collision that can transfer axial energy from an antiproton to a plasma positron. Different values of  $\rho_{max}$  pertain to different physical processes within plasmas. For example,  $r_c$ , the cyclotron radius of a plasma particle, is the value of  $\rho_{max}$  relevant for the equipartition of energy within a plasma [30], while  $\lambda_D$ , the Debye length, is the value of  $\rho_{max}$  that describes cross field transport of energy and particles within a plasma [64]. It was initially suggested [65] that the appropriate value to describe the positron cooling of antiprotons would be the positron cyclotron radius. However, we believe that the Debye length of the positron plasma is a better choice. Collisions with  $\rho_{max} < \lambda_D$  can change the velocities of the particles parallel to the magnetic field and for impact parameters beyond  $\lambda_D$ , the Coulomb interaction between two particles is screened out. Thus, it seems that collisions with  $\rho_{max} < \lambda_D$  will be able to transfer axial energy from antiprotons to positrons and thus, contribute to the cooling.

To test this hypothesis, the predicted and observed cooling rates are compared in Fig. 5.13 for several values of  $\rho_{max}$ . Choosing  $\rho_{max} \lesssim 3r_c$  yields a predicted cooling time of  $\approx 1000$  s. For  $\rho_{max}$  near  $r_c$ , the cooling rate is low near a positron temperature of 4.2 K but increases rapidly thereafter. With  $\rho_{max} \lesssim 3r_c$  the initial cooling does not heat positrons sufficiently to access the higher cooling rate. The best agreement to both the 15 V and 10 V data is given by  $\rho_{max} \approx \lambda_D$ , although it can be seen from Figs. 5.13c-f that increasing  $\rho_{max}$  much beyond  $100r_c$  changes the predicted cooling rate only slightly. Thus, it appears that the appropriate choice of  $\rho_{max}$  for this process is close to the Debye length of the positron plasma. The authors of [65] now agree.

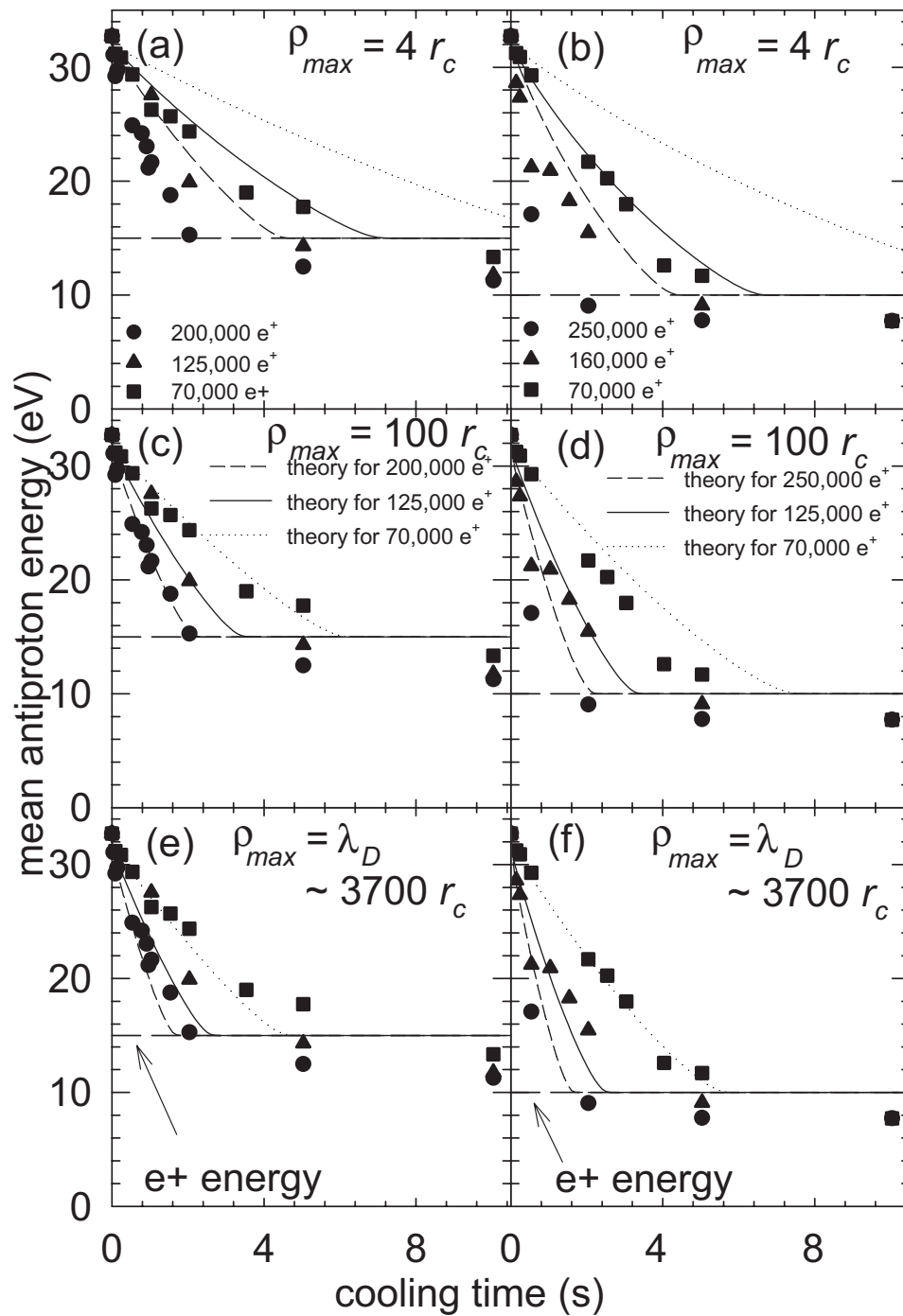


Figure 5.13: The antiproton cooling rate measured compared to that predicted by [62] (solid curves) for various values of  $\rho_{max}$ .

The solutions of the rate equation with  $\rho_{max} \approx \lambda_D$  (Fig. 5.14) have substantially altered our view of what occurs during the positron cooling of antiprotons. The initial cooling rate is rather high (Fig. 5.14e,f), which leads to rapid heating of the positron cloud (Fig. 5.14c,d). This heating sharply reduces the initial cooling rate. Eventually, the energy being emitted by the positrons via synchrotron radiation becomes larger than that being gained from the antiprotons and the positron temperature begins to decrease. However, the reduction of the antiproton energy ensures that the cooling rate also decreases. Finally, as the antiprotons near the energy level of the positrons there is little energy left to be transferred to the positrons and the positron temperature falls sharply. Increasing  $\rho_{max}$  increases the cooling rate (Fig. 5.14e,f). But increasing the cooling rate results in more energy being transferred to the positron cloud and thus a higher maximum positron temperature (Fig. 5.14c,d). This counteracts the higher cooling rate to a large extent, resulting in similar predicted cooling times for the two values of  $\rho_{max}$  displayed. This makes it difficult to use such data to choose between  $\rho_{max} = 100r_c$  and  $\rho_{max} = \lambda_D \approx 3700r_c$  although clearly,  $\rho_{max} > 100r_c$ , and  $\lambda_D$  seems the most plausible choice.

During these cooling studies, the positrons temporarily reach a temperature much higher than the 4.2 K of the Penning trap, inhibiting recombination, since the three-body recombination rate scales as  $T_{e^+}^{-9/2}$  [7]. Although it is likely that this simply ensures that little antihydrogen is produced until the antiprotons cool to low energies (Sec. 6.3), experiments seeking to produce antihydrogen should be designed to keep the positron temperature close to that of the surroundings. This can be achieved by keeping the initial antiproton energy as low as possible and the ratio of positrons

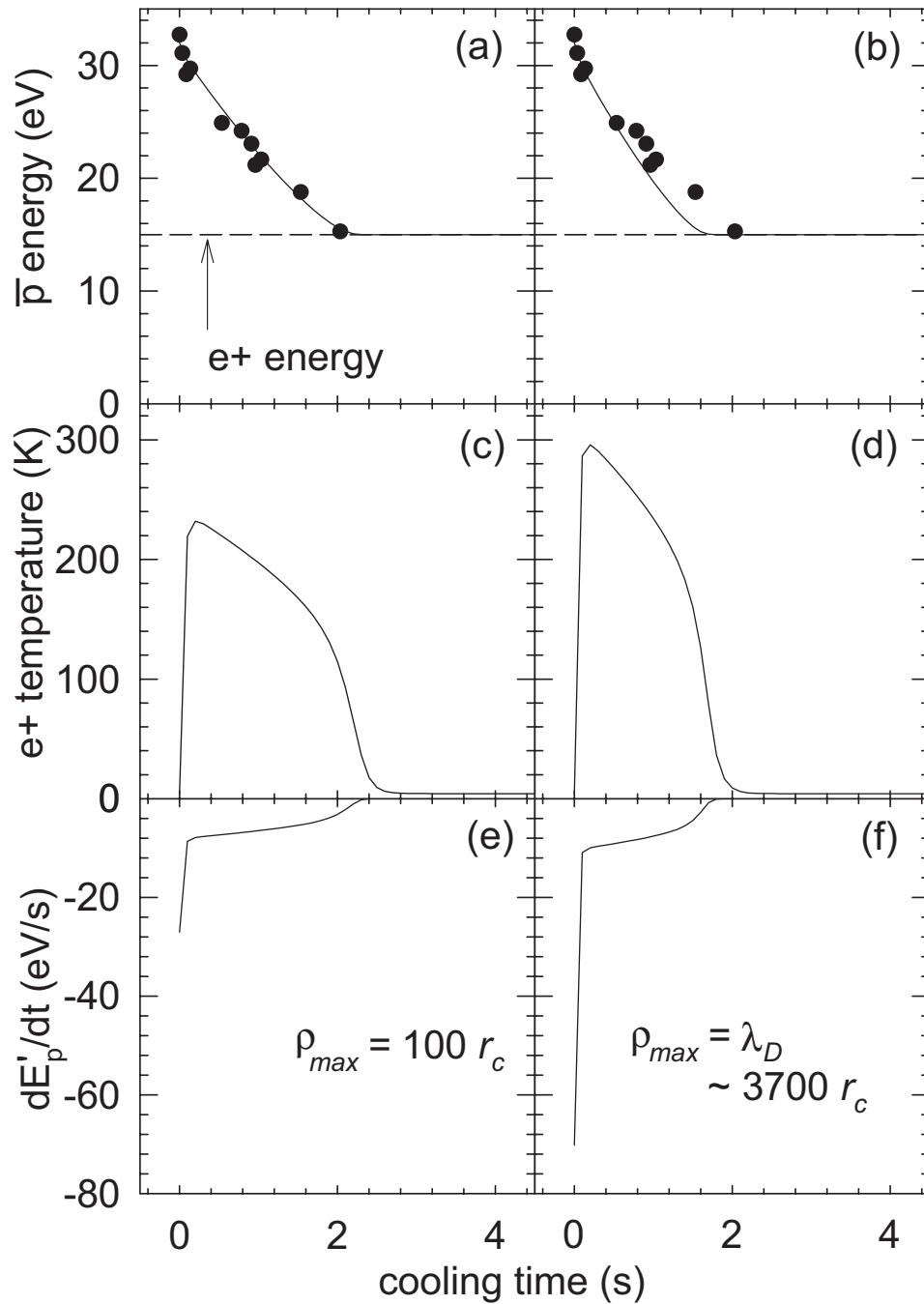


Figure 5.14: (a),(d) Antiproton energy as a function of interaction time. (b),(e) As energy is transferred from the antiprotons to the positrons, the positron temperature increases. (c),(f) The cooling rate, adjusted for the fraction of time that the antiprotons spend in the positron plasma.

to antiprotons as high as possible. One approach to reducing the initial antiproton energy is to gently drive antiprotons from the side wells of the nested Penning trap through the positron cloud [60, 28]; the antiprotons then have a low energy relative to the positrons.

## 5.4 Recycled evaporative cooling

Interesting and unexplained structure is seen in Fig. 5.9a-f, with the antiprotons tending to linger at energies near that of the central well and a “gap” appearing in the energy spectrum above the central well. Also, it can be seen that antiprotons cool below the level of the positrons in the side wells of the nested Penning trap. Initially, this was an unexpected result; once an antiproton has cooled below the positrons it has no way of losing energy by itself. Instead, this effect seems to be due to a collisional redistribution of axial energy amongst the antiprotons. Antiprotons that gain axial energy from collisions can be cooled again by the positrons, resulting in a net reduction of axial energy that we term recycled evaporative cooling.

Another signature of recycled evaporative cooling is that antiprotons can be found in a side well sometime after that side of the nested Penning trap has been analyzed. As the cooling progresses antiprotons cool into both side wells. If one of these is emptied, collisions amongst the antiprotons in the other side well can result in particles having enough axial energy to pass through the positron plasma again and cool into the emptied side well. This could not occur if the additional loss of axial energy was due simply to inefficient ejection of the electrons used to initially cool the antiprotons. Although the collisional energy redistribution results in some antiprotons

continuing to interact with the positron plasma, most antiprotons “sink” into the side wells before they can recombine with a positron. Thus, this effect is detrimental to recombination, but it does indicate that some antiprotons maintain contact with positrons for longer times.

The collisional axial energy redistribution is seen even without positrons present in the nested Penning trap. Fig. 5.15b displays the axial energy spectrum that results when 100,000 antiprotons are held in a nested Penning trap for 95 s with no positrons present in the central well. For comparison, Fig. 5.15a is the result if positrons are placed in the central well. Note that there is an unexplained “gap” above the central well energy as before, both with and without positrons. Also, note that when there are no positrons present the antiproton energy spectrum extends to the top of the outer well. By the collisional redistribution, some antiprotons have gained axial energy, while others have lost it. It is clear that axial energy has not been conserved in the case without positrons; the average axial energy is less than the injection energy. As will be discussed in the next section, particles are being lost from the nested Penning trap, some evaporate over the top of the well and some escape radially. Even if all the loss were over the top of the well, it would not be sufficient to account for the reduction in total axial energy seen in Fig. 5.15b. This may be because energy has been transferred to the cyclotron motion of the particles. Collisions exchange axial energy amongst antiprotons, but can also transfer energy from the axial motion to the cyclotron motion.

Collisions are most likely to occur between antiprotons with similar velocities [64]. This effect is demonstrated in Fig. 5.16. Antiprotons are loaded in two bunches of

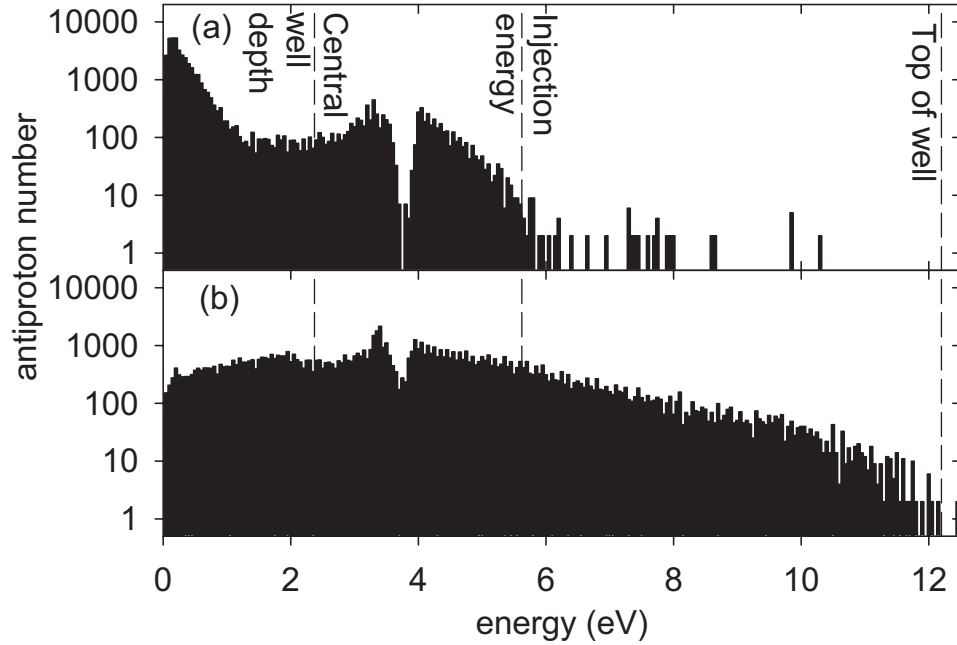


Figure 5.15: Antiproton axial energy spectra taken (a) with and (b) without positrons in the central well.

similar size. In Fig. 5.16a, one bunch is placed in the side well of a nested Penning trap, while the other is launched into the nested Penning trap with about 22 V of axial energy. It can be seen that the two bunches are well separated in axial energy. When the axial energy spectrum is obtained 45 s after the second bunch was launched, the effect of antiproton-antiproton collisions is clearly visible; the second bunch has a very large axial energy spread. Fig. 5.16b offers a comparison. This spectrum is the superposition of two independent experiments. In the first, a bunch of particles is held in the side well of a nested Penning trap for 45 s, while in the second a bunch of antiproton is injected into an empty nested Penning trap with about 22 V of axial energy and held for 45 s. Figs. 5.16 a and b look very similar, confirming that antiproton-antiproton collisions are more likely to occur between particles with similar axial energy. The average energy of the cold portion in Fig. 5.16a is slightly

higher than that in Fig. 5.16b, while the average energy of the hot portion of Fig. 5.16a is slightly lower than that in Fig. 5.16b, suggesting that there has been some axial energy transfer between the hot and cold bunches in Fig. 5.16a. However, this effect is small compared to the energy redistribution that has occurred amongst the hot antiprotons.

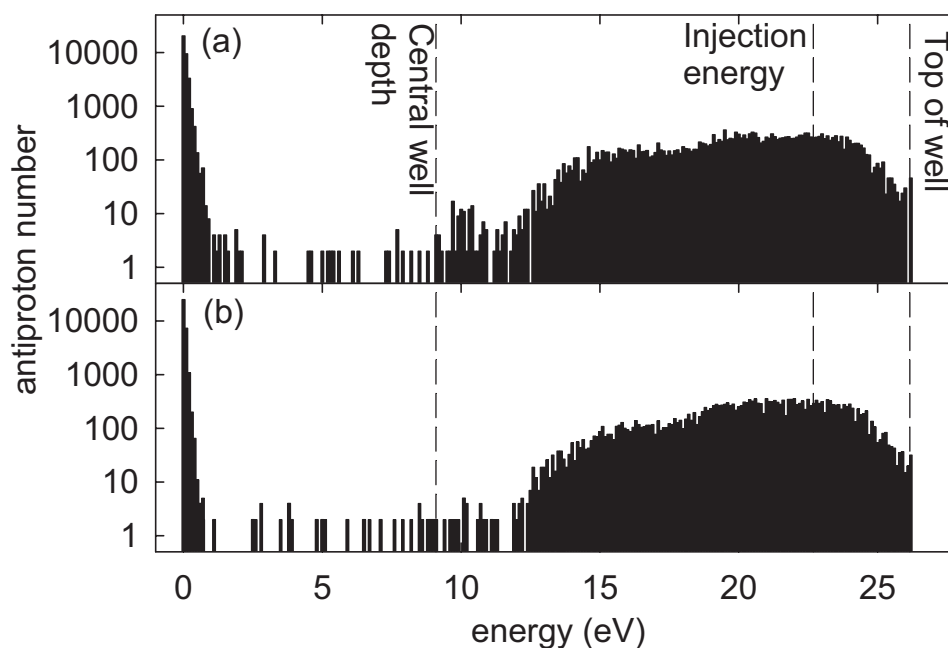


Figure 5.16: (a) Antiproton axial energy spectra resulting from the interaction of a bunch of antiprotons placed in a side well with a bunch of antiprotons launched into the nested Penning trap. (b) Superposition of two independent antiproton axial energy spectra, one from launching a bunch into an otherwise empty nested Penning trap, the other from a bunch placed in a side well.

## 5.5 Particle loss from the nested Penning trap

Any antihydrogen formed in a nested Penning trap would not be confined by the trapping fields, and would thus be lost against the matter walls. This would

be a desirable form of loss. However, we observe antiproton loss from the nested Penning trap even when no positrons are present. The integrated loss that results from injecting 100,000 antiprotons into the nested Penning trap shown in Fig. 5.17 is displayed as Fig. 5.18. With positrons present, the loss begins immediately, quickly reaches a peak, and then diminishes. Without positrons, antiproton loss begins slowly many seconds after injection into the nested Penning trap and builds up to a nearly constant rate. It is important to note that when antiprotons are placed in the side wells of this nested Penning trap no loss is observed.

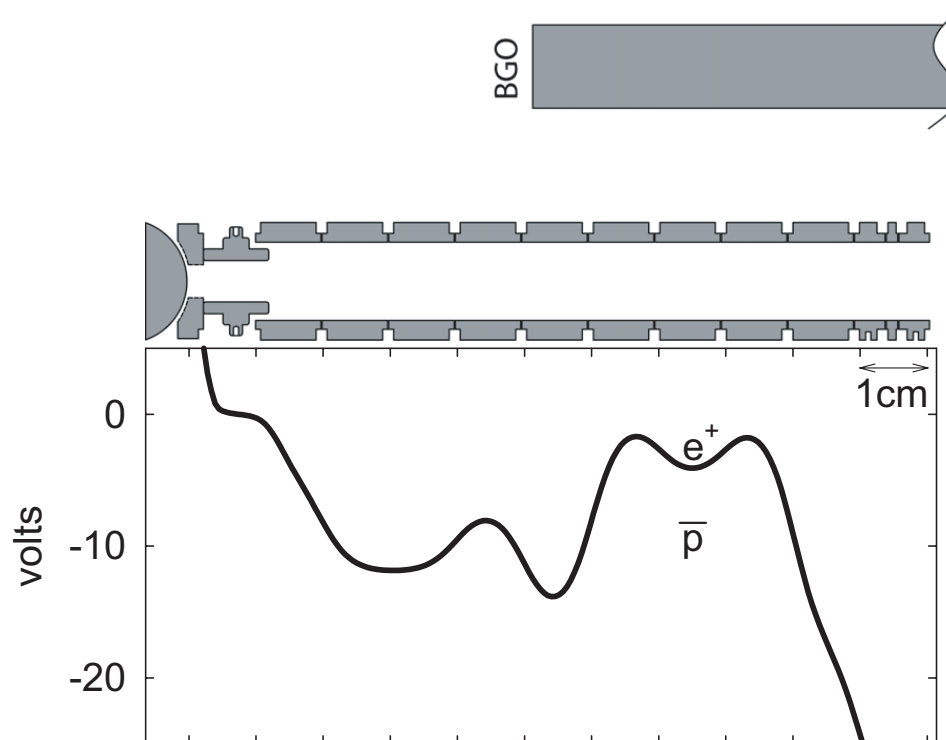


Figure 5.17: Nested Penning trap used to localize the antiproton loss.

Knowledge of the form of the loss, i.e. whether the loss is axial (e.g. particles leaving over the top of the outer well along magnetic field lines) or radial (particles

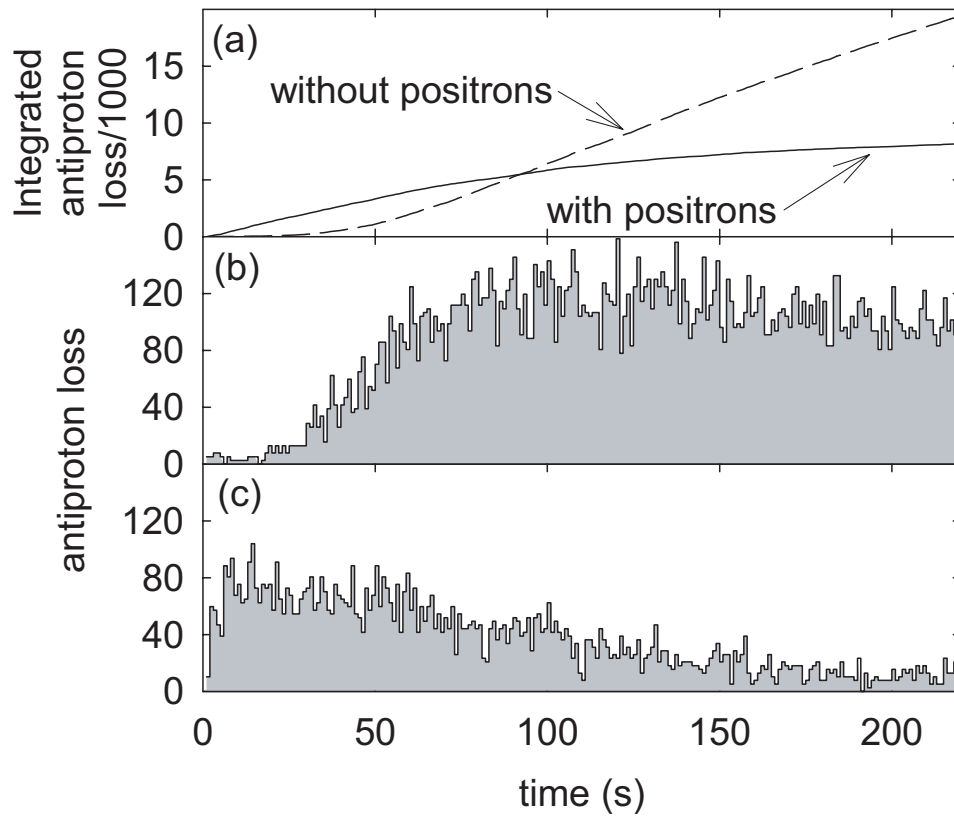


Figure 5.18: (a) Integrated antiproton loss. Antiproton loss per second (b) without and (c) with positrons.

moving perpendicular to the magnetic field and striking the trap electrodes), was desired as this could help determine the cause of the loss and also has important consequences for the detection of antihydrogen (Sec. 6.1.1). The form of the loss was determined using the multi-segment BGO detector. If an antiproton is lost in a region that is within the BGO detector, many BGO crystals will be hit and the event will have a high multiplicity. If the particle is lost outside the BGO detector, the event will have a low multiplicity. The potential structure used is shown in Fig 5.17, as is the relative position of the BGO detector. Any particles lost axially must move to the left and strike the end with poor BGO coverage, whereas radial loss within the nested Penning trap has good coverage, thus providing maximum contrast.

To calibrate the position sensitivity, we intentionally dump particles axially and radially. The resulting multiplicity spectra are shown in Fig. 5.19a-b. As expected, antiprotons dumped axially give a spectrum that is centered on a lower multiplicity than those dumped radially. The multiplicity spectra of the loss seen in Fig. 5.18 are shown in Fig. 5.19c (without positrons) and Fig. 5.19d (with positrons). Comparison with the calibrations reveals that the loss from the nested Penning trap is predominantly radial in each case.

The observation of the loss described above suggests that it is associated with some feature of the nested Penning trap at an axial energy lower than the energy with which antiprotons are injected. First, the loss is mostly radial, which is to say that it is not simply due to antiprotons acquiring enough axial energy to leave over the top of the outer well. Second, consider the time structure of the loss with and without positrons. Without positrons, the loss takes many seconds to begin, suggesting that

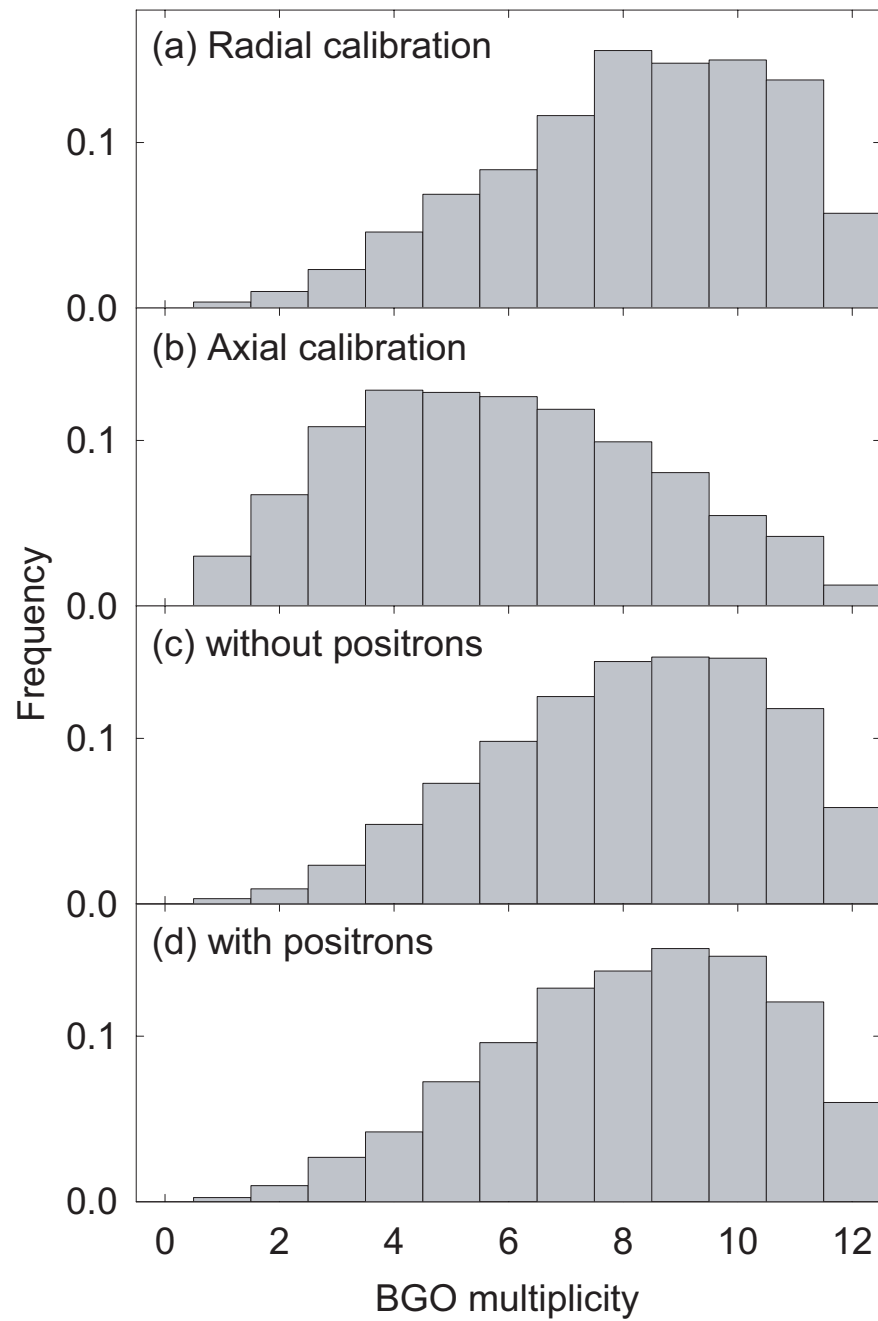


Figure 5.19: BGO multiplicity spectra.

this much time is needed for antiprotons to reach the axial energy at which the trap is lossy. This is consistent with the energy spectra shown in Fig. 5.15. It is clear that it takes longer for antiprotons to move to lower axial energies without positrons than it does with them. In addition, it can be seen that the loss with positrons tapers off, suggesting that by this time most antiprotons have moved through the lossy region of the nested Penning trap. By contrast, the loss without positrons stays steady at a higher rate than that with positrons. This is consistent: As the rate at which the axial energy changes is lower without positrons, any given antiproton will spend longer in the lossy region, and thus have a greater chance of being lost. The loss rate stays high as all the particles can not cool into the side wells.

The region that is lossy could be identified by taking many “snapshots” at different times, as was done in Fig. 5.9, without positrons present in the central well and correlating the time at which the loss begins to a particular axial energy. Due to the limited availability of antiproton beam time, these experiments have yet to be done.

# Chapter 6

## Production and Detection of Cold Antihydrogen

Having studied the interaction of positrons and antiprotons in the nested Penning trap, we apply the knowledge gained to our main goal: producing cold antihydrogen. Antihydrogen was produced during the positron cooling experiments of Ch. 5, but here we describe the unambiguous way in which we detect it. For reasons to be discussed, identifying antihydrogen via its annihilation products was not possible in this apparatus. Instead, a detection technique was developed that utilized field ionization, much in the same way that it was utilized to accumulate positrons.

### 6.1 Antihydrogen detection

The most simple scheme for detecting the production of antihydrogen in a nested Penning trap would be as follows: mix positrons and antiprotons as described in

Sec. 5.3, and watch for antiproton annihilations. As a control, one would repeat the experiment without positrons, and hope to observe no antiprotons leaving the nested Penning trap. One then assumes that there is no mechanism that can cause antiprotons to leave the nested Penning trap with positrons present, other than antihydrogen.

However, as we have already seen (Sec. 5.5), antiprotons leave the nested Penning trap even when no positrons are present and even if that were not the case there are potential loss mechanisms other than antihydrogen (e.g. ambipolar diffusion [66]). While one could imagine that all the loss observed with positrons is due to antihydrogen, this is not so, since similar loss occurs without positrons. Thus, more sophisticated detection techniques are required.

### 6.1.1 Antihydrogen detection using annihilation detectors

Since antiprotons leave the nested Penning trap even with no positrons present, to detect antihydrogen with annihilation detectors we must be able to distinguish between the annihilation of an antiproton and an antihydrogen atom. That is, we must be able to detect the annihilation of an antiproton and a positron in spatial and temporal coincidence. However, this is a difficult task, since the annihilation of an antiproton releases  $\approx 2$  GeV of energy and thus can create many other particles, including positrons. Thus, one must be able to distinguish between positrons produced by antihydrogen annihilations and antiproton annihilations.

To do this on an event-by-event basis, a detector with sufficient spatial resolution to accurately determine the locations at which antiprotons and positrons annihilate

is required. Antiproton annihilations will produce positrons via pair production from high energy  $\gamma$ -rays. These  $\gamma$ -rays are produced at the annihilation site, either from the decay of  $\pi^0$  mesons or from the de-excitation of a daughter nuclei produced when an antiproton annihilates on a heavy nuclei. The distance from the antiproton annihilation site that an electron-positron pair will be created depends upon the amount of material that the  $\gamma$ -ray traverses and the  $\gamma$ -ray energy. To be able to distinguish between positron annihilations due to antihydrogen and those simply due to antiprotons, the spatial resolution of the detector must be higher than the average distance that a  $\gamma$ -ray travels before conversion.

The detector installed in our apparatus does not provide the  $< 1$  cm spatial resolution along the magnetic field direction that would be needed to make clean observations of antihydrogen. The fiber detector is unable to localize antiproton annihilations on an event-by-event basis, primarily due to the large number of particles produced when an antiproton annihilates. On average, 5 fibers are hit during an antiproton annihilation. Since the twisted fibers cross many straight fibers, this many hits yields several possible hit locations, making accurate localization difficult.<sup>1</sup>

Antihydrogen detection by this method has been demonstrated by ATHENA [9]. In this experiment, positrons and antiprotons are mixed in an identical fashion to that suggested in [7] and first demonstrated in [61, 8]. They employ a detector with a resolution of  $\pm 8$  mm and  $\pm 5$   $\mu$ s for both antiproton and  $\gamma$ -ray detection. Only a small fraction of antiproton annihilations will also produce a positron annihilation in this range (Ap. B).

---

<sup>1</sup>Combining the results of many antiproton annihilations can yield a rough average  $z$  position, similar to that obtained using the BGO detector [67].

Of course, this must be verified experimentally. In particular, control experiments using no positrons are essential. We have seen that radial antiproton loss can occur in a nested Penning trap without positrons, implying that such radial loss of antiprotons alone is also likely to occur with positrons present. Thus, control experiments that explicitly dump antiprotons radially must be carried out. If such controls produce no antihydrogen signal, while mixing of positrons and antiprotons does, then it is likely that antihydrogen has been produced. In the ATHENA report [9] it is not stated that such controls were completed, but hopefully these will be reported soon.

### 6.1.2 Antihydrogen detection via field ionization

To detect antihydrogen, we take advantage of a property of the expected recombination mechanism, three-body recombination (TBR). As discussed in Sec. 1.3, atoms produced via TBR are initially expected to be in weakly bound states. By placing an ionization well, similar to that used to accumulate positrons (Sec. 3.2.1) adjacent to the nested Penning trap, we can field ionize any weakly bound antihydrogen that might be travelling along the axis of the Penning trap. Careful design of the ionization well structure ensures that the antiproton from the antihydrogen remains trapped in a Penning trap well, and that no other antiprotons can become trapped in that well.

We can detect antiprotons in a well with essentially no background by performing a low voltage ramp (LVR). The voltage ramp has a duration of less than 20 ms and “trigger” counts (Sec. 2.2.4) are recorded. Because of the short duration of the ramp and low background count rate of the “trigger” combination (1 per second), this is a very sensitive measurement – even a single antiproton, and thus antihydrogen, can

be reliably detected.

## 6.2 Antihydrogen production experiments

### 6.2.1 Potential structure used for antihydrogen production

The centerpiece of the antihydrogen production and detection potential structure (Fig. 6.1) is, of course, a nested Penning trap [7]. The central well for positrons is relatively deep, which yields a high positron density ( $\approx 5 \times 10^7 \text{ cm}^{-3}$ ). This is advantageous for recombination, since the TBR rate scales as  $n^2$ . Care must be taken not to make the central well too deep, since the applied trapping electric fields can also strip antihydrogen atoms before they reach the ionization well.

Although these experiments were conducted before the analysis of Sec. 5.3 was completed, one of the lessons learned was anticipated. Compared to the cooling studies, the offset well from which the antiprotons are launched into the nested Penning trap is placed at a potential close to that of the positron well. This was done so that antiprotons will have less energy that needs to be extracted via the positrons, and the positrons will be heated less.

An ionization well is placed adjacent to the nested Penning trap. Close examination of Fig. 6.1 and numerical modelling [68] reveals that antihydrogen atoms that are stripped by a field of less than 20 V/cm will be destroyed before they leave the nested Penning trap, while those that are stripped by a field between 35 V/cm and 95 V/cm will deposit an antiproton in the ionization well. It should be noted from Fig. 6.1b that the “lip” of the ionization well (electrode T8) is at a lower potential

than the “lip” of the nested Penning trap (electrode T3). This is an essential feature for the success of the field ionization detection method – it ensures that any antiprotons that gain enough axial energy to leave the nested Penning trap travel to the left after only one pass, away from the ionization well. And even in the unlikely event that an antiproton gained enough axial energy to reach the ionization well, there is no mechanism that could remove enough energy from it in one pass for it to become trapped. Further, when positrons are placed in the central well, antiproton energies will tend to be reduced. This makes it even more difficult to get antiprotons into the ionization well by any means other than ionization of antihydrogen.

Two electrodes (T7 and T8) are used to form the potential barrier between the nested Penning trap and the ionization well. This configuration smooths the electric field that atoms traverse when leaving the nested Penning trap, while still allowing the ionization well “lip” to be at a lower potential than that applied to electrode T3. The potential applied to T7 and T8 is chosen so that the electric field is of the same magnitude as that found inside the nested Penning trap. This provides the maximum potential difference between T3 and T8, while not ionizing any additional antihydrogen atoms before they reach the ionization well. The effect of placing more electrodes between the ionization and production well is examined in Sec. 6.2.4.

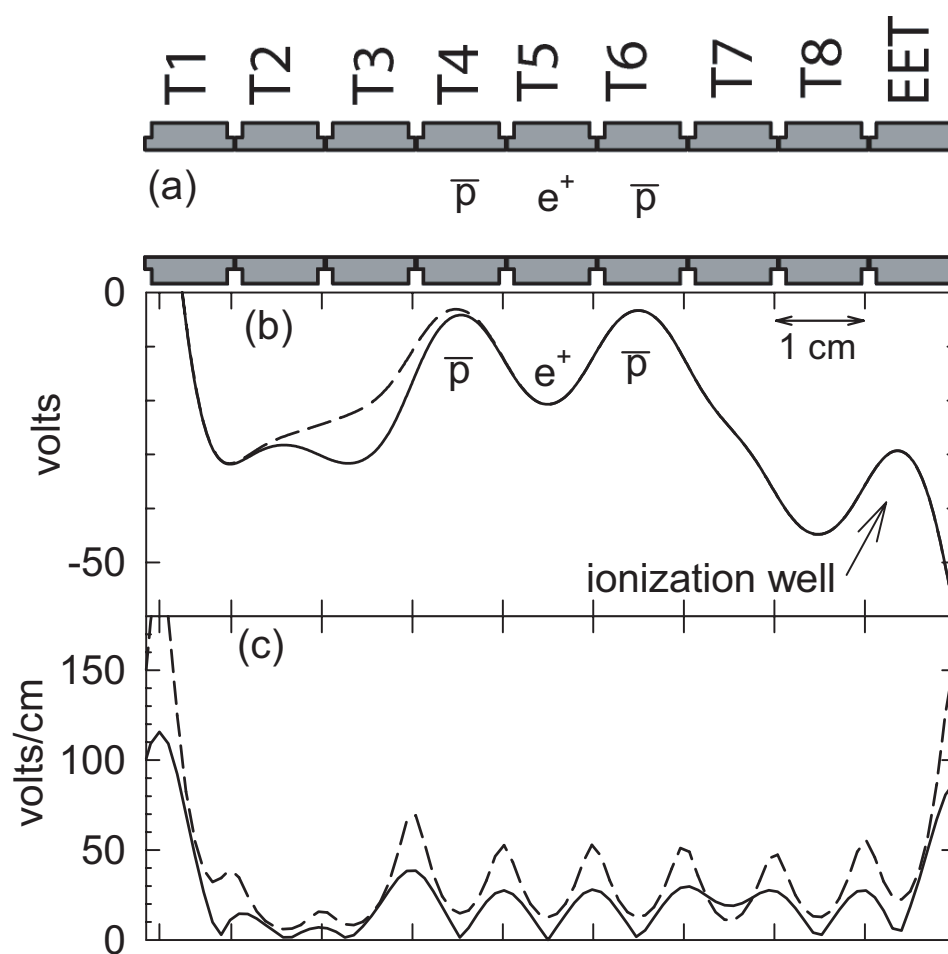


Figure 6.1: (a) Electrodes used in antihydrogen production experiments. (b) Potentials structure used to produce antihydrogen. Antiprotons are introduced into the nested well by pulsing open an offset well (dashed line). (c) Electric field magnitude on the axis of the Penning trap (solid) and 4 mm off axis (dashed).

## 6.2.2 Cold antihydrogen production

Having designed the potential structure, particles were introduced. Typically, 150,000 antiprotons were released into the nested Penning trap using a voltage pulse, while positrons were placed in the central well in advance. The positron numbers used varied between 0 and 1.7 million. During the interaction time of  $\approx 120$  s, antiproton loss from the nested Penning trap was observed. To ensure that this loss did not affect the interrogation of the ionization well, all particles remaining in the nested Penning trap were dumped to the ball valve. Thus, when a LVR was applied to the ionization well, the background “trigger” count rate was only that intrinsic to the detectors (1 per second). Given that the voltage ramp length is only 20 ms, we would expect a background count in the ramp window only once every 50 trials.

Displayed in Fig. 6.2 is the sum of all antiproton counts observed as the ionization well is ramped open, both with and without positrons present in the central well. The data represents 11 trials with positrons and 6 without. Note that no counts are observed without positrons – the carefully designed potential structure ensures that only antihydrogen atoms can deposit antiprotons in the ionization well and the antihydrogen detection method is completely free of background. While we have no direct measure of the temperature of these atoms, it can be no more than that corresponding to the initial axial energy of the antiprotons in the nested Penning trap (6 eV). It is appropriate to describe these atoms as cold, as their kinetic energy is very much less than any observed in previous accelerator experiments [16, 17]. Indeed, there are indications (to be discussed below) that the energy of the produced antihydrogen is much less than the initial antiproton energy.

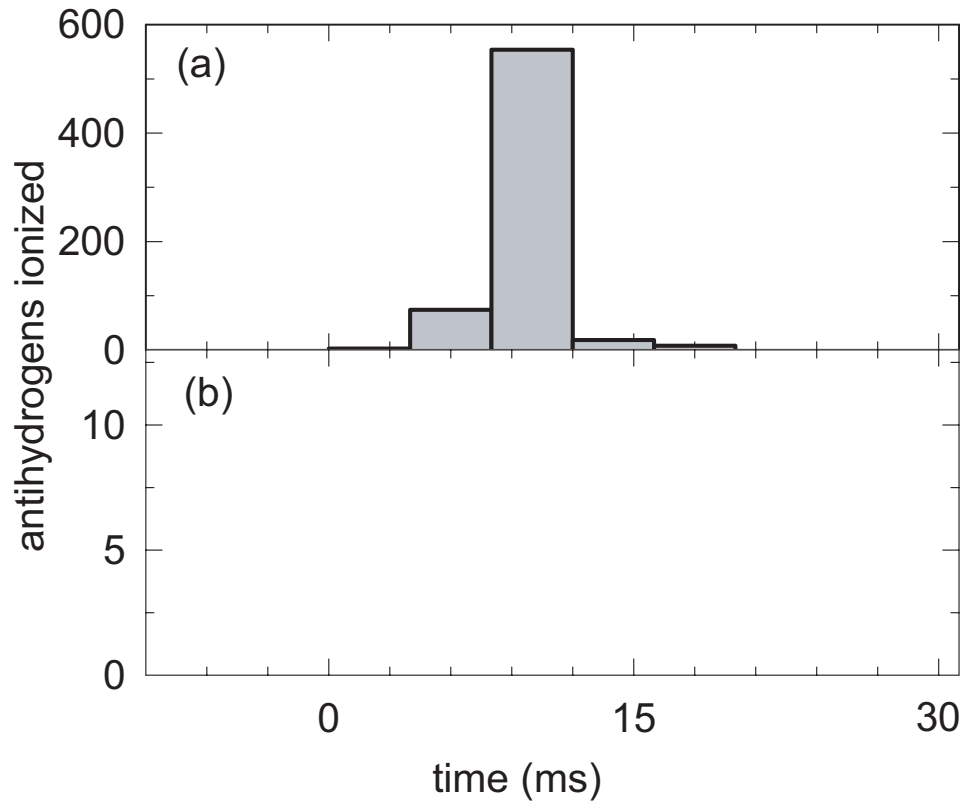


Figure 6.2: 657 antiproton (antihydrogen) counts seen in the ionization well with positrons (a) and zero seen without positrons (b). At the time this result was published [1], this was more than the total number of antihydrogen atoms that had been observed in all other experiments [16, 17, 9].

Taking the single most efficient trial as an example, we can examine the overall antihydrogen production efficiency that is being achieved. In a single trial using 148,000 antiprotons accumulated from 8 AD pulses and 430,000 positrons, 66 antihydrogen atoms were ionized. This corresponds to 8 antihydrogen atoms per AD pulse, and 1 antihydrogen per 2,200 antiprotons launched into the nested Penning trap. In contrast, the comparable values for the only similar experiment at the time [9] were  $1/4$  and  $1/12000$ . This production rate is likely limited by the antiproton–antiproton collisions, which cause the interaction of positrons and antiprotons to be

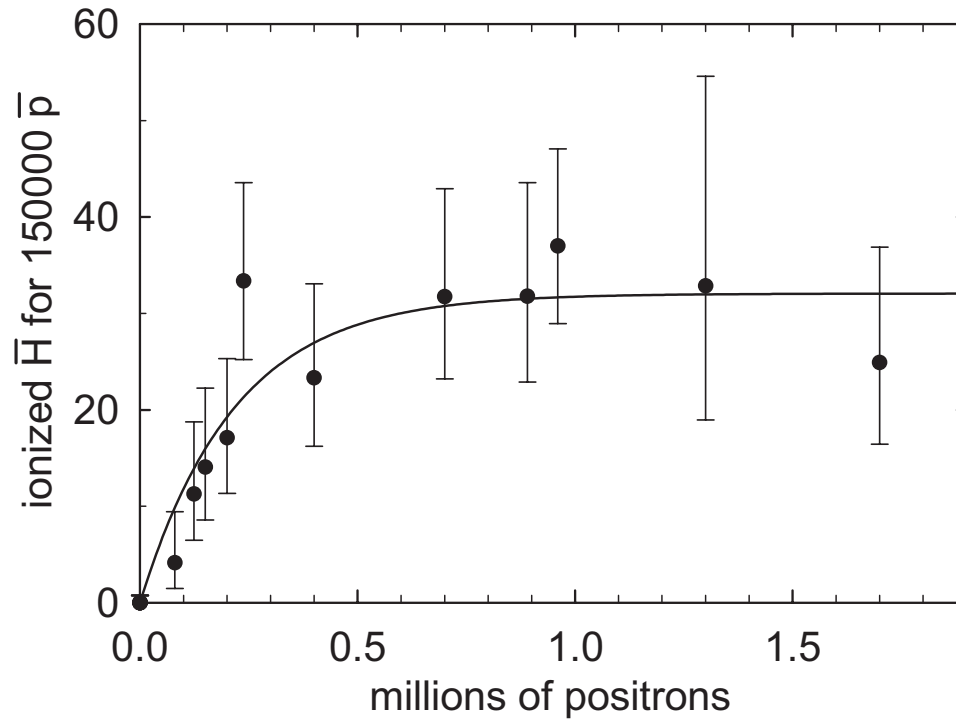


Figure 6.3: Dependence of antihydrogen production on positron number.

curtailed.

### 6.2.3 Dependence of antihydrogen production rate on positron number

The dependence of the antihydrogen production rate upon positron number was investigated (Fig. 6.3). Initially, the production rate increases but, at a positron number of  $\approx 0.5$  million it appears to saturate. This is somewhat surprising, since as the number of positrons is increased, the length of the positron cloud increases. This increases the interaction time of the positrons and antiprotons and thus, presumably the production rate.

### 6.2.4 Dependence of antihydrogen production rate on detection well distance

Because the momentum vector of any antihydrogen formed will be almost identical to that of the antiproton before recombination, the angular distribution of the antihydrogen will depend on the axial and radial velocity distributions of the antiprotons when recombination occurs. When the antiprotons are launched into the nested Penning trap, we expect the radial distribution to be at a temperature close to the 4.2 K (0.3 meV) of the cooling electrons, while the axial energy will be several eV. If recombination were to occur at this point, the antihydrogen produced would form a beam with low divergence. It is only at the very end of the cooling, as the antiproton axial temperature becomes equal to the radial temperature, that an isotropic distribution would be obtained. Hence, a definitive measurement of the angular distribution would be important, as it would allow a limit to be placed on the kinetic energy of the antihydrogen being produced. This is an important parameter for future experiments, as it determines how many antihydrogen atoms would be caught in a magnetic trap.

To investigate this aspect of the produced antihydrogen, the production rate was measured as function of the separation between the central well and the ionization well (Fig. 6.4). For these experiments, 125,000 positrons were placed in the central well. When the ionization well is moved to a distance further from the central well than that shown in Fig. 6.1, the intervening potential barrier is carefully shaped to keep the electric field at or below that found in the nested Penning trap.

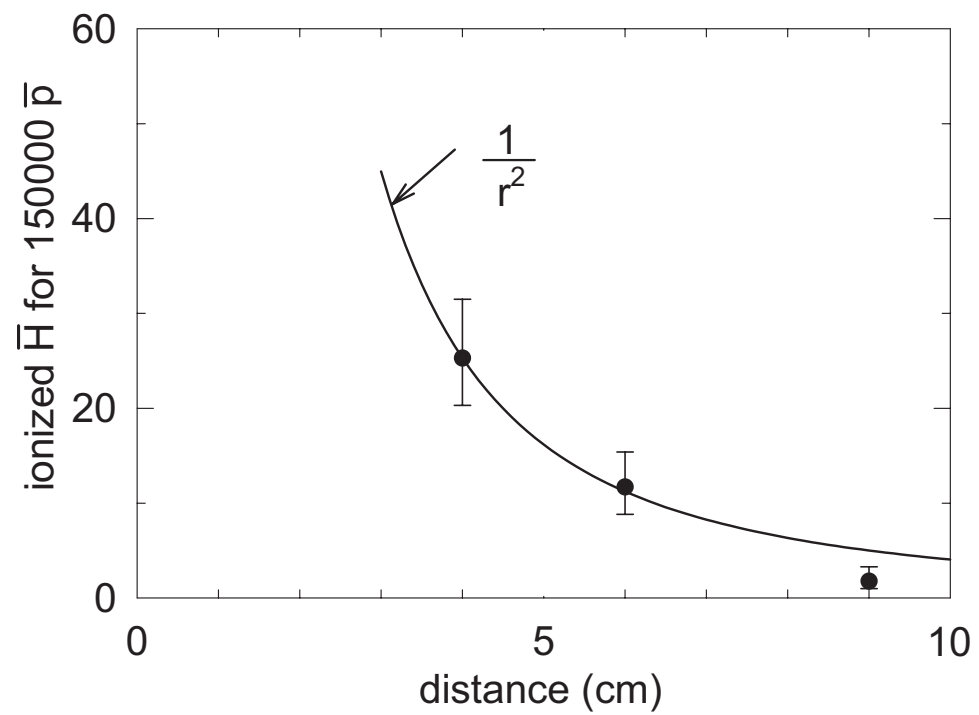


Figure 6.4: Detected antihydrogen number as a function of ionization well distance.

The amount of antihydrogen detected appears to vary as the inverse square of the distance to the ionization well, consistent with an isotropic distribution or a beam that is broad compared to the diameter of the ionization well. More detailed investigations would be required to distinguish between these two cases. Assuming the distribution is indeed isotropic, we can estimate the peak absolute production rate: The solid angle subtended by the ionization well in its closest position is  $4\pi/260$ ,<sup>2</sup> so that for the example described above,  $260/2200 \approx 12\%$  of antiprotons would be recombined to form antihydrogen.

To take the other extreme, we assume the antihydrogen is produced in a broad “beam” that has a radius of 5 mm at a distance of 4 cm, with a radial temperature of 4.2 K. The approximate axial energy of the antihydrogen is then 20 meV, or 270 K, and  $2/2200$  or 0.1% of antiprotons are converted to detectable antihydrogen.

### 6.3 Cooling rate analysis

The antihydrogen production results obtained above can be further investigated using the cooling theory described in Sec. 5.3. In particular, we can calculate the predicted rate at which the injected antiprotons are cooled by the positrons and thus, determine the fraction of time that the antiprotons spend in the positron cloud and the positron temperature as a function of interaction time. From these two parameters, we can calculate the predicted recombination rate as a function of interaction time or antiproton axial energy.

---

<sup>2</sup>This is a conservative estimate, assuming that particles can be held in the ionization well out to a radius of 5 mm.

The rate at which TBR is predicted to occur in a strong magnetic field is [24]

$$\alpha_{\text{TBR}} = 0.07 n^2 v_{th} R_T^5, \quad (6.1)$$

where  $n$  is the positron density,  $v_{th} = \sqrt{kT_{e^+}/m_{e^+}}$  is the positron thermal velocity, and  $R_T = e^2/4\pi\epsilon_0 kT_{e^+}$  is the Thompson radius or classical distance of closest approach. Equivalently, we can define the characteristic time required for TBR to occur

$$\begin{aligned} \tau_{\text{TBR}} &= 1/\alpha_{\text{TBR}} \\ &= 160 \mu\text{S} \left( \frac{T_{e^+}}{4.2 \text{ K}} \right)^{9/2} \left( \frac{10^8 \text{ cm}^{-3}}{n} \right)^2, \end{aligned} \quad (6.2)$$

expressed in experimentally convenient units. Approximately, the probability of an antiproton of axial energy  $E_{\bar{p}}$  recombining via TBR during a single pass through a positron plasma of length  $l$  is

$$p_{\text{single pass}}(T_{e^+}, n, l, E_{\bar{p}}) = \frac{t_{\text{single pass}}(l, E_{\bar{p}})}{\tau_{\text{TBR}}(T_{e^+}, n)}, \quad (6.3)$$

where  $t_{\text{single pass}}(l, E_{\bar{p}})$  is the time that it takes the antiproton to transit the positron cloud. Similarly, the probability of recombining after  $N$  passes through the positron cloud is

$$P_{N \text{ passes}}(n, l) = \sum_{i=1}^N \frac{t_{\text{single pass}}(l, E_{\bar{p}_i})}{\tau_{\text{TBR}}(T_{e_i^+}, n)}, \quad (6.4)$$

where  $E_{\bar{p}_i}$  and  $T_{e_i^+}$  are the antiproton axial energy and positron temperature during the  $i$ th pass through the cloud, respectively. Since the time for each pass ( $\approx 1 \mu\text{s}$ ) is small compared to the time over which the antiproton axial energy changes ( $\approx 1 \text{ s}$ ), we can replace the sum over the number of passes with an integral over the total interaction time. Of course, the antiprotons do not spend all their time in the positron

cloud, so we replace  $t_{\text{single pass}}(l, E_{\bar{p}})$  with  $f(l, E_{\bar{p}})dt$ , where  $f(l, E_{\bar{p}})$  is the fraction of time that an antiproton of axial energy  $E_{\bar{p}}$  spends inside a positron cloud of length  $l$  in the specified nested Penning trap. The probability of recombining in a time  $t_{\text{max}}$  is then

$$P_{\text{TBR}}(n, l, t_{\text{max}}) = \int_0^{t_{\text{max}}} \frac{f(l, E_{\bar{p}}(t))}{\tau_{\text{TBR}}(T_{e^+}(t), n)} dt. \quad (6.5)$$

Note that in Eqn. 6.5, the antiproton axial energy and positron temperature vary in time, just as these parameters were varied in the sum of Eq. 6.4. The kernel of integral is then the temporal distribution of the antihydrogen production:

$$p_{\text{TBR}}(n, l, t) = \frac{f(l, E_{\bar{p}}(t))}{\tau_{\text{TBR}}(T_{e^+}(t), n)}, \quad (6.6)$$

or more usefully we can express this as the energy distribution:

$$p_{\text{TBR}}(n, l, E_{\bar{p}}) = \frac{f(l, E_{\bar{p}})}{\tau_{\text{TBR}}(T_{e^+}(E_{\bar{p}}), n)}. \quad (6.7)$$

The variation of antiproton axial energy and positron temperature in time can be easily determined using the theory described in Sec. 5.3. To calculate the cooling rate, we require the positron cloud parameters (Fig. 6.5), the ratio of the number of positrons to antiprotons used (Fig. 6.6), the initial antiproton energy relative to the antiprotons (6 eV), and  $f(l, E_{\bar{p}})$ , which is determined by numerical integration as in Sec. 5.3. Using these parameters, we determine  $E_{\bar{p}}(t)$  and  $T_{e^+}(t)$  for each positron number used in the antihydrogen production experiments (see, for example, Fig. 6.7). Although the initial antiproton energy has been reduced compared to the cooling studies, the positron temperature is still predicted to be rather high ( $\approx 800$  K in most cases). This is because the ratio of antiprotons to positrons is higher in this case.

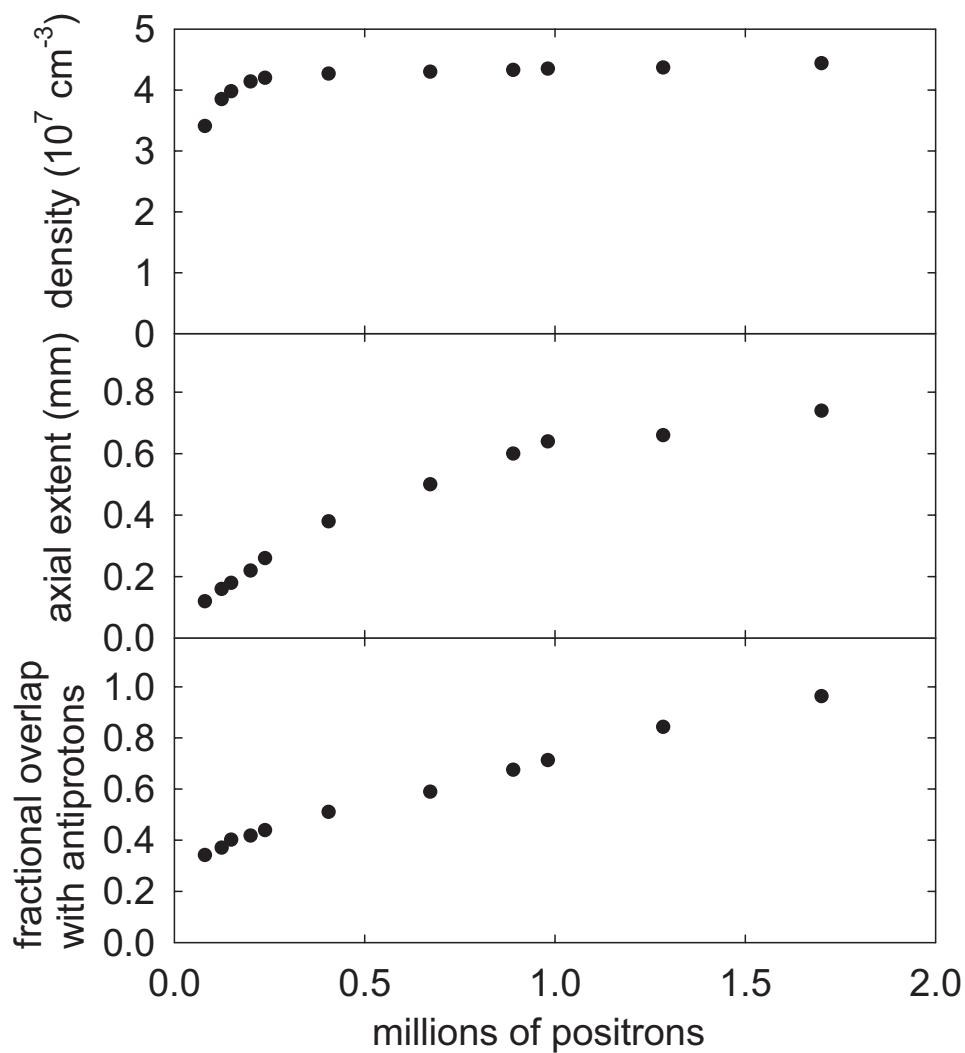


Figure 6.5: (a) Positron cloud density, (b) axial extent, and (c) overlap with a cloud of 150,000 antiprotons, as determined by P. K. Oxley, using the methods described in [59, 28].

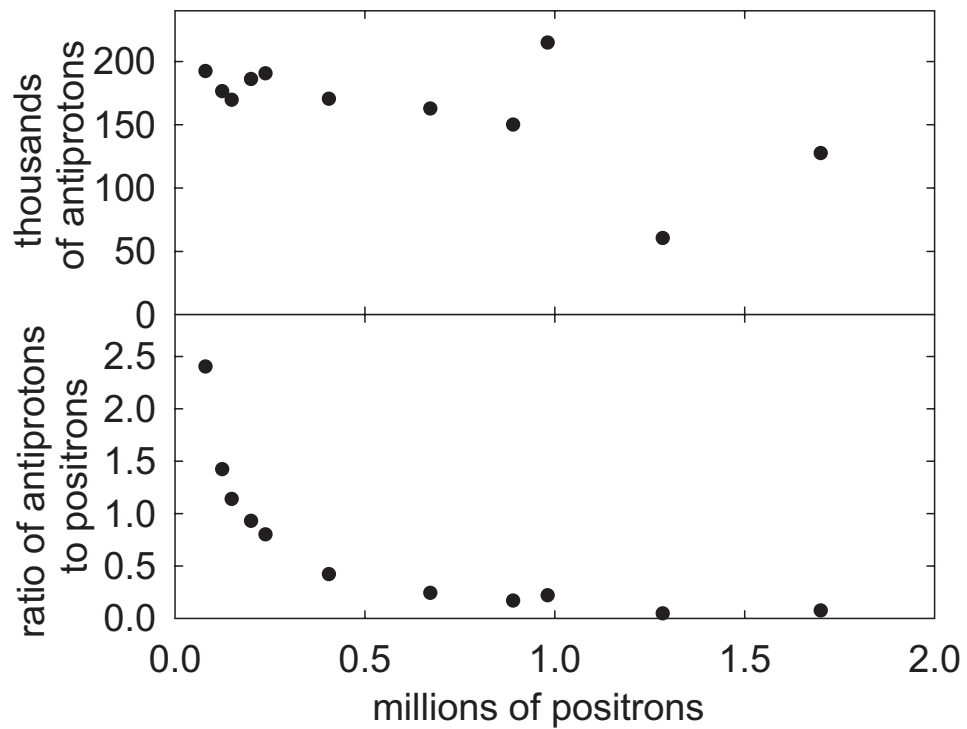


Figure 6.6: (a) The number of antiprotons and (b) ratio of number of antiprotons to positrons used in the antihydrogen production experiments.

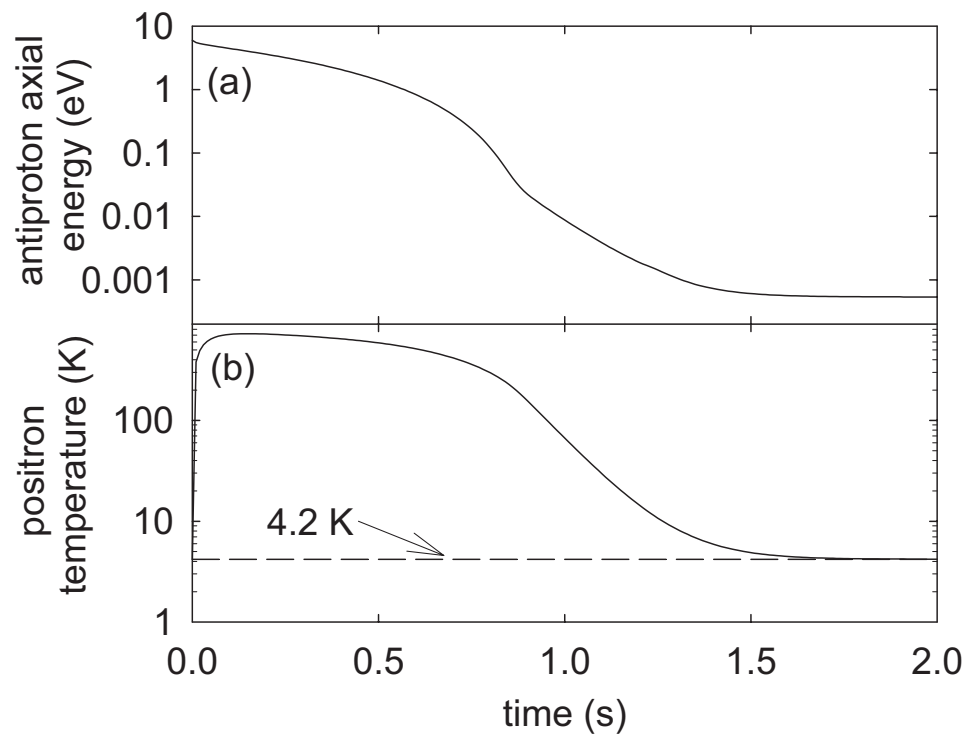


Figure 6.7: (a) The predicted antiproton energy and (b) positron temperature for 1.7 million positrons.

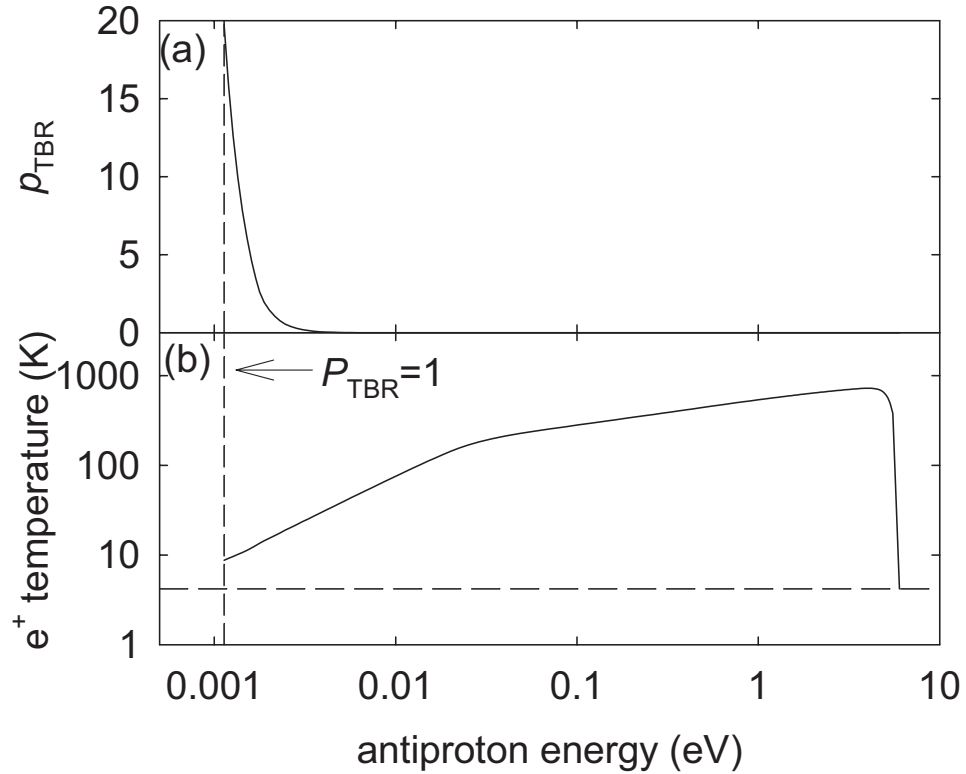


Figure 6.8: (a) The predicted recombination probability distribution and (b) positron temperature as a function of antiproton energy for 1.7 million positrons.

Inverting  $E_{\bar{p}}(t)$  yields  $T_{e^+}(E_{\bar{p}})$  and thus,  $p_{\text{TBR}}(n, l, E_{\bar{p}})$ . This is displayed for the 1.7 million positron case in Fig. 6.8. Results for other positron numbers are similar. It can be seen that the high positron temperature inhibits recombination during most of the cooling progression, due to the strong  $T_{e^+}^{-9/2}$  dependence of the recombination rate: It is only once the antiprotons have cooled to a low energy that the positrons cool sufficiently to make recombination likely. In this case the heating of the positrons by the high energy antiprotons is actually beneficial, as it “turns off” recombination until the antiprotons have a low energy, ensuring that cold antihydrogen is produced.

In the experiments described above, we can not measure  $p_{\text{TBR}}(E_{\bar{p}})$ , but rather  $P_{\text{TBR}}(t_{\text{max}})$ , the total probability that an antiproton will recombine during an interaction time of  $t_{\text{max}}$ . The appropriate choice of  $t_{\text{max}}$  is not clear. As we have seen above, most recombination is predicted to occur only at very low energies relative to the positron well, but we have also seen in Ch. 5 that collisions amongst antiprotons become important in this region. Thus, these collisions may mean that the appropriate  $t_{\text{max}}$  to use is that corresponding to an antiproton energy where little recombination occurs.

For an initial analysis,  $t_{\text{max}}$  is chosen so that  $P_{\text{TBR}}(t_{\text{max}}) = 1$ , i.e. the interaction time required for a single antiproton interacting with the positron cloud to definitely recombine.<sup>3</sup> The energy at which this occurs for the 1.7 million positron case is marked on Fig. 6.8. We can now determine average quantities using the distribution, e.g. the average antihydrogen axial energy is 25 K and the average positron temperature at which recombination occurs is 10.5 K. Note that we would not be able to make this prediction with the cooling rate theory developed in Sec. 5.3.

## 6.4 Extensions to the cooling rate analysis

There are several factors that have not been included in the above analysis. First, as mentioned above, antiproton-antiproton collisions appear to limit the positron-antiproton interaction time. It is interesting to note the variation of  $t_{\text{max}}$  with positron number (Fig. 6.9(a)). With fewer positrons present, the cooling to the lower relative en-

---

<sup>3</sup>Most recombined atoms will be too weakly bound to exit the nested Penning trap and travel to the ionization well, the effect of which will be discussed in the next section.

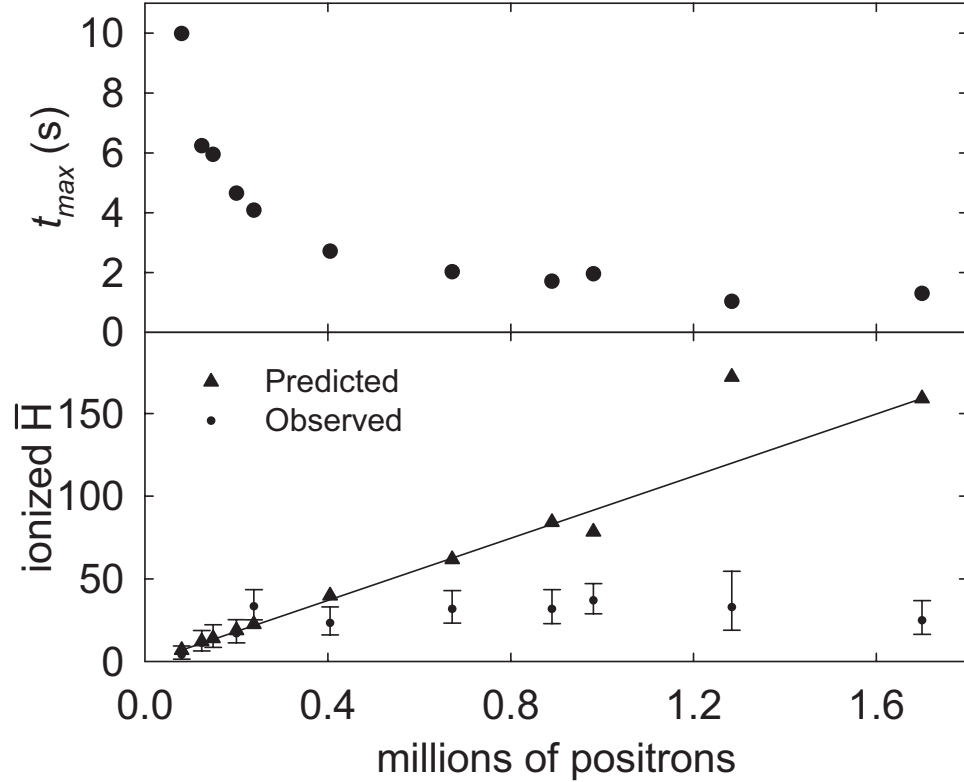


Figure 6.9: (a)  $t_{\max}$  that yields  $P_{\text{TBR}}(t_{\max}) = 1$  as a function of positron number. (b) Predicted recombination yield, as determined from  $(\text{cloud overlap})/t_{\max}$  compared with experimental results. Predicted yield is scaled to match observed yield at 0.15 million positrons.

ergy level where recombination is predicted to occur takes longer. This would allow longer for collisions amongst antiprotons to occur, presumably reducing the number of antiprotons that interact with the positrons when their temperature is low. In this case, the recombination yield might scale as  $1/t_{\max}$  – the positron-antiproton cloud overlap/ $t_{\max}$  is plotted in Fig. 6.9(b). In comparison to the experimental data, the shape of this scaling is in reasonable agreement for small positron number, but does not reproduce the observed saturation in yield for higher positron number. Hence, a more sophisticated description of the effect of these collisions is required.

Secondly, the possibility of the angular distribution being different for different positron numbers has not been considered. Insofar as the analysis above is correct, this is only a small correction since the predicted axial energy distribution of the recombined antihydrogen is similar in all cases. This can be confirmed by determining the fraction of antihydrogen atoms that would enter the ionization well when a Maxwellian radial velocity distribution is added. Only if the radial velocity component is small enough, will atoms be travelling towards the ionization well. Such a calculation does not alter the results presented in Fig. 6.9(b), and can also be compared to the results presented in Sec. 6.2.4. The resulting angular antihydrogen distribution is shown in Fig. 6.10 for several radial temperatures, while a comparison to the experimental results is shown in Fig. 6.11. Upon calculating the fraction of antihydrogen atoms that would travel in the direction of the ionization well, a variation with positron number of less than 2% is found. Also, as can be seen in Fig. 6.11, the variation of the antihydrogen detection efficiency with detection well distance is predicted to be almost insensitive to the radial temperature.

Most importantly, we have yet to consider the state distribution of the antihydrogen produced. If, for example, every antihydrogen was produced in a state that was field ionized by an electric field of less than 20 V/cm, no signal would be observed. As discussed in Sec. 1.3, the radial separation,  $\rho$ , of the antiproton and positron in an atom formed via TBR is  $\approx R_T$ , the Thompson radius, and the separation is further reduced via collisional de-excitation while the antihydrogen atom remains in the positron cloud. The dynamics of such atoms has recently been studied [69]. The atom is a close analog of a particle in a Penning trap, with the positron performing

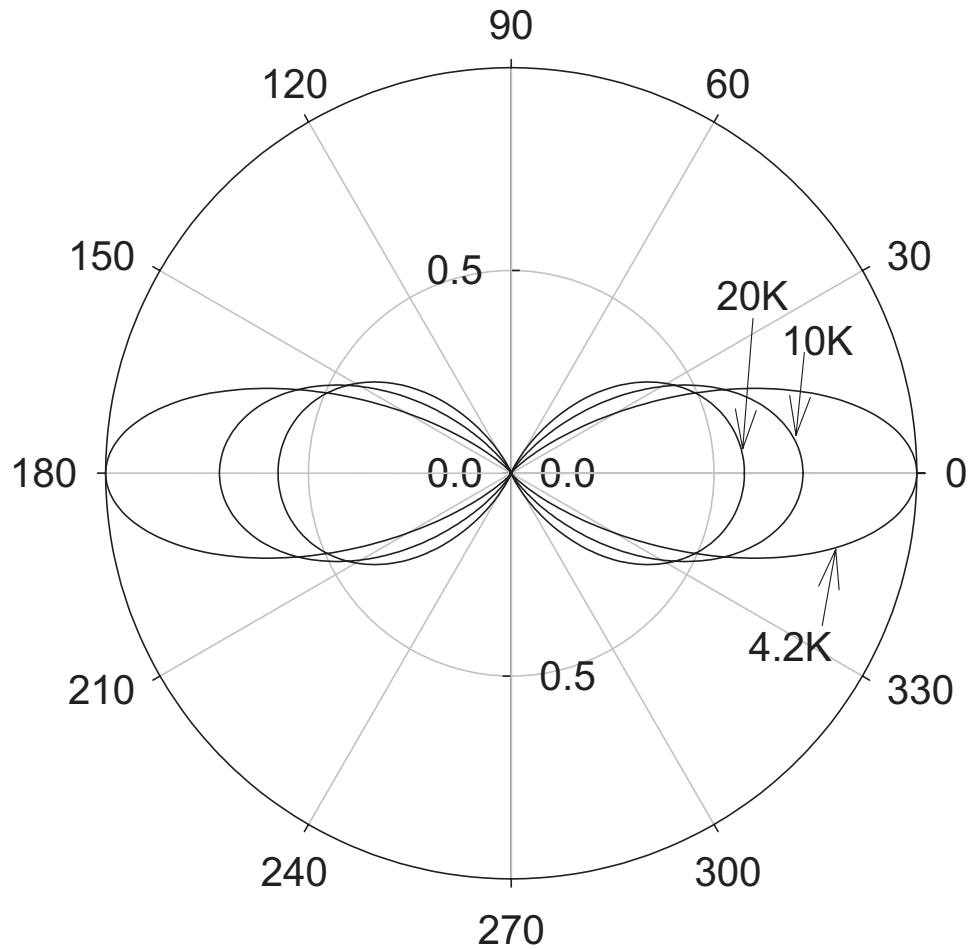


Figure 6.10: The predicted antihydrogen angular distribution for radial antiproton temperatures of 4.2 K, 10 K, and 20 K.  $0^\circ$  corresponds to the positive  $z$ -axis. There is no predicted emission at  $90^\circ$  or  $270^\circ$ , since antiprotons never reach zero axial energy.

a cyclotron motion about magnetic field lines, an axial motion along magnetic field lines, and a large magnetron orbit of radius  $\rho$  about the antiproton. The application of an axial electric field opens the axial well confining the positron. Should the positron have sufficient axial energy for a given applied electric field, it will escape and the atom will ionize (Fig. 6.12).

In the analysis of the previous section, the average positron temperature when atoms were formed was  $\approx 10$  K. It is thought [24] that the axial motion of the

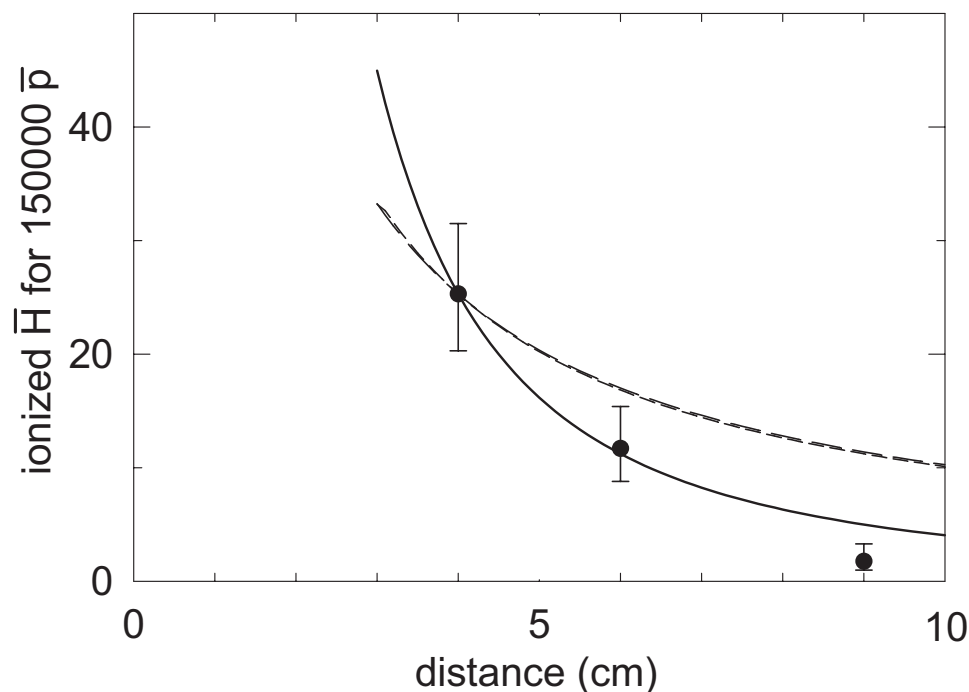


Figure 6.11: The predicted dependence of the recombination rate on ionization well distance for 4.2 K and 420 K (dashed lines). The predictions have been scaled to match the experimental data at 4 cm (solid line is  $1/r^2$  fit to experimental data).

recombined positron rapidly comes into thermal equilibrium with the surrounding positrons, so the axial energy of the recombined positron is also likely to be close to 10 K. Hence, to be stripped by the ionization well, a recombined atom must have a radial separation of  $\approx 0.25 \mu\text{m}$ . Given that  $R_T$  varies between  $4 \mu\text{m}$  and  $1.6 \mu\text{m}$  between 4.2 K and 10 K, considerable collisional de-excitation must occur for any signal to be seen.

Collisions with an impact parameter less than  $\rho$  (replacement collisions) are the initial means of de-excitation [24, 25], perhaps followed by longer range collisions giving rise to inward diffusion of the bound positron (transverse collisional drift<sup>4</sup>) [25].

<sup>4</sup>Recent investigations suggest that the presence of an adiabatic invariant halts this process just as it begins [70].

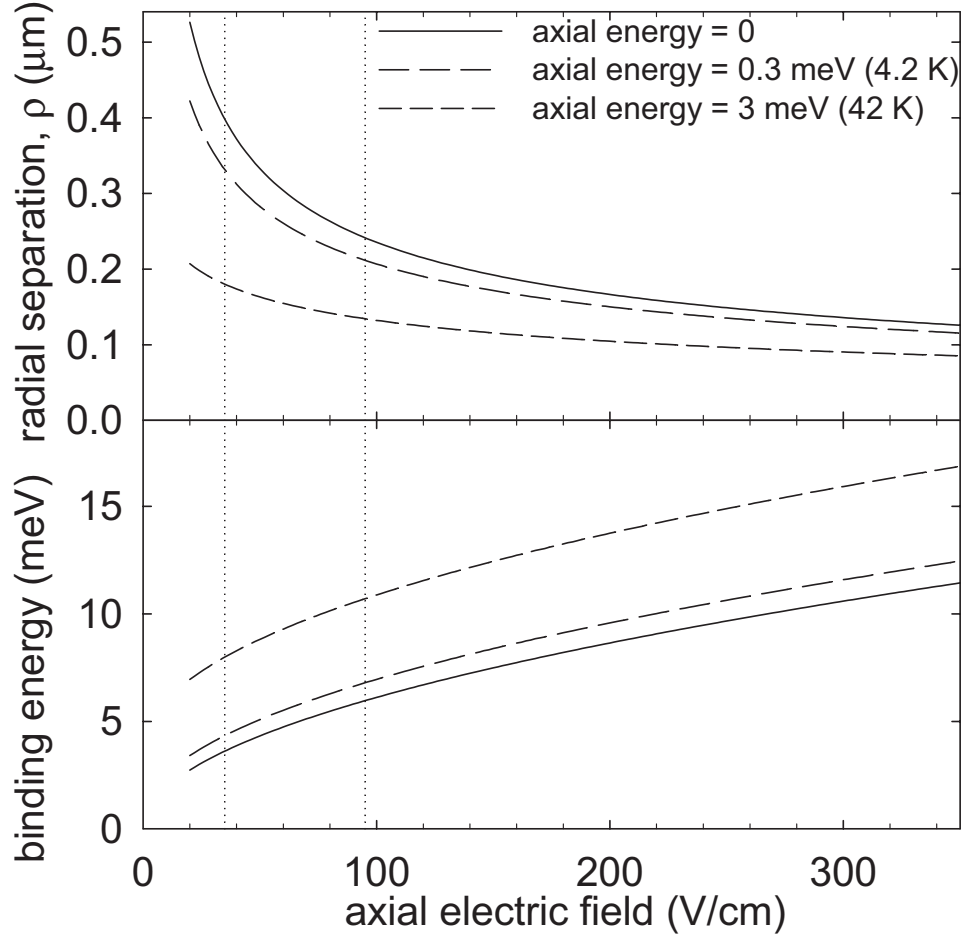


Figure 6.12: The applied axial electric field required to ionize an atom with radial separation  $\rho$  (a) or binding energy  $E_b$  (b). The dotted vertical lines mark the electric field range of the ionization well. Taken from [69].

Of course, these processes can occur only during the time that the antihydrogen atom remains in the positron cloud. In [25] these two processes are described by the rate at which they change  $\rho$ :

$$\begin{aligned} \frac{d\rho}{dt} &= \frac{d\rho_r}{dt} + \frac{d\rho_d}{dt} \\ &= -n_{e^+} v_{th} \rho^3 - \frac{D}{kT} \frac{e^2}{4\pi\epsilon_0\rho^2}, \end{aligned} \quad (6.8)$$

where  $D$  is a diffusion constant. Numerical solutions to this equation for relevant

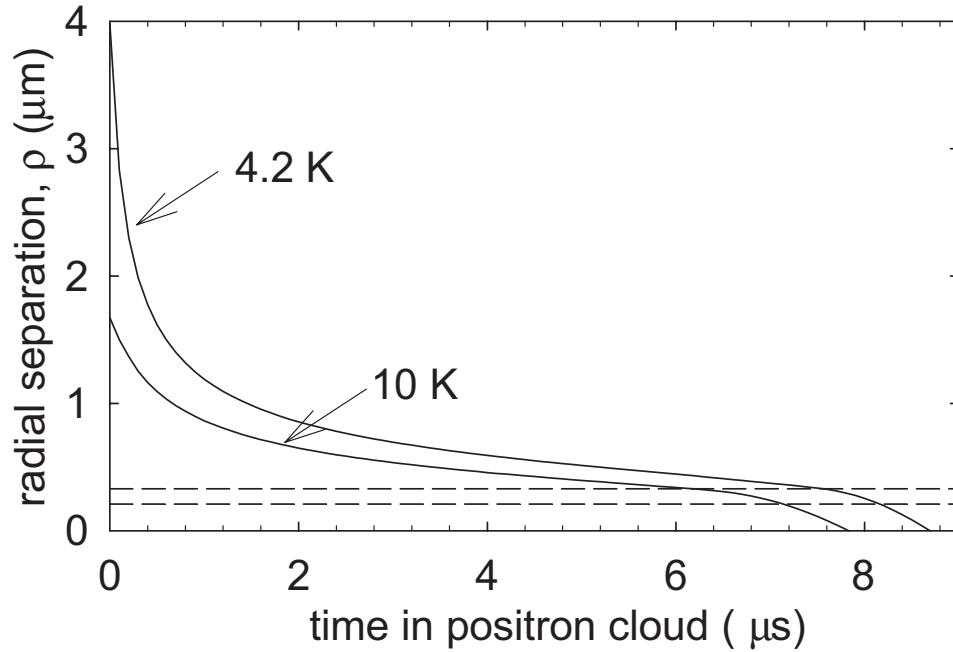


Figure 6.13: The time evolution of  $\rho$  for  $T_{e^+} = 4.2$  K and 10 K, as described by Eqn. 6.8. Dashed horizontal lines give the approximate range between which atoms are stripped by the ionization well.

positron temperatures are shown in Fig. 6.13. It is clear from Fig. 6.13 that the use of large (longer) positron clouds results in the production of more deeply bound states. Bearing in mind that for even the largest positron cloud used, the longest time that can be spent in the positron cloud is  $\approx 1 \mu\text{s}$ , we see that this theory predicts no production of antihydrogen bound deeply enough to be detected.

However, the progression described by Eqn. 6.8 is the average rate of change of the separation. Of course, there are fluctuations about the mean value: Some atoms will experience more collisions than the average, while others will experience less. This was studied for replacements collisions in [24] by means of a Monte Carlo simulation. As was recently pointed out [71], the distribution of bound states produced after a single pass through a positron cloud is observed to relax towards a distribution of the

form

$$W_{th}(\epsilon) = \left( \frac{5\pi^{3/2}}{4} \right) n_{e^+} R_T^3 \epsilon^{-7/2} \exp(\epsilon), \quad (6.9)$$

where  $\epsilon = E_b/kT_{e^+}$  is the scaled binding energy of the antihydrogen atom. The distribution is filled to a depth  $\epsilon_0 = (t_c/\tau)^{1/2}$ , that depends upon the time spent in the positron cloud after recombination,  $t_c$ , scaled by the average positron-positron collision time,  $\tau = (n_{e^+} v_{th} R_T^2)^{-1}$ . Beyond a binding energy of  $\epsilon_0 kT_{e^+}$ , there is a low probability tail that is observed to scale as

$$W(\epsilon, \epsilon_0) \approx \left( \frac{\epsilon}{\epsilon_0} \right)^{-8} W_{th}(\epsilon). \quad (6.10)$$

Clearly, states bound more deeply than  $\epsilon_0$  are strongly suppressed. Thus, the total distribution function is

$$W_{total}(\epsilon, \epsilon_0) \approx \left( H(\epsilon_0 - \epsilon) \left( \frac{\epsilon}{\epsilon_0} \right)^{-8} + H(\epsilon - \epsilon_0) \right) W_{th}(\epsilon), \quad (6.11)$$

where  $H(x)$  is a step function.

It is important to note that the distribution given by Eq. 6.11 has a surprising temperature dependence [71],

$$W_{total} \propto T_{e^+}^{5/2}, \quad (6.12)$$

so that greater amounts of antihydrogen are predicted to be produced at higher temperatures, contrary to scaling predicted by Eq. 6.1. As yet there is no explanation for this substantial discrepancy, and accordingly, it is unclear that it is appropriate to use  $W_{total}$  to predict the amount of deeply bound antihydrogen that we are producing. However, there is an important observation that can be made. The atoms that are observed via the ionization well are those that have undergone many de-exciting collisions. These are more likely to occur the slower the antihydrogen is

moving through the positron cloud and thus, the observed atoms are likely to have a lower than average kinetic energy. Hence, it is likely that the average energy of the antihydrogen that we observe is less than the 25 K calculated above.

To make further progress in this analysis we require a means of modelling the effect of antiproton-antiproton collisions and the de-excitation process. It is possible that in both cases unlikely events are those that are important; it may be that the antiprotons that recombine into deeply bound antihydrogen are those few that do not suffer any antiproton-antiproton collisions while at low energies relative to the positron cloud and that once recombined suffer an above average number of collisions with positrons. This would be most readily studied via a Monte-Carlo simulation.

# Chapter 7

## Conclusion

Using the highly successful techniques developed by our collaboration to accumulate both positrons [5, 6] and antiprotons [3], and to make them interact [7, 8] we have been able to produce cold antihydrogen. This is a crucial first step towards a precision test of *CPT* invariance using cold, trapped antihydrogen, and our results point towards many future areas of investigation.

All of the techniques mentioned above have been further investigated and refined here. The careful installation of a much more intense radioactive source has increased the positron accumulation rate by more than an order of magnitude compared to that obtained in [6], and new manipulation techniques have been developed to make more efficient use of those positrons.

The stacking of cold antiprotons is essential to the success of our experiments, since this is the only available technique for accumulating the large numbers of antiprotons that we require. Here, we have demonstrated the ability to accumulate as many as 400,000 cold antiprotons [4], a number more than sufficient for our present needs.

Should future experiments require yet greater numbers, the careful addition of more electron cooling wells should provide this capability.

Amongst the most important investigations presented here are those that study the interaction of positrons and antiprotons in the nested Penning trap [7] – the only device in which the production of cold antihydrogen has been observed [9, 1, 60]. Following our collaboration’s first demonstration of the positron cooling of antiprotons [8], we have conducted a much more detailed investigation. By making many measurements of the rate of the cooling under different experimental circumstances we have been able to constrain the value of a theoretical cutoff parameter. Not only does this provide new insight into the physics of the cooling process, but it has also allowed us to calculate important parameters that can not otherwise be measured, e.g. the variation of the positron temperature as the cooling progresses.

Despite the great success of the nested Penning trap as a device for producing antihydrogen, our studies have also discovered two disadvantageous features. In each case, methods have been developed to overcome these problems. First, collisional redistribution of axial energy amongst antiprotons causes many to reach energies below that at which the positrons reside, inhibiting recombination. Further collisions amongst antiprotons in the side wells of the nested Penning trap allow a small fraction to continue interacting with the positrons, resulting in recycled evaporative cooling. This problem is alleviated by the application of a gentle axial drive to the antiprotons in the side well [60, 28] which are given enough axial energy to interact with the positrons so that recombination can proceed.

The second disadvantageous feature of the nested Penning trap is the unexplained

radial loss of antiprotons. When positrons are present, it is likely that some of the loss is due to the formation of antihydrogen. However, given that radial loss is also observed without positrons, it is very likely that some of the loss is simply antiprotons leaving the trap without being bound to a positron. As antiproton annihilations can generate positrons, an antihydrogen detection scheme based upon the simultaneous detection of positron and antiproton annihilations must include careful control experiments in which antiprotons are dumped radially to the electrodes. We have avoided this problem completely by the use of the direct field ionization detection method. This detection method was carefully designed so as to be insensitive to antiproton losses from the nested Penning trap.

As mentioned above, we have successfully applied theoretical results to our positron cooling measurements, and thus have gained further insight into the physical processes occurring. Other areas that would gain from theoretical insight are the unexplained antiproton loss from the nested Penning trap (if this could be avoided more antihydrogen would be produced from antiprotons that would otherwise be lost), a description of the antiproton-antiproton collisions to complement the cooling rate theory, and investigations into surface layers that might increase the Rydberg positronium formation rate for positron accumulation.

Looking to the future, the next step for ATRAP is the de-excitation and trapping of antihydrogen. These two aims are complementary: The very coldest antihydrogen produced will move slowly through the remainder of the positron cloud after recombination, and will thus suffer more de-excitating collisions. The crucial technique will thus be the ability to introduce antiprotons into the positron cloud with very little ki-

netic energy. Again, the driven technique of [60, 28] seems ideal. With careful tuning of the drive strength and frequency it might be possible to just “trickle” antiprotons over the central well and slowly through the positron cloud.

Of course, larger positron clouds would aid the de-excitation. The techniques developed here to accumulate and transfer large clouds have already been used to conduct interaction experiments using 5 million positrons, but it is likely that even more positrons will be required to produce substantial numbers of ground state atoms. Thus, work should continue on the accumulation and manipulation of large electron clouds, so that these can be used to accumulate positrons. The possibility of using large electron clouds placed outside the nested Penning trap to de-excite antihydrogen travelling along the trap axis could also be investigated. The other reason that such work on electron clouds is important is the strong dependence of the positron accumulation rate upon the magnetic field strength. To allow antihydrogen trapping, the Penning trap magnetic field will have to be reduced. Unless an additional solenoid is added solely around the positron accumulation region or a new high efficient surface layer is found, a different accumulation technique will be required, e.g. electron cooling of moderated positrons.

Work presently being carried out on laser-assisted de-excitation and recombination schemes is important, especially due to the experience that will be gained bringing lasers into the cryogenic Penning trap environment. Of course, this experience will prove invaluable when the time comes to laser-cool trapped antihydrogen and perform spectroscopic measurements upon it.

# Appendix A

## Radiation Shielding Calculation

Here we calculate the thickness of lead shielding required to reduce the dose rate 1 m from the 150 mCi  $^{22}\text{Na}$  source to the background level ( 0.015 mrem/hr).

First we calculate the dose rate without shielding. The total dose rate  $D$  in mrem/hr is given by [72];

$$D = \frac{0.5A \sum_i n_i E_i}{d^2}, \quad (\text{A.1})$$

where  $A$  is the source activity in mCi,  $d$  is the distance from the source in meters,  $i$  is the number of distinct  $\gamma$ -rays that the source emits,  $E_i$  is the  $\gamma$ -ray energy in MeV, and  $n_i$  is the number of  $\gamma$ -rays of energy  $E_i$  emitted per decay.

For  $^{22}\text{Na}$  there are two distinct  $\gamma$ -rays (Fig. 3.1); on average each decay produces a single 1.275 MeV  $\gamma$ -ray and 1.8 0.511 MeV  $\gamma$ -rays. Thus,

$$\begin{aligned} D_{\text{total}} &= D_{1.275} + D_{0.511} \\ &= 95.6 \text{ mrem/hr} + 68.4 \text{ mrem/hr} \end{aligned}$$

$$= 164 \text{ mrem/hr}, \quad (\text{A.2})$$

which is very much larger than background.

To accurately calculate the thickness of shielding required we can not simply use the usual exponential attenuation formula for  $\gamma$ -rays:

$$D = D_0 e^{-\mu x}, \quad (\text{A.3})$$

where  $\mu$  is the linear attenuation coefficient, and  $x$  is the thickness of the shielding. This formula only accounts for scattering of the primary  $\gamma$ -rays; it does not account for the scattered  $\gamma$ -rays, and thus overestimates the effectiveness of the shielding. The effect of the scattered  $\gamma$ -rays can be estimated by modifying Eqn. A.3 to include a “buildup” factor,  $B$  [73]

$$D = B(x) D_0 e^{-\mu x}. \quad (\text{A.4})$$

Values for  $B$  are tabulated in [73] for various materials as a function of  $\gamma$ -ray energy and shielding thickness. In this case we wish to solve Eqn. A.4 for  $x$  given  $D$  and  $D_0$ . Since the functional form of  $B(x)$  is not known, we make successive approximations until we find that value of  $x$  which satisfies Eqn. A.4. In fact, since there two distinct  $\gamma$ -rays involved, we must find a value for  $x$  such that the sum of the attenuated dose rates is equal to our desired value.

We begin by considering the “harder” of the two  $\gamma$ -rays at 1.275 MeV. At this energy the  $1/\mu_{\text{lead}} = 1.52 \text{ cm}^1$ . Our initial guess for the target activity is 0.01 mrem/hr, and initially assuming no buildup, our first guess for  $x$  is obtained by solving:

$$0.01 = 95.6 \times e^{-x/1.52}, \quad (\text{A.5})$$

---

<sup>1</sup>Mass attenuation coefficients as a function of energy can be found for many materials at <http://physics.nist.gov/PhysRefData/XrayMassCoef/cover.html>

yielding  $x \approx 14$  cm. But for lead at 1.275 MeV,  $B(14_{\text{cm}}) \approx 4.5$ , hence more shielding will be required. We guess that about 2 cm more thickness will be required. Then the dose rate will be:

$$D_{1.275} \approx 4.6 \times 95.6 \times e^{-16/1.52} \approx 0.011 \text{ mrem/hr.} \quad (\text{A.6})$$

We now calculate the dose rate from the 0.511 MeV  $\gamma$ -rays with this shielding thickness. At this energy,  $1/\mu_{\text{lead}} = 1.82$  cm, and  $B(16_{\text{cm}}) \approx 2.1$  and thus the dose rate will be:

$$D_{0.511} \approx 2.1 \times 68.4 \times e^{-16/1.82} \approx 0.021 \text{ mrem/hr,} \quad (\text{A.7})$$

so that the total dose rate with 16 cm of lead would be  $\approx 0.03$  mrem/hr, or twice the background rate. Note that even though the lower energy  $\gamma$ -rays have a smaller build up factor and a smaller initial dose, they are less effectively attenuated than the 1.275 MeV  $\gamma$ -rays and at this thickness contribute a higher dose.

To reach a dose equivalent to background, we will need more than 16 cm of lead. Evaluating the total dose for 17.5 cm we find:

$$\begin{aligned} D_{\text{total}} &= 2.2 \times 68.4 \times e^{-17.5/1.82} + 5.3 \times 95.6 \times e^{-17.5/1.52} \\ &= 0.009 \text{ mrem/hr} + 0.005 \text{ mrem/hr} \\ &= 0.014 \text{ mrem/hr,} \end{aligned} \quad (\text{A.8})$$

which is less than the background dose rate.

# Appendix B

## Positron Production Calculation

Here we make only a rough estimates of the likelihood of an antiproton annihilation producing a positron within a certain range. The problem is complicated, and is probably best treated via a Monte Carlo simulation.

We begin by considering the ATHENA apparatus. Antihydrogen and antiprotons will annihilate on the electrodes, which are made of gold plated aluminum. We consider only the worst case, that is annihilation products travelling along the electrodes, interacting with the maximum amount of material. We estimate the likelihood of a positron being produced by an antiproton annihilation within the 8 mm position sensitivity claimed for the ATHENA detector.

There are two ways in which positrons might be created. In the first a  $\pi^0$  meson produced by an antiproton annihilation decays into two  $\gamma$ -rays. These  $\gamma$ -rays can then produce electron-positron pairs during interactions with matter:

$$\pi^0 \rightarrow 2\gamma$$

$$\gamma + Z \rightarrow e^- + e^+ + \gamma' + Z.$$

The  $\gamma$ -rays have an energy of at least 67 MeV, while the positron can be produced with an energy ranging from 0 to  $\approx (E_\gamma - 1.022)/2$  MeV. Taking the worst case, we will consider a  $\gamma$ -ray energy of 100 MeV and a positron energy of 0 MeV. The linear attenuation coefficient of aluminum in this energy range is  $\approx 8 \times 10^{-2}/\text{cm}$ . Assuming this is all due to pair production (again the worst case), the probability of producing a positron that will annihilate within 8 mm is

$$(1 - e^{-0.8 \times 8 \times 10^{-2}}) = 0.062. \quad (\text{B.1})$$

The second possibility for producing a positron is via a  $\gamma$ -ray emitted by a gold nuclei upon which the antiproton annihilates. Let us suppose this  $\gamma$ -ray has an energy of 10 MeV. The linear attenuation coefficient in aluminum is then is  $\approx 6 \times 10^{-2}/\text{cm}$  and the probability of producing a positron is

$$(1 - e^{-0.8 \times 6 \times 10^{-2}}) = 0.047. \quad (\text{B.2})$$

So even in this worst case estimate, the probability of producing a positron within the resolution of the detector is low.

Turning our attention to the ATRAP apparatus, the situation is somewhat different. The material involved is gold plated copper, and resolution of the detector is poor. For example, for positron detection there is no resolution long the  $z$ -axis. Hence, if we consider annihilation products travelling along the electrodes, they could travel the entire length of the electrode stack before converting to a positron. Let us estimate the conversion probability within 5 cm of annihilation site. For a 100 MeV  $\gamma$ -ray the linear attenuation coefficient is  $\approx 1.3 \times 10^{-1}$ , so that the approximate

conversion probability in 5 cm is

$$(1 - e^{-5 \times 1.3 \times 10^{-1}}) = 0.48, \quad (\text{B.3})$$

and for a 10 MeV  $\gamma$ -ray it is

$$(1 - e^{-5 \times 8 \times 10^{-2}}) = 0.33. \quad (\text{B.4})$$

Clearly, the situation is worst for the ATRAP apparatus, due both to the more dense material used and the lack of spatial resolution.

# Bibliography

- [1] G. Gabrielse, N. S. Bowden, P. Oxley, A. Speck, C. H. Storry, J. N. Tan, M. Wessels, D. Grzonka, W. Oelert, G. Schepers, T. Sefzick, J. Walz, H. Pittner, T. W. Hansch, and E. A. Hessels, *Phys. Rev. Lett.* **89**, 213401 (2002).
- [2] G. Gabrielse, in *Fundamental Symmetries*, edited by P. Bloch, P. Paulopoulos, and R. Klapisch (Plenum, New York, 1987), p. 59.
- [3] G. Gabrielse, *Adv. At. Mol. Opt. Phys.* **45**, 1 (2000).
- [4] G. Gabrielse, N. S. Bowden, P. Oxley, A. Speck, C. H. Storry, J. N. Tan, M. Wessels, D. Grzonka, W. Oelert, G. Schepers, T. Sefzick, J. Walz, H. Pittner, T. W. Hansch, and E. A. Hessels, *Phys. Lett. B* **548**, 140 (2002).
- [5] G. Gabrielse, D.S. Hall, T. Roach, P. Yesley, A. Khabbaz, J. Estrada, C. Heimann, and H. Kalinowsky, *Phys. Lett. B* **455**, 311 (1999).
- [6] J. Estrada, T. Roach, J. N. Tan, P. Yesley, and G. Gabrielse, *Phys. Rev. Lett.* **84**, 859 (2000).
- [7] G. Gabrielse, S. L. Rolston, L. Haarsma, and W. Kells, *Phys. Lett.* **A129**, 38 (1988).
- [8] G. Gabrielse, J. Estrada, J. N. Tan, P. Yesley, N. S. Bowden, P. Oxley, T. Roach, C. H. Storry, M. Wessels, J. Tan, D. Grzonka, W. Oelert, G. Schepers, T. Sefzick, W. Breunlich, M. Carngelli, H. Fuhrmann, R. King, R. Ursin, H. Zmeskal, H. Kalinowsky, C. Wesdorp, J. Walz, K. S. E. Eikema, and T. W. Hansch, *Phys. Lett. B* **507**, 1 (2001).
- [9] M. Amoretti, C. Amsler, G. Bonomi, A. Bouchta, P. Bowe, C. Carraro, C. L. Cesar, M. Charlton, M. J. T. Collier, M. Doser, V. Filippiniq, K. S. Fine, A. Fontanaq, M. C. Fujiwara, R. Funakoshi, P. Genova, J. S. Hangst, R. S. Hayano, M. H. Holzscheiter, L. V. Jrgensen, V. Lagomarsino, R. Landua, D. Lindelo, E. Lodi Rizzini, M. Macry, N. Madsen, G. Manuzio, M. Marchesottiq, P. Montagnaq, H. Pruys, C. Regenfus, P. Riedler, J. Rochet, A. Rotondiq, G. Rouleau, G. Testera, A. Variola, T. L. Watson, and D. P. van der Werf, *Nature* **419**, 456 (2002).

- 
- [10] R.G. Sachs, *The Physics of Time Reversal* (University of Chicago Press, Chicago, 1987).
- [11] T. D. Lee and C. N. Yang, Phys. Rev. **104**, 254 (1956).
- [12] C. S. Wu, E. Ambler, R. W. Hayward, D. D. Hoppes, and R. P. Hudson, Phys. Rev. **105**, 1413 (1957).
- [13] J. H. Christenson, J. W. Cronin, V. L. Fitch, and R. Turlay, Phys. Rev. Lett. **13**, 138 (1964).
- [14] R. Bluhm, V. A. Kostelecky, and N. Russell, Phys. Rev. Lett. **82**, 2252 (1999).
- [15] M. Niering, R. Holzwarth, J. Reichert, P. Pokasov, M. Weitz Th. Udem and, T. W. Hansch, P. Lemonde, G. Santarelli, M. Abgrall, P. Laurent, C. Salomon, and A. Clairon, Phys. Rev. Lett. **84**, 5496 (2000).
- [16] G. Baur, G. Boero, S. Brauksiepe, A. Buzzo, W. Eyrich, R. Geyer, D. Grzonka, J. Hauffe, K. Kilian, M. Lo Vetereb, M. Macrib, M. Moosburgerc, R. Nellen, W. Oelert, S. Passaggio, A. Pozzo, K. Rhrich, K. Sachs, G. Schepers, T. Sefzick, R. S. Simon, R. Stratmann, F. Stinzing, , and M. Wolke, Phys. Lett. B **368**, 251 (1996).
- [17] G. Blanford, D. C. Christian, K. Gollwitzer, M. Mandelkern, C. T. Munger, J. Schultz, , and G. Zioulas, Phys. Rev. Lett. **80**, 3037 (1998).
- [18] T.M. Squires, P. Yesley, and G. Gabrielse, Phys. Rev. Lett. **86**, 5266 (2001).
- [19] K. S. E. Eikema, J. Walz, and T. W. Hansch, Phys. Rev. Lett. **83**, 3828 (1999).
- [20] J. W. Humberston, M. Charlton, F. J. Jacobsen, and B. I. Deutch, J. Phys. B **20**, 25 (1987).
- [21] M. Charlton, Phys. Rev. A **143**, 143 (1990).
- [22] E. A. Hessels, D. M. Homan, and M. J. Cavagnero, Phys. Rev. A **57**, 1668 (1998).
- [23] C. Wesdorp, F. Robicheaux, and L. D. Noordam, Phys. Rev. Lett. **84**, 3799 (2000).
- [24] M. E. Glinsky and T. M. O'Neil, Phys. Fluids B **3**, 1279 (1991).
- [25] P. O. Fedichev, Phys. Lett. A **226**, 289 (1997).
- [26] Hans A. Bethe and Edwin E. Salpeter, *Quantum Mechanics of One and Two Electron Atoms* (Springer Verlag, New York, 1957).

- 
- [27] G. Gabrielse, X. Fei, L.A. Orozco, R.L. Tjoelker, J. Haas, H. Kalinowsky, T. Trainor, and W. Kells, *Phys. Rev. Lett.* **63**, 1360 (1989).
- [28] P. K. Oxley, Ph.D. thesis, Harvard University, 2003.
- [29] L. S. Brown and G. Gabrielse, *Rev. Mod. Phys.* **58**, 233 (1986).
- [30] M. E. Glinsky, T. M. O'Neil, M. N. Rosenbluth, K. Tsuruta, and S. Ichimaru, *Phys. Fluids B* **4**, 1156 (1992).
- [31] G. Gabrielse, L. Haarsma, and S. L. Rolston, *Intl. J. of Mass Spec. and Ion Proc.* **88**, 319 (1989).
- [32] P.S. Yesley, Ph.D. thesis, Harvard University, 2001.
- [33] G. Gabrielse, X. Fei, L.A. Orozco, R.L. Tjoelker, J. Haas, H. Kalinowsky, T. Trainor, and W. Kells, *Phys. Rev. Lett.* **65**, 1317 (1990).
- [34] B. D'urso, Ph.D. thesis, Harvard University, 2003.
- [35] D. S. Hall, Ph.D. thesis, Harvard University, 1997.
- [36] H. Stelzer, *Nucl. Insrt. and Meth.* **133**, 409 (1976).
- [37] G. Gabrielse, X. Fei, L.A. Orozco, S.L. Rolston, R.L. Tjoekler, T.A. Trainor, J. Haas, H. Kalinowsky, and W. Kells, *Rapid Comm. Of Physics Rev. A* **40**, 481 (1989).
- [38] X. Fei, Ph.D. thesis, Harvard University, 1990.
- [39] T. Goetz, Diploma thesis, Forschungszentrum Juelich, 2001.
- [40] G. Schepers, ATRAP Collaboration Internal Report (unpublished).
- [41] D. A. Edwards and M. J. Syphers, *An Introduction to the Physics of High Energy Accelerators* (Wiley, New York, 1993).
- [42] W. Kells, in *Physics of High Energy Particle Accelerators* (AIP Conf. Proc. 87, New York, 1982).
- [43] P. J. Schultz and K. G. Lynn, *Rev. Mod. Phys.* **60**, 701 (1988).
- [44] L. D. Hulett, J. M. Dale, and S. Pendyala, *Surf. Interf. Anal.* **2**, 204 (1980).
- [45] G. R. Massoumi, Peter J. Schultz, W. N. Lennard, and J. Ociepa, *Nucl. Insrt. and Meth. B* **30**, 592 (1988).
- [46] T. Roach, ATRAP Collaboration Internal Report (unpublished).

- [47] D. F. Wilcock, *Bearing Design and Application* (McGraw-Hill, New York, 1957).
- [48] J. K. Estrada, Ph.D. thesis, M.I.T., 2002.
- [49] J. Schou, Nucl. Insrt. and Meth. B **27**, 188 (1987).
- [50] F. Golek and E. Bauer, Surf. Sci. **369**, 415 (1996).
- [51] W. S. Vogan, S. G. Walton, and R. L. Champion, Surf. Sci. **459**, 14 (2000).
- [52] D. P. van der Werf, L. V. Jrgensen, T. L. Watson, M. Charlton, M. J. T. Collier, M. Doser, and R. Funakoshi, Appl. Surf. Sci. **194**, 312 (2002).
- [53] Nagayasu Oshima, Takao M. Kojima, Dana Dumitriu, Akihiro Mohri, Hitoshi Oyama, Tadashi Kambara, Yasuyuki Kanai, Yoichi Nakai, Michiharu Wada, , and Yasunori Yamazaki, RIKEN Review **31**, 65 (2000).
- [54] N. Oshima, Private Communication.
- [55] C. Gahn, G. D. Tsakiris, G. Pretzler, , K. J. Witte, P. Thirolf, D. Habs, C. Delfin, and C.-G. Wahlstrom, Phys. Plasmas **9**, 987 (2002).
- [56] G. Gabrielse, X. Fei, K. Helmerson, S. L. Rolston, R. Tjoelker, T. A. Trainor, H. Kalinowsky, J. Haas, and W. Kells, Phys. Rev. Lett. **57**, 2504 (1986).
- [57] R. L. Tjoelker, Ph.D. thesis, Harvard University, 1990.
- [58] S. L. Rolston and G. Gabrielse, Hyperfine Interactions **44**, 233 (1988).
- [59] P. K. Oxley *et al.*, To be published.
- [60] G. Gabrielse, N. S. Bowden, P. Oxley, A. Speck, C. H. Storry, J. N. Tan, M. Wessels, D. Grzonka, W. Oelert, G. Schepers, T. Sefzick, J. Walz, H. Pittner, T. W. Hansch, and E. A. Hessels, Phys. Rev. Lett. **89**, 233401 (2002).
- [61] D. S. Hall and G. Gabrielse, Phys. Rev. Lett. **77**, 1962 (1996).
- [62] Yongbin Chang and C. A. Ordonez, Phys. Rev. E **62**, 8564 (2000).
- [63] J. R. Correa, Yongbin Chang, and C. A. Ordonez, in *Physics of Nonneutral Plasma Physics IV*, edited by F. Anderegg, L. Schweikhard, and C. F. Driscoll (AIP Conf. Proc. No. **606**, AIP, Melville, NY, 2002), p. 544.
- [64] D. H. E. Dubin, Phys. Plasmas **5**, 1688 (1998).
- [65] C. A. Ordonez, D. D. Dolliver, Yongbin Chang, and J. R. Correa, Phys. Plasmas **9**, 3289 (2002).

- 
- [66] R. J. Goldston and P. H. Rutherford, *Intoduction to Plasma Physics* (IOP, London, 1995).
- [67] G. Schepers, Private Communication.
- [68] A. Speck, Private Communication.
- [69] D. Vinceanu, B. E. Granger, R. Parrott, H. R. Sadeghpour, L. Cederbaum, A. Mody, J. N. Tan, and G. Gabrielse, To be published.
- [70] G. Gabrielse, Private Communication.
- [71] C. F. Driscoll, Comment submitted to Phys. Rev. Lett. (2003).
- [72] J. Shapiro, *Radiation Protection* (Harvard University Press, Cambridge, 1990).
- [73] J. E. Turner, *Atoms, Radiation, and Radiation Protection* (Pergamon Press, New York, 1986).